



HAL
open science

Conception, construction and validation of scientific instruments to study the spectrum of cold ionic species

Raghd Bejjani

► **To cite this version:**

Raghd Bejjani. Conception, construction and validation of scientific instruments to study the spectrum of cold ionic species. Instrumentation and Detectors [physics.ins-det]. Université de Rennes 1; Université Catholique de Louvain (Belgique), 2021. English. NNT: . tel-03430562v1

HAL Id: tel-03430562

<https://hal.science/tel-03430562v1>

Submitted on 16 Nov 2021 (v1), last revised 11 Jan 2022 (v2)

HAL is a multi-disciplinary open access archive for the deposit and dissemination of scientific research documents, whether they are published or not. The documents may come from teaching and research institutions in France or abroad, or from public or private research centers.

L'archive ouverte pluridisciplinaire **HAL**, est destinée au dépôt et à la diffusion de documents scientifiques de niveau recherche, publiés ou non, émanant des établissements d'enseignement et de recherche français ou étrangers, des laboratoires publics ou privés.

THÈSE DE DOCTORAT DE

L'UNIVERSITÉ DE RENNES 1

ÉCOLE DOCTORALE N° 596

Matière, Molécules, Matériaux

Spécialité : « *Ecole doctorale matière, Molécule et Matériaux (3M)* »

Par

« **Raghd BEJJANI** »

« **Conception, construction and validation of scientific instruments to study the spectrum of cold ionic species** »

« Thèse en Physique »

Thèse présentée et soutenue à « **Rennes - France** », le « **8 octobre 2021** »

Unité de recherche : « **Institut de physique de Rennes** »

Rapporteurs avant soutenance :

Pierre Asselin Sorbonne université, France
Olivier Pirali Université Paris-Saclay, France

Composition du Jury :

Président :	Arnaud Delcorte	UCLouvain, Belgique
Examineurs :	Annemieke Petrignani	Université d'Amsterdam, Pays-Bas
	Clément Lauzin	UCLouvain - Belgique
	Abdessamad Benidar	Université de Rennes 1, France
Dir. de thèse :	Xavier Urbain	UCLouvain, Belgique
	Robert Georges	Université de Rennes 1, France

ACKNOWLEDGEMENT

First of all, I would like to express my gratitude to the members of the jury: **Olivier Pirali**, **Pierre Asselin**, **Arnaud Delcorte**, and **Annemieke Petrignani**. Thank you for taking the time to read and evaluate my dissertation, for your insightful questions and valuable comments.

As soon as I arrived in Belgium, **Clément Lauzin**, made sure of my well-being at work. Clément helped me to reach a higher potential and to think outside the box. His professional advice and guidance took my thesis to where it is now. I would also like to underline his remarkable work ethic, his attention to detail, as well as his constant scientific and personal support. I will always be grateful for his ruthless honesty, from which I have learned a lot, and the time he invested in my development as a researcher. We were successful in solving most of the issues we encountered regarding paperwork and technical issues during the development of the STARGATE instrument.

I feel lucky to have worked with **Xavier Urbain**. I would like to thank him for his precious advices and suggestions during my stay at UCLouvain. I learned from him that for every problem encountered, there is a simple and effective solution. His enthusiasm for physics, his invaluable knowledge and his critical mind have in part shaped my way of thinking and guided my understanding of the subject. I also want to express my deep gratitude to **Daniel Dedouaire**, besides his positive and fun attitude, he has helped me solve most of the technical issues I have encountered, and I have learned a lot from his solid experience in vacuum physics and design of mechanical parts.

I would like to thank all the other members of the laboratory, starting with **Guilhem Vanlancker** for his responsiveness, for having benefited from his skills in electronics, and for his involvement in the development of STARGATE, **Hervé Laurent**, I continue with the whole team of the mechanical workshop, **Laurence Lenoir** for her struggle with the administrative paperwork and for her kindness that I will never forget and all the members of NAPS. I would also like to thank **Anthony Roucou** for taking over the STARGATE instrument and turning all our efforts into a scientific publication.

Finally, I am happy to have met a friend and a colleague **Alexis Libert**. He first introduced himself by showing me how to stabilize a laser (the best icebreaker ever). He

helped me during my stay in Belgium in many ways, socially by making me meet a lot of his friends, scientifically by helping me in my research and mentally by showing me that a person can do whatever he wants (he is an engineer, physicist, carpenter, beekeeper, and arborist and will undoubtedly develop many other talents in the future). I was happy that he visited me in Lebanon and met my family and friends.

I would like to thank **Abdessamad Benidar** for his welcome and his support in Rennes. We worked hard to implement the new setup and got the first result later in my first year in Rennes. He helped me understand the principles of the Laval nozzle, and helped me a lot with the jet simulations.

I will never forget **Robert Georges** for his scientific advice and his cool attitude which made our daily discussions more interesting, especially in the last months of this thesis. I learned a lot from him and his knowledge of supersonic jet expansion and spectroscopy. I thank him for the time he gave me, especially the time to correct this manuscript and for helping to prepare my thesis defense.

I would like to thank the whole IPR group without forgetting anyone, in particular my colleagues, **Eszter**, **Ahmad** and **Olivier**.

My friends in Lebanon, Belgium and France have produced a lot of memories. I appreciated their presence during this period. Finally, I could not go to the end of these thanks without mentioning my family in Lebanon who always supported me even if they had no idea what I was doing! they always stayed close, despite the distance that separated us.

FOREWORD

This thesis was performed under the joint supervision of the Institute of Physics of Rennes (IPR-France) and the Institute of Condensed Matter and Nanosciences of Louvain-la-Neuve (IMCN / UCLouvain-Belgium). The first part of the thesis (29 months), which is related specifically to the development of the STARGATE instrument to study the spectrum of cation species was carried out in UCLouvain(Belgium) under the supervision of **Clément Lauzin** and **Xavier Urbain**. This work was then continued by the postdoctoral researcher **Anthony Roucou**.

The second part of this thesis (18 months) oriented around the absorption spectroscopy of ions for astrophysics applications took place in Université de Rennes (France) in the team of Laboratory Astrophysics of the IPR under the supervision of **Abdessamad Benidar** and **Robert Georges**. In both institutes the work was performed in collaboration with other experimentalists and with the support of a mechanical and electronic workshop. This work was funded by the 'Fonds spécial de la recherche (FSR, Uclouvain)' and 'Allocation de Recherche Doctorale de la Région Bretagne (ARED)'. This thesis led to the publication of two **peer reviewed articles** listed below and attached at the end of the manuscript:

1. Published article in Review of scientific instruments 92, 033307 April 2021:
 - **Title** : STARGATE : a new instrument for high-resolution photodissociation spectroscopy of cold ionic species
 - **Authors**: R. Bejjani, A. Roucou, X. Urbain, K. Moshkunov, G. Vanlancker, C. Lauzin
2. Published article Chemical Physics Letters 774, 138606 July 2021:
 - **Title** : The rotationally resolved symmetric 2OH excitation in H₂O-CO₂ observed using pulsed supersonic expansion and CW-CRDS
 - **Authors**: A.S. Bogomolovab, A. Roucou, R. Bejjani, M. Herman, N. Moazzen-Ahmadi, C. Lauzin

This thesis work was also presented in different national and international conferences as a poster or an oral presentation listed below and ordered by publication type, and date:

1. Poster presentation

- (a) METAMORPHOSE:
 - **Title** : The production and the study of ionic clusters
 - **Authors**: R. Bejjani, X. Urbain and C. Lauzin
 - **Location-Date** Louvain-la-Neuve-Belgium (23 May 2018)
- (b) IMCN PhD student day:
 - **Title** : The development of an ultra-sensitive spectrometer to study cold ionic clusters
 - **Authors**: R. Bejjani, X. Urbain and C. Lauzin
 - **Location-Date** Louvain-la-Neuve-Belgium (25 May 2018)
- (c) JSM-Creteil2019: Molecular Spectroscopy Days:
 - **Title** : Instrumentation for Fourier transform incoherent broadband cavity enhanced absorption spectroscopy of astrophysical anions
 - **Authors**: R. Bejjani, L. Biennier, R. Georges, A. Benidar
 - **Location-Date** Paris-France (21-23 May 2019)
- (d) The 26th Colloquium on High-Resolution Molecular Spectroscopy (HRMS):
 - **Poster presentation 1**:
 - **Title** : Finding the signature of astrophysical anions using Fourier-Transform Incoherent Broadband Cavity Enhanced Absorption Spectroscopy (IBB-CEAS)
 - **Authors**: R. Bejjani, L. Biennier, R. Georges and A. Benidar
 - **Poster presentation 2**:
 - **Title** : Homemade instrument to study ions by high-resolution photodissociation spectroscopy
 - **Authors**: R. Bejjani, X. Urbain, A. Roucou, K. Moshkunov, C. Lauzin
 - **Location-Date** Dijon-France (26-30 August 2019)

2. Oral presentation

- (a) Young researchers day (Specmo):
 - **Title** : Development and characterization of an ionic complexes source for high-resolution photodissociation spectroscopy
 - **Authors**: R. Bejjani, X. Urbain, D. Dedouaire, C. Lauzin
 - **Location-Date** Lille-France (22 May 2017)
- (b) 25th international conference on high resolution molecular spectroscopy:
 - **Title** : Production, and study of ionic clusters by photodissociation spectroscopy
 - **Authors**: R. Bejjani, X. Urbain and C. Lauzin
 - **Location-Date** Bilbao-Spain (3-7 September 2018)
- (c) Ph-day 2019 (Université de Rennes 1):
 - **Title** : High resolution spectroscopy of jet-cooled ionic species for atmospheric and astrophysical interest

- **Authors:** R. Bejjani, A. Benidar, X. Urbain, C. Lauzin
- **Location-Date** Rennes-France (23 April 2019)
- (d) 3M Nantes Doctoral School Day 2019 - At the heart of the matter:
 - **Title :** Fourier Transform incoherent broadband cavity enhanced absorption spectroscopy of astrophysical anions
 - **Authors:** R. Bejjani, A. Benidar
 - **Location-Date** Nantes-France (27 June 2019)

LIST OF SYMBOLS

D	diameter	v	velocity
P_0	initial pressure	\bar{v}	mean velocity
T_0	initial temperature	v_s	speed of sound
ρ_0	initial volumetric mass	$v_{s,0}$	initial speed of sound
n_0	initial density	v_{\perp}	transverse velocity
μ	dynamic viscosity	v_p	most probable velocity
P_{throat}	nozzle throat pressure	$v_{//}$	radial velocity
T_{throat}	nozzle throat temperature	v_{∞}	velocity limit of the jet
P^*	critical pressure	Sv	velocity ratio
T^*	critical temperature	S^*	throat diameter
ρ^*	critical volumetric mass	μ_{ref}	reference dynamic viscosity
μ^*	critical dynamic viscosity	T_{ref}	reference temperature
Re^*	critical Reynolds number	S_{μ}	Sutherland constant
v^*	critical velocity	γ	specific heat ratio
P_e	nozzle exit pressure	c_p	specific heat capacity/mass unit at constant pressure
T_e	nozzle exit temperature	c_v	specific heat capacity/mass unit at constant volume
ρ_e	nozzle exit volumetric mass	δ	dimensionless distance number
P	local pressure	d	distance
T	local temperature	k	Boltzmann constant
T_t	translational temperature	Re	Reynolds number
$T_{//}$	radial temperature	M	Mach number
T_{\perp}	transverse temperature	Kn	Knudsen number
T_v	vibrational temperature	λ_0	mean free path
T_r	rotational temperature	σ	collisional cross section
ρ	local volumetric mass	s	entropy
n	local density	Q	heat quantity
V	volume	M_n	molar mass
S	section	X_T	sonic region distance limit
S^*	throat section	X_M	Mach disk position
S_e	exit section	D_M	Mach disk diameter
R	ideal gas constant	δ_0	boundary layer of Laval nozzle after correction
r	ideal gas constant per mass unit	δ_1	correction of the boundary layer of Laval nozzle
P_b	chamber pressure	r_c	throat radius after correction
T_b	chamber temperature	r_u	Laval nozzle radius before correction
ρ_b	chamber volumetric mass	r_w	Laval nozzle radius after correction
n_b	chamber density	L	isentropic core diameter

f	repetition rate	τ	time decay
ψ	pumping duty cycle	L_{eff}	effective length
V	voltage	R_{eff}	effective reflectance
γ_{se}	secondary electron emission coefficient	c	celerity
n_0	initial density	T_c	cavity transfer function
A	saturation ionization energy	w_0	laser waist
B	constant related to the excitation and ionization energies	z	position
U_e	electrical potential energy	B''	rotational constant
qe	charge	D''	centrifugal distortion
F	force	A''	spin orbit constant
E_x	electric field	p and q	λ -doubling parameters
σ_{sb}	Stefan-Boltzmann constant		
ϵ	emissivity		
B_r	Richardson constant		
J	current density		
C_f	correction factor		
W_f	work function		
n_e	number of electrons		
θ	angle		
E_k	kinetic energy		
m	mass		
TOF (a enlever)	time-of-flight		
n_i	number of ions		
S/N	signal-to-noise ratio		
Q_V	volumetric flow rate		
Ra	Radius		
$DC(aenlever)$	direct current		
$RF(aenlever)$	radio-frequency		
$I(x)$	wavelength intensity		
ν	wavelength		
α	absorption coefficient		
$A(\nu)$	wavelength absorbance		
$n(\nu)$	chamber pressure		
T	transmittance		
R	reflectance		
F	finesse		

LIST OF FIGURES

1.1	On the left, cold spectrum of $^{16}\text{O}^{12}\text{C}^{16}\text{O}$ in grey and $^{18}\text{O}^{12}\text{C}^{17}\text{O}$ in red (70 K). On the right, room temperature (300 K) spectrum of the same species. The absorption noise level is set to ± 0.5 . This figure shows the interest of cold temperature measurements for low abundance species.	35
1.2	Schematic representation of the physical system composed of a gas reservoir, and a vacuum chamber at low pressure. The gas expands into the vacuum chamber through a hole of diameter D	36
1.3	The equilibrium curves of argon are plotted in a P, T diagram using a logarithm scale. The reservoir conditions are 291 K and 420 Torr. The adiabatic expansion brings the gas to 11.64 K and 0.13 Torr. The gas phase is conserved due to the rapid cooling of the adiabatic expansion.	37
1.4	On top the impact pressure measurement by a pitot tube is shown. The flow parameters have been extracted from the measurements relative to the plane of symmetry : Knudsen number on the left and the Mach number on the right.	40
1.5	Schematic representation of the conversion of a part of the thermal energy of the gas in the reservoir into kinetic energy in the expansion in the vacuum chamber, after undergoing a high number of collisions which is represented in green. On the other hand, in the jet, the thermal agitation is super reduced. It is therefore necessary to mark two points 1. Speeds have increased in the laboratory referential 2. Speeds have considerably decreased in the gas referential 1. and 2. are the two key points of a supersonic flow. A reduction in the distribution of velocities along the instrument's axis v_x and an increase in the flow velocity, v . The width of the velocity distribution of the supersonic beam narrows during the expansion into the vacuum chamber.	42
1.6	The Maxwell-Boltzmann velocity distribution of argon in the reservoir compared to the distribution of the jet for different Mach numbers. The maximum velocity is almost reached for $M = 1$. The full width at half maximum (FWHM) represents the translation temperature T_t of the gas.	46
1.7	Schematic representation of the evolution of translational velocities distributions $v_{//}$ and v_{\perp} along the beam path. According to the Sudden Freeze Quitting Surface Model.	48

LIST OF FIGURES

1.8 Schematic illustration of the flow structure of an axially symmetric supersonic free jet, with the different zones that are labelled. A supersonic expansion cone is formed thanks to the gas expansion from the high-pressure gas reservoir P_0 into the vacuum chamber through the nozzle. A region located just behind the nozzle exit called the cooling region makes the transition from the continuum to the free molecular flow. Shock waves called the Mach disk and the barrel shock limit an isentropic region so-called the zone of silence. Figure is adapted from [37]. 50

1.9 Evolution of the distance X_M/D between the nozzle exit and the Mach disk location with respect to the pressure ratio. 51

1.10 Evolution of the Mach M number along the centreline of the supersonic jet with respect to the ratio of the distance downstream of the nozzle exit and the nozzle diameter x/D 52

1.11 Evolution of the temperatures, pressures, and density ratios T/T_0 , P/P_0 , ρ/ρ_0 with respect to $\delta = x/D$ for an axisymmetric and a planar configuration. 53

1.12 Evolution of the ratio of jet velocity v/v_{max} and sound velocity $v_s/v_{s,max}$ along the centreline of an axisymmetric supersonic jet with respect to $\delta = x/D$ 54

1.13 The evolution of the flow regime from a turbulent flow to Laminar flow with respect to the Mach number for the source used at UCLouvain. The flow is turbulent at the beginning and tends to be laminar for higher Mach number. 55

1.14 The evolution of the flow regime from a turbulent flow to Laminar flow with respect to the Mach number for the source used in Rennes. 56

1.15 The representation of the Laval nozzle profiling method: For the determination of the exit radius $r_{u,exit}$, the latter is related to the flow velocity and to the debit of the flow as a function of the Mach number at the nozzle exit. Since the flow rate is conserved in all the sections of the nozzle, by imposing the Mach number at the exit of the nozzle, we obtain the value of $r_{u,exit}$ as a function of the nozzle throat diameter and Mach number at the exit of the nozzle. The length of the nozzle is determined by the arbitrary choice of a certain parameter and it is then calculated to find for which length the uniformity is conserved. A too short nozzle length may open too much the angle of divergence of the nozzle profile, possibly leads to the separation of the boundary layer while choosing a too long length risks the preponderance of the boundary layer over the isentropic core of the jet, a compromise is needed. 58

-
- 2.1 Design of STARGATE TOF-MS (bottom) with (1) source of ionic compounds, (2) skimmer, (3) TOF mass spectrometer, (4) electrostatic lens, (5) pulsed 2D deflector, (6) differential pumping tube, (7) laser and ion beam interaction region, (8) 90° cylindrical energy analyser and (9) MCP detector. Optical bench (upper part) with pulsed dye oscillator and dual amplifier associated with a frequency doubling BBO crystal and pumped by a Nd:YAG laser, (10) prism separating the second harmonic doubled Nd:YAG laser (307-327 nm) used for photodissociation spectroscopy from the fundamental dye beam (614-654 nm) used for the frequency calibration of the spectra, (11) hollow cathode (Ne/Mn) and (12) temperature-regulated vacuum solid state etalon. The calibration atomic Ne lines are measured from the helium filled hollow cathode (Ne/Mn), the ionic photofragments are detected by the MCP detector, the power of the laser and the Fabry Perot interferometer (solid state etalon) are measured by a photodiode (13) and a pyroelectric detector (14), in combination with an oscilloscope (Agilent DSO-X 3104A). Items (1), (3) and (5) are all connected to a digital delay generator, the associated chronograph is displayed in Figure 2.2. The photodissociation spectra are recorded from the oscilloscope connected to a computer via USB. A Labview[®] interface controls the scan of the pulsed dye laser, the transfer of the averaged data from the oscilloscope to the computer, and the integration of the time gated signal. 60
- 2.2 Chronograph for applied voltages to study cations using STARGATE. The time scale origin is defined as the rising slope of the pulsed molecular jet valve trigger (black). The two steps of the gating bunching of the ions separated by 40 ns (red and green) and the mass selection of the pulsed 2D deflector (blue) are represented. The time scale origin used for the mass spectrum of N_2O^+ measured with the MCP detector at $t_{TOF} = 22.4 \mu s$ (orange) is defined from the beginning of the TOF corresponding to the gating ($L = 1.5$ m with a kinetic energy of 1 keV). In addition, a dye laser pulse of 5 ns duration interacts with the ions after 1 m in the drift tube for photo-dissociation spectroscopy ($\simeq 15 \mu s$ for N_2O^+) . . . 62
- 2.3 Principle of operation: (a) The valve is closed with the flexible bar resting on the O-ring. (b) After the application of the current pulse 64
- 2.4 Even-lavie valve cross section along with all the mechanical parts. Figure from reference [82]. 65
- 2.5 a) Photo of the inside of the cantilever piezovalve, with the relevant dimensions indicated. The O-ring is glued to the back side of the piezo, which forms the vacuum seal to the nozzle hole. The nozzle to seal distance can be carefully adjusted with three set screws as indicated. The piezo free cantilever length is about 5 to 6 mm. The length of the cantilever can be easily adjusted by moving the clamp. b) Photo of the closed valve which has an outer body diameter of 44 mm. c) Photo of the piezo valve body mounted in a heatable holder on a standard *ISO160* vacuum flange. An electrically isolated skimmer is also attached to the holder 66

LIST OF FIGURES

2.6 a) Profile view: Assembly drawing of the piezoelectric valve from reference [84]. (1) Valve body; (2) front plate; (3) nozzle plate; (4) threaded piece of tubing (mounting hole for nozzle plate), welded into the front plate; the total number of mounting holes is four; (5) holding the rod for disk translator; a total of four of these rods are welded into the front plate at equal intervals on a circle of 45.0 mm diameter; (6a) vertical adjustment nut for plunger; (6b) plastic nut; (6c) plunger (with slit for screwdriver on top); (6d) lock-nut; (6e) Viton gasket (0.7 mm thick); (6f) sealing o-ring; inner diameter: 1.5 mm, width: 1.5 mm; (7a) ring supporting the disk translator; (7b) o-ring; inner diameter 38.0 mm, width 2.0 mm; 8: coaxial feed through with MHV connector (Ceramseal); (9) gas inlet; 10: hole for M3 screw drawn 22.5° out of true position; a total of eight holes are equally spaced on a circle of 62.0 mm diameter; 11: mounting hole for valve (M3) (four holes). For clarity, parts (4), (5), (6), (8), (9) and the disk translator are not hatched. Parts (1), (2), (3), (4), (5), (7a) and (9) are made of stainless steel, parts (6a), (6c), and (6d) of aluminium; b) Top view of the home-made valve copied from the original design. 68

2.7 Electric circuit of the switch used to control the piezoelectric element. 69

2.8 Paschen curves for different gases, using the expression 2.3.2 for the breaking voltage as a function of Pd from reference [93]. 72

2.9 Discharge glow image using an expansion of pure argon 74

2.10 Schematic representation of basic plasma processes in a glow discharge reproduced from [107]. The application of a potential difference between electrodes causes the breakdown of the gas into electrons and cations. The electrons can induce secondary electron emission. The new emitted electrons can collide with gas molecules to cause excitation (followed by de-excitation and then, light emission) or ionization. 75

2.11 a) The supersonic jet expansion can be ionized by applying a negative voltage (-800 to -1400 V) on the circular electrode (in blue (a)) enclosed in Teflon insulators fixed on the valve. The plunger (in orange (a)) is fixed to the flexing disk of piezo material (in green (a)). b) The SIMION® simulation of the two electrodes showing the electric field lines in red. c) Photo of the insulators and the negatively charged cathode. 76

2.12 On the left a Solidwork design of the cross-section of the home-made electron gun along with its different parts and on the right a photo of the electron gun operating in vacuum. The filament is radiating and therefore emitting electrons that are accelerated and focused into the jet expansion. 78

2.13 Solidworks drawing for the electro gun and some of its important dimensions. 78

2.14 a) Schematic representation and (b) SIMION® simulation of the electron beam produced by the tungsten filament and focused by *Pierce* emission electrodes and collected by the anode. The simulation showed the ability to focus the electron beam in the region of the intersection with the jet expansion for a maximum ionisation. 79

2.15	The bottom trace displays a schematic of the voltage if measured using a HV probe when the valve is not operating. The top trace displays the voltage measured at one of the discharge electrodes when the pulse gas is applied. Arrow "a" divided by the resistor of the power supply is a measure of the discharge current. Applied voltage -600V subtracted by "a" is the measure of the discharge voltage. Arrow "b" is the corresponding time of the opening time of the valve.	80
2.16	On the top figure, the DC voltage discharge signal is plotted with respect to the time. On the bottom figure, the signal from the photodiode detecting the discharge radiation is plotted against time.	81
2.17	Maximum repetition rate achieved by the valve, the signal is recorded using two methods, in black is the signal of the photodiode and in red is the signal of the DC current drop (both signals were rescaled for a better representation)	82
2.18	The pressure in the chamber for two different voltages 200V in red and 250V in black. In this figure we observe the need to operate for frequencies between 30 and 60 Hz and for a voltage around 250 V.	82
2.19	Helium free jet zone of silence shown with (bottom) and without skimmer (top) in the region of the expansion. The experimental conditions are presented on the right of the two figures. The example is from reference [116].	83
2.20	Comparison between a shadowgraph and a Schlieren image from reference [117].	84
2.21	Schematic representation of the Schlieren optical system, reproduced from [112].	85
2.22	1) Corresponds to the case of a pressure of 3 bar in the reservoir and 2) correspond to the case of a higher pressure of 4 bar. a) corresponds to the direct measurement of the signal, b) corresponds to the image in grayscale and c) corresponds to the addition of RGB colours. b) and c) were done using Matlab© in order to enhance the contrast. The enhanced contrast obtained using the image processing allows us to observe a succession of shock waves. The diameter of the used nozzle is equal to 500 μm and it is represented in blue.	86
2.23	Schematic representation of the Michelson interferometer adapted in order to observe the shock waves of the supersonic expansion.	87
2.24	Photos of the interferogram produced by Michelson interferometer represented in Figure 2.23 before and after the application of an air spray (a.), and before and after the application of a flame (b.) both placed just after the lens L_3	88
2.25	Representation of the area in which the jet was simulated, formed by the nozzle coupled to the discharge electrode and insulators as indicated. The surface used for the simulation is represented in green.	89
2.26	Mesh Fluent view, showing the density and the precision in the areas close to the nozzle and to the axis of symmetry. The nozzle diameter is equal to 500 μm	89
2.27	Top panel: contour plot of Mach number. Bottom panel: Mach number evolution along the jet axis.	91
2.28	Top panel: Temperature contour plot. Bottom panel: Temperature plot along the x direction.	92

LIST OF FIGURES

2.29 Top panel: Density contour plot. Bottom panel: Density plot along the x-direction. The y-axis (density) is in logarithmic scale in order to visualize the density variation. 93

2.30 On the top the contours of the static temperature magnitude is presented. On the bottom the plot of the temperature evolution on the axe during the jet expansion is presented. . . 94

2.31 Schematic representation of a linear TOF mass spectrometer from reference [130]. Ions of various mass-to-charge ratios are accelerated with energy E_k via electrodes and travel a distance d in a drift tube. The ions of same m/z form packets and each packet corresponds to a time of flight t to travel the distance d . A detector allows the ion packets to be detected at the end of the drift tube. 96

2.32 Time-of-flight spectrum of an expansion of N_2O and H_2O 97

2.33 Quadratic curve fitting of the mass-to-charge ratio with respect to the time of flight. The equation of the fitting is $m/z = 0.1015(t - 0.3805)^2$. The coefficient of determination of the fit is $r = 0.99908$. The two masses used to calibrate the spectrum are also presented with their corresponding TOF and mass. 98

2.34 a)The solidworks design of the TOF unit with the x and y dimensions, the acceleration electrodes are separated by resistors of 100 k Ω each. The first and the last electrodes are at ground potential. The ions are accelerated between the first and the 6th electrodes, the latter have a potential of 1 kV. b) Photo of the unit attached to the stainless steel that hold the skimmer which is also in the photo 100

2.35 a) Typical capacitor where equipotential lines of value V_a are represented by dashed red lines. Electric fields of value \vec{E}_a are represented by blue vectors. Cations inside the capacitor are accelerated in the direction of the black arrow which correspond also to the direction of the electric field. b) Two electrodes with a hole in the center. The only difference is that the potential lines and the electric field are slightly curved in the area of the hole. The electric field can accelerate the cations in the direction of the electric field through the two holes of the electrodes. 101

2.36 The solidworks design of the electrodes used for the acceleration with its dimensions. The electrode is represented in red in Figure 2.37. 102

2.37 The representation of the unit where we can find in red the acceleration electrodes and the positive ions in green. The ions gain gradually a kinetic energy to finally reach the electrode at -1000 kV. The rest of the unit is explained in the following sections 102

2.38 The solidworks design of one gating electrode shaped like a cup with the relevant dimensions. The electrode is represented in blue in Figure 2.39 103

2.39 The representation of the unit where we can find in blue the gating electrodes that each form a pair with the neighbour red electrode. Gating is performed when at t_1 the cations in green are inside the two cups and the potential of the two cups is switched to ground. The result is that the first gate is closed by creating an intense electric field with the electrode at $-1kV$, the second gate is opened and the selected packet of ions could travel to the detector to arrive at a time t_2 , the cations are in blue at this time. The time of flight is measured by calculating $t_2 - t_1$ 104

2.40	The characterization of the rising time of the switches. In black the rising time of the switch that controls the voltage on the electrode of the first gate switching from a negative value of the potential (-1 kV) to a positive value (400 V). In red the second switch rising time is represented. It flips from -1 kV to 0 V. Both rising times are close to 200 ns. . . .	105
2.41	The representation of the gating and bunching unit where we can find in blue the gating electrodes that each form a pair with the neighbour red electrode. Bunching is performed when at t_1 the cations in green are inside the two cups and the potential of the first cups is switched to a positive value (100 V in our case), the second cup is switched to ground potential to open the gate. The result is that at the position of the interaction with the laser, the cations represented in blue are axially bunched.	106
2.42	Comparison between the N_2O^+ m/z bunched (red) and not bunched (black) spectra, the x-axis is the time of flight after the gating. The bunching and the associated improvement of the MRP allow the $^{14}N^{15}N^{16}O^+$ isotopologue to be observed.	107
2.43	SIMION [®] sectional view of the unit before switching. Electrodes are represented by brown squares and numbered from 1 to 9. The applied potential before and after the switching is described in the text. The red lines represent the equipotential lines. The oblique dashed line corresponds to the skimmer placed before the unit. The initial conditions of the ions are detailed in the text. The drift tube follows this unit and it is not represented in this figure.	108
2.44	TOF distribution of argon ions measured at the detector with bunching (black) and without bunching (green). The histograms are fitted in red with a Gaussian function enabling us to find the FWHM that can be used to find the resolution. FWHM without bunching $\approx 0.3 \mu s$. FWHM with bunching $\approx 0.03 \mu s$	111
2.45	The Solidworks [®] generated figure of the electrostatic lens used in the setup and the corresponding applied voltages.	112
2.46	The Solidworks [®] generated figure of the deflector. The blue plates are the active electrodes one of them is grounded and the second one is polarized. The voltage used is tuned during the experiment for a maximum signal.	113
2.47	Schematic representation of the deflector (left) that is composed of two parallel metal plates of length L between which a potential difference V_a is applied. The plates are separated by a distance d . Ions come from a source with an initial potential of V_s and the difference of potential V_a deflects their trajectory of an angle θ that gives a deflection vertical distance of z_0	113
2.48	a) The m/z spectrum measured with continuous deflection from N_2O gas injection and electric discharge (in red) is compared with b) the spectrum measured with a pulsed deflection of $1 \mu s$ to select only N_2O^+ (in black).	115
2.49	The solidworks dimensions details of the skimmer.	117
2.50	Drawing representation of the differential pumping tube along with its dimensions.	117
2.51	The logarithmic plot of the transmission probability of the particles for a distance $l = 2$ m when considering argon ions for different chamber pressures.	118

LIST OF FIGURES

- 2.52 The results of the test carried out to measure the beam spatial diameter. It is an important parameter to evaluate the overlap between the laser and the ion beam. The signal was recorded for different voltages of the deflector that made possible the scanning of the ionic beam. 119
- 2.53 A plot to show the difference between the products of a jet with a back-pressure equal to 2 bar (black) and 3 bar (red). The chamber pressure is maintained at 5×10^{-5} mbar, The discharge voltage is equal to -350 V. 120
- 2.54 Two plots showing on top the result of a jet using a nozzle of a diameter of 0.5 mm and on the bottom the result using a bigger diameter of 1 mm. 121
- 2.55 Results of the test using two extreme voltage values. The result of applying a voltage of -350 V is shown in black and the result for applying a voltage of -1000 V is shown in red. A jet of Argon bubbling in water was used for a back-pressure of 3 Bar, a chamber pressure of 5×10^{-5} mbar and a nozzle diameter of 500 μm 122
- 2.56 The result of using a jet of 10% of N_2O seeded in argon (black), a jet of pure N_2O red and a jet of 10% of N_2O seeded in helium blue. Back-pressure = 3 bar, chamber pressure = 5×10^{-5} mbar and the diameter is about 500 μm . The discharge voltage is equal to -350 V for the case of argon as a seeding gas and pure N_2O , and it is equal to -450 V in the case of helium as a seeding gas. 123
- 2.57 The influence of changing the distance nozzle-skimmer on the products of a jet of N_2O seeded in Helium. The shorter distances (15 mm) enhance the production of lower masses (NO^+), while longer distances enhance the production of bigger masses $(\text{N}_2\text{O}^+)/(\text{N}_2\text{O}^+)_2$. 124
- 2.58 a) Production of $\text{H}(\text{H}_2\text{O})_n^+$ ionic clusters up to $n = 38$ from argon bubbling in water with a backing pressure of 2 bar using a nozzle of 1.5 mm of diameter with an average pressure of 10^{-5} mbar in the jet chamber and the valve operating at 30 Hz. b) Production of $(\text{N}_2\text{O})_n^+$ ($n = 1 - 5$), $(\text{N}_2\text{O}) \cdot (\text{H}_2\text{O})_n^+$ ($n = 1 - 2$), $(\text{H}_2\text{O}) \cdot (\text{N}_2\text{O})_n^+$ ($n = 1 - 4$) and $(\text{NO}) \cdot (\text{N}_2\text{O})_n^+$ ($n = 1 - 4$) ionic clusters from N_2O and residual water in the gas line. c) Production of anions using the electron gun with N_2O at a backing pressure of 3 bar. 126
- 2.59 The production of $[(\text{CO}_2) \cdot (\text{H}_2\text{O})]^+$, $(\text{CO}_2)_2^+$ and other interesting complexes using a jet of CO_2 seeded in helium. 127
- 2.60 Schematic representation of electronic dissociation through different mechanisms: a) direct dissociation, b) Herzberg type I predissociation c) Herzberg type II predissociation d) two photon dissociation process. This Figure is adapted from reference [136]. 128
- 2.61 Schematic representation of infrared dissociation. One or more infrared photon are absorbed exciting the ion to an upper state, after a certain duration the energy is redistributed and if this energy is higher than the binding energy, the complex is dissociated. 129

- 2.62 a) The 90° electrostatic deflector is represented with the bias cell surrounding the laser interaction region. b) SIMION® simulation performed for the selection of the NO⁺ photo-fragments ($m = 30$ uma, $E_{NO^+} = 602$ eV) represented in black, by excluding the non-dissociated N₂O⁺ parent ions having a larger kinetic energy represented in blue ($m = 44$ uma, $E_{N_2O^+} = 1$ keV) and NO⁺ fragments resulting from collisions with the neutral residual gas in the drift tube represented in red ($m = 30$ uma, $E_{NO^+} = 680$ eV). The positive and negative electric equipotential lines are represented in green and blue, respectively, with an increment of 30 V. The voltages applied in the simulation are -250 V for the middle electrode and $\pm V = \pm 135$ V for each plate of the deflector. The initial energy of the photo-fragments is $E_{NO^+} = E_{N_2O^+} \times m_{NO^+}/m_{N_2O^+} = 852$ eV with $E_{N_2O^+} = 1250$ eV in the middle of the electrostatic field generated by the electrostatic lens. 131
- 2.63 Results of the test done to evaluate the energy dispersion of an argon ion beam. The test was done by measuring the signal on the detector for different voltages on the deflector. . . 132
- 2.64 The representation of the beam energy dispersion. 132
- 2.65 Laser interaction time profile measured from the NO⁺ photo-fragments by tuning the time delay between the N₂O⁺ ion bunch and the laser pulse. The measurements are depicted in black squares and are fitted by a Gaussian profile presented in red. The laser frequency was fixed to the top of the Q branch frequency of the $\tilde{A}^2\Sigma^+(002) \leftarrow \tilde{X}^2\Pi_{3/2}(000)$ rovibronic band (30908.5 cm⁻¹). The origin of the x-axis is arbitrary. 133
- 2.66 Potential energy curves of N₂O⁺ as a function of the N-NO distance R_{N-NO} from reference [141]. The blue curves are the electronic states involved in the predissociation path shown by the red arrows. 134
- 2.67 The photodissociation spectrum (black) has been measured from the interaction of the N₂O⁺ beam with a frequency doubled dye laser (0.6 mJ/pulse) for an average of 30 counts per laser step. The simulation (red) was performed with the PGOPHER software[162] using the parameters of Fellows *et al.* [145] for the $\tilde{X}^2\Pi_{1/2,3/2}(000)$ ground state and those of Table 2.10 for the $\tilde{A}^2\Sigma^+(002)$ state. A temperature of 300 K and a Voigt lineprofile have been considered for the simulation, with Gaussian and Lorentzian contributions of 0.2 cm⁻¹ and 0.1 cm⁻¹ (FWHM), respectively. 136
- 2.68 (a) Q branch region of the $\tilde{A}^2\Sigma^+(002) \leftarrow \tilde{X}^2\Pi_{3/2}(000)$ photodissociation spectrum of N₂O⁺, from bottom to top measured with the bias cell at 0 V (DC off), at -250 V (DC on) and simulated using the PGOPHER software. Blue and green mass spectra of the panels b) and c) are the NO⁺ fragments measured at the maximal intensity of the Q branch for the bias cell on and off, respectively. The mass spectra measured without UV laser are presented in black in panels b) and c). 137
- 2.69 Illustration of the two zones that are responsible of the apparition of NO⁺ and N₂⁺ in the photodissociation signal. In red and yellow we can observe the illustration of the trajectory of these ions from zone (i) and in purple the trajectory of these ions already produced in zone (ii). 138

LIST OF FIGURES

2.70	Fabry Perot etalon composed of: 1) KF fitting for etalon evacuation, 2) external chamber diam. 2", 3) 1" wedged window, 4) 50:50 beamsplitters AR coated for 400-700 nm, 5) invar ring of 1.99 mm long, 6) PVC spacer to maintain the position of the stainless steel enclosure in the vacuum chamber, 7) 1.5" wedge windows and 8) stainless steel enclosure. The exploded view of the etalon and its content is presented below.	140
2.71	Photodissociation spectrum (black) measured from a gas mixture of 1% N ₂ O with 99%Ar ($P_0 = 5$ bar). The simulation (blue) have been done using the PGOPHER software [162] for $T_{\text{rot}} = 40$ K.	142
2.72	a) The first acceleration scheme inspired from Dedman <i>et al.</i> [132] b)The second acceleration scheme. c) Before switching, the gating process simulation from SIMION® on the second acceleration scheme. d) After switching, the first part of the unit is at +400 V to close the first gate and bunch the ions at the end of the TOF. The second part of the unit is switched to 0 V to let the ions enter the drifting tube.	143
2.73	The photodissociation spectra (black) have been measured from the interaction of the N ₂ O ⁺ beam with a doubled dye laser (0.6 mJ/pulse) by probing different parts of the ionic beam using different ion extraction timings and distances between the nozzle and the skimmer. An average of 30 counts per laser step allowed to reach a $S/N = 200$ for each spectrum. The simulations has been done for each measured spectrum using the PGOPHER software [162] for $T_{\text{rot}} = 305$ K (red) and $T_{\text{rot}} = 110$ K (blue)	144
2.74	Probing different zone of the jet giving two different temperatures (1 = 305 K 2 = 110 K) as shown in the spectra in previous Figure 2.73.	145
2.75	A picture of the quadrupole filter available in our lab. A schematic of the rods is represented, along with the voltages applied and resulting in a stable trajectory and other unstable trajectories defined by the voltages applied (U is for the DC voltage and V_0 is the amplitude of the RF signal. Adapted from [122].	146
2.76	IRPD spectrum of the [H ₂ O-CO ₂] ⁺ ion, reproduced from [13].	147
3.1	Electronic structure of C ₃ ⁻ and C ₄ ⁻ produced using data from [163]	150
3.2	Absorption spectrum of C ₄ ⁻ in a 5 K neon matrix [152].	151
3.3	Photo of the cold ionic source.	152
3.4	Schematic of the source designed at IPR. The reservoir is made of polyoxymethylene(POM), the discharge electrodes are made of copper, the electrodes profiling the divergent part of the nozzle are made of aluminium , the surface of which is coated by a deposit of a carbon film in order to prevent the detachment of the electrons. The conditions to obtain a uniform expansion are also listed.	153
3.5	An example of two geometries, on the left an axisymmetric profiled Laval nozzle and on the right a planar profiled nozzle. Both require a convergent part and a divergent calculated profile to generate a uniform supersonic beam expansion.	154
3.6	CFD Contour plot of a cross section of the supersonic flow produced by a Laval nozzle working in its adapted regime. Left: axisymmetric Laval nozzle. Right: Planar Laval nozzle. The laser probing zone is indicated by a red arrow.	155

3.7	Adopted meshing to run the CFD simulations. The red arrows indicate the outlet regions.	156
3.8	Scaled residuals of the continuity, energy, x-velocity and y-velocity equations.	156
3.9	Left top: Contours of the Mach number. Bottom left: Mach number evolution on the jet axis. Top right: photo of a plasma jet of argon obtained in adapted flow conditions. . . .	158
3.10	Top panel: Temperature contour plot. Bottom panel: Temperature plot along the x direction.	159
3.11	Top panel: Density contour plot. Bottom panel: Density plot along the x direction. The density axis is in logarithmic scale in order to better visualise the density variation.	160
3.12	a) CFD simulation showing the contour plot of the temperature of a jet of helium expanded in a nozzle designed to operate with argon. b) Static temperature plot along the nozzle axis showing a strong variation. c) CFD simulation of Mach number. d) Photo of the jet visualized with a plasma of helium which explains the light blue color. Helium has a different mass and viscosity producing a different jet structure than argon.	162
3.13	a) CFD simulation showing the contour plot of the temperature of a jet of nitrogen expanded in a nozzle designed to operate with argon. b) Static temperature plot along the nozzle axis showing a strong variation. c) CFD simulation of Mach number. d) Photo of the jet visualized with a plasma of nitrogen which explains the red light color. Nitrogen has a different specific heat ratio, its molar mass is different from the one of argon and also its viscosity producing a different jet structure.	163
3.14	Photo of the electronics controlling the polarisation of the electrodes, along with a schematic of the electrodes.	164
3.15	SIMION [®] simulation of the trajectory of the ions. The anions are represented in red. The electrons in black and the protons in blue.	166
3.16	Comsol representation of the electric fields and the value of the potential on the electrodes following the application of the RF voltage.	168
3.17	Comsol representation of the electric fields and the value of the potential on the electrodes following the application of the DC voltages.	169
3.18	Comsol representation of the plot of the potential resulting from the two applied DC and RF voltages. In blue, the profile of the total electric potential on the axis of the flow is represented. In green, the value of the electric potential on the level of the electrodes is represented.	169
3.19	Comsol simulation representation of the ions trajectory of Ar ⁺ ions seeded in argon gas in the absence of voltages on the electrodes.	170
3.20	Comsol trajectory simulation of Ar ⁺ seeded in argon after applying the DC and RF voltages on the electrodes. A focusing effect is obtained around 30 mm away from the nozzle throat.	171
3.21	Classification of cavity-enhanced absorption approaches and detection schemes, the size of the arrow indicates the weight of occurrences of type of approach in the literature (reproduced from [179]).	175
3.22	Sketch of the IBB-CEAS principle, a schematic visualisation leading to understand the transmitted intensity I	176
3.23	Cavity transmission for a resonant <i>CEAS</i> in black and direct absorption over the same effective pathlength in red.	181

LIST OF FIGURES

3.24 Absorption coefficient α as a function of I_0/I for an optical cavity of length $d = 10$ cm and for different reflectivity. 183

3.25 Timeline of the different light sources used in the literature, reproduced from [194]. 188

3.26 Experimental setup of the *FT-IBB-CEAS*. It consists of a supercontinuum laser injected into the vacuum chamber using a fiber optic with a built in collimator at the end. The basic elements of this setup are: (1) adapted window, (2) optical filter, (3) two planar mirrors, (4) and (5) two achromatic lenses, (6) optical cavity, (7) iris. The transmitted light is coupled to the Fourier transform spectrometer. (8) planar mirror, (9) concave mirror, (10) spectrometer aperture, (11) beam splitter, (12) fixed mirror, (13) moving mirror and (14) detector. The signal is then analysed using a computer. The cavity length is $L = 23$ cm, and the supersonic expansion diameter is 10 cm which correspond to the interaction length for a single passage of the light. The planar cold jet of molecules is represented in blue. 194

3.27 YSL Photonics SC-Pro 195

3.28 On the left, the emission spectrum given by the product manual sheet and on the right the emission spectrum of the laser with a power set to 50% for different modulation values. 195

3.29 Photo of the wedged window used for the injection of the laser light into the vacuum chamber, taken from *Thorlabs* 196

3.30 The reflectance of the window given by *Thorlabs* and reproduced. 196

3.31 The conception assembly of the mechanical part used to introduce the light into the vacuum chamber and the KF-40 hinge clamp attached to it. 197

3.32 Photo of the two motors fixed on the mirror, making it easy to control and steer the mirror in the x and y direction with a simple controller outside of the chamber 197

3.33 The beam diameter relatively to the distance from the fiber output. The details are explained in the text and the diamonds markers correspond to the different testing positions. The beam divergence θ is also presented in the figure. 199

3.34 Gaussian profile of the laser beam where the diameter at the output of the laser is ~ 3 mm and the waist w_0 is approximatively equal to 0.5775 mm positioned at ~ 4535 mm from the laser output. 200

3.35 The representation of the different calculated lengths between different optical components starting from the output of the laser beam to the exit of the cavity. This figure also illustrates the width of the beam in the optical system represented by a blue color. 202

3.36 On the left, a photo of the white cell scheme while operating, the glowing goes to the discharge of a portion of methane seeded in argon (50%), the parallel mirrors are separated by 10 cm. The dots on the mirrors corresponds to the laser light. On the right a simple illustration of the path of the laser light on the mirrors, in this illustration the light undergoes seven reflections before getting out. In our case the light was able to undergo 39 reflections which correspond to 4 m of interaction with the cold molecules. 204

3.37 Top panel: Spectrum of cold methane recorded using the Laval nozzle. Bottom panel: Spectrum of the same band of methane at ambient temperature. These spectra were recorded using the White cell scheme and a relatively high gas pressure. 205

3.38	Transmitted broadband spectrum using different optical filters represented by different colors covering the region of the reflectivity of cavity mirrors.	206
3.39	Transmitted broadband spectrum using a Pellin-Broca prism that also covers the region of the reflectivity of the mirrors.	207
3.40	Absorption line of jet-cooled acetylene around 9632 cm^{-1} recorded with an instrumental resolution of 0.02 cm^{-1} (red curve) and a resolution of 0.01 cm^{-1} (black curve).	208
3.41	Representation of the different detectors, giving their efficiency for different region in the electromagnetic spectrum.	209
3.42	Evolution of the signal-to-noise ratio versus the number of co-added scans measured in jet conditions with an instrumental resolution of 0.02 cm^{-1} and a scanning velocity of 10 kHz . Each point corresponds to the evaluation of the S/N for a certain number of measurements. The result was fitted using \sqrt{N} function.	210
3.43	Beam splitters table, giving the efficiency of different beam splitters for different region in the electromagnetic spectrum.	210
3.44	Fringing effects from both the interferogram (on the left) and spectrum perspective (on the right). The data processing consists of the removal of the parasitic centerbursts marked by two circles on the top interferogram. Absorption lines of CH_4 molecules are distinguished after the data processing.	211
3.45	Plot of the calculated reflectivity of the cavity mirrors.	212
3.46	Comparison between the simulation of the absorption band at 9650 cm^{-1} of 0.1 torr of acetylene at room temperature for an interaction length of 600 m and the corresponding measured spectrum. The number of scans is equal to 600	213
3.47	Mirrors reflectivity between 9550 cm^{-1} and 9720 cm^{-1}	214
3.48	Comparison between the simulation of the absorption band at 11250 cm^{-1} of a concentration of 0.3 torr of methane for an interaction length of 500 m and the corresponding measured spectrum. the number of scans is equal to 600 scans.	216
3.49	On the top a photo of the source and the cavity showing the areas of hot gases in red and cold gases in blue. The lower is the pressure of the chamber, the lower is the concentration of hot gases. On the bottom the corresponding spectrum for each case is presented. We can see clearly the contribution of hot gases because of the absorption of higher rotation energy states that are depopulated at lower temperatures.	217
3.50	Photo of the cavity and the nozzle showing the difference in the interaction length between a static measurement that corresponds to 0.23 m and a cold jet measurement with 0.1 m of interaction.	218
3.51	Absorbance spectrum of cold acetylene recorded using the nozzle in non adapted conditions (red). Simulated spectrum using the HITRAN database (black).	219
3.52	Absorbance spectrum of acetylene recorded at low and room temperatures.	219
3.53	Absorbance spectrum of cold methane recorded using the nozzle in non adapted conditions (red). Simulated spectrum using the HITRAN database and a temperature of 50 K (black).	220
3.54	Absorbance spectrum of cold methane recorded using the nozzle in non adapted conditions (red). Simulated spectrum using the HITRAN database and a temperature of 100 K (black).	221

LIST OF FIGURES

B.1 Distribution of the modulus of velocities for argon and helium for two different temperatures (250K and 100K). We notice that a lowering of the temperature is accompanied by a reduction in the width of the distributions and a reduction in the most probable velocity v_p which is also presented in this figure in *red*. also with the mean velocity \bar{v} in *blue*. and The mean square speed \bar{v}^2 in *green*. 236

C.1 On the left, a schematic design of the nozzle. On the right a photo showing the nozzle and the teflon/ stainless steel pieces used to initiate a discharge and to insure a planar geometry at the exit of the nozzle. 237

C.2 Time profile of the transmission of a laser pulse after several round trips in a high-finesse optical cavity. G is the spectral profile of the laser pulse that extends over the cavity modes. 239

D.1 Distribution of the transverse mode of the intensity of the first Hermites-Gauss modes $TEM_{m,n}$ under each photo the value of m, n is indicated. This photo is reproduced from reference [225]. 244

D.2 Stability diagram for a two-mirror cavity. Shaded areas corresponds to a stable configuration. Cavities at points exactly on the line are marginally stable, reproduced from [226]. 250

D.3 An example of calculated transmission of a cavity having mirror reflectivity equal to 80% and the finesse equal to 14, assuming a perfect spatial and frequency mode-matching. . . 251

D.4 An example of calculated transmission of a cavity having mirror reflectivity of 90% and finesse equal to 29.8. 251

TABLE OF CONTENTS

Introduction	29
1 Supersonic expansion	33
1.1 Fast cooling in an adiabatic expansion	35
1.1.1 Advantage of cooling for absorption spectroscopy	35
1.1.2 Adiabatic expansion	35
1.1.3 Supersaturation	37
1.2 Dimensionless numbers	38
1.2.1 Reynolds number	38
1.2.2 Mach number	38
1.2.3 Knudsen number	39
1.3 Isentropic equations	42
1.4 Velocity distribution	45
1.5 Seeded expansion	47
1.6 Decoupling of the molecular different degrees of freedom	47
1.7 Free jet expansion	49
1.7.1 Flow structure	49
1.7.2 Mach disk location and diameter	51
1.7.3 The evolution of the Mach number in the expansion	52
1.7.4 Evolution of the quantities: T/T_0 , P/P_0 and ρ/ρ_0 parameters and characteristic velocities in the jet expansion:	53
1.7.5 Evolution of the Reynolds number in the jet expansion:	54
1.8 Uniform supersonic jet expansion	56
2 STARGATE apparatus: Spectroscopy of Transient Anions and Radicals by Gated and Accelerated Time-of-flight Experiment	59
2.1 Introduction	59
2.2 Instrument layout	61
2.3 Source of ions	63
2.3.1 Pulsed supersonic jet expansion	63
2.3.2 Ionization methods	71
2.3.3 Characterization of the pulsed supersonic jet expansion	79
2.4 Home-made time-of-flight mass spectrometer	95
2.4.1 Mass calibration	97
2.4.2 Definition of the resolution for a time-of-flight mass spectrometer	99

TABLE OF CONTENTS

2.4.3	Ion separation, gating, bunching, and re-referencing	100
2.4.4	Electrostatic lens	112
2.4.5	Two dimensional deflector	113
2.4.6	Pumping capacity	116
2.5	Results of mass spectrometry	118
2.5.1	Mean free path	118
2.5.2	Beam divergence	119
2.5.3	Mass spectrometric analysis.	120
2.6	Photodissociation spectroscopy	128
2.6.1	Kinetic energy selection	129
2.6.2	Temporal and spatial overlap of the N_2O^+ ion beam with the pulsed dye laser	132
2.6.3	Application to the high resolution spectroscopy of N_2O^+ , the $\tilde{A}^2\Sigma^+(002) \leftarrow \tilde{X}^2\Pi(000)$ vibronic band in N_2O^+	134
2.6.4	Effect of the bias cell	136
2.6.5	Calibration of the frequency scale	139
2.6.6	Rotational temperature	140
2.7	Perspectives	143
2.7.1	Extraction scheme	143
2.7.2	Quadrupole mass filter	146
2.7.3	Photodissociation spectroscopy of $[H_2O-CO_2]^+$	147
3	The Fourier Transform Incoherent Broadband Cavity Enhanced Absorption Spectroscopy (FT-IBB-CEAS) instrument	149
3.1	Uniform planar discharge Nozzle	152
3.1.1	Conception of the Laval nozzle	152
3.1.2	Computational Fluid Dynamics (CFD) simulations	155
3.1.3	Ions optics	164
3.2	High-sensitivity absorption techniques	172
3.2.1	Cavity Enhanced Absorption Spectroscopy <i>CEAS</i>	175
3.2.2	Incoherent Broadband Cavity Enhanced Absorption Spectroscopy IBB-CEAS	177
3.2.3	The light source choice	185
3.2.4	Cavity consideration	189
3.2.5	Detection using a Fourier Transform (FT) spectrometer	191
3.3	IBB-CEAS using a supercontinuum laser coupled to a high finesse cavity and a Fourier transform spectrometer, for the characterization of cold acetylene and cold methane	193
3.3.1	Experimental setup	193
3.3.2	Mode matching	198
3.4	Results and perspectives	204
3.4.1	Spectral bandwidth of the instrument	205
3.4.2	Resolution and acquisition speed	206
3.4.3	Interference fringes feature and their elimination	211

3.4.4	Sensitivity of the instrument	212
3.4.5	Jet cooled spectra of acetylene and methane	217
Conclusion		223
A Appendix: Fluid dynamics		227
A.1	Mass conservation, continuity equation	228
A.1.1	Momentum conservation	229
A.1.2	Energy conservation	229
A.1.3	Navier-Stokes model, compressible real fluid	231
B Appendix: Statistical physics		232
C Appendix: Additional pulsed supersonic source		237
D Appendix: Gaussian Beams and optical cavities		242
D.1	Transverse cavity modes	242
D.2	Quality factor M^2	246
D.3	Ray transfer matrices	246
D.4	Stability of the optical cavity	247
D.5	Optical cavity finesse	249
D.6	Mode matching calculation	252
Bibliography		257

INTRODUCTION

Space and terrestrial observatories have led to the discovery of an interesting variety of complex molecules in the interstellar medium [1] and in different planetary atmospheres [2], which could lead to the understanding of different phenomena like star formation, or a better knowledge of the molecular composition of the universe which is not simply composed of single atoms or simple ionic species, as it was still thought a few decades ago. The main goal of Laboratory Astrophysics is to progress in our understanding of the Universe through theoretical and experimental research. One of the major objectives of this discipline is to determine the nature and abundance of molecules in various astrophysical environments (planetary atmospheres, interstellar clouds, circumstantial envelopes). Achieving this goal requires spectroscopic identification, which presents the advantage to provide information on the temperature of the different degrees of freedom of the detected species, and allows for remote detection in environments not amenable to mass spectrometry (interstellar medium, exoplanets, etc).

The list of detected cations is growing regularly [3]. In addition to molecular cations, species even less abundant were detected, i.e. ionic molecular complexes and anions. The first molecular anion detection dates back to 2007 [4].

In our solar system, anions and anionic clusters were detected, but only by mass spectrometry i.e. in Titan's atmosphere [5] with a mass-to-charge ratio (m/z) going up to 10000 and with tentative assignment of only a part of the observed molecular anions [6]. In Enceladus protonated water clusters were detected with additional peaks corresponding to the addition of sodium atoms. This detection took place in the E-ring of Saturn [7] and was assigned to the emission of plumes of water taking place at the surface of Enceladus. The laboratory determination of reliable spectral data in the gas phase is the first essential step towards the discovery of any new astrophysical species. For what concerns ionic molecular complexes, many detections have been performed in our atmosphere [2, 8] between 70 and 100 km) by mass spectrometry, with a m/z ratio most corresponding to different species such as $H^+-(H_2O)_n$ with n ranging from 1 to 20. The anions such as CO_3^- , HCO_3^- , Cl^- and OH^- were also detected at this altitude. No direct spectroscopic detection of those species has yet been achieved, partly due to the lack of laboratory reference measurements. In addition, ionic complexes and anions are believed to play an important role in the chemistry of the atmosphere through elementary chemical reactions involving few molecules [2]. Since the detection of anions and clusters in the earth's atmosphere, the mechanism of their formation was intensively studied both theoretically and experimentally [9, 10, 11, 12], but reliable detection of other similar species, as well as the determination of their molecular structures, rely on future high-resolution spectroscopic studies, as for example the high resolution study of the ionic complex $[CO_2-H_2O]^+$ that was only studied by photodissociation spectroscopy at low resolution [13]. A large number of radicals and ions are unstable under normal conditions of pressure and temperature, complicating the characterization of their properties. Yet, they play a key role in the physical chemistry of astrophysical environments. Their characterization relies on developed new techniques capable of producing these

species under certain conditions like in a supersonic expansion.

In addition to astrophysics/atmospheric detection, ionic complexes present an interest in other fields. From a molecular physics perspective, ionic complexes are interesting because the intermolecular bond strength is typically located between that of van der Waals and covalent bonds. Moreover, such species usually present open shell electronic structure and interesting couplings between the different degrees of freedom. The study of molecular complexes and clusters of systematically increasing size allows studying, molecule per molecule, the transition between the gas and the condensed phase, which is relevant from a chemical point of view. The motivations for studying these species are therefore (i) to allow their identification; (ii) to confirm their suspected importance in the chemistry of different atmospheres and astrophysical environments; (iii) but also to study in detail non-rigidity, solvation and chemical reactivity at the molecular level [2, 14, 15].

This thesis aims at developing competitive instruments and an experimental methodology to study astrophysical and relevant atmospherical ionic molecular species by high-resolution, rotationally resolved spectroscopy, and mass spectrometry. Which will make possible the detection of large anion carbon chains (i.e. C_4^- , C_6^- , C_8^- , ... C_n^-) and cationic molecular complexes (i.e. $[CO_2-H_2O]^+$, H_3^+-Kr). Due to space charge effects and to the weakly bound nature of ionic complexes, the density of the targeted species produced in the laboratory is extremely low. Great efforts are therefore required on both sides, on the optimization of the production of ionic complexes and on the sensitivity of the used spectroscopic techniques. This research work was partly conducted at the Université catholique de Louvain (UCLouvain) and partly at the Université de Rennes 1 (UR1). The complementary expertise of the two research teams was used to tackle those challenges.

The development of the instrument dedicated to the spectroscopic characterization of anionic carbon chains was undertaken at UR1 by Fourier Transform Incoherent Broadband Cavity Enhanced Absorption Spectroscopy (FT-IBBCEAS), while the investigation of the ionic species (molecular ions, small clusters, or ion complexes) took place in UCLouvain by means of photodissociation spectroscopy. Even if several examples exist in the literature, the production of such charged species in sufficient concentration to record their spectroscopic signature is very challenging. In this work we have chosen to use a supersonic jet expansion coupled to different ionization techniques like the electric discharge [16, 17]; or the use of an electron gun that showed some efficiency to produce both cationic and anionic complexes, and offers the possibility to partly tune the ionization energy by adjusting the acceleration potential of the electrons. Neumark's group, among others, has used this method to produce a large variety of negatively charged species [18] including long anionic carbon chains [19], C_n^- with $n = 4, 6, 8$.

The first chapter will be focused on supersonic jet expansion, used intensively in both laboratories. Different equations and theorems will be recalled. The jet expansion will be treated by combining mechanical/thermodynamical and statistical approaches to derive the variation of different key quantities i.e. pressure, temperature, density and velocity. The difference between planar and axisymmetric jets will also be recalled as well as the difference between a so-called free-jet and a jet produced by a de Laval nozzle.

For the spectroscopic characterization of charged clusters/complexes, the STARGATE (Spectroscopy of Transient Anions and Radicals by Gated and Accelerated Time-of-flight Experiment) apparatus we developed at UCLouvain is based on the photodissociation of mass selected complexes and the detection of fragment ions. This experimental approach, in addition being a background-free method, also helps to overcome the challenges mentioned before, that is to say (i) low density, through extreme detection sensitivity (a single ion can be detected), and (ii) the avoidance of spectral overlap of different species, through mass selection prior to any light absorption. The second chapter is thus dedicated to the description of this technique. We will start by introducing the STARGATE instrument with its different functionalities. Each part of the instrument will be detailed and compared to other methods used in the literature. We will present the results obtained by recording a spectrum obtained by monitoring the charged fragments as a tunable laser is scanned. At the end of the second chapter, we will present the photodissociation spectrum of N_2O^+ recorded with a dye laser. This measurement was used to optimize the different experimental parameters and characterize the performance of the experimental setup.

The third chapter will be dedicated to the description of the instrument developed at UR1 to characterize anionic species. The goal is to determine the spectral signature of unstable species (radicals, ions) in the visible and near-infrared region. The approach selected in this work combines an ion source based on a planar discharge in a uniform supersonic flow, and a high-sensitivity spectrometer. The coupling of a broadband light source to a high finesse optical cavity will be described, as well as the performances of the planar nozzle in terms of temperature and density. First spectra of the overtone absorption spectrum of acetylene and methane at ambient and cold temperatures will be presented that helped to evaluate the performance of the experimental setup, by determining the effective interaction length, the reflectivity of the mirrors, the resolution that could be attained and the sensitivity of the instrument.

SUPERSONIC EXPANSION

In this thesis we used the supersonic jet expansion technique for the production of the desired species. This production is coupled to two different sensitive characterization methods, the photodissociation spectroscopy (chapter 2) and the Fourier transform cavity enhanced absorption spectroscopy (chapter 3). In fact, an efficient production of these species in terms of density (10^{15} - 10^{17} particles/cm³) and low temperature (10 K - 70 K) in the gas phase is required even with the implementation of extremely sensitive characterization techniques. The motivation for cooling the molecules is threefold: (i) to promote partial condensation in order to produce clusters if desired, (ii) to reduce spectral congestion and to simplify the recorded spectral signature in order to simplify its analysis, (iii) and to reach a high level of state selectivity by cooling internal degrees of freedom, with large populations in the molecular states of interest which can enhance the signal-to-noise ratio.

Many sophisticated techniques to cool a gas are mentioned in the literature. Laser-cooling [20] relies on the fact that when an atom absorbs and re-emits a photon its momentum changes. For an ensemble of particles, their thermodynamic temperature is related to the variance in their velocity. That is, more homogeneous velocities among particles corresponds to a lower temperature. Laser cooling techniques combine atomic spectroscopy with the above-mentioned mechanical effect of light to compress the velocity distribution of an ensemble of particles, thereby cooling the particles. An interesting example of the literature is the one of alkali dimers that are created from laser-cooled alkali atoms using photo-association [21]. Another method is the Feshbach resonances [22]. Briefly, it can occur upon collision of two slow atoms, when they temporarily stick together forming an unstable compound with short lifetime (so-called resonance); for more details the reader could refer to [23]. Another method is the one of buffer gas cooling. This method is more commonly implemented than the previous ones, and generally it is done by the circulation of a cryogenic fluid between the two walls of a doubled walled cryogenic cell. The cell is filled with helium gas thermalized with the cell wall. The gas sample is cooled by collisions with the helium buffer gas before it condensates on the walls of the cell. This method is, however, less used than the technique of the supersonic jet expansion given the significant condensation on the walls and the resulting uncertainty on the measured concentration [24]. An example from the literature is the combination of mass spectrometry, cryogenic ion traps, and laser spectroscopy to interrogate individual conformations of peptides and proteins [25]. Another example is the one of the recent study by Changala *et al.*, they have recorded the infrared spectrum of C₆₀ in the gas phase [26].

Supersonic jet expansion has played a major role in chemical physics research [27]. This technique was pioneered by Levy and co-workers in the 70s [28, 29]; this method also contributed to the winning of eleven Nobel prizes [30], and became very popular in many fields of physical sciences such as spectroscopy,

chemical dynamics, fluid mechanics, and surface studies [31]. A jet is a flow generated by a difference of pressure between both sides of a suitable orifice that can be a pinhole, a confining flow nozzle, a slit or multi-nozzle assembly, which leads to an ejection speed characterized by a high Mach number. The flow can be constrained to expand through a convergent-divergent duct, called de Laval or more frequently Laval nozzle, before to expand freely in the low-pressure chamber. These two methods, free jet or Laval nozzle jet will be discussed and compared in terms of density and temperature.

To start, dimensionless numbers as Reynolds and Mach number are introduced along with their corresponding flow regime and nature. Then the case of an isentropic expansion is treated using a thermodynamic approach, and then a statistical approach. The definition of the Maxwell-Boltzmann velocity distribution is also introduced. Attention is paid to the determination of the evolution of the temperatures during the isentropic expansion side to side with the description of the effects of the nozzle design on the expansion. A comparison between a planar and a coaxial nozzle in terms of pressure, temperature, and density evolution for different carrier gases will also be carefully done. This chapter will be therefore a theoretical introduction to the two production methods used in this thesis.

1.1 Fast cooling in an adiabatic expansion

1.1.1 Advantage of cooling for absorption spectroscopy

Figure 1.1 shows the simulation of the absorption spectrum of the isotopologue $^{18}\text{O}^{12}\text{C}^{17}\text{O}$ which has a density ratio 10,000 times lower than the main isotopologue $^{16}\text{O}^{12}\text{C}^{16}\text{O}$. We added to the simulation a noise equal to ± 0.5 on the absorbance. At ambient temperature the $^{18}\text{O}^{12}\text{C}^{17}\text{O}$ band is below the noise threshold and also eclipsed by the dense spectrum of CO_2 (Iso1). On the other hand, at a temperature of 70 K, the high rotational states are depopulated and the CO_2 spectrum becomes less congested. Therefore the $^{18}\text{O}^{12}\text{C}^{17}\text{O}$ band concentrates its intensity in a reduced number of rovibrational transitions leading to a more important signal-to-noise ratio. This effect is all the more marked the lower the temperature. This simple figure therefore illustrates the interest of supersonic cooling for absorption spectroscopy.

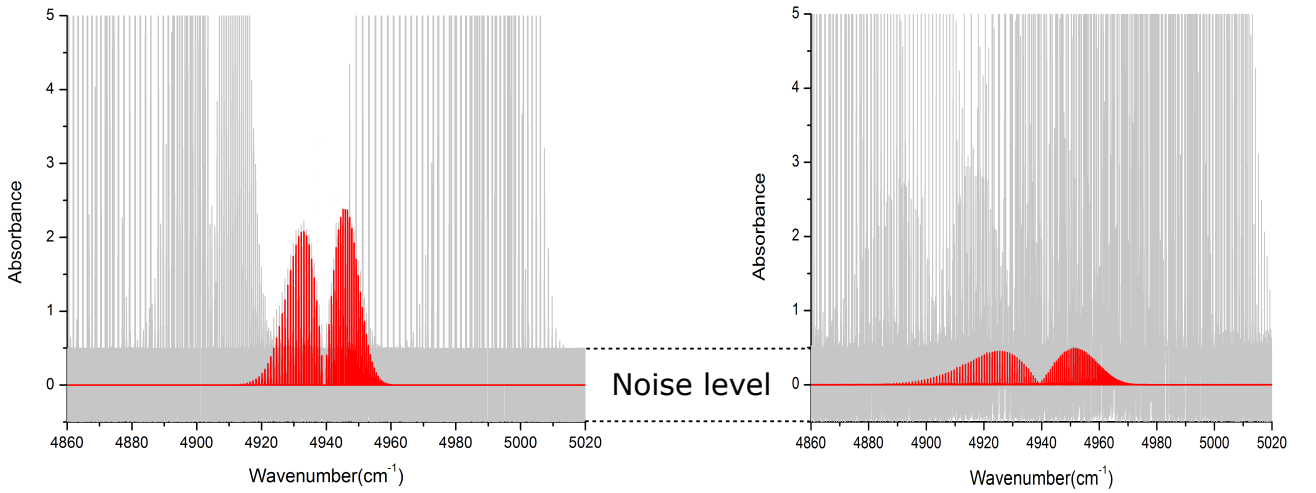


Figure 1.1 – On the left, cold spectrum of $^{16}\text{O}^{12}\text{C}^{16}\text{O}$ in grey and $^{18}\text{O}^{12}\text{C}^{17}\text{O}$ in red (70 K). On the right, room temperature (300 K) spectrum of the same species. The absorption noise level is set to ± 0.5 . This figure shows the interest of cold temperature measurements for low abundance species.

1.1.2 Adiabatic expansion

In order to understand the advantage of the fast cooling in an adiabatic expansion, we start this chapter by considering an example of an isolated system as illustrated in Figure 1.2, composed of a reservoir containing a gas at high pressure. The gas can flow through an orifice of diameter D into a low-pressure chamber. In the reservoir, the pressure is P_0 , the temperature T_0 and the initial density is equal to ρ_0 , while the background chamber has the physical parameters P_b , T_b and ρ_b . If the difference in pressure between the two compartments is not zero, a flow will be generated with a velocity v composed of a radial or transverse velocity $v_{//}$ parallel to the direction of the flow and a transverse velocity v_{\perp} perpendicular to it as we are dealing with the case of an axisymmetric flow. Such a configuration gives rise to two distinct families of global particle motions, defined as effusive and isentropic expansion, respectively, with very different characteristics.

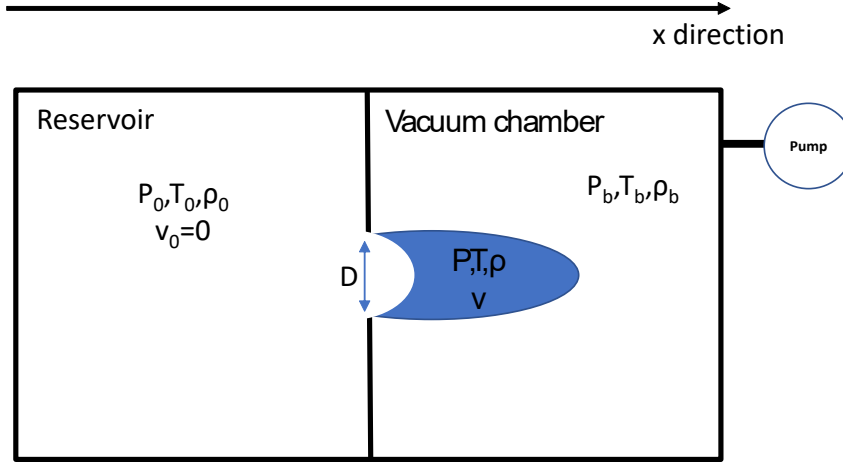


Figure 1.2 – Schematic representation of the physical system composed of a gas reservoir, and a vacuum chamber at low pressure. The gas expands into the vacuum chamber through a hole of diameter D

As a reminder, c_P and c_V are the specific heat capacity per mass at constant pressure and volume respectively and specific heat ratio $\gamma = c_P/c_V$. If we assume that the fluid used in this study is considered as an ideal gas. The ideal gas law allows writing $P/\rho = rT$ where $r = R/Mn$ with R the ideal gas constant and Mn the molar mass of the gas:

We consider an initial state (p_0, T_0, ρ_0) and a final state (p_b, T_b, ρ_b) we obtain Equation 1.1

$$\left(\frac{\rho_b}{\rho_0}\right) = \left(\frac{T_b}{T_0}\right)^{\frac{1}{1-\gamma}} \quad (1.1)$$

By introducing the final particle density n_b such that $P_b = n_b k T_b$, where k is Boltzmann's constant, using the equation of an ideal gas and rearranging the expression, the relations that describe the general isentropic process are given by Equation 1.2 :

$$\frac{P_b}{P_0} = \left(\frac{\rho_b}{\rho_0}\right)^\gamma = \left(\frac{n_b}{n_0}\right)^\gamma = \left(\frac{T_b}{T_0}\right)^{\frac{\gamma}{\gamma-1}} \quad (1.2)$$

Using these equations, we can predict the final temperature and density in this case below:

- (a) $T_0 = 291$ K
- (b) $n_0 = 4.85 \times 10^{25}$ number of particles/m³
- (c) $P_0 = 420$ Torr
- (d) $P_b = 0.13$ Torr

If we consider the use of argon adiabatic expansion, the temperature evolves down to $T_b = 11.64$ K and the density evolves down to $n_b = 2.06 \times 10^{13}$ number of particles/m³. Therefore, we can conclude that the adiabatic expansion of a gas, makes it possible to reach extremely low temperatures, close to 1 K and even lower in certain cases [32].

1.1.3 Supersaturation

A question could arise, reaching for such low temperatures will not lead to a change of the sample gas phase, leading to condensation? The fast cooling of the jet (rate of $dT/dt \approx -10^8$ K/s), leads to the supersaturation of the expanded gas preventing its condensation. As illustrated in Figure 1.3 plotted for a supersonic expansion of pure argon, during its adiabatic expansion the gas penetrates very deeply into the solid phase with a typical pressure which is several orders of magnitude above its pressure of saturated vapour at this temperature. The gas is therefore highly supersaturated, which means that the density of the gas is much higher than that obtained by probing a sample of gas at equilibrium in a static cryogenic gas cell maintained at the same temperature. Equation 1.2 one can plot the evolution of $\ln P$ versus $\ln T$ as following :

$$\ln P = \frac{\gamma}{\gamma - 1} \ln T + \ln\left(\frac{P_0}{T_0^{\frac{\gamma}{\gamma-1}}}\right) \quad (1.3)$$

This equation gives a linear curve characterized by a slope $\frac{\gamma}{\gamma-1}$, and a y-intercept equal to $\ln\left(\frac{P_0}{T_0^{\frac{\gamma}{\gamma-1}}}\right)$

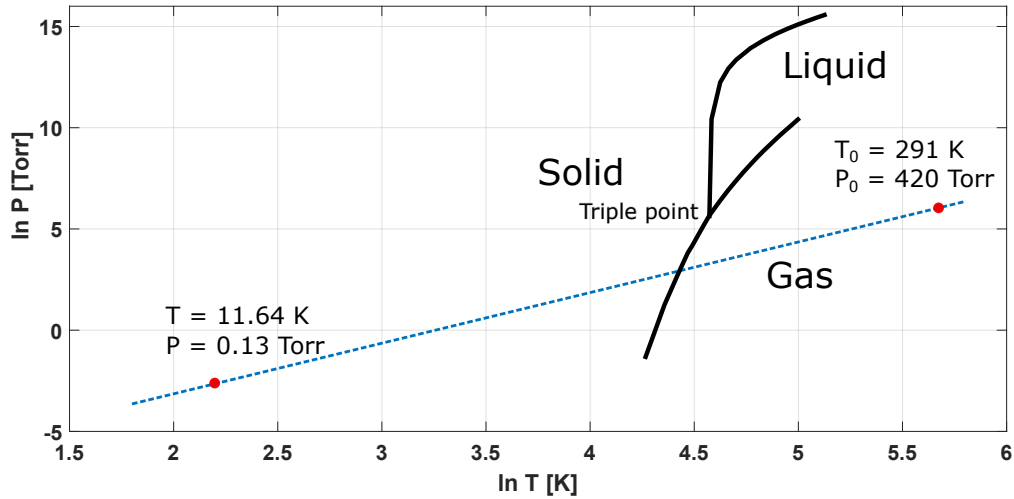


Figure 1.3 – The equilibrium curves of argon are plotted in a P, T diagram using a logarithm scale. The reservoir conditions are 291 K and 420 Torr. The adiabatic expansion brings the gas to 11.64 K and 0.13 Torr. The gas phase is conserved due to the rapid cooling of the adiabatic expansion.

1.2 Dimensionless numbers

Dimensionless numbers are important to define the regime and the initial conditions of the flow and these numbers are calculated and used in Chapter 2 (Section 2.3.3) in order to correctly model the free supersonic jet and in Chapter 3 (Section 3.1.2) to correctly model the uniform supersonic jet expansion using a Laval nozzle.

1.2.1 Reynolds number

The Reynolds number Re of the jet represents the ratio of inertial and viscous forces. It characterizes the nature of the flow regime, namely laminar, transient, or turbulent, whatever the nature of the fluid. We can calculate this number using Equation 1.4 where μ as the dynamic viscosity:

$$Re = \frac{\rho v D}{\mu} \quad (1.4)$$

If $Re < 2000$ viscosity forces are dominant and the flux is laminar. If $2000 < Re < 3000$ the flux is inertial, it means the flow is still laminar but in a transition phase. If $Re > 3000$ the flow is turbulent, and due to the agitation factor the cooling of the species in the jet is less efficient. Later in section 1.7.5, we calculate the Reynolds number for the two sources used in this thesis. We show as well the evolution of the different physical quantities of interest (density, velocity and viscosity). Different regimes (turbulent or laminar) could be identified in different zones of the jet.

1.2.2 Mach number

If we consider a compressible fluid, we can calculate the speed of sound v_s . It is defined as the propagation velocity of a disruption of pressure in the fluid and it represents the pressure-density relation for the fluid [33]. In the case of an isentropic expansion of an ideal gas, v_s can be calculated by using Equation (1.5).

$$v_s = \sqrt{\frac{\partial P}{\partial \rho}} = \sqrt{\gamma P \rho^{-1}} = \sqrt{\gamma r T} \quad (1.5)$$

Mach number represents the ratio of the velocity of the flow and the speed of sound. It measures the amount of thermal energy that was transformed adiabatically into kinetic energy. When all the thermal energy has been converted into kinetic energy then Mach tends towards an infinite value because the speed of sound tends to 0 as the temperature tends to 0 K. This explains the need to produce flows with very high Mach numbers. The Mach number is expressed as a function of the speed of sound v_s as shown in Equation 1.6:

$$M = \frac{v}{v_s} \quad (1.6)$$

For $M < 0.3$, the compressibility effects are negligible. For $M = 0.3$, the compressibility of the studied gas increases dramatically and must be taken into account because it affects the mass flow expressed by $\rho v V$ in which S is the passage section. The volumetric mass collapses when the Mach number tends

towards high values. Therefore, to maintain a constant mass flow for an increasing Mach number above 1, that is to say above the speed of sound, it is necessary for the gas to increase its passage section S . This explains the divergent profile diameter of the Laval nozzles. Upstream the throat, the flow is subsonic ($M < 1$), sonic at the throat ($M = 1$) and supersonic downstream $M > 1$.

1.2.3 Knudsen number

The mean free path is the length that a particle can travel before encountering a collision with a second particle. It is defined by:

$$\lambda_0 = \frac{kT_0}{\sqrt{2}P\sigma} \quad (1.7)$$

with $k = 1.38 \times 10^{-23} \text{J} \cdot \text{K}^{-1}$ the Boltzmann constant and σ the collisional cross section.

The Knudsen number is a commonly used number for identifying the flow regime in terms of continuity. It is defined by the ratio of the MFP and the nozzle diameter D :

$$Kn = \frac{\lambda_0}{D} \quad (1.8)$$

Two cases are to be distinguished at the position of the throat, depending on the relative size of the nozzle diameter D , nozzle throat or slit width, compared to the mean free path λ_0 of the molecules under stagnation conditions. If $Kn > 1$, the beam is called effusive and the gas molecules can travel a distance greater than D without undergoing any collisions. The Maxwell-Boltzmann velocity distribution of the gas molecules does not change when the gas passes through the nozzle from the gas reservoir into the vacuum chamber. Under such conditions, the effusive beam does not lead to any cooling effect. In the opposite case, if $Kn < 1$, the molecules undergo a large number of collisions when they pass through the nozzle to expand into the vacuum chamber, at least during the first stage of the expansion. The molecules exchange energies and the velocity will have a Maxwell-Boltzmann distribution, different than the one of the reservoir. The effect of heat transfer is minor, the flow is treated as isentropic.

Regime	Knudsen number	Equations
Continuous regime	$Kn < 10^{-2}$	Euler
Creeping flow	$10^{-2} < Kn < 10^{-1}$	Navier-Stokes
Transient regime	$10^{-1} < Kn < 10$	Boltzmann
Free molecular regime	$Kn > 10$	Boltzmann

Table 1.1 – Definition of the different flows regimes using the Knudsen number as a reference. The appropriate corresponding equations used to describe each flow regime are also mentioned in this table.

An example from the literature [34], shows the evolution of the Knudsen number, and Mach number with respect to the distance from the nozzle in the case of slit jet expansion. As displayed in Figure 1.4, Kn starts from values as low as 10^{-2} which is the case of a continuous flow and attains a value of 0.125 just before the shock wave which corresponds to a creeping flow, on the other hand, the Mach number attains values up to 17 which indicates an important enthalpy conversion.

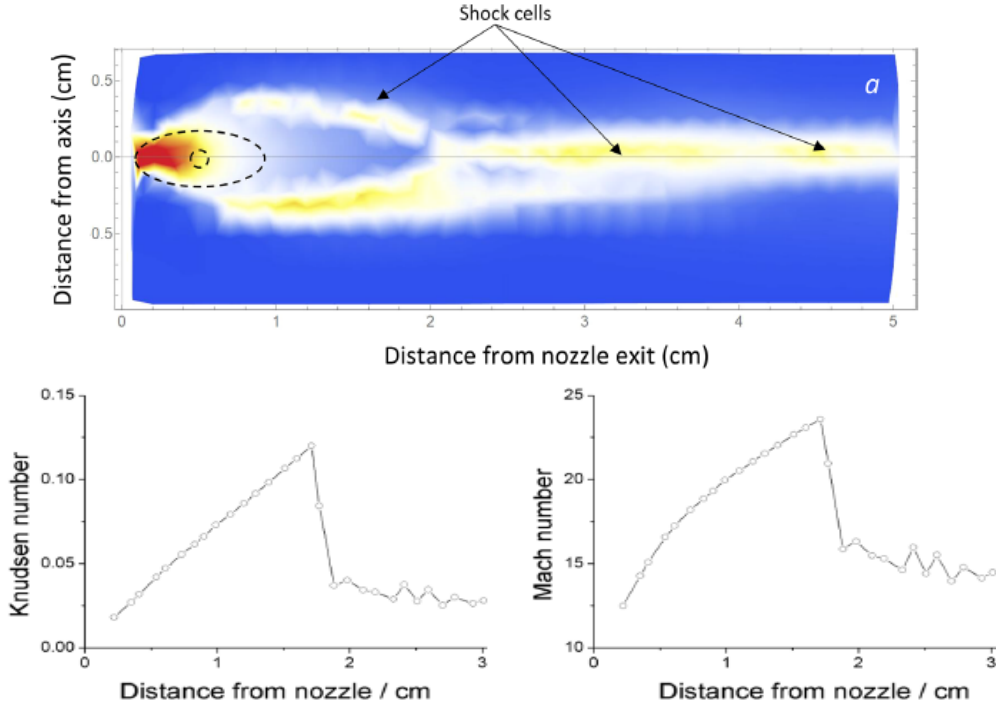


Figure 1.4 – On top the impact pressure measurement by a pitot tube is shown. The flow parameters have been extracted from the measurements relative to the plane of symmetry : Knudsen number on the left and the Mach number on the right.

In the case of the source at UClouvain consists of a jet of argon atoms with:

1. $D = 1$ mm.
2. $P_{throat} = 2$ bar
3. $T_{throat} = 220.15$ K
4. $\sigma \approx 1.58 \times 10^{-20}$ m²

Equation (1.8) gives $\lambda_0 \approx 9.2 \times 10^{-7}$ m and $Kn \approx 4.61 \times 10^{-3}$. The flow undergoes a lot of collisions at the nozzle throat; this configuration gives also rise to an isentropic expansion. Then the pressure of the chamber decreases along with temperature which cause the Kn number to increase to values higher than 10 giving rise to a free molecular regime.

In the case of the source at Rennes consists of a jet of argon atoms with:

1. $D = 1$ mm.
2. $P_{throat} = 0.4$ bar
3. $T_{throat} = 220.15$ K
4. $\sigma \approx 1.58 \times 10^{-20}$ m²

Equation (1.8) gives $\lambda_0 \approx 9.2 \times 10^{-7}$ m and $Kn \approx 9.2 \times 10^{-4}$. The flow undergoes a lot of collisions at the nozzle throat; this configuration gives rise to an isentropic expansion. Then the pressure of the chamber

decreases to $P_b = 10^{-4}$ mbar along with the temperature which cause the Kn number to increase and that the flow reaches a creeping flow.

1.3 Isentropic equations

Supersonic cooling is based on the thermodynamic properties of the isentropic expansion of a fluid.

Let's Consider the expression of the entropy variation per unit of mass ds of a system of particles given by Equation 1.9 that is composed of internal and external variations of entropy.

$$ds = \delta_e s + \delta_i s = \frac{\delta Q}{T} + \delta_i s \tag{1.9}$$

Where δQ is the quantity of heat per unit of mass exchanged between the system and its surroundings. In our case we assume an isentropic expansion. Indeed for a reversible transformation, $\delta_i s = 0$ leading to $\delta Q = Tds$. In the case of the production of charged species, due to the plasma discharge the heat produced is communicated to the gas between the tank and the outlet. For jets without the production of plasma, $\delta Q = 0$ (adiabatic expansion).

The equation that reflects the conservation of energy per unit mass is resolved in Appendix A, we recall the resulting formula for its importance to describe the jet from a thermodynamical point of view:

$$\underbrace{c_P T_0}_{[1]} = \underbrace{c_P T}_{[2]} + \underbrace{\frac{1}{2} v^2}_{[3]} \tag{1.10}$$

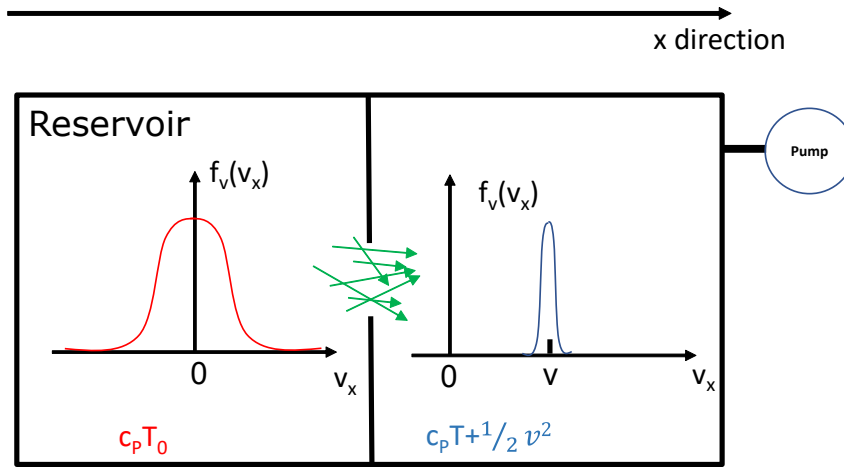


Figure 1.5 – Schematic representation of the conversion of a part of the thermal energy of the gas in the reservoir into kinetic energy in the expansion in the vacuum chamber, after undergoing a high number of collisions which is represented in green. On the other hand, in the jet, the thermal agitation is super reduced. It is therefore necessary to mark two points 1. Speeds have increased in the laboratory referential 2. Speeds have considerably decreased in the gas referential 1. and 2. are the two key points of a supersonic flow. A reduction in the distribution of velocities along the instrument's axis v_x and an increase in the flow velocity, v . The width of the velocity distribution of the supersonic beam narrows during the expansion into the vacuum chamber.

The term [1] of Equation A.15 represents the thermal energy associated with the motion of the particles in the reservoir, the term [2] is the thermal energy of particles for the gas in expansion in the vacuum chamber and the last term [3] is the kinetic energy associated with the directed motion of the gas

particles in the expansion. Thus the stagnation enthalpy, characterizing the regions where the gas velocity is zero on average, corresponds to the internal energy fraction capable of being converted into kinetic energy. This setting in motion of the fluid results in a drastic decrease in translational temperature.

This thermodynamic property is crucial in our study since the decrease in temperature is advantageous to reduce the congestion in the measured spectra, and to amplify the signal-to-noise for a better analysis of the obtained gases spectra. When all the internal energy has transformed into kinetic energy, we can establish the following relation by assuming that the temperature T , tend to 0 K:

$$v_{\infty} = \sqrt{2c_P T_0} \quad (1.11)$$

Equation 1.11 allows us to estimate the speed limit v_{∞} of the used gas. Therefore, we can conclude that the higher the temperature of the tank, the greater the maximum achievable speed that could be attained.

In order to characterize the flow in expansion from a thermodynamics point of view. Equation A.15 that describes well isentropic expansion can be used to express T, P, ρ and v in term of the Mach number M . For a perfect gas, $c_P = \gamma R / (\gamma - 1)$ and the square of the sound velocity $v_s^2 = \gamma RT$. Substituting for c_P and v_s^2 into Equation A.15 gives Equation 1.12 :

$$\frac{v_{s,0}^2}{\gamma - 1} = \frac{v_s^2}{\gamma - 1} + \frac{u^2}{2} \quad (1.12)$$

Introducing $M = v/v_s$ into Equation 1.12 and rearranging gives Equation 1.13

$$v_{s,0}^2 \left(\frac{1}{\gamma - 1} \right) = v_s^2 \left(1 + \frac{\gamma - 1}{2} M^2 \right) \quad (1.13)$$

Finally, by using $v_s^2 = \gamma RT$ and the Equation 1.2 that makes the relation between pressure, density and temperature. These isentropic equations for temperature, pressure, volumetric mass and velocity are obtained and given respectively below as a function of the Mach number:

$$\frac{T_0}{T} = 1 + \frac{\gamma - 1}{2} M^2 \quad (1.14a)$$

$$\frac{P_0}{P} = \left(1 + \frac{\gamma - 1}{2} M^2 \right)^{\gamma/(\gamma - 1)} \quad (1.14b)$$

$$\frac{\rho_0}{\rho} = \left(1 + \frac{\gamma - 1}{2} M^2 \right)^{1/(\gamma - 1)} \quad (1.14c)$$

$$v = v_{s,0} \sqrt{\left(\frac{2M^2}{2 + (\gamma - 1)M^2} \right)} \quad (1.14d)$$

The expansion of the high-pressure reservoir into the vacuum chamber takes place using a nozzle. It is an energy converter able to accelerate the gas up to supersonic speeds. Among others, the geometry of the nozzle could be circular, planar, conical, convergent-divergent or other geometries. A study in the literature [35] and more recently [36] compared the different geometries and it could be interesting for the reader. A simple circular nozzle will be considered in our experiment at Louvain-la-Neuve. The main

difference between the simple circular nozzle with the de Laval nozzle is that in the case of the simple convergent nozzle the beam is not confined by walls at the exit of the nozzle (i.e. there is no divergent part after the throat). Without the well calculated divergent profile of the Laval nozzle after the throat, the produced jet is said to be "free". At the smallest section of the nozzle $M = 1$ we can calculate the throat initial conditions, P^* , ρ^* and T^* that are called critical pressure, density and temperature of the flow [37]. Injecting $M = 1$ into the equations of temperatures, pressures and volumetric mass ratios of Equations 1.14, gives Equation 1.15

$$\frac{P^*}{P_0} = \left(\frac{\rho^*}{\rho_0}\right)^\gamma = \left(\frac{T^*}{T_0}\right)^{\frac{\gamma}{\gamma-1}} = \left(\frac{2}{\gamma+1}\right)^{\frac{\gamma}{\gamma-1}} \quad (1.15)$$

In the case of the expansion of a monatomic gas ($\gamma = 5/3$) and a diatomic gas ($\gamma = 7/5$) with the conditions used at UCLouvain a pressure in the reservoir of $P_0 = 2$ bar, according to Equation (1.15), P_b must be well smaller than 0.49 bar and 0.53 bar respectively and in our experiment it is equal to $P_b = 10^{-5}$ mbar. Under this condition, the flow will expand supersonically in a region that is limited by the interaction of the flow with the residual molecules present in the vacuum chamber. As we will see in the next section, these interactions create discontinuous regions so-called shock waves (section 1.7.1) beyond which the beam becomes again subsonic.

1.4 Velocity distribution

A fundamental property of all supersonic jets is that the different degrees of freedom of the molecules are in a none equilibrium state [38]. Later in section 1.6, we are going to define the translational, rotational and vibrational temperatures that corresponds to the different degree of freedom of the molecules. In this section we are going to develop the Maxwell-Boltzmann's theory of gas kinetics applied to the classical ideal gas. This approach will allow us to make the link between the notion of statistical distribution and temperature. This approach will give us an idea on the distribution of the velocity inside the reservoir and then after the expansion. To determine the velocity distribution of a supersonic expansion, we have to take in consideration the static gas in the reservoir and then we have to consider the effect of the expansion of this distribution. Therefore, in this section 1.4 we will first describe mathematically the distribution of the velocity in the reservoir for $\bar{v} = 0$ and then this distribution is calculated for different seeding gases and for different temperatures. Secondly, we will calculate the distribution of velocities during the expansion after the nozzle exit. In this part of the jet, velocities tend to have a certain organization and a motion with nearly equal velocities. To better understand, a schematic representation of Equation A.15 is given in Figure 1.5, based on Figure 1.2, in which we show the two different corresponding estimated distributions. The distribution $f_v(v_i)$ of a velocity component v_i [m/s] in i -direction for a static gas is given by Equation 1.16. The reader can refer to Appendix D.

$$f_v(v_i) = \sqrt{\frac{M_n}{2\pi RT}} \exp\left[-\frac{M_n v_i^2}{2RT}\right] \quad (1.16)$$

As we can see from the equation, the velocity distribution depends on the molar mass of the gas we are using and the temperature of the reservoir. Noble gases from the 18th group of the periodic table are used as seeding gas for the supersonic expansions for their efficiency of cooling and of reducing heating due to their inert nature that prevents reactions with the precursor molecule. These gases are monatomic, thus the absence of the rotational and vibrational energies, it is much easier to reduce just one degree of freedom which is the translational temperature.

The FWHM of the Gaussian distribution is proportional to the temperature of the reservoir and to the mass of the molecules.

During the expansion from the high-pressure reservoir to the low-pressure chamber, the molecules undergo a very large number of collisions in the outlet channel and then in its outer vicinity. The density of the gas and the frequency of the collisions will gradually decrease as it moves away from the orifice and also the frequency of the collisions. A fundamental property of all molecular supersonic jets is the difference between the different temperatures at a non-equilibrium state, which increases with distance to the nozzle. Since the number density decreases with expansion (proportional to the distance⁻² for the case of a axisymmetric jet and to the distance⁻¹ for the case of a planar expansion) the difference between the different temperature (translational and rotational) is correlated with the rarefaction. It must be emphasized, however, that large differences are attained easily in laboratory free jets under modest rarefaction [39]. Unlike the case of an effusive jet in which the thermodynamic properties remain intact, the molecules exchange energies in the area of high collisions and cool down during the expansion.

Thus, relating to the Equation A.15, when the beam expands, the transformation of the thermal energy into kinetic energy will induce a narrowing in the distribution with a gain of a certain velocity v

that depends essentially on the used seeding gas. We can represent the distribution of the velocities for argon for different Mach numbers [40].

$$f_v(v_x) = \left(\frac{M_n}{RT_0}\right)^{\frac{3}{2}} \left(1 + \frac{\gamma-1}{2}M^2\right)^{\frac{3}{2}} v_x^3 \exp\left(-\left[\left(\frac{M_n}{2RT_0}\right)^{\frac{1}{2}} \left(1 + \frac{\gamma-1}{2}M^2\right)^{\frac{1}{2}} v_x - \left(\frac{\gamma}{2}\right)^{1/2} M\right]^2\right) \quad (1.17)$$

An example of the change of the velocity component distribution $f_v(v_x)$ of the gas particles in the x-direction is illustrated for argon for different Mach numbers by the curves plotted in Figure 1.6.

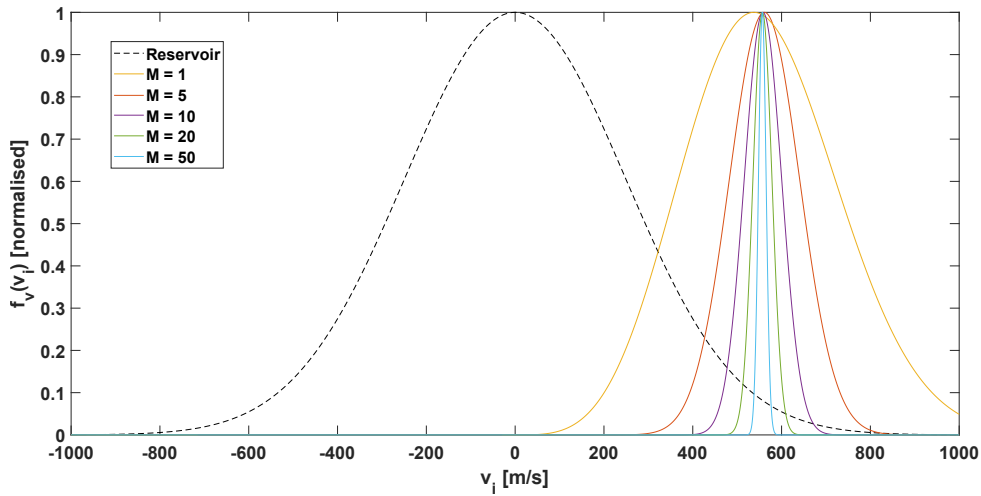


Figure 1.6 – The Maxwell-Boltzmann velocity distribution of argon in the reservoir compared to the distribution of the jet for different Mach numbers. The maximum velocity is almost reached for $M = 1$. The full width at half maximum (FWHM) represents the translation temperature T_t of the gas.

We can conclude that in the reservoir, the molecular velocity distribution for a particular direction is maximum at velocity equal to zero, since the probability for the motion in the forward direction is the same as in the opposite direction. So, the Maxwell-Boltzmann distribution gives a symmetric bell-shaped curve that depends on the nature of the gas used and its temperature. When the gas expands supersonically the distribution keeps its bell shape. However, the distribution gets narrower when the Mach number is getting higher as illustrated in Figure 1.6. That corresponds to the cooling of the gas induced by the isentropic expansion. Unlike the traditional cooling methods where the gas stays at $v_0 \approx 0$, the increase of M due to the isentropic expansion induces a shift of the maximum of the distribution to higher velocities since the gas flows in a particular direction, and the decrease of the temperature induces a decrease of the FWHM. We can observe that the maximum velocity that could be attained is already reached for $M = 5$.

Helium ≈ 1765 [m/s]	Neon ≈ 760 [m/s]	Argon ≈ 560 [m/s]	krypton ≈ 388 [m/s]
-----------------------------	--------------------------	---------------------------	-----------------------------

Table 1.2 – Maximum velocities for different gases during the expansion if the reservoir is at 300K

1.5 Seeded expansion

During an isentropic expansion, the cooling is more efficient for a monatomic gas ($\gamma = 5/3$) than for a diatomic gas ($\gamma = 7/5$). It is due to the fact that atoms do not store energy in rotational and vibrational degrees of freedom contrary to molecules. The seeding technique consists in using a gas mixture that is composed of a low concentration ($\leq 10\%$) of the studied molecules mixed with a high concentration of a carrier monatomic gas, like helium or argon [41, 37]. The small concentration of the molecules only affects the gas velocity and the Mach number, which are mostly determined by the carrier gas. The isentropic expansion allows decreasing T_t of the monatomic carrier gas forming a so-called "cold bath". The collisions between the molecules and the carrier gas particles will allow a more efficient cooling of the considered molecules. It is also shown in the literature that the translational temperature of different molecules could be cooled differently using different carrier gases and it becomes more efficient if the molar mass of the seeding gas is close to the one of the studied gas [42]. A publication showed that using helium as a seeding gas is more efficient than argon to cool down the vibration of CN radicals [43]. On the other hand, the seeding gas parameters influence the jet nature, the beam could be less or more divergent and have a low or a high velocity. These two properties are important for some applications. Thus, the divergence of the jet should be taken into consideration because it will influence the density of the transmitted gas through the skimmer.

1.6 Decoupling of the molecular different degrees of freedom

The important decrease of the gas density induced by the supersonic expansion causes an out-of-equilibrium state of the gas molecules. This imbalance is related to different molecules energies each associated to different temperatures : translational, vibrational and rotational presented as T_t , T_v and T_r respectively and they are assumed to be independent [44]. The translational temperature is divided into radial and transverse temperature $T_{//}$ and T_{\perp} . These temperatures are associated with the radial and transverse-velocity components $v_{//}$ and v_{\perp} of the molecules that are defined with respect to streamlines. In steady state, these streamlines represent the trajectories of the molecules in the flow. The evolution of the temperatures in the vacuum chamber can be described briefly by using the Sudden Freeze Quitting Surface Model [45]. According to this model, two regions can be defined after the nozzle exit : a continuous region characterized by a Knudsen number below 10^{-2} and a free-molecular region giving a Knudsen number higher than 10. These regions are separated by a surface called the quitting surface and the passage from the continuous region of the free-molecular region is sudden.

In the continuous region located just behind the nozzle exit, the distribution of v_{\perp} and $v_{//}$ narrows equivalently during the isentropic expansion, due to the many molecular collisions present in the continuous region. These narrowing effects induce a translational cooling, both $T_{//}$ and T_{\perp} decrease and an equilibrium state is finally reached such as $T_{//} = T_{\perp}$. The collisions allow exchanging energy between the cooled translational degree and the other degrees of freedom, and then $T_v = T_r = T_{//} = T_{\perp}$. The model assumes that the region is continuous and isentropic, i.e. continuous region in Figure 1.7.

Then, at a certain distance from the nozzle exit the collisions become so rare that $v_{//}$ stops narrowing, and $v_{//}$ freezes at a quitting surface and only v_{\perp} continues to decrease under natural geometric segregation. The thermal equilibrium between the degrees of freedom is broken, and $T_v > T_r > T_{//} > T_{\perp}$. The regime is now discontinuous, out of equilibrium and the beam is a free molecular beam. A schematic representation of the evolution of the velocities distributions along the beam path is given in Figure 1.7.

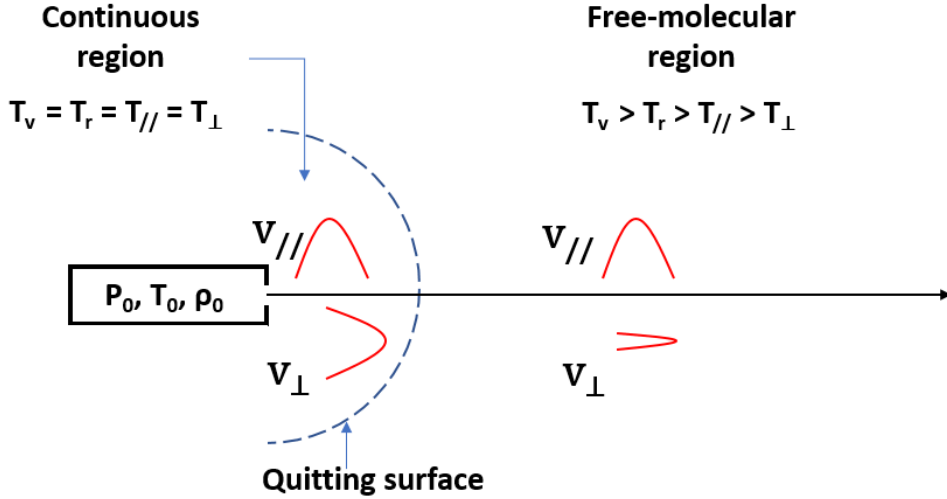


Figure 1.7 – Schematic representation of the evolution of translational velocities distributions $v_{//}$ and v_{\perp} along the beam path. According to the Sudden Freeze Quitting Surface Model.

In practice, the different temperatures are not determined by the same method. $T_{//}$ could be determined by using the technique of time-of-flight (TOF) measurement [46]. For example, from a TOF distribution of a gas composed of 100% argon, the velocity distribution of argon in x-direction such as represented in Figure 1.6 can be obtained. This distribution illustrates well the narrowing of the $v_{//}$ distribution. One can define a quantity called the velocity ratio $Sv = \frac{\bar{v}}{v_p}$ as the ratio of the mean velocity \bar{v} of the gas and the most probable velocity v_p of molecules.

An empirical estimation of S is obtained from FWHM $\Delta v_{//}$ of the distribution and the velocity of the gas v . This empirical expression is given by Equation (1.18):

$$Sv \approx 1.66 \frac{\bar{v}}{\Delta v_{//}} \quad (1.18)$$

There is also an empirical expression of $T_{//}$ given by Equation (1.19)

$$T_{//} \approx 2.5 \frac{T_0}{Sv^2} \quad (1.19)$$

$T_{//}$ and Sv have been calculated from the distributions in Figure 1.6 for different Mach numbers as represented in Table 1.3.

	$M = 0$	$M = 5$	$M = 10$	$M = 25$	$M = 50$
Sv [//]	0	5.18	9.27	23.1	46.2
$T_{//}$ [K]	298.15	27.77	8.67	1.4	0.35

Table 1.3 – Speed ratio Sv and radial translational temperature $T_{//}$ of Ar gas in supersonic expansion for different Mach numbers M . The results are based on the velocity distributions in Figure 1.6 and calculated from the empirical expression of Sv and $T_{//}$ given by Equation (1.18) and Equation (1.19).

1.7 Free jet expansion

1.7.1 Flow structure

The under-expanded condition of a jet [47] is assured by the expansion of the gas from a high pressure on the nozzle exit into a lower pressure chamber. It creates a state of pressure imbalances that leads to a process to reach equilibrium. This process takes place out of the nozzle by forming an expansion fan of the nozzle lip to balance the jet pressure with the chamber pressure. The expansion waves, however, reflect on the free boundaries as weak compression waves leading to generate shock waves. The gas within the jet continues to expand by decreasing its pressure and increasing its Mach number. Therefore, shock waves are discontinuity regions in a fluid across which the flow parameters (the velocity, the temperature, the density and the Mach number) are strongly variable over a distance of the order of a few local mean free path.

Different types of jets could be obtained depending on the pressure ratio (P_0/P_b). A moderately under-expanded jet is characterized by the diamond or "X" pattern which is observed due to regular reflection of the oblique shock.

When the driving pressure ratio becomes very high, a normal shock also called as *Mach disk* appears to increase the jet pressure to an adequate value, because the flow attains a very low pressure during expansion that cannot be balanced with the ambience by just an oblique shock. The *Mach disk* is a shock wave perpendicular to the direction of the flow with a nearly flat form.

If the pressure ratio is further increased, which is the case of our experiment, the resulting jet is termed as extremely under-expanded jet Figure 1.8. In this case shock cell pattern disappears and the jet becomes entirely single shock cell structure with a *barrel shock*, terminated by a *Mach disk*. Inside this cell, supersonic flow further expands to high Mach numbers. These two shocks define three regions for the flow regime. First, the so-called cooling zone located just downstream the nozzle exit. That is the zone where number of collisions take place to cool the molecules and relatively monochromatize their velocities. The second region is the so-called zone of silence located downstream of the cooling zone, it extends from X_T that limits the sonic region to X_M . The flow in that zone contains fewer collisions. In the zone of silence, the flow is supersonic ($M \gg 1$) because the gas velocity was increased by the collisions in the cooling zone and the velocity of sound is nearly equal to zero. The zone of silence represents the interesting area in order to benefit from the free molecular flow regime (molecules can be treated as isolated ones). Since that is an isentropic area, the equations given in section 2.4 well describe the behaviour of the gas. Finally, beyond the Mach disk the flow is subsonic ($M < 1$) because of the randomization of the molecules velocities induced by collisions with the residual gas.

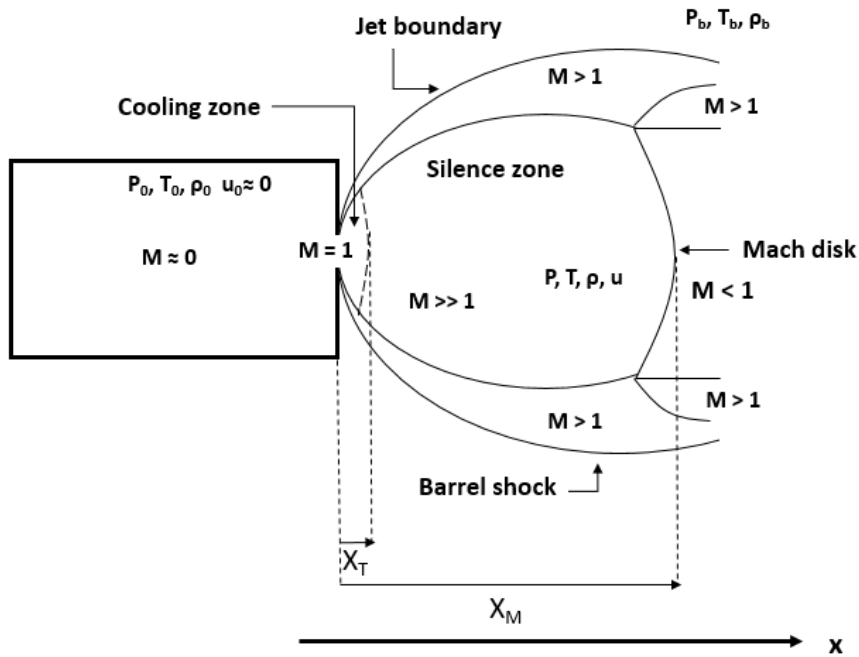


Figure 1.8 – Schematic illustration of the flow structure of an axially symmetric supersonic free jet, with the different zones that are labelled. A supersonic expansion cone is formed thanks to the gas expansion from the high-pressure gas reservoir P_0 into the vacuum chamber through the nozzle. A region located just behind the nozzle exit called the cooling region makes the transition from the continuum to the free molecular flow. Shock waves called the Mach disk and the barrel shock limit an isentropic region so-called the zone of silence. Figure is adapted from [37].

1.7.2 Mach disk location and diameter

For a pressure ratio $P_0/P_b = 29.4$ to $P_0/P_b = 915.6$ for air, the following correlation is suggested to predict the location of the Mach disk (X_M) [48]

$$\frac{X_M}{D} = \left(\frac{1}{j+1} \gamma M_e^2 \frac{P_e}{P_b} \right)^{\frac{1}{j+1}} (\gamma M_e)^{j-1} \quad (1.20)$$

In this equation M_e and P_e are the Mach number and the pressure at the exit of the nozzle in our case $M_e = 1$, $P_e = 10^{-5}$ mbar and j takes the value of 0 for 2-D flows and 1 for axisymmetric flows. The pressure ratio in our experiment is in the order of 10^8 which does not fit into the conditions of the equation but if we try it for an approximation we will find $X_M = 6.4$ m which is considered high.

In order to better visualize and understand the dependence of the Mach disk position on the chamber pressure, the evolution of X_M/D for a range of the pressure ratio $\frac{P_e}{P_b} = [1 : 25]$ is presented in Figure 1.9 for different diameters of the nozzle.

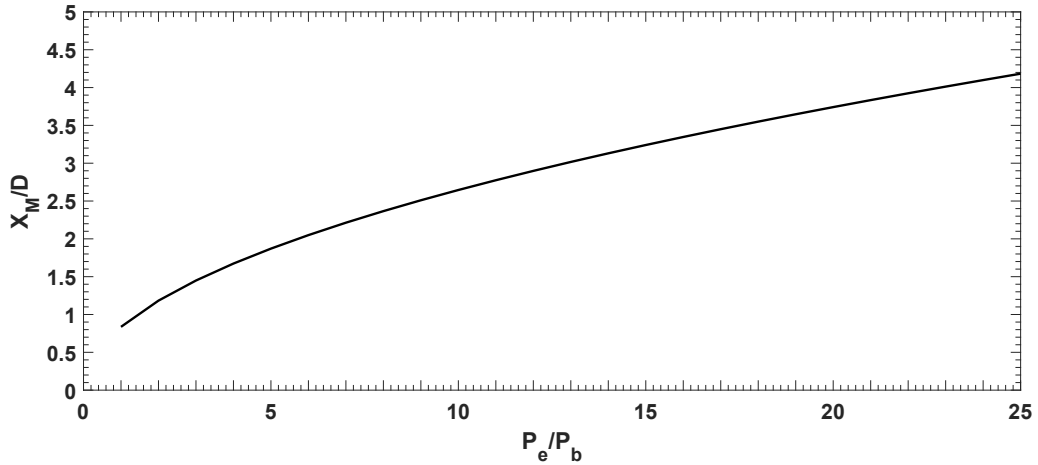


Figure 1.9 – Evolution of the distance X_M/D between the nozzle exit and the Mach disk location with respect to the pressure ratio.

In order to estimate Mach disk diameter (D_M), an empirical relation was proposed [49] for a sonic orifice as shown in Equation 1.21:

$$\frac{D_M}{D} = 0.31 \left(\frac{P_0}{P_b} - 5.0 \right)^{0.5} \quad (1.21)$$

1.7.3 The evolution of the Mach number in the expansion

The dimensionless distance $\delta = x/D$ is of paramount importance when one wants to characterize the different parameters of the jet. The Mach number $M(\delta)$ evolves during the expansion due to the change in the downstream distance x of the flow velocity $v(\delta)$ and the local speed of sound $v_s(\delta)$. The expressions of the evolution of the centreline Mach number for an axisymmetric jet and for a planar jet is given by empirical expressions [46] and works only for a free not-adapted jet.

$$M = (\delta)^{\frac{\gamma-1}{j}} \sum_{n=0}^{n=3} \left(\frac{A_n}{(\delta)^n} \right), \text{ for } \delta > 0.5 \tag{1.22}$$

$$M = 1.0 + a_2(\delta)^2 + a_3(\delta)^3, \text{ for } 0 < \delta < 1.0$$

In these two equations, j is equal to 1 in the case of an axisymmetric expansion, and to 2 for a planar expansion. a_2, a_3, A_n are adjustment parameters that depend on γ . The values of the adjustment parameters are given in the following table (table 1.4) for different γ from reference [46]:

j	γ	A_0	A_1	A_2	A_3	a_2	a_3
1	5/7	3.232	-0.7563	0.3937	-0.0729	3.337	-1.541
1	7/5	3.606	-1.742	0.9226	-0.2069	3.190	-1.610
1	9/7	3.971	-2.327	1.326	-0.311	3.6092	-1.950
2	5/3	3.038	-1.629	0.9587	-0.2229	2.339	-1.194
2	7/5	3.185	-2.195	1.391	-0.3436	2.261	-1.224
2	9/7	3.252	-2.473	1.616	-0.4068	2.219	-1.231

Table 1.4

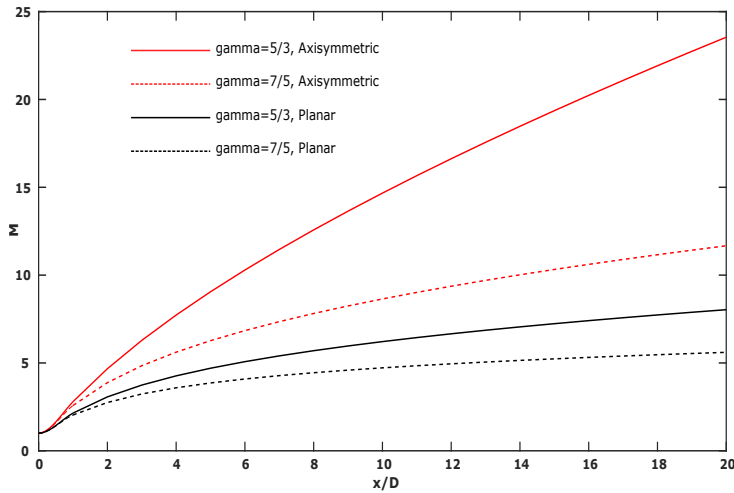


Figure 1.10 – Evolution of the Mach M number along the centreline of the supersonic jet with respect to the ratio of the distance downstream of the nozzle exit and the nozzle diameter x/D .

1.7.4 Evolution of the quantities: T/T_0 , P/P_0 and ρ/ρ_0 parameters and characteristic velocities in the jet expansion:

Since the thermodynamics properties of the jet depends on the Mach number as mentioned in Equations 1.14 the evolution of the ratios T/T_0 , P/P_0 and ρ/ρ_0 along the centreline of the jet can be represented (Figure 1.11) for both axisymmetric and planar jet expansion. The temperature of the jet will tend to 0 with moving away from the nozzle exit along the centreline of the jet. Then, by using the equation of the velocity u of the gas in the isentropic expansion from equations 1.14 for $T \rightarrow 0$ we can isolate the maximal velocity u_{max} reached by the beam in the supersonic expansion. While the beam speed increases, the speed of sound decreases to tend to 0. The evolution of the beam speed ratio v/v_{max} and the speed of sound ratio $v_s/v_{s,max}$ are therefore, represented in Figure 1.12.

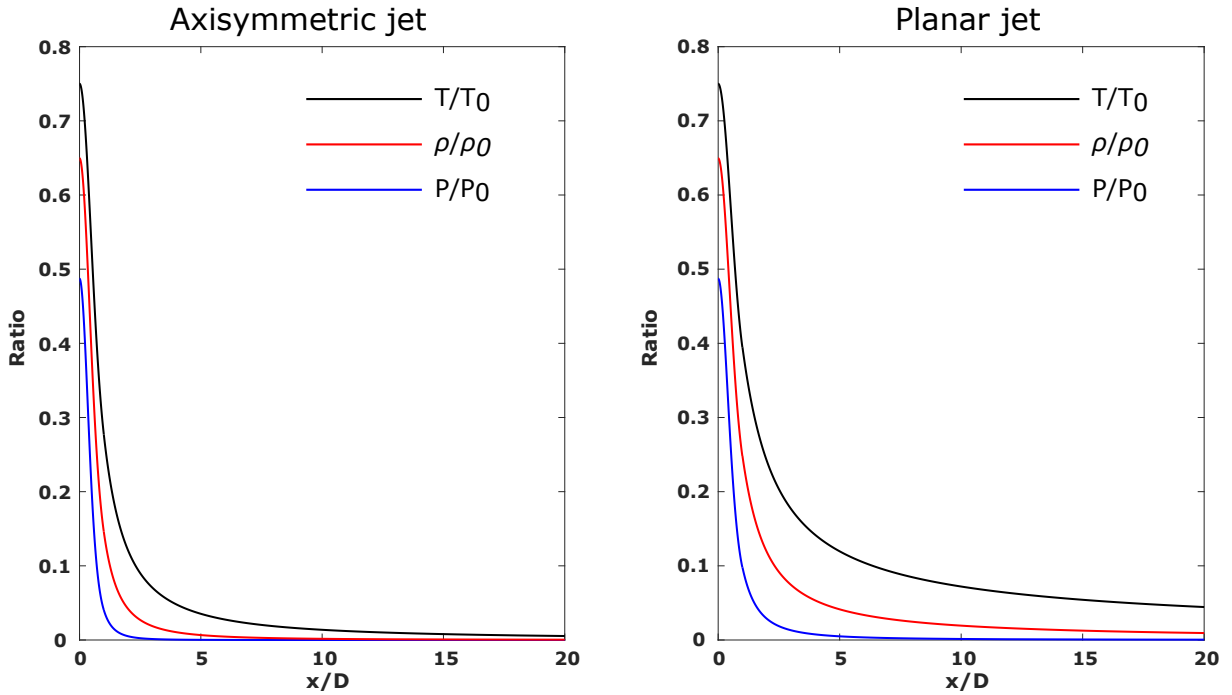


Figure 1.11 – Evolution of the temperatures, pressures, and density ratios T/T_0 , P/P_0 , ρ/ρ_0 with respect to $\delta = x/D$ for an axisymmetric and a planar configuration.

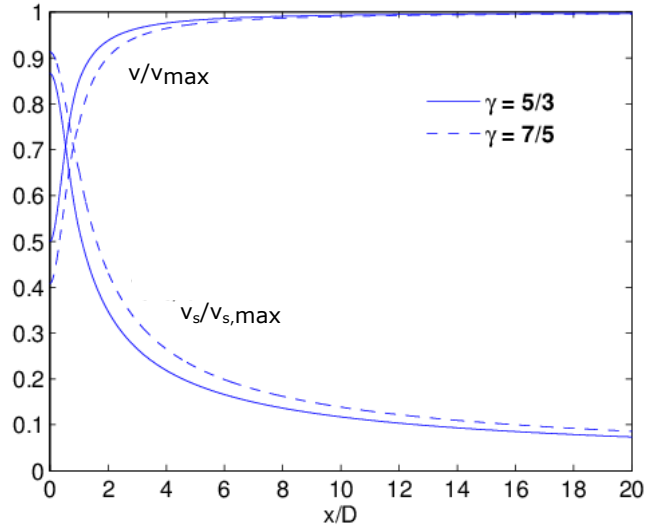


Figure 1.12 – Evolution of the ratio of jet velocity v/v_{max} and sound velocity $v_s/v_{s,max}$ along the centreline of an axisymmetric supersonic jet with respect to $\delta = x/D$.

1.7.5 Evolution of the Reynolds number in the jet expansion:

Considering the case of the free jet expansion used in this thesis, argon was used as a carrier gas which is characterised by a volumetric mass density $\rho_0 = 1.7835$ [kg/m³] in the reservoir, a dynamic viscosity of $\mu = 2.1017 \times 10^{-5}$ [kg/m.s] at room temperature (296 K). The gas expands through the axisymmetric nozzle reaching a sonic speed at the throat. The diameter used at UCLouvain is equal to $D = 0.5 \times 10^{-3}$ [mm] and at UR1 $D = 0.08 \times 10^{-3}$ [mm].

Using Equation 1.15 we can find the following quantities for $M = 1$ at the throat of the nozzle:

1. The density (ρ^*) :

$$\frac{\rho_0}{\rho^*} = \left(1 + \frac{\gamma - 1}{2}\right)^{\frac{1}{\gamma - 1}} \quad (1.23)$$

Equation 1.23 gives $\rho^* = 1.1584$ [kg/m³]

2. temperature (T^*) :

$$\frac{T_0}{T^*} = 1 + \frac{\gamma - 1}{2} \quad (1.24)$$

Equation 1.24 gives $T^* = 220$ K

3. The speed of the jet (v^*) is equal to the speed of sound for $M = 1$; therefore, using equation 1.5 and by replacing the corresponding temperature by $T^* = 220$ K, we find $v^* = \sqrt{\gamma r T^*} = 277.32$ [m/s]

4. The dynamic viscosity depends on the temperature, and the empirical equation that can be used to find the viscosity for different temperatures is given by :

$$\mu = \mu_{ref} \left(\frac{T}{T_{ref}} \right)^{3/2} \frac{T_{ref} + S_\mu}{T + S_\mu} \quad (1.25)$$

Using data from CRC handbook and data in the NIST online database : $\mu_{ref} = 55.8 \times 10^{-6}$ [kg/m.s] $T_{ref} = 1000$ K and $S_\mu = 164.2$ K we obtain for $T^* = 220$ K $\mu^* = 1.7595 \times 10^{-5}$ [kg/m.s]

Using these quantities, we can calculate Reynolds number using equation 1.4 at the throat: $Re^* = 16000 > 3000$ the flow is turbulent at the beginning of the expansion. Figure ?? shows the evolution of the Reynolds number for the source used in UCLouvain.

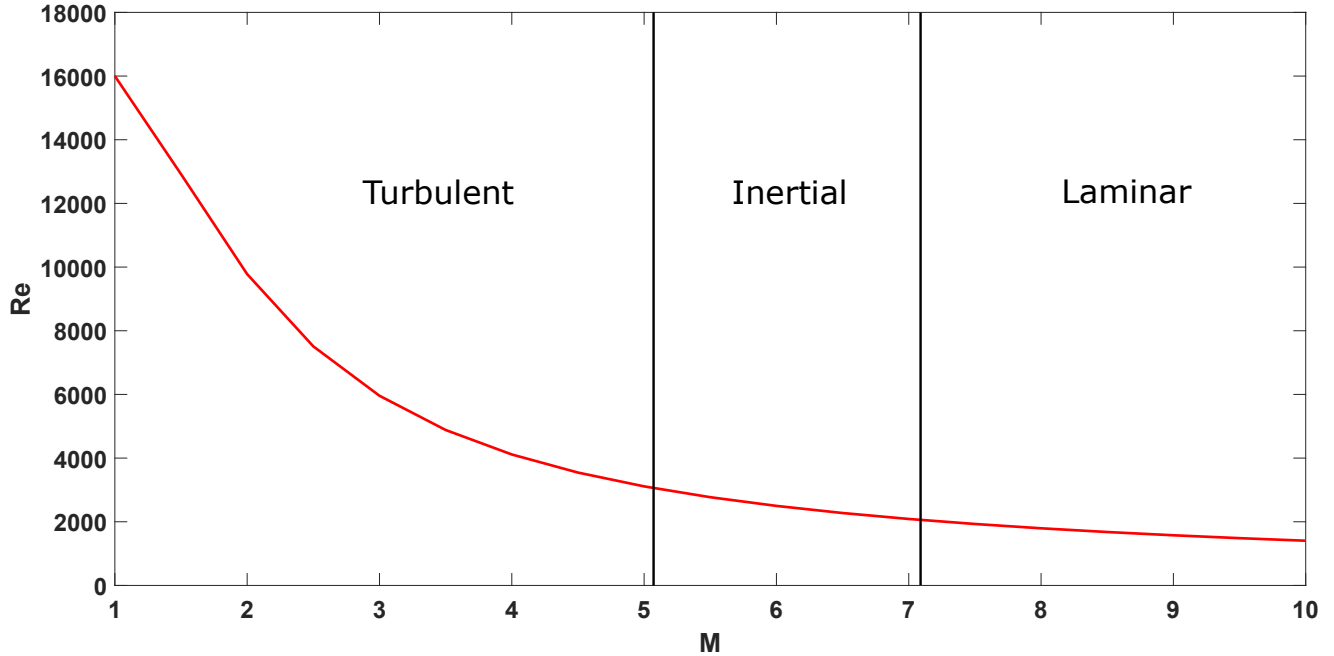


Figure 1.13 – The evolution of the flow regime from a turbulent flow to Laminar flow with respect to the Mach number for the source used at UCLouvain. The flow is turbulent at the beginning and tends to be laminar for higher Mach number.

Considering the source of Rennes, the only difference is the diameter size giving the evolution of the Reynolds number as follows:

Later in the CFD simulations for both sources, the flow will be considered laminar. The reason is that turbulent flows are harder to solve. The simulation results are therefore an approximation for the measurement of the physical quantities. Experimental characterization is then made by spectroscopic means, giving the exact values of the physical quantities.

One can refer to Figure 1.10 in order to estimate the distance for different Mach numbers for the planar source and the axisymmetric source.

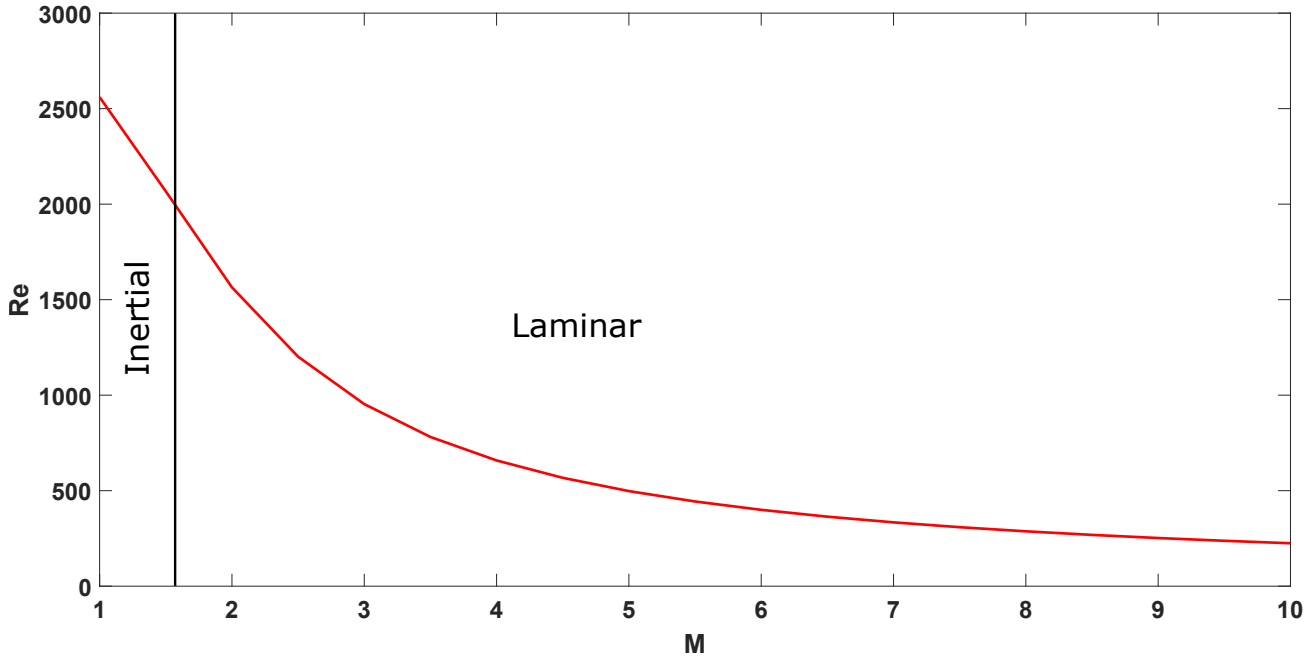


Figure 1.14 – The evolution of the flow regime from a turbulent flow to Laminar flow with respect to the Mach number for the source used in Rennes.

1.8 Uniform supersonic jet expansion

While free jets are formed by simply expanding gas through an orifice into a vacuum chamber, the production of a uniform expansion is more involved. To do so, a specific geometry of the nozzle needs to be designed known as perfectly adapted Laval nozzle. It is a convergent-divergent duct that is pinched in the middle, having an asymmetric hourglass shape. It is widely used in some types of steam turbines and rocket engine nozzles. This duct is also used in supersonic jet engines [50]. The application of this technique for kinetics studies at low-temperature is well known and begun in the aerodynamics laboratory in Meudon [51]. To generate uniform flows, the pioneers of the CRESU technique (a French acronym standing for *cinétique de réaction en écoulement supersonique uniforme*, or reaction kinetics in uniform supersonic flow) studies have developed a method of profiling Laval nozzles for rarefied jets [52].

Unlike the case of the free jet, the Laval nozzle jet is dominated by the high number of collisions promoting chemistry. Another advantage relatively to the free jet is that the density is higher and can attain values of the order of $10^{16} - 10^{17} \text{ cm}^{-3}$, which is important in our case; the higher the density the higher the signal-to-noise is when doing spectroscopic measurements. The uniformity of the jet in terms of temperature and density could be maintained at the heart of the flow over several tens of centimetres.

In the laboratory, this type of nozzle is designed in terms of throat size, profile and length of a certain backing to chamber pressure ratio to generate a uniform supersonic flow for a specific density and temperature for the given carrier gas. Strictly speaking, finding the profile of this type of nozzle is a question of solving Navier-Stokes equations (see Appendix A). Although this approach is far too complex, other approximations could be done (and explained in the next section).

As already explained, the Mach number of the jet M is an appropriate and important number to define the flow in each section of the nozzle, and the logic is similar to the one of an axisymmetric nozzle. The difference is that the final Mach number of the Laval nozzle is fixed and tends to be constant at the exit of the nozzle. The Mach number is related to the area ratio between nozzle throat (S^*) and exit (S_e) by this equation [53]:

$$\frac{S_e}{S^*} = \frac{1}{M} \left[\left(\frac{2}{\gamma + 1} \right) \left(1 + \frac{\gamma - 1}{2} M^2 \right) \right]^{(\gamma + 1)/[2(\gamma - 1)]} \quad (1.26)$$

The quality of the flow at the nozzle outlet depends crucially on the profile of the divergent part but also the pressure ratio between the chamber and the tank. If this ratio is not suitable, shock waves could form in the jet and the uniform flow will be destroyed.

The profiling of Laval nozzles is done in two stages [52]:

1. The isentropic nucleus of a fluid considered ideal is calculated using cylindrical symmetry (z_s, r_u) [51]. The resulting equations are solved by the method of the characteristics according to [54].
2. The second stage consists of using the calculated profile of the isentropic nucleus as a start and initial condition in order to find δ_1 , the displacement thickness of the boundary layer of the jet. δ_1 is important to find by how much the wall of the nozzle should be moved to maintain an unchanged uniform flow in the jet.

The coordinates of the nozzle (z_w, r_w) are then obtained. The boundary layers are resolved by adding a displacement thickness δ_0 to the profile of the isentropic nucleus:

$$z_w = z_s \quad (1.27)$$

$$r_w = r_u + \delta_0 \quad (1.28)$$

For a good quality flow, the boundary layer δ_0 should be very thin compared to the size of the diameter of the isentropic core devoted as L , because the boundary layer is turbulent and slows down the gas. If the boundary layer is too large compared to the isentropic core so the latter will gradually shrink and the flow is denatured. It is therefore necessary to minimize this ratio δ_0/L which is linked to the number of Reynolds Re characterizing the flow by the equation:

$$\frac{\delta_0}{L} = \frac{1}{\sqrt{Re}} \quad (1.29)$$

We therefore seek to maximize the Reynolds number without reaching a turbulent flow ($Re < 3000$) to obtain a uniform laminar flow (refer to Figure 1.14). It requires a high-pumping capacity and this is why the chamber used in the IPR is equipped with two parallel root pumps with a maximum pumping capacity of $15000 \text{ m}^3\text{h}^{-1}$ to achieve temperatures as low as 20-10 K.

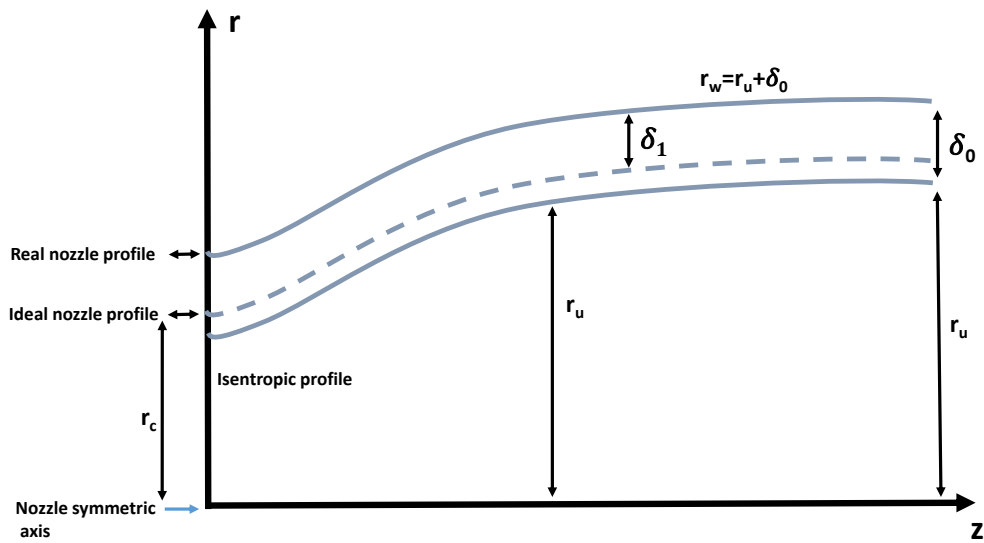


Figure 1.15 – The representation of the Laval nozzle profiling method: For the determination of the exit radius $r_{u,exit}$, the latter is related to the flow velocity and to the debit of the flow as a function of the Mach number at the nozzle exit. Since the flow rate is conserved in all the sections of the nozzle, by imposing the Mach number at the exit of the nozzle, we obtain the value of $r_{u,exit}$ as a function of the nozzle throat diameter and Mach number at the exit of the nozzle. The length of the nozzle is determined by the arbitrary choice of a certain parameter and it is then calculated to find for which length the uniformity is conserved. A too short nozzle length may open too much the angle of divergence of the nozzle profile, possibly leads to the separation of the boundary layer while choosing a too long length risks the preponderance of the boundary layer over the isentropic core of the jet, a compromise is needed.

STARGATE APPARATUS: SPECTROSCOPY OF TRANSIENT ANIONS AND RADICALS BY GATED AND ACCELERATED TIME-OF-FLIGHT EXPERIMENT

2.1 Introduction

Action spectroscopy has witnessed a tremendous development in several scientific directions since the first studies in atomic and molecular physics combining the sensitivity of mass spectrometry and tunability of laser radiation [55, 56]. After these pioneering works, ionic cluster spectroscopy has started with the works of Schwartz [57] and the important contribution of Y. T. Lee [58, 59, 60]. Since then this track has been expanded by many other [61, 62, 63, 64]. Over the years several improvements have been reported for every part of a typical action spectrometer, i.e. the ion source, the mass spectrometer and the light source. The supersonic beams [65] and electrospray [66] have been implemented for ion production. A variety of mass spectrometers has been used as the quadrupole mass filter, the time of flight-mass spectrometer (TOF-MS) and the use of Fourier-transform ion cyclotron resonance (FT-ICR). Several continuous and pulsed light sources were also used as dye lasers, OPO, free electron and Kr^+ lasers and synchrotron radiation. Variations on the measured quantity were reported including the counting of electrons [67], fragmentation products [62], products of light-induced bimolecular reactions [68] or recently the inhibition of complex formation [69]. This last example has led to the measurement of the high-resolution spectra of numerous molecular cations including C_{60}^+ [70] and CH_5^+ [71] in the infrared. In parallel the measurement of photo-electronic spectra of neutral molecules [72] and anions [67], has been the subject of important developments to retrieve information on the ionization threshold [73], the cation structure [74] and transition states in chemical reactions [75]. Finally, such techniques were also applied to study biological molecules such as peptides or glucans [76, 77, 78].

In this chapter we report the experimental development of a photo-fragmentation spectrometer which aims at measuring spectral properties of positively or negatively charged molecules and/or of ionic com-

plexes. We start by citing briefly the different parts of the STARGATE instrument (Section 2.2). Then each part of the instrument is detailed, including the ion source (Section 2.3) which is composed of a supersonic jet expansion source coupled to an ionization mean. Then, the TOF-MS is described in section 2.4 and finally the details regarding the photodissociation setup in section 2.6. The application of high resolution photodissociation spectroscopy is discussed using the rotationally resolved $\tilde{A}^2\Sigma^+(002) \leftarrow \tilde{X}^2\Pi_{3/2}(000)$ rovibronic band of N_2O^+ as a reference, where the vibrational quantum numbers v_1, v_2, v_3 are indicated in parentheses. Besides giving access to the rotational temperature of the cations, these spectra allowed us to evaluate the required measurement time and achievable signal-to-noise ratio. Finally, ongoing developments and ideas to improve the quality of our set-up are discussed.

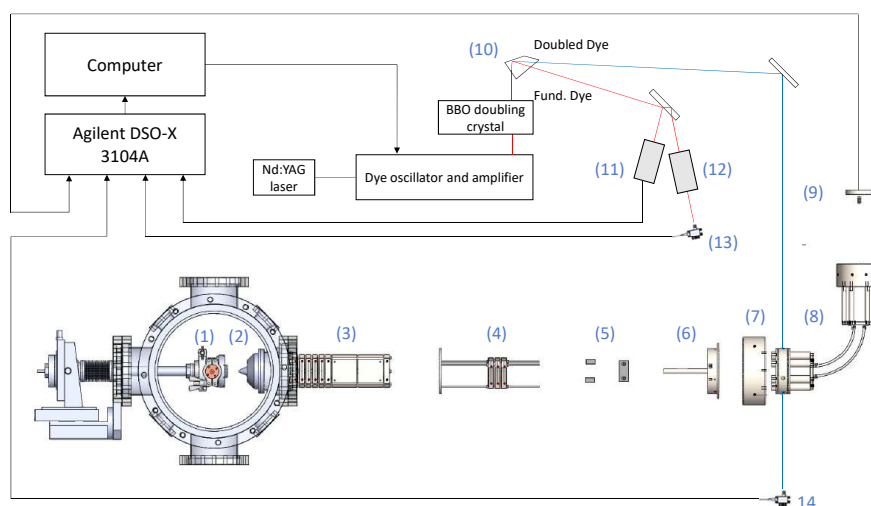


Figure 2.1 – Design of STARGATE TOF-MS (bottom) with (1) source of ionic compounds, (2) skimmer, (3) TOF mass spectrometer, (4) electrostatic lens, (5) pulsed 2D deflector, (6) differential pumping tube, (7) laser and ion beam interaction region, (8) 90° cylindrical energy analyser and (9) MCP detector. Optical bench (upper part) with pulsed dye oscillator and dual amplifier associated with a frequency doubling BBO crystal and pumped by a Nd:YAG laser, (10) prism separating the second harmonic doubled Nd:YAG laser (307-327 nm) used for photodissociation spectroscopy from the fundamental dye beam (614-654 nm) used for the frequency calibration of the spectra, (11) hollow cathode (Ne/Mn) and (12) temperature-regulated vacuum solid state etalon. The calibration atomic Ne lines are measured from the helium filled hollow cathode (Ne/Mn), the ionic photofragments are detected by the MCP detector, the power of the laser and the Fabry Perot interferometer (solid state etalon) are measured by a photodiode (13) and a pyroelectric detector (14), in combination with an oscilloscope (Agilent DSO-X 3104A). Items (1), (3) and (5) are all connected to a digital delay generator, the associated chronograph is displayed in Figure 2.2. The photodissociation spectra are recorded from the oscilloscope connected to a computer via USB. A Labview[®] interface controls the scan of the pulsed dye laser, the transfer of the averaged data from the oscilloscope to the computer, and the integration of the time gated signal.

2.2 Instrument layout

STARGATE instrument is presented in Figure 2.1. It is essentially composed of a pulsed supersonic expansion coupled to ionization mean (electric discharge or electron gun)(1). The jet goes through a skimmer(2), which allows for differential pumping and spatial selection of a part of the expansion. Ions are then accelerated and enter the TOF-MS indicated as item 3. The heart of the TOF-MS includes a single unit able to perform acceleration, bunching, gating of the ionic beam and while re-referencing it to the ground potential. The ions are focused (4) and deflected using a pulsed deflection unit (5). A second differential pumping tube (6) is implemented. The interaction with a pulsed dye laser at a right angle is performed inside a biased cell before the ions enter an energy analyser (8). The ions are then detected using a micro channel plate stack(MCP, Photonics APD-TOF) and the mass spectra are recorded using a digital oscilloscope (Agilent Technologies DSO-X 3104A, 1 GHz). The timing of the various elements are controlled using a multi-channel digital delay generator (Model 577 - BNC) and pulses are generated from Behlke push-pull high voltage (HV) switches supplied by high-voltage DC power supplies (FUG). A chronograph of the STARGATE instrument is presented in Figure 2.2. This figure details the duration and the relative timing of the pulsed jet, the two steps of the gating bunching of the ion beam, and the mass selection with the pulsed deflector.

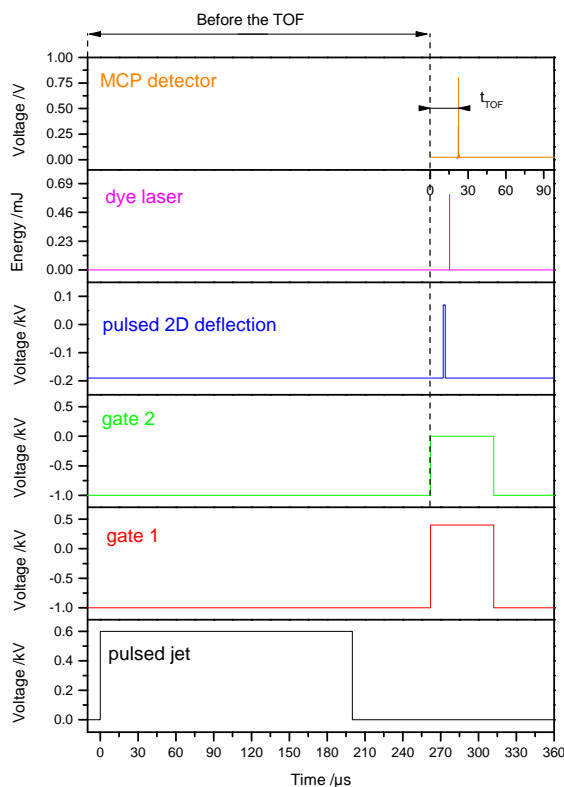


Figure 2.2 – Chronograph for applied voltages to study cations using STARGATE. The time scale origin is defined as the rising slope of the pulsed molecular jet valve trigger (black). The two steps of the gating bunching of the ions separated by 40 ns (red and green) and the mass selection of the pulsed 2D deflector (blue) are represented. The time scale origin used for the mass spectrum of N_2O^+ measured with the MCP detector at $t_{TOF} = 22.4 \mu\text{s}$ (orange) is defined from the beginning of the TOF corresponding to the gating ($L = 1.5 \text{ m}$ with a kinetic energy of 1 keV). In addition, a dye laser pulse of 5 ns duration interacts with the ions after 1 m in the drift tube for photo-dissociation spectroscopy ($\simeq 15 \mu\text{s}$ for N_2O^+)

SIMION[®] is used for a prior prediction of the voltages that are needed to be applied to manipulate the ions. In fact, in the following sections we will present the simulation for each part of the instrument. In section 2.3.2 we will show the simulation of the electric fields and the trajectory of the electrons produced by the discharge plates and the electron gun. In section 2.4 the different functions of the unit (gating bunching re-referencing) are tested. In sections 2.4.4 and 2.4.5 we will show the simulation for the ion's trajectory following the implemented ion optics. Finally, in section 2.6.1 we describe the new idea of the energy analyser coupled to a biased cell.

2.3 Source of ions

2.3.1 Pulsed supersonic jet expansion

Two valves operation modes are commonly used in order to produce supersonic beams: continuous and pulsed. As demonstrated in the first chapter devoted to supersonic jet expansion, achieving low temperatures (or high Mach numbers) in an axisymmetric jet requires large values of the pressure-diameter product, P_0D . Since the mass throughput of the nozzle is proportional to P_0D^2 , pumping considerations will ultimately determine the cooling attainable for a given nozzle diameter D . Cooling is essential :(i) to promote partial condensation, (ii) to simplify the recorded spectra, (iii) to increase the density of molecules on few quantum states and hence to increase the signal-to-noise ratio (S/N). In the case of a continuous beam that pumps loads can be very large due to the large flux of molecules leaving the nozzle. A practical solution is to employ a pulsed supersonic expansion, thereby reducing the duty cycle and the pumping requirements considerably. Pulsed beams are particularly useful for our application which involves a pulsed laser as we can adapt the gas pulse repetition rate ν to the one of the laser, for a minimum gas pulse duration δt . The pulsed regime is produced by implementing a valve with an actuating mechanism. Reducing the pumping requirements comes from reducing the duty cycle and it is defined by equation (2.1)

$$\psi = \frac{\delta t}{\Delta t} \times 100\% = f\delta t \times 100\%. \quad (2.1)$$

where the width of the ideal rectangular-shaped pulse is δt , the time interval between two successive pulses is Δt , and the repetition rate is f .

If we decide to minimize the pulse duration δt , we need to note that there exists a minimum opening time of the valve needed to maintain the full development of the supersonic expansion [79]. Equation (2.2) gives the dependence of the pulse duration of the nozzle diameter D and the velocity of sound in the reservoir $v_{s,0}$

$$\delta t \geq \frac{4D}{v_{s,0}} \quad (2.2)$$

For example, the minimum opening time for helium and argon could be calculated for the parameters below, the velocity of helium and argon in the jet are already calculated in the first chapter:

- (a) $D = 1$ mm
- (b) For helium : $v_{s,0} = 1016$ m/s
- (c) For argon : $v_{s,0} = 321.5$ m/s

The minimal duration of the pulse is $3.9 \mu\text{s}$ and $12.4 \mu\text{s}$ respectively for the full development of the supersonic flow. For now, no mechanical design exists for a pulsed valve to open and close within this limited time.

In the literature numerous pulsed valve designs have been described, and some are commercially available. Three types of pulsed valves are commonly distinguished by their actuating mechanism and they are mainly characterized by their opening time duration : current loop, solenoid and piezoelectric

valves. Examples of each valve type are often cited :

- The Jordan valve (based on the pulsed valve developed by Gentry and Giese [80]) is composed of two metal strips through which high opposite currents pass creating a magnetic repulsion and then, opening the valve as shown in Figure 2.3. That design allows minimum opening times of 80 - 150 μ s FWHM for pressure in the vacuum chamber of about 10^{-5} mbar and could operate up to 1 Hz [81]

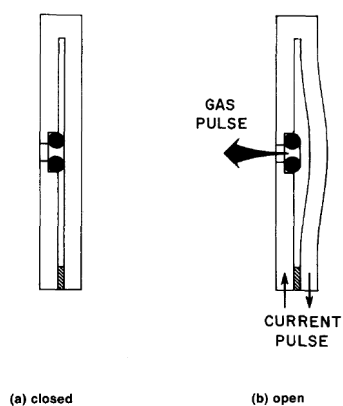
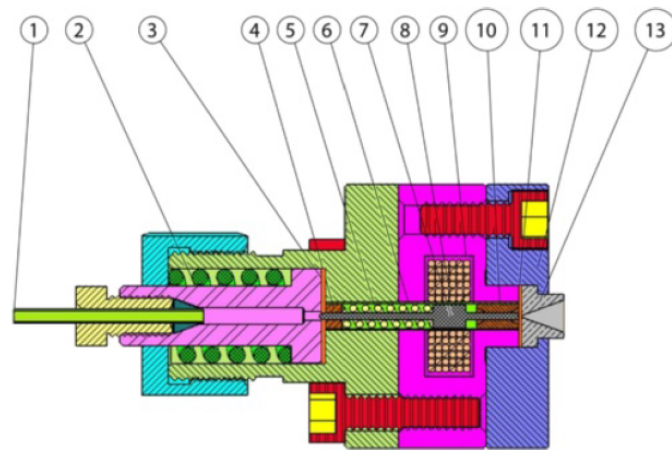


Figure 2.3 – Principle of operation: (a) The valve is closed with the flexible bar resting on the O-ring. (b) After the application of the current pulse

- The Even-Lavie valve [82] is an electromagnetic actuated device that is composed of a solenoid creating a magnetic field in order to lift a plunger to open the valve. The design produces gas pulses of minimum opening time of $25\mu\text{s}$ FWHM for a pressure in the vacuum chamber lower than 10^{-5} mbar for a repetition rate from 1 Hz to 500 Hz. This valve is based on a more commonly used solenoid valve called the Parker General Valve [83] whose minimum opening time is $300\mu\text{s}$ FWHM. The source used by Even-lavie in which the valve is used is detailed in Figure 2.4



1. Stainless gas inlet tube (1/16").
2. Tightening spring (100N) and pressure relief valve.
3. Kapton foil gasket (rear, 0.125 mm. thickness).
4. Ruby rear guiding ferrule.
5. Return spring (Nimonic 19 alloy).
6. Thin walled pressure vessel (Inconel 625 alloy).
7. Reciprocating plunger (magnetic stainless steel alloy 750).
8. Kapton insulated copper coil (0.6 mm wire diameter 6x6 winding).
9. Magnetic shield (alloy 17/4PH) and field concentrator.
10. Ruby front guiding ferrule.
11. Kapton foil gasket (front, 0.125 mm. thickness).
12. Front flange (stainless or copper).
13. Conical (or trumpet) shape expansion nozzle (Zirconia ceramic or hardened stainless steel).

Figure 2.4 – Even-lavie valve cross section along with all the mechanical parts. Figure from reference [82].

- Finally, different piezoelectric transducer (PZT) valves were developed [84, 85, 86, 87]. Among the piezo valves two categories were studied : the piezocantilever valve [85] shown in Figure 2.5 and the piezo-disk-activated plunger [84, 86] shown in Figure 2.6.



Figure 2.5 – a) Photo of the inside of the cantilever piezovalve, with the relevant dimensions indicated. The O-ring is glued to the back side of the piezo, which forms the vacuum seal to the nozzle hole. The nozzle to seal distance can be carefully adjusted with three set screws as indicated. The piezo free cantilever length is about 5 to 6 mm. The length of the cantilever can be easily adjusted by moving the clamp. b) Photo of the closed valve which has an outer body diameter of 44 mm. c) Photo of the piezo valve body mounted in a heatable holder on a standard *ISO160* vacuum flange. An electrically isolated skimmer is also attached to the holder

The piezocantilever valve was developed and characterized by M. Janssen [85] and marketed under the name "Amsterdam Piezo Valve". It can operate in pulsed mode at repetition frequencies up to 5 kHz and give pulse length as low as 7 μ s FWHM for a pressure of about 6×10^{-6} mbar inside the vacuum chamber. That valve is composed of a cantilever in piezoelectric ceramic located near the nozzle input. Applying a voltage allows the deflection of the cantilever and then opens the nozzle input. It seems to be an effective technique for producing pulsed beams, and its use could be appropriate for the production of ionic complexes in future work.

An older kind of PZT valve was developed in particular by D. Proch and T. Trickl in 1989. They have studied a piezoelectric disk that flexes when a voltage is applied to it [84]. It allows it to generate minimum pulse lengths between 150 μ s and 250 μ s FWHM with the upper limit for the repetition rate of 1 kHz.

Table 2.1 gives the characteristics of the valves used in the literature.

Valve name	Type	Minimum opening time	Frequency
Jordan valve	Current loop	80-150 μ s	up to 1 Hz
Even-Lavie	Solenoid	25 μ s	1-500 Hz
Amsterdam valve	Piezocantilever	7 μ s	up to 5 kHz
Proch and Trickl	Piezoelectric disk actuator	150-250 μ s	up to 1 kHz

Table 2.1 – Different valves used in the literature, their working principle, minimum opening time and operating frequency.

In this work, a piezoelectric valve based on the one designed by D. Proch and T. Trickl was used. In fact, we decided to use this valve because a prototype was already operational in the laboratory. Building a complete scientific instrument without having to change and optimize the ion source allowed our team to save time and go straight to the results. We will be working on the development and testing of other valves in the near future. The assembly drawing is given in Figure 2.6, and photographs of the top part of the valve and a schematic representation with the dimensions of the piezoelectric actuator are given.

The piezoelectric actuator of the pulsed valve is a bimorph actuator manufactured by *Physik Instrumente (PI)* (model P-286). It is composed of a piezo disk in ceramic (PZT) and a metal disk (passive layer) that are stacked one on top of the other. By applying a voltage, the inverse piezoelectric effect [88], allows to change the shape of the piezoelectric material. That causes the deflection of the metal substrate that is proportional to the applied voltage and then, a gas pulse can pass. In our case, we will couple this type of valve with an electric discharge in order to ionize the gas pulse as it will be detailed in section 2.3.2. A standard home-made nozzle of different replaceable diameters (250, 500 or 1500 μ m) has been used with a repetition rate of 30 Hz matching the one of the dye laser. A minimum opening of 200 μ s has been measured as shown in section 2.3.3. A maximum repetition rate of 1 kHz has been obtained for the 500 μ m orifice. The piezo disk is controlled by 0.3-1.0 kV pulses generated by a home-made push-pull switch whose rise time has been damped by adding a resistor in series. The fine-threaded aluminium plunger is screwed to the piezo disk, and may be tightened and tuned while operating under vacuum. The pulsed duration is controlled by the multi-channel digital delay generator and it is limited by the physical properties of the piezo.

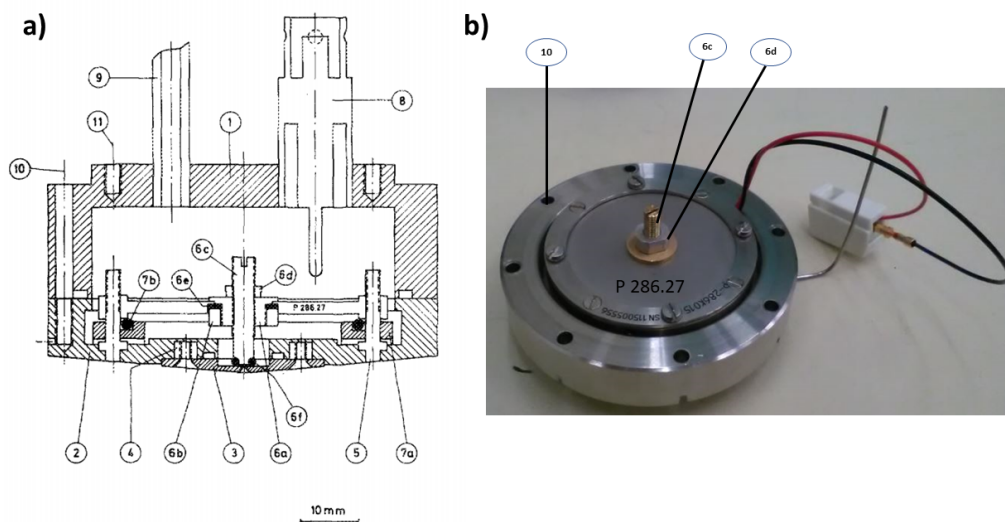


Figure 2.6 – a) Profile view: Assembly drawing of the piezoelectric valve from reference [84]. (1) Valve body; (2) front plate; (3) nozzle plate; (4) threaded piece of tubing (mounting hole for nozzle plate), welded into the front plate; the total number of mounting holes is four; (5) holding the rod for disk translator; a total of four of these rods are welded into the front plate at equal intervals on a circle of 45.0 mm diameter; (6a) vertical adjustment nut for plunger; (6b) plastic nut; (6c) plunger (with slit for screwdriver on top); (6d) lock-nut; (6e) Viton gasket (0.7 mm thick); (6f) sealing o-ring; inner diameter: 1.5 mm, width: 1.5 mm; (7a) ring supporting the disk translator; (7b) o-ring; inner diameter 38.0 mm, width 2.0 mm; 8: coaxial feed through with MHV connector (Ceramseal); (9) gas inlet; 10: hole for M3 screw drawn 22.5° out of true position; a total of eight holes are equally spaced on a circle of 62.0 mm diameter; 11: mounting hole for valve (M3) (four holes). For clarity, parts (4), (5), (6), (8), (9) and the disk translator are not hatched. Parts (1), (2), (3), (4), (5), (7a) and (9) are made of stainless steel, parts (6a), (6c), and (6d) of aluminium;

b) Top view of the home-made valve copied from the original design.

A schematic of the home-made switch is presented in Figure 2.7 using LTspice software.

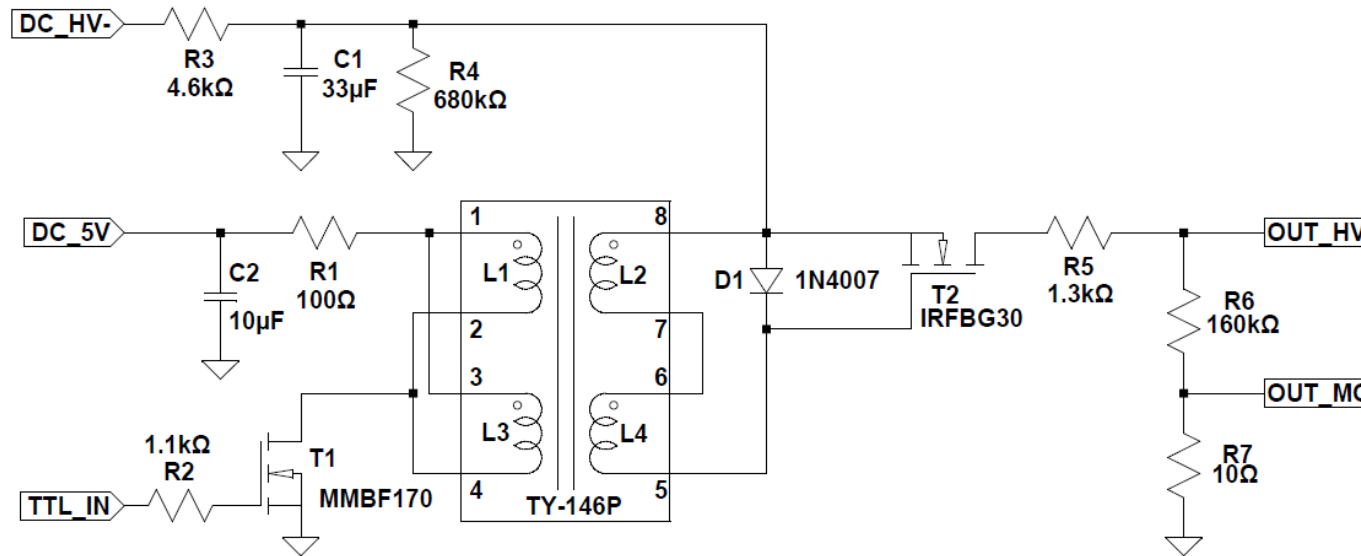


Figure 2.7 – Electric circuit of the switch used to control the piezoelectric element.

The description of the working principle of the switch is as follows:

1. A 5V power supply is connected to **DC-5V** to activate the switch.
2. A negative high voltage is connected to **DC-HV** that goes from (0-1000V DC) that defines the discharge voltage. A TTL input positive signal is connected to a TTL pulse generator(30Hz/5V/100μs) and the output high voltage **OUT-HV** is connected to the piezo.
3. While the **TTL-IN** signal is 0, the n-channel mosfet **T1** is **OFF** so the transformer is not operational therefore **T2** is OFF ; the **OUT-HV** voltage grounded through **R6** and **R7**. In consequence, there is no high voltage on the piezo and gas is not flowing.
4. When the **TTL-IN** signal is 5V: **T1** is **ON**, the current is limited by **R1** passing through **L1** and **L3** of the transformer (TY-146P) increase, inducing a current in **L2** and **L4** that charges the gate of the Mosfet **T2**. **T2** is now **ON**. A current flows through **T2**'s N-channel and **R5** to charge the piezo, when the voltage on the piezo is high enough to bend the ceramic, the gas is flowing.
5. When **TTL-IN** passes to 0V again: **T1** is **OFF**, the current passing through **L1** and **L3** decrease inducing a reversed current in **L2** and **L4**. The reversed current discharges the gate of **T2**. **T2** is then **OFF**. The current stops flowing to the piezo and because of the presence of the two resistors **R6** and **R7** connected to the ground , the voltage on the piezo decreases. When the voltage on the piezo is low enough, the ceramic goes back to its initial position and the gas stops flowing. **D1** acts as a reverse voltage protection of the gate of **T2**.
6. As the piezo is recharging through **R5** (1.3kΩ) and discharging through **R6+R7**(160k) , the time to recharge and discharge are different (fast recharge / slow discharge)
7. To have an electrical circuit that is able to recharge and discharge faster than the initial circuit

a short cut of **R5** is done, and a voltage divider (**R8**=511 Ω and **R9**= 551 Ω) was connected between **OUT-HV** and **GND**, while the piezo was connected to **OUT-HV/2** (between the two 511 Ω resistors). In this configuration we had to double the **DC-HV**- negative high-voltage input because of the division by 2 of the **OUT-HV**. In this situation the piezo is charging through the resistor of 511 Ω and discharging through the other resistor of 511 Ω connected to **the ground**. As a result, approximately, the same charging and discharging time constant was obtained. An improvement should be done to obtain a better push-pull timing and it could be done by using a Behlke switch as the one used for the time-of-flight switches described in section 2.4.3.

2.3.2 Ionization methods

State-of-the-art

Plasma is believed to make up more than 99% of the known matter in the universe [89]. Also, the stars are all in this state. Plasma is defined as a quasi electrically neutral gas, containing charged particles and neutrals which exhibit a collective behaviour [90]. It contains electrons, neutrals, electronically and vibrationally excited species, ions, radicals and atoms. It is classified into two types. (1) Thermal plasma that is in thermodynamic equilibrium, the electron and ion temperatures are the same and could attain values as high as 3000 K to 5000 K. (2) On the other hand, there is the non-thermal plasma. It has a low enthalpy which makes its study simpler. This type is also known as cold plasma as the electrons is much hotter than the ions and it is the case of gas discharges which are the subject of this section. In the laboratory, plasmas are produced by using different methods. Generally, electrons and ions are created during this process.

In this thesis the technique, we used is the electron impact ionization (EI); it consists of bombarding a gas with electrons ejecting ions and radicals, or using a field ionization technique to make a gas discharge which ionizes the molecules by a strong external electric field explained in the following section. One of the EI techniques is the glow discharge. It is the result of a potential difference of 10 to 60 kV between electrodes that are at ≈ 50 cm apart will lead to a "high-voltage glow discharge" if the space between the electrodes is filled with a gas at pressure between 10^{-1} and 10^{-3} torr [91]. It is then important to introduce Paschen's law. It is an equation that gives the breakdown voltage necessary to start a discharge or electric arc, between two electrodes in a gas as a function of pressure and gap length [92]. The equation is as following:

$$V = \frac{BPd}{\ln(APd) - \ln[\ln(1 + \frac{1}{\gamma_{se}})]}$$

In equation 2.3.2, the Paschen law, V is the breakdown voltage in volts, P is the pressure in pascals, d is the gap distance in meters, γ_{se} is the secondary electron emission coefficient, A is the saturation ionization in the gas and B is related to the excitation and ionization energies. These last two constants are determined experimentally and found to be roughly constant over a restricted range of the electric field to pressure ratio (E/P) for a given gas. For example, for air with an E/P between 450 and 7500 V/(kPa.cm), $A = 112.50$ V/kPa.cm and $B = 2737.5$ V/kPa.cm [93]. An example of the Paschen curve is shown in Figure 2.8.

From Figure 2.8 we can conclude that with a constant gap length, the voltage necessary to arc across the gap decreases as the pressure is reduced and then increases gradually, exceeding its original value. With a constant pressure, the voltage needed to cause an arc decreases as the gap size is reduced but only to a point. As the gap is reduced further, the voltage required to cause an arc begins to rise and again exceeding its original value. For a given gas, the voltage is only a function of the product of the pressure and gap length.

Many other techniques exist in the literature; like the photoionization, in which in place of using a beam of electrons, a beam of photons is used to ionize the particles. The energy of the electromagnetic radiation is inversely proportional to its wavelength. In the case of large molecules, whose ionization

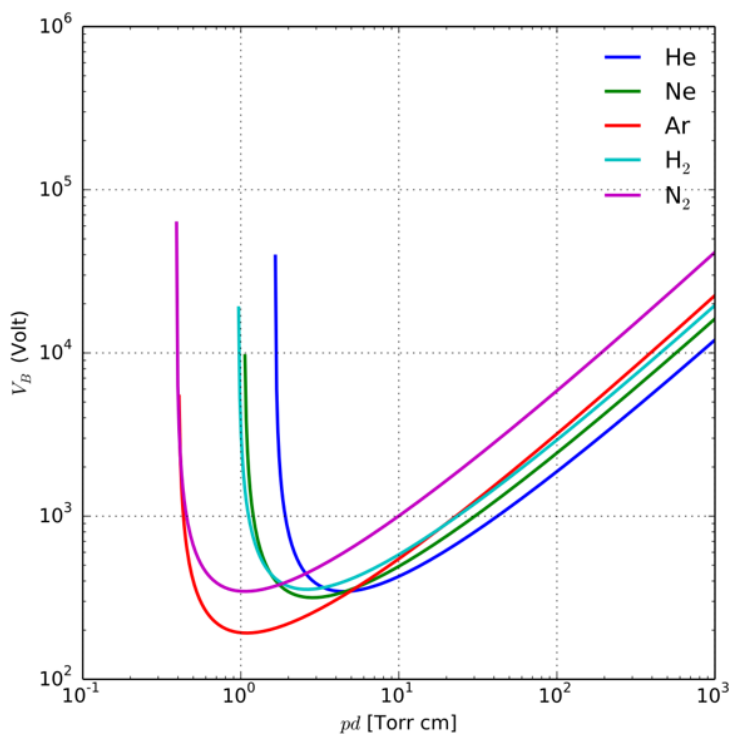


Figure 2.8 – Paschen curves for different gases, using the expression 2.3.2 for the breaking voltage as a function of Pd from reference [93]

potential is generally between 15 and 6.1 eV, the radiation used is therefore in the vacuum ultraviolet known as VUV radiation between 83 and 177 nm. Operating in this range of wavelengths imposes considerable technical difficulties like generating the VUV radiation and finding the specific adapted windows. A recent work of F.Gunzer *et al.* detailed the photoionization and photodissociation in mass spectrometry for the visible and UV range of the spectrum [94]. Compared to EI sources the efficiency of the photoionization sources is not high but, on the other hand, the energy of the incident photons can be controlled very precisely using laser technology. Therefore, photoionization could be a powerful means of measuring ionization potentials.

An alternative to the use of photoionization in mass spectrometry is the thermal ionization, which consists of providing the necessary thermal energy to remove an electron from an atom or a molecule. The inconvenient is that the ionization potential of most elements are far too high. Therefore, this method is restricted to a few metals. It could also be combined with the impact of a focused pulsed laser on a solid which could be then thermally ionized [95].

Another ionization method is ion bombardment. It consists of the collision of an accelerated ion with a neutral molecule which may result in the ionization of the latter. Penning ionization consists of using species as the rare gases that possess a neutral metastable excited states, which could ionize a neutral gas by a process known as Penning ionization:



An interesting application of Penning ionization in the literature is the ionization provided by the intersection of excited rare gas atoms produced in a pulsed jet discharge and another supersonic expansion containing the targeted molecule or a carefully chosen precursor. The advantage of this method is to maintain a low electronic and vibrational temperature [96]. We can also mention chemical ionization: a molecule could be ionized following a chemical reaction with an ion. This technique is the second most used technique and there is a lot of examples in the literature[97] finally there are other interesting techniques that are not limited for gas phase precursors like electrospray ionization, fast atom bombardment of a surface and the matrix-assisted laser desorption ionization(MALDI) [98]. In this work we chose as gaseous ionization mechanism the electron - impact (EI) ionization technique which is commonly used because of its relative simplicity. In addition, coupling of the EI ionization with a supersonic beam source gives rise to an efficient production of ionic species. Two methods were tested. The first method which is the electric discharge is explained in the first subsection that follows. Most of the spectra recorded in this work were done using this method, the ionization takes place in the early part of the expansion i.e. close to the nozzle exit, where three-body and two-body collisions can lead to the production of colder ions and complexes. This method consists of using two polarized metallic rings separated by an insulator. In general, to classify gas discharges we have to differentiate between two categories,(1) DC discharges based on direct current under the influence of a static electric field :

1. Glow discharge [91]
2. Corona discharge [99]
3. Hollow cathode [100]

and (2) AC discharges, the alternating current discharges are under the influence of a time-varying, periodic electric field :

1. Dielectric barrier [101]
2. Radio frequency (RF) [102]
3. Microwave [103]

The second method consists of forming ions in the collision-free part of the expansion (i.e. the zone of silence) by bombarding the neutrals with electrons. It requires the use of an electron gun as described in the second subsection.

Direct current electric discharge driven by an external field

A gas discharge is mainly an electric current across a volume of gas. It starts when an atom or molecule in the gas phase is subject to the influence of an external electrical field. The mechanism of this gas breakdown can be the result of the few electrons that are emitted from the electrodes due to the omnipresent cosmic radiation, or more likely, by sharp edges. When a difference of potential is applied, the electrons are accelerated toward the positive potential by the electric field created between the two electrodes. As a result, the electrons collide with the neutral atoms or molecules. Since the electrical potential energy U_e is the voltage V multiplied by the charge qe

$$U_e = qeV \tag{2.3}$$

And the force on the charge qe is calculated via:

$$F = -\frac{dU_e}{dx} = -qe\frac{dV}{dx} = -qeE_x \quad (2.4)$$

Here, E_x is the electric field and F is the Coulomb force. Ions of charge q , thus, will respond to the applied voltage, to create an electric current to form what is called a discharge current. Inelastic collisions with the electrons in the discharge can lead to excitation and ionization.

1. **Elastic collisions** : $e^- + M \rightarrow e^- + M$
2. **Excitation** : $e^- + M \rightarrow e^- + M^*$ if the kinetic energy of the incident electron is greater or equal to the minimum energy required for excitation
3. **Ionization** : $e^- + M \rightarrow 2e^- + M^+$ if the kinetic energy of the incident electron is greater or equal to the minimum energy required for ionization

The elastic collisions maintain the kinetic energy without any change of internal energies and are the dominant collisions.

The excitation/de-excitation are responsible for the glowing of the discharge as shown in Figure 2.9.

An excitation reaction requires an electron kinetic energy of a few to many eV. Therefore the reason a discharge glows is because once the neutral is excited, it will relax back to its ground state. During this process, it releases the energy difference in the form of a photon, and if the energy gap coincides with a visible wavelength, the photon is visible. The discharge of neon usually gives a bright orange while a discharge in argon is deep purple as shown in Figure 2.9. Furthermore, some states are more stable than others, some atoms stay in their excited state for a relatively long time due to the lack of dipole-allowed transitions to lower states, and these are called metastable. At sufficient kinetic energy, a free electron may cause an electron to detach from the neutral resulting in a second free electron and an ion. The ionization energy for this reaction is usually between 10 to 20 eV. New electrons are then accelerated and can in turn collide with other neutrals giving rise to new electrons and ions. This avalanche process makes the discharge a self-sustaining plasma. An electric discharge consists of applying

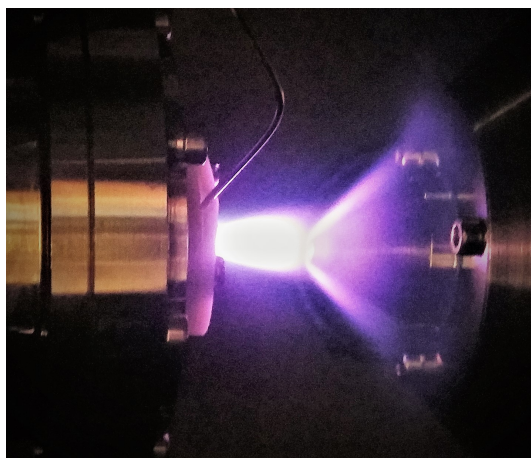


Figure 2.9 – Discharge glow image using an expansion of pure argon

a high-voltage difference between two electrodes as shown in Figure 2.10. This ion production method was first demonstrated experimentally in 1951 [104]. Y Endo *et al.* [16] designed a pulsed discharge conical nozzle for producing van der Waals complexes containing short-lived open-shell species. The same pulse discharge nozzle (PDN) design was also used by D. Osborn *et al.* [18] in order to form negative ions and negative ion clusters. PDN can also be used as a pulsed discharge positive ion source. For instance, slit-jet PDN was coupled to the technique of cavity ring-down spectroscopy (CRDS) in order to study the visible absorption spectra of the cold, free, gas-phase naphthalene ($C_{10}H_8^+$) and acenaphthylene ($C_{12}H_{10}^+$) cations [105]. Another example is the combination of slit supersonic expansions with pulsed electric discharge for high-resolution IR studies of jet-cooled molecular radicals like methyl radical [106].

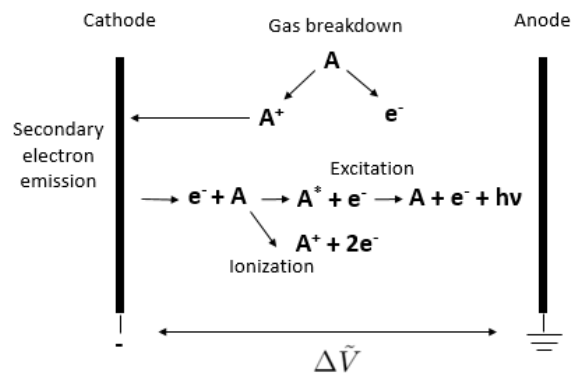


Figure 2.10 – Schematic representation of basic plasma processes in a glow discharge reproduced from [107]. The application of a potential difference between electrodes causes the breakdown of the gas into electrons and cations. The electrons can induce secondary electron emission. The new emitted electrons can collide with gas molecules to cause excitation (followed by de-excitation and then, light emission) or ionization.

In practice, in our design, the nozzle is the inner anode which it is grounded, and another metal stainless steel ring of 3 mm diameter is the outer electrode that acts as a cathode on which a negative DC voltage is applied typically between 0.8 and 1.4 kV. As illustrated in Figure 2.11, the electrode is surrounded by two circular 10-mm-thick Teflon insulators with a diameter opening equal to 3 mm. The results and the influence of the voltage and the polarization of the discharge are shown in section 2.5.

The quite low thermal conductivity and electrical conductivity of Teflon allow the insulators to resist high temperatures of the produced electrons. A first indication of the production of the pulsed glow gas discharge is the light produced by the excitation - de-excitation processes present in the plasma. A higher voltage is initially required to ignite the discharge then the voltage is lowered by observing and controlling the produced ions in real time. The discharge tends to be more stable after 10 to 15 minutes of operation, whatever the operation parameters are.

The produced electrons and cations can make new excitation and ionization processes to give rise to a so-called glow discharge. The discharge can operate in a rare gas (*e.g.* Ar or He), in a reactive gas (*e.g.* N_2 , O_2 or H_2) or in a mixture of these gases. In order to cause the ionization of elements, the kinetic energy of the incident electron E_{elec} must be equal to or greater than the energy required for the ionization E_I . Table 2.2 gives the ionization energies of various atoms and molecules.

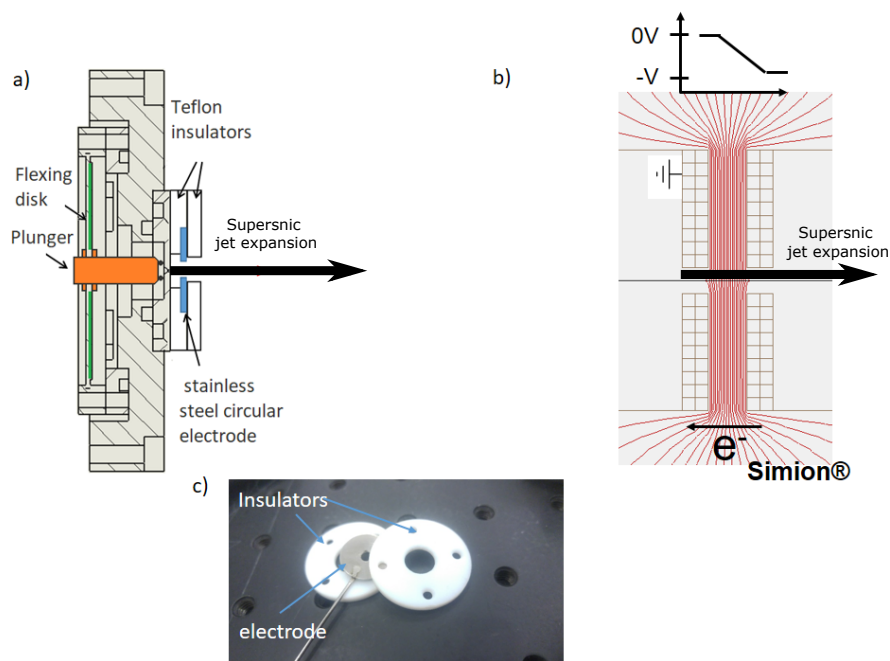


Figure 2.11 – a) The supersonic jet expansion can be ionized by applying a negative voltage (-800 to -1400 V) on the circular electrode (in blue (a)) enclosed in Teflon insulators fixed on the valve. The plunger (in orange (a)) is fixed to the flexing disk of piezo material (in green (a)). b) The SIMION[®] simulation of the two electrodes showing the electric field lines in red. c) Photo of the insulators and the negatively charged cathode.

Gas	E_I [eV]	Ionization process
Ar	15.7	$Ar \rightarrow Ar^+ + e^-$
He	24.5	$He \rightarrow He^+ + e^-$
N_2	15.6	$N_2 \rightarrow N_2^+ + e^-$
	24.5	$\rightarrow N^+ + N + e^-$
O_2	12.5	$O_2 \rightarrow O_2^+ + e^-$
	20	$\rightarrow O^+ + O + e^-$
CO_2	14	$CO_2 \rightarrow CO_2^+ + e^-$
H_2O	12.6	$H_2O \rightarrow H_2O^+ + e^-$

Table 2.2 – Ionization (E_I) energies of various atoms and molecules. From reference : [108, 109]

Electron gun

Electron beams are being used in a large number of scientific instruments [110]. The role of the electron gun is to ionize molecules by EI. Electrons are produced and lensed to efficiently interact with the area of interest in the jet.

Preliminary computer simulations using SIMION[®], played an important role in the design and the optimization of the electron gun. It is basically composed of the cathode to produce the electrons by

thermionic emission from a throated tungsten filament, and of focusing lateral electrodes to accelerate and focus the electron beam in the area of the intersection with the supersonic jet expansion. An anode is placed to collect the electrons and can also be used for the acceleration of the electrons. The thermionic emission may be understood using Stefan-Boltzmann's law. The latter expresses that for the power P radiated from the surface of a hot filament depends on the surface area S , the temperature T of the filament, the temperature T_0 of the environment. The relation is given by Equation 2.5 [111]:

$$P = \epsilon\sigma_{sb}S(T^4 - T_0^4) \quad (2.5)$$

with the Stefan-Boltzmann constant $\sigma_{sb} = 5.6 \times 10^{-8} \text{ W/m}^2\text{K}^4$ and the emissivity $\epsilon \approx 0.35$ for a tungsten filament at high temperature (i.e. in the order of 2000 K). If $T \gg T_0$, then T_0 may be neglected. Assuming a voltage V and a current, I , are applied to the filament and assuming that the radiated power is equal to $P = IV$ Equation 2.5 can be written as Equation 2.6:

$$T = \left(\frac{IV}{\epsilon\sigma_{sb}S}\right)^{1/4} \quad (2.6)$$

The thermionic emission of electrons from the tungsten filament can be described by the current density emitted from the filament and is given by the Richardson-Dushman equation i.e. Equation 2.7 [111]:

$$J = B_r C_f T^2 e^{-W_f/k_b T} \quad (2.7)$$

with the Richardson constant B_r , multiplied by a material correction factor C_f that gives $BC_f \approx 60 \text{ A/cm}^2\text{K}^2$ for tungsten, the work function $W_f \approx 4.54 \text{ eV}$ for tungsten, the Boltzmann constant $k = 8.617 \times 10^{-5} \text{ eV/K}$. Giving a numerical example, if we apply a current of $I = 10 \text{ A}$ and a voltage $V = 30 \text{ V}$ on a tungsten filament with a surface area of roughly $S = 10 \text{ cm}^2$, the temperature of the filament would be about $T = 1978 \text{ K}$. The current density emitted from the filament would be then $J = 63.5 \text{ mA/cm}^2$. If the 10^{-2} cm^2 filament is heated during $t = 1 \text{ s}$, the magnitude of the charge is $q = J \times S \times t = 0.635 \text{ C}$ and then, the total number of emitted electrons is about $n_e = q/e \approx 3.96 \times 10^{18}$. The emitted electrons can collide with species of the jet and then, induce an EI ionization of the gas. Some current is applied on the filament to emit electrons and on the appropriate voltages are applied to the filament and the electrodes focusing the electron beam in a particular direction, as first tested by SIMION[®] simulations. A schematic representation of a cross section of our electron gun and a picture of the actual set-up are given in Figure 2.12, and some of the electron gun most important dimensions in Figure 2.13.

A barrier to the production of a directed electron beam is the presence of a cloud of electrons that surrounds the filament, induced by the heating of the filament. That excess of charged particles is called a space charge region. That region induces forces that increase the divergence of the electron beam. In order to take into account this effect, the emission electrodes are inclined at the so-called *Pierce* angle which is equal to 22.5° with respect to the outer edge of the cathode (Figure 2.14). That shape of electrodes allows an optimal focusing of the beam of electrons [111]. The emitted electrons are then accelerated toward the anode. Between the cathode and the anode, the electrons could meet gas particles that pass through the electron gun unit in a direction perpendicular to the electron direction. The collisions occur in a volume delimited by grids. Figure 2.14 shows a schematic overview of the ion source and a SIMION[®] simulation

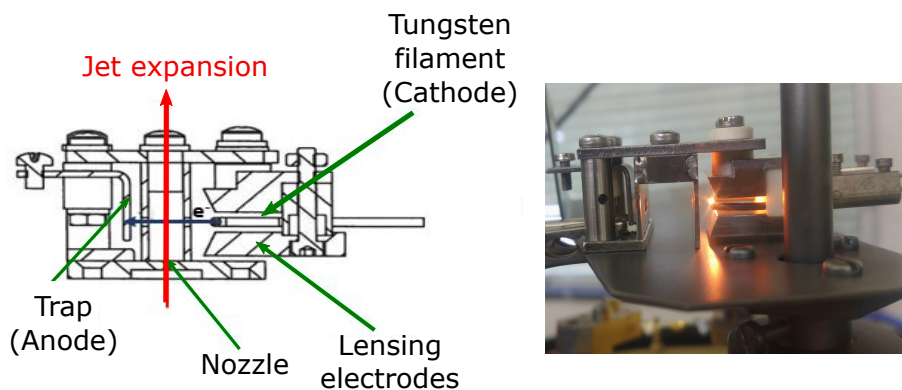


Figure 2.12 – On the left a Solidwork design of the cross-section of the home-made electron gun along with its different parts and on the right a photo of the electron gun operating in vacuum. The filament is radiating and therefore emitting electrons that are accelerated and focused into the jet expansion.

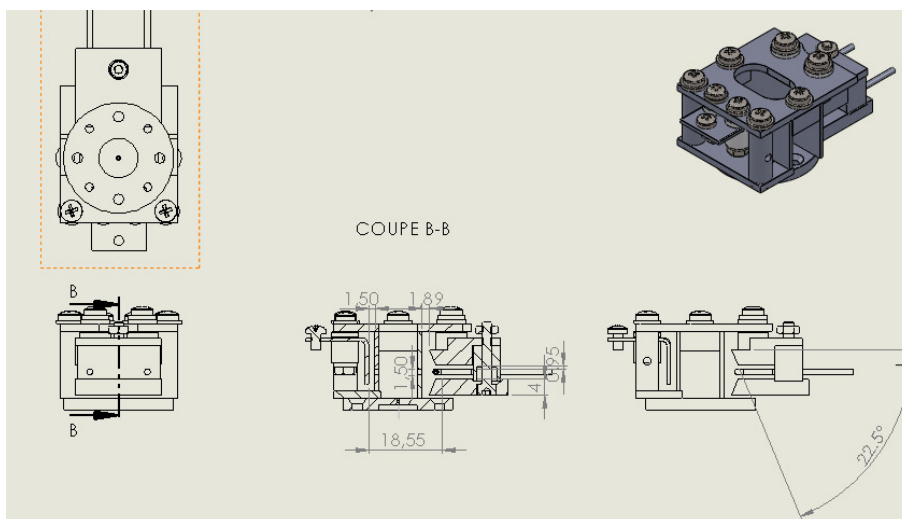


Figure 2.13 – Solidworks drawing for the electro gun and some of its important dimensions.

of the electron beam with the optimized voltages. The energy of the emitted electrons could be changed by varying the potential difference between the electrodes. The electron-gun showed the ability to better form negatively charged ions and clusters, than the discharge as shown in section 2.5.

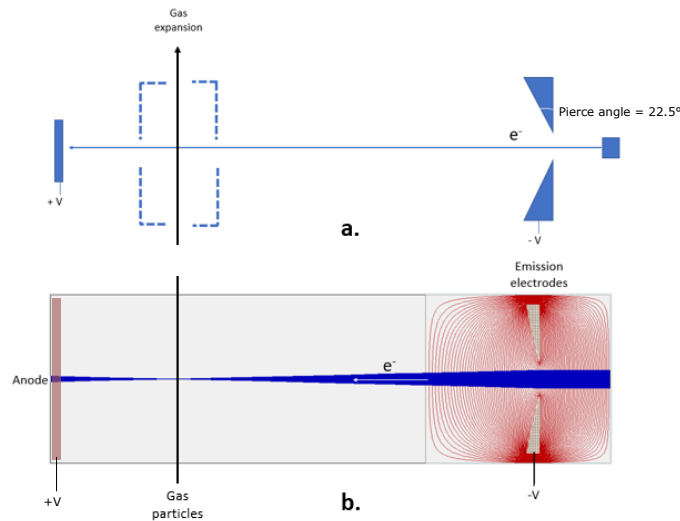


Figure 2.14 – a) Schematic representation and (b) SIMION[®] simulation of the electron beam produced by the tungsten filament and focused by *Pierce* emission electrodes and collected by the anode. The simulation showed the ability to focus the electron beam in the region of the intersection with the jet expansion for a maximum ionisation.

2.3.3 Characterization of the pulsed supersonic jet expansion

Determination of the valve performances in terms of pulse duration and repetition rate

The gas pulse properties, as its duration and its repetition rate are controlled by a series of important experimental parameters. (i) The TTL pulse signal which controls the opening duration and the repetition rate of the valve, (ii) the plunger tightening which could be adjusted while operating under vacuum and by screwing precisely the plunger in a way that it touches the nozzle with no leaks if it is not electrically supplied, but can open easily for voltages between 100 V and 700 V. The testing of the valve performance in terms of the minimum opening duration and maximum frequency is carried out using three methods. The first method consists of measuring the duration of the drop of the potential of the DC discharge of an argon pulsed jet. In fact as the pulsed valve opens, the pressure between the polarized electrode and the grounded nozzle rises and ignites a discharge which leads to a drop of the voltage applied. A cartoon of the time profile of the voltage at the discharge electrode is shown in Figure 2.15.

The drop of the electrode voltage magnitude is a measure of the voltage drop across the resistor of the power supply that could be measured using an electric probe as presented in Figure 2.15. This current accurately maps out the actual gas density for different pulse duration which is controlled using the multi-channel digital delay generator. The discharge current is maintained throughout the duration of the gas pulse and it is turned off as the valve closes. The results are shown in Figure 2.16.

Another technique to determine the shortest possible pulse is by detecting the light from the glowing discharge of ionized argon signal by a photodiode. The light that could be visible is emitted during the gas discharge at the nozzle exit. Indeed, as already mentioned in section 2.3.2, excitation-de-excitation

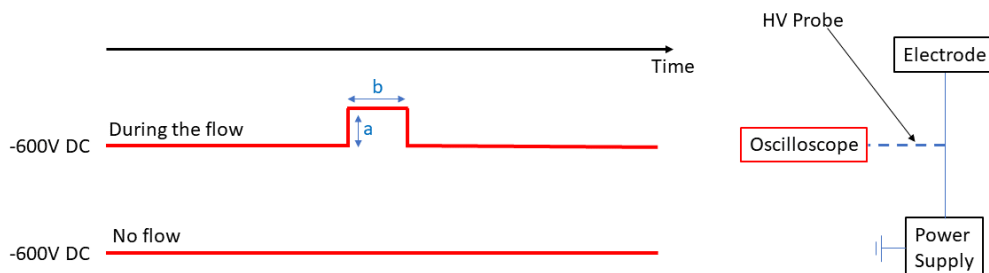


Figure 2.15 – The bottom trace displays a schematic of the voltage if measured using a HV probe when the valve is not operating. The top trace displays the voltage measured at one of the discharge electrodes when the pulse gas is applied. Arrow "a" divided by the resistor of the power supply is a measure of the discharge current. Applied voltage -600V subtracted by "a" is the measure of the discharge voltage. Arrow "b" is the corresponding time of the opening time of the valve.

processes take place in addition to ionization processes during the discharge. Therefore, photons are emitted with a particular frequency ν that depends on the gas and the discharge energy imposed by the potential of the electrode. The recorded signal is shown in Figure 2.16.

These two measurements give an idea of how the valve responds in term of opening time if we impose a certain duration for it. As we can observe in these two figures both signals agree and we can conclude that we are limited to a minimum opening time of approximately $250 \mu\text{s}$. The amplitude of the signal depends basically on the flux of charged species which in turn is proportional to the effective diameter. For longer opening time the effective diameter is larger allowing the amplitude of the signal to be higher. In this measurement we used a high voltage to ignite the discharge as fast as possible so that it could match the opening time of the piezo (1 kV).

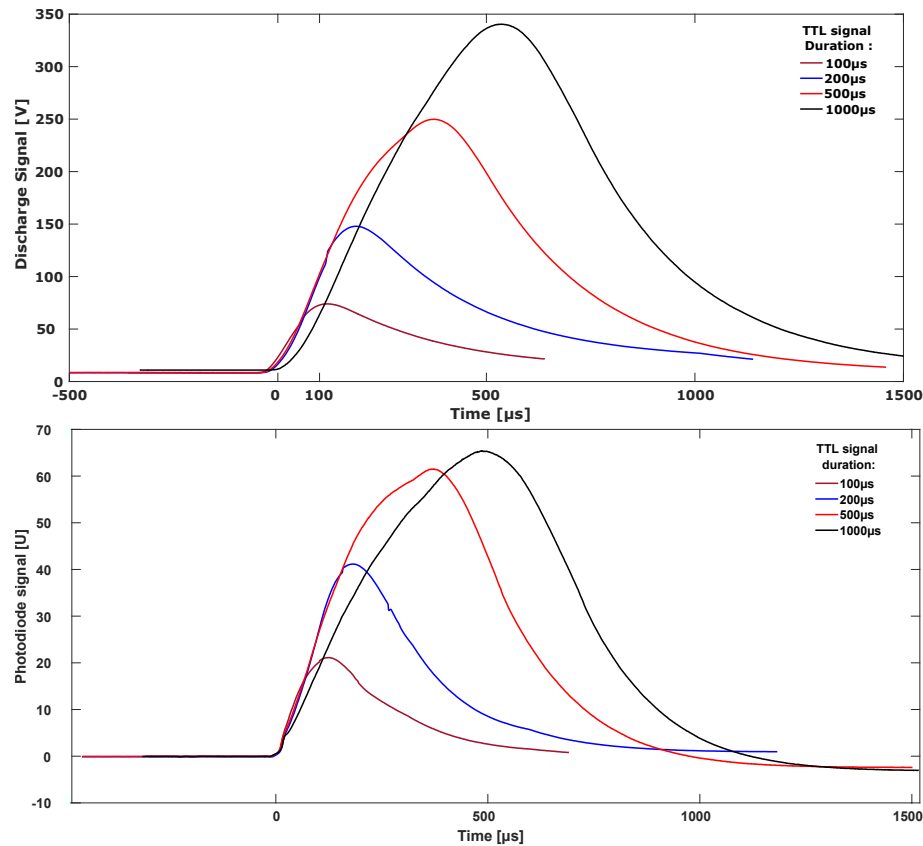


Figure 2.16 – On the top figure, the DC voltage discharge signal is plotted with respect to the time. On the bottom figure, the signal from the photodiode detecting the discharge radiation is plotted against time.

Characterization of the valve repetition rate

The frequency response of the valve is controlled and defined by the frequency imposed by the pulse generator. We started the tests by choosing a frequency of 1 Hz for different applied voltages on the piezo. We realized that the valve could operate for frequencies going from 1 Hz to 1 kHz. The tightening of the plunger depends on the desired frequency. In order to test the limits of our valve, the frequency is fixed to 1 kHz and the voltage is set on 600V and as we can see from Figure 2.17 and by detecting the light emitted by the discharge using a photodiode, the valve is able to operate on frequencies up to 1 kHz.

The plunger tightening was then optimized to operate on frequencies between 30 and 60 Hz. But, another question could be asked, how much voltage we should apply for an optimized signal for a certain frequency. The answer is shown in Figure 2.18. We concluded that (i) the higher the frequency, the larger the current needed by the valve to open. (ii) For increasing voltages the pressure in the chamber goes higher to attain a maximum value before going down until the next pulse.

One problem we noticed with this valve design is the rebound of the plunger after each pulse. This effect is detected while operating on low pressure with high tightening of the plunger, or at low frequencies

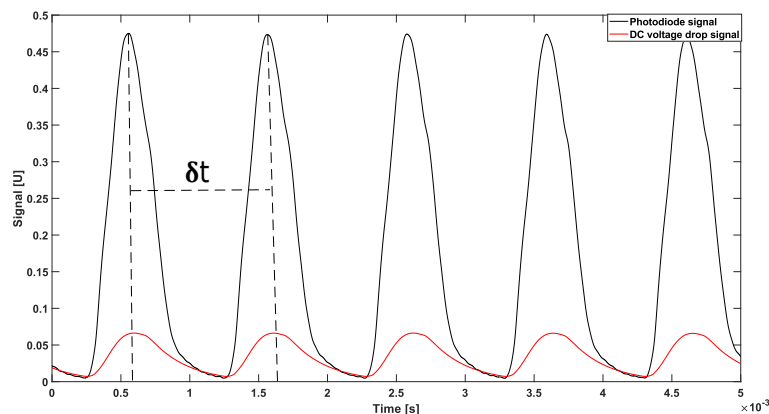


Figure 2.17 – Maximum repetition rate achieved by the valve, the signal is recorded using two methods, in black is the signal of the photodiode and in red is the signal of the DC current drop (both signals were rescaled for a better representation)

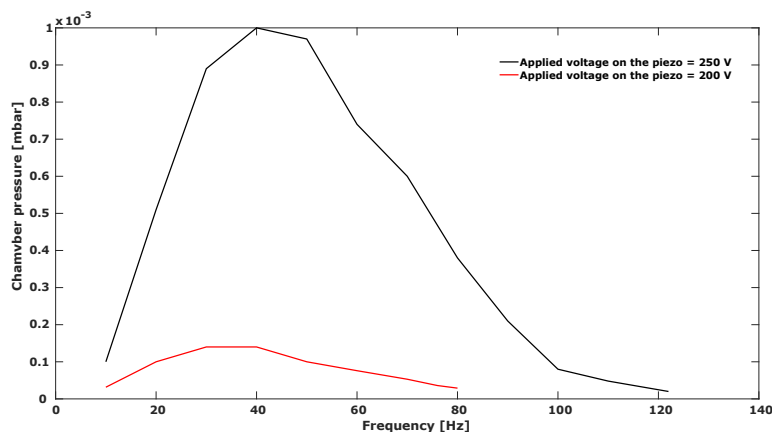


Figure 2.18 – The pressure in the chamber for two different voltages 200V in red and 250V in black. In this figure we observe the need to operate for frequencies between 30 and 60 Hz and for a voltage around 250 V.

and when a higher voltage is applied to the piezo.

Optical characterization of the jet

An interesting optical method to visualize the jet produced by different nozzle diameters was done during this thesis. In this way we can have an idea about the experimental parameters that could lead to shock waves before the extraction. The shock waves are not desired in our experiment because it is a consequence of a compression of the gas that is known to heat it up, therefore heat up the molecules. The difficulty is to find a method to produce visible and analysable images of the shock waves. Optical probing systems such as Schlieren [112, 113], Shadowgraph [41, 112, 114] and Mach-Zehnder interferograms [115] have been used in different studies that involved supersonic expansions.

In this section, a brief explanation of the operation of the different imaging beam techniques (Schlieren, shadowgraph, Mach-Zehnder) is given. Then, the Michelson interferometer mounted and used in the laboratory is presented. The Schlieren and shadowgraph techniques are both based on the linear dependence of the index of refraction n of gas to the gas density ρ ($n - 1 = c\rho$, with c the so-called Gladstone-Dale coefficient [112]). When parallel light rays cross perpendicularly a 1-D flow with a non-uniform density in x -direction, the rays are refracted and deflected at an angle θ that is proportional to the first derivative of the density :

$$\theta \propto \frac{\partial \rho}{\partial x} \quad (2.8)$$

Campargue studied the skimmer interference problems and visualized the free jet expansion using Schlieren technique [116], an example of his work is presented in Figure 2.19.

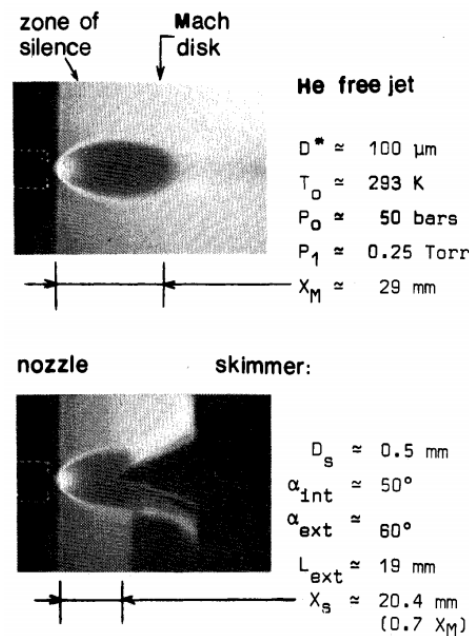


Figure 2.19 – Helium free jet zone of silence shown with (bottom) and without skimmer (top) in the region of the expansion. The experimental conditions are presented on the right of the two figures. The example is from reference [116].

The transmitted light gives the image on a screen where bright spots are the culmination of the light rays and the shadows correspond to the location of the rays divergence. Being a rise in density, the shock waves will appear as a shadow on the screen. The divergence or convergence of the light rays is proportional to $\frac{\partial \theta}{\partial x}$ and then, by Equation (2.8) the illumination in a shadowgraph is proportional to the second derivative of the density $\frac{\partial^2 \rho}{\partial x^2}$. For a Schlieren image the same principle as for the shadowgraph is also in application but the refracted light is intercepted by focusing via a lens the transmitted light on a razor blade. The latter allows blocking the light that was deflected by the regions in the flow where a change of density appeared, as for example a shock wave. The dark regions are then more visible on the screen and in that configuration since the illumination of the Schlieren image is proportional to the first

derivative of the volumetric mass $\frac{\partial \rho}{\partial x}$. The difference between the two methods is shown in Figure 2.20.

a) Schlieren



b) Shadowgraph

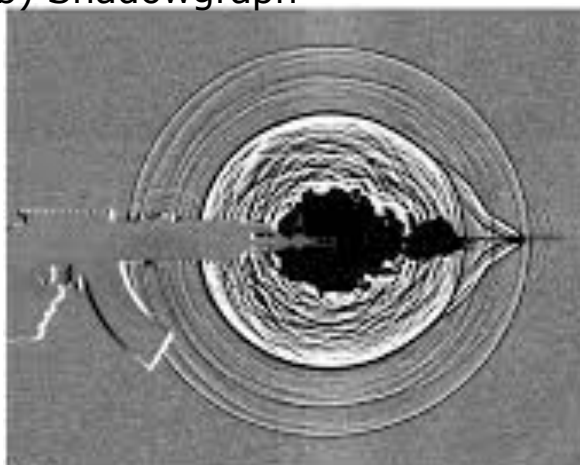


Figure 2.20 – Comparison between a shadowgraph and a Schlieren image from reference [117].

A schematic diagram is represented in Figure 2.21.

We attempted to apply the Schlieren technique for characterizing the jet in a vacuum. The absence of signal was attributed to a lack of contrast and the low density of the jet. On the other hand, measurements were done using the reservoir at a high-pressure P_0 and by visualizing the expansion at the atmospheric pressure and not at the vacuum pressure. In order to compare the structure of the jet produced by nozzles of different diameters, each of 5 nozzles with 100 μm , 250 μm , 300 μm , 500 μm , 1500 μm diameters were tested using argon and helium as test gases in the reservoir for different pressures P_0 (2 bar, 3 bar, 4 bar).

For the experiment a He:Ne laser (wave length $\tilde{\lambda} = 633\text{nm}$) was used with a spherical mirror of focal length equal to 1.5 m. The transmitted light is projected using a lens L ($D = 25.4 \text{ mm}$, $F = 50 \text{ mm}$) to

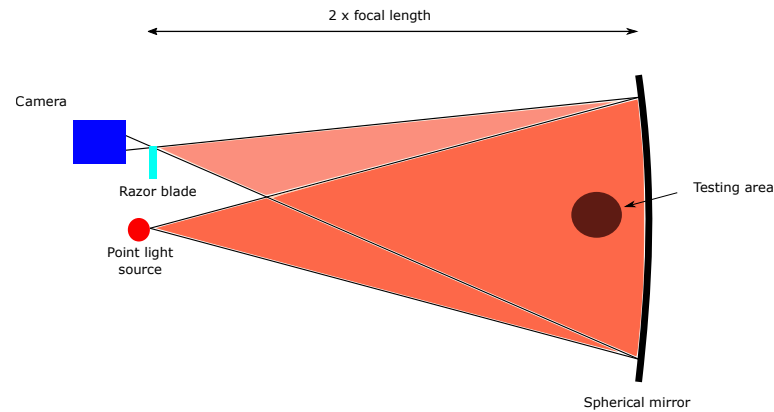


Figure 2.21 – Schematic representation of the Schlieren optical system, reproduced from [112].

illuminates a screen. A camera allows taking pictures/videos of the image on the screen. Small videos of the jet in a continuous mode were taken for each case and an image processing was done via MATLAB© software. In fact, two images were selected from a video, a reference one, where the jet is not present and another one where the jet is present. Two methods were used. In one case, just a difference between the two images was done and in the other case, a grayscale of the two images was done and then, a grayscale image of the difference between the two images was obtained to enhance the contrast. An example of photo of the jet in expansion in air atmosphere ($P_b = 1$ bar) through a nozzle of diameter equal to $500 \mu\text{m}$ using argon to fill the reservoir at a pressure of $P_0 = 4$ bar and another test in which the reservoir was maintained at a pressure of $P_0 = 3$ bar is given in Figure 2.22. In this figure, we show first that the Schlieren optical system is relatively easy to implement for visualizing supersonic jets. For a higher pressure we observed the formation of shock waves, but this happened for the case of an expansion of 4 bar of argon into atmospheric pressure. We could not obtain significant contrast when measuring an expansion in vacuum (10^{-5} mbar). This may be due to the low density contrast, indeed the optical system should be more sensitive, but due to lack of time the measurements stopped here.

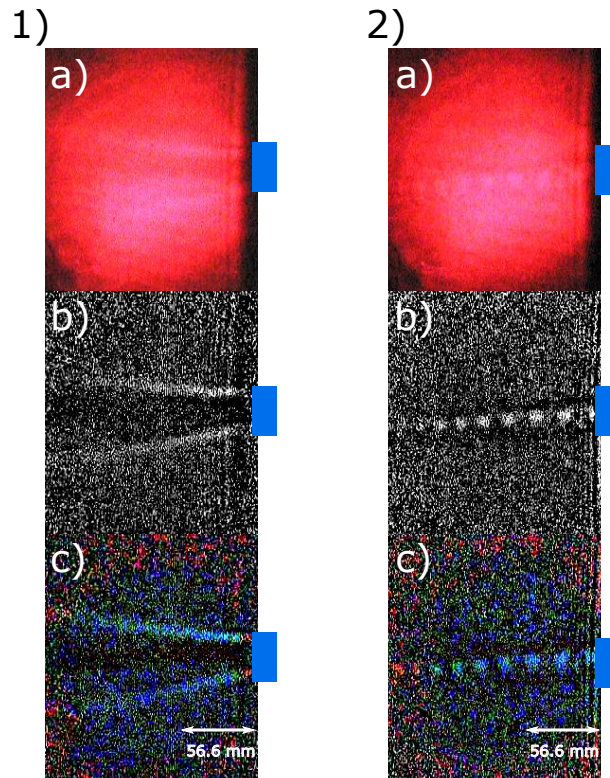


Figure 2.22 – 1) Corresponds to the case of a pressure of 3 bar in the reservoir and 2) correspond to the case of a higher pressure of 4 bar. a) corresponds to the direct measurement of the signal, b) corresponds to the image in grayscale and c) corresponds to the addition of RGB colours. b) and c) were done using Matlab© in order to enhance the contrast. The enhanced contrast obtained using the image processing allows us to observe a succession of shock waves. The diameter of the used nozzle is equal to $500 \mu\text{m}$ and it is represented in blue.

A recording of an interference pattern, so-called interferogram, can be used to visualize the shock waves produced by the supersonic expansion. The interferogram can be generated by using a Michelson interferometer [118]. A schematic representation of the used Michelson interferometer is given in Figure 2.23 a.. Assume a coherent red light source (wave length $\tilde{\lambda} = 633 \text{ nm}$), a He:Ne laser, that illuminates a plane mirror M_1 . The mirror reflects the light perpendicularly to its initial direction and, before the light reaches the interferometer. Two lenses L_1 ($D = 5 \text{ mm}$, $F = 10 \text{ mm}$) and L_2 ($D = 2.7 \text{ mm}$, $F = -50 \text{ mm}$) allows increasing the waist of the beam while keeping a well-collimated beam, with D and F the diameter and the focal point of the lenses. Then, the light passes through the aperture of a diaphragm and a beam splitter oriented at 45 degrees with respect to the incident beam splits the light. A part of the light is reflected towards plane mirror M_2 and another part is transmitted towards plane mirror M_3 . The beam splitter is assumed to be ideal i.e. it gives 50% reflection and 50% transmission of the intensity, and the mirror to be uniform. Then, the two waves emerging from the beam splitter are reflected on mirrors M_2 and M_3 , and come back to the beam splitter where they are recombined. The beams are coherent and will produce interference fringes. Finally, a third lens L_3 ($D = 25.4 \text{ mm}$, $F = 50 \text{ mm}$) projects the beams on a screen. The produced image can be recorded using a camera that is placed near the screen.

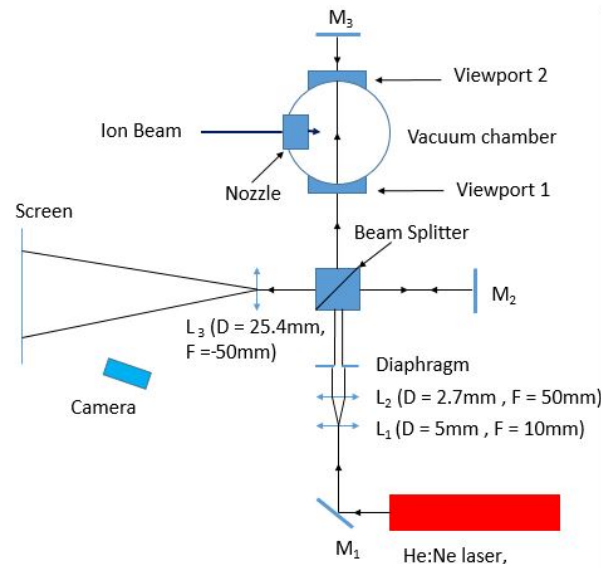


Figure 2.23 – Schematic representation of the Michelson interferometer adapted in order to observe the shock waves of the supersonic expansion.

Constructive and destructive interference fringes can be observed.

The objective is to place the vacuum chamber between the beam splitter and the mirror M_3 in order to cross the supersonic jet with one of the light beam just behind the nozzle exit. Indeed, this light beam passes through a first view port (Viewport 1), it crosses the supersonic jet just at the exit of the nozzle, it passes through a second viewport (Viewport 2) and then it will reach mirror M_3 . Then, it is reflected towards the chamber and it is recombined at the beam splitter with the other light beam. This other beam will be the reference one of the interferogram. The shock waves that are density disturbances induce interference fringes shifts. From the produced interferogram, the fringe shifts could be measured and give the refractive indexes. From the indexes, a density distribution of the supersonic flow could be obtained, as illustrated by J. Winckler [115]. Naturally, interferogram also allows visualizing the geometric features of the supersonic jet, showing the produced shock waves.

Unfortunately, such a method has not allowed to obtain significant results. The main reason would be the instability and the vibrations due to the vacuum system and the poor isolation between the vacuum system and the expansion chamber.

In order to illustrate the type of perturbation caused by a jet in an interferogram, an air spray and a flame were placed just behind the lens L_3 and perturbed the interferogram. Photos of the perturbed interferograms are presented in Figure 2.24.

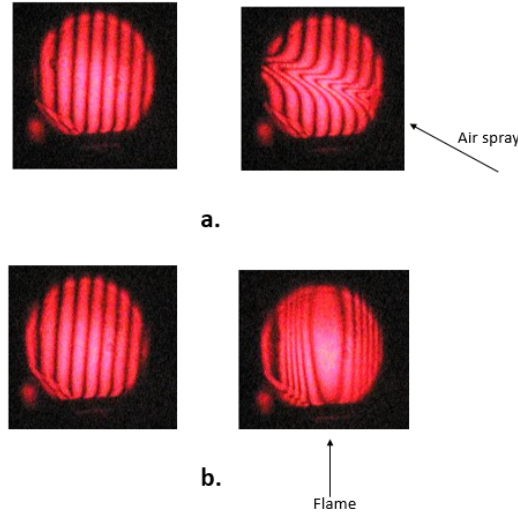


Figure 2.24 – Photos of the interferogram produced by Michelson interferometer represented in Figure 2.23 before and after the application of an air spray (a.), and before and after the application of a flame (b.) both placed just after the lens L_3 .

Flow simulations

Computational fluid dynamics (CFD) simulations is a powerful tool to predict the fluid flow properties in our supersonic jet expansion. Ansys fluent is one of the famous commercial CFD software packages, and it is based on a finite volume method approach. The Ansys fluent solver uses cell-centred finite volumes in which the flow variables are stored at the centre of the mesh elements. This solver, offers several solutions approaches like density-based and pressure-based methods. The numerical equations used in fluent are Navier-Stokes equations developed in Appendix A which include the continuity and momentum equations. In this section, analysis of the nozzle used for the experimental setup is carried out. It is important to verify the minimum temperatures that we can attain and to optimize the geometries of the nozzle and the discharge parts that can influence the jet expansion. Firstly, the processing, the initial conditions and the used equations are presented. Secondly, velocity, temperature and pressure profiles of the nozzle are calculated. The supersonic source was modelled. The shape of the nozzle coupled to the two insulators and to the discharge electrode were used as shown in Figure 2.26.

Mesh was created of unstructured trigonal elements. A higher density is adopted near the nozzle and on the axis of symmetry. A part of the meshing is presented in Figure 2.26. For the processing of the nozzle, 2D and double precision settings were used while reading the mesh. In the following, the details for the problem set (Table 2.3) and the solution parameters (Table 2.4) are presented. The solution is considered converged after 3500 iterations and the order of scaled residuals was below 10^{-3} . The conditions of temperature and pressure at the inlet correspond to the conditions for a shocked jet. Therefore Mach number is equal to 1. P^* is the pressure at the pinhole is calculated via :

$$P^* = P_0 / \left(1 + \frac{\gamma - 1}{2}\right)^{\frac{\gamma}{\gamma - 1}} = 2.43 \text{ atm} \quad (2.9)$$

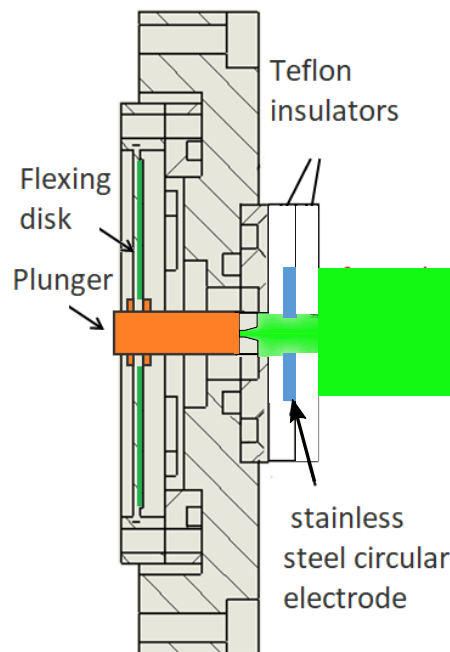


Figure 2.25 – Representation of the area in which the jet was simulated, formed by the nozzle coupled to the discharge electrode and insulators as indicated. The surface used for the simulation is represented in green.

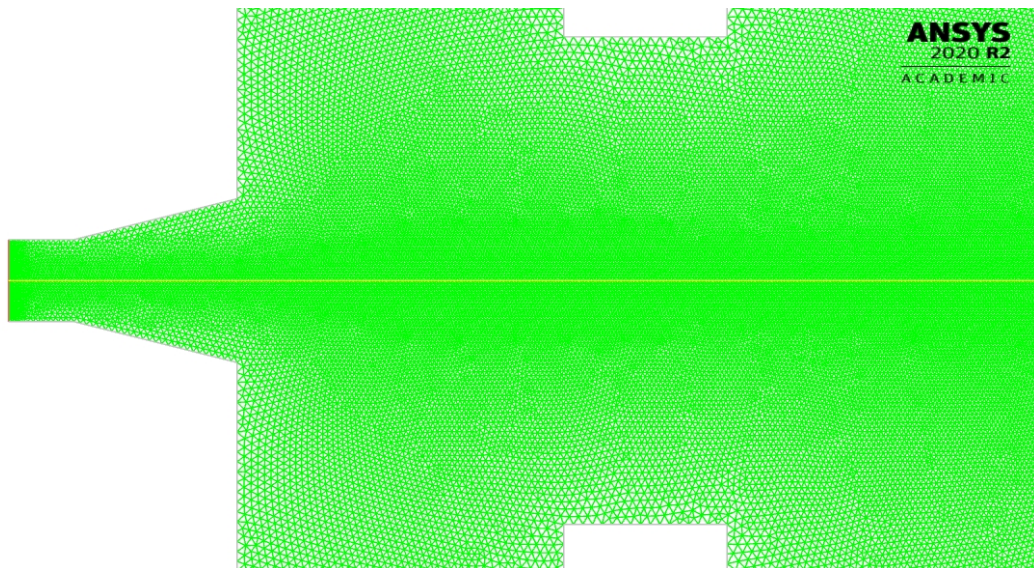


Figure 2.26 – Mesh Fluent view, showing the density and the precision in the areas close to the nozzle and to the axis of symmetry. The nozzle diameter is equal to $500 \mu\text{m}$.

The temperature at the nozzle (T^*) is calculated via

$$T^* = T_0 / \frac{1 + \gamma}{2} = 220 \text{ K} \quad (2.10)$$

These equations were already explained in the first chapter.

General	Solver type: Density-based
Models	Energy equation: On Viscous model: Laminar
Materials	Density: Ideal gas $c_p = 520.64 \text{ J/kg.K}$ Viscosity: Sutherland Thermal conductivity = 0.0158 w/m.K Molecular weight: Argon = 39.948 g/mol
Boundary conditions	Inlet pressure = Pressure far field = 2.43 atm Inlet temperature = 220 K Outlet pressure = 10^{-8} atm Outlet temperature = 300 K For initialization purpose only

Table 2.3 – Problem setup used in the simulation.

Solution controls	Courant number = 5 Time: Steady Space: axisymmetric Methods: Implicit least squares cell based
Solution initialization	Hybrid Relative to cell zone
Run calculation	No. of iteration 3500

Table 2.4 – Solution parameters used in the simulation.

Mach number, temperature and density profiles

in the following the contour plots that were obtained:

1. **Mach number:** As expected for a supersonic nozzle, the Mach number magnitude is equal to 1 at the throat section of the nozzle. This condition is known as shocked flow condition as discussed in chapter 1. The velocity at the nozzle exit is approximately equal to 525 m/s. Figure 3.9 shows the contour and the xy plots of Mach number. Mach number reaches 8 close to the outlet. We can also observe two relaxation due to the geometry of the plates used for discharge that disturbs the jet, but the effect is not affecting much cooling process.

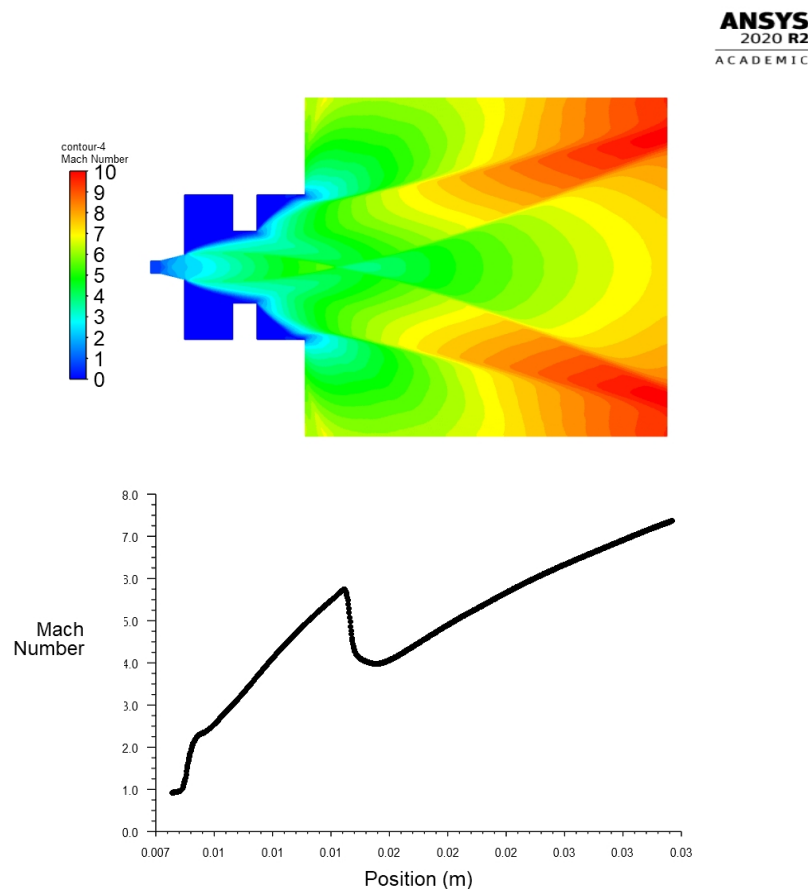


Figure 2.27 – Top panel: contour plot of Mach number. Bottom panel: Mach number evolution along the jet axis.

2. **Temperature:** Figure 2.28 shows the contour plot and the xy plot of the temperature of the jet along the axis of propagation. The temperature is maximum at the inlet ($T^* = 220$ K) and decreases gradually until the outlet. We observe a small shock wave at 0.015 m where the temperature reaches 50 K followed by a second gas expansion that cools down the gas. The magnitude of temperature at the outlet is less than 10 K.

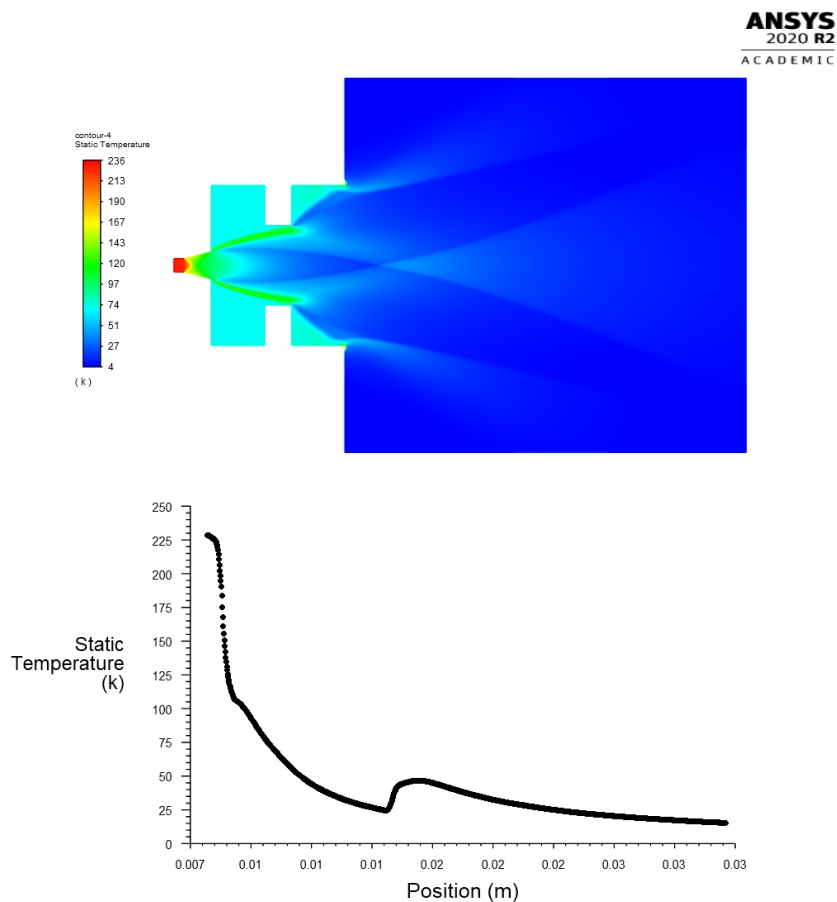


Figure 2.28 – Top panel: Temperature contour plot. Bottom panel: Temperature plot along the x direction.

3. **Density:** The density is maximum at the inlet, it decreases dramatically downstream the nozzle exit. This density is lower in a free jet expansion than the one of a uniform jet expansion (Figure 2.29).

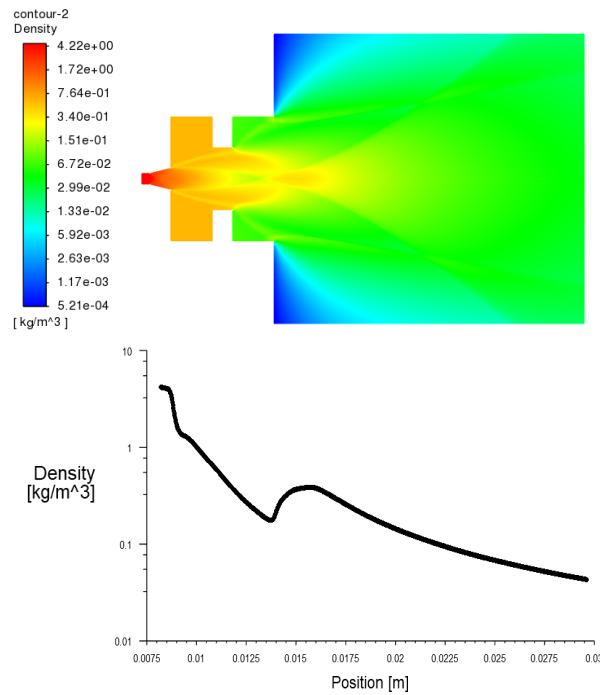


Figure 2.29 – Top panel: Density contour plot. Bottom panel: Density plot along the x-direction. The y-axis (density) is in logarithmic scale in order to visualize the density variation.

In conclusion, the simulations of the flow through the nozzle and the plates used for the discharge at the exit of the nozzle, showed the ability to produce a cold jet that can reach temperatures as low as 10 K. The variation of the temperature along the axis of propagation could be a way to measure spectra at different temperatures. Another parameter that we have to take in consideration is the temperature that is generated when the discharge is operational. The question that is important to our study : can we still reach low temperatures if the source was heated? The cooling of the gas is progressive and we should also reach low temperatures at a certain distance from the nozzle. To make sure we did additional simulations as follows:

Adding heat from the discharge

The simulation consisted of setting a temperature of the walls at 700 K which is a little bit exaggerated. The choice of this temperature was done so we can make sure that we are able to reach low temperature even for extreme discharge heating. The results are shown in Figure 2.30 for Mach number contour plot and xy plot. In Figure 2.30 we show the temperature contour plot and xy plot.

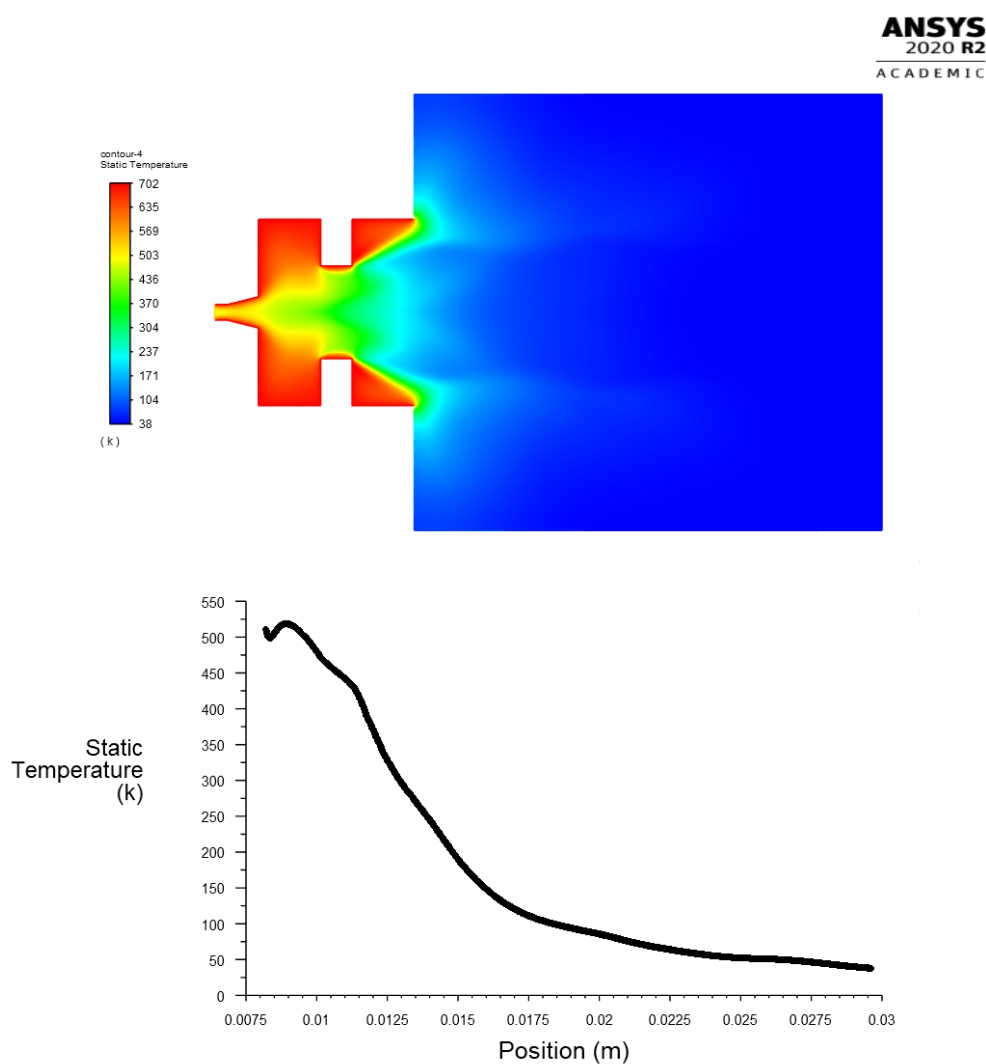


Figure 2.30 – On the top the contours of the static temperature magnitude is presented. On the bottom the plot of the temperature evolution on the axe during the jet expansion is presented.

As a result, we were able to reach temperatures as low as 40 K at a distance of 30 mm from the nozzle.

2.4 Home-made time-of-flight mass spectrometer

The next step in the characterization of our supersonic beam is to infer its chemical composition. Therefore, a time-of-flight mass spectrometer was built. In this section we start by a short review of mass spectrometry. Then, we describe our design in detail with its different characteristics, as the ability to produce bunched packets of mass selected ions and to produce a photodissociation spectrum. The first scientist to establish the principle of mass spectrometry was Joseph Thomson. He developed an apparatus for separating atoms by their mass and was able to show the existence of stable isotopes of neon in 1912 [119]. Nevertheless the first invention of the modern mass spectrometer is often attributed to Arthur Jeffrey Dempster in 1918 [120]. This spectrometer, a magnetic analyser, was used to detect selectively ions produced by electronic impact, using the modulation of the potential of an electrostatic accelerator to guide them to a collector after a 180-degree deflection. This method was improved by F.W. Aston, who was Thomson's assistant, by constructing the first mass spectrometer with a separation of ions according to their speed, for which he received a Nobel Prize for this work [121]. Another type of mass analysers is the quadrupole mass spectrometer. As the name implies, it consists of four cylindrical rods parallel to each other, having a certain geometry and it is able to separate ions with respect to their mass-to-charge ratio by applying a DC and a RF electric field on the rods. It was also used for photodissociation spectroscopy [122][123].

On the other hand, the first-time-of-flight mass spectrometer was the idea of Stephens in 1946 and it was set up by Cameron and Eggers in 1948 [124, 125]. In 1955, Wiley and McLaren published a seminal paper on time-flight mass spectrometry [126], by proposing a time focusing of ions with the same mass to charge ratio by a dual ion acceleration region to increase resolution. Notable time-of-flight mass spectrometers were then brought by B.A. Mamyrin and his collaborators in 1972 [127] via the introduction of a reflectron to correct the kinetic energy distribution of ions and dramatically increase mass resolution. Then in 1989 J.H.J. Dawson and M. Guilhaus [128] implemented an extraction of ions in a tube orthogonal to the source flow in order to increase the frequency of the ion extraction. Time-of-flight mass spectrometry is a very rich instrumental field and has rapidly evolved during the past 20 years in various disciplines. In practice, time-of-flight mass spectrometry (TOF-MS) allows separating ionized species, according to their mass-to-charge ratio m/z [129]. When a kinetic energy E_k is given to all the produced ions by applying an acceleration potential V via electrodes, ions with different m/z will have different velocities as they travel a certain distance d in so called the drift tube to finally reach the detector.

The ions with the same ratio m/z form a packet in the drift tube and have a corresponding time of flight t . There are two well-known formulas that apply to time-of-flight analysis and calibration. One is the formula for the kinetic energy:

$$E_k = \frac{1}{2}mv^2 \quad (2.11)$$

Which is solved by replacing v by d/t , the mass-to-charge ratio is calculated for each ion by using Equation (2.12).

$$\frac{m}{z} = 2 \frac{E_k t^2}{d^2} \quad (2.12)$$

It is important to keep a constant homogeneous applied energy E_k , in order to lower the energy

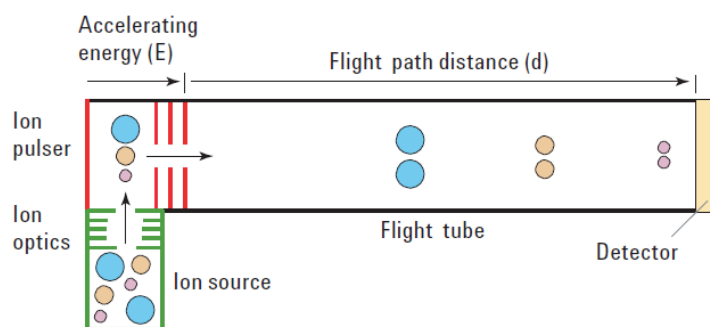


Figure 2.31 – Schematic representation of a linear TOF mass spectrometer from reference [130]. Ions of various mass-to-charge ratios are accelerated with energy E_k via electrodes and travel a distance d in a drift tube. The ions of same m/z form packets and each packet corresponds to a time of flight t to travel the distance d . A detector allows the ion packets to be detected at the end of the drift tube.

spread given to ions. Indeed the energy spread affects the resolution which will be discussed in the next subsection 2.4.2. As the energy and the drift tube length are held constant, they could be combined into a single term C and the t is the difference between the initial time t_0 and the time when the ion hits the detector t_f . The basic formula to find the corresponding mass will become :

$$m = C(t_f - t_0)^2 \quad (2.13)$$

2.4.1 Mass calibration

To make the conversion of measured time-of-flight mass, the values of C and t_0 must be determined. In other words, a reliable mass determination of ions requires a quadratic calibration of the m/z scale. The calibration is done by injecting a well-known gas into the spectrometer to obtain their corresponding time-of-flight. An example representing the calibration of a time-of-flight spectrum of a mixture of N_2O and H_2O expansion is shown in Figure 2.32:

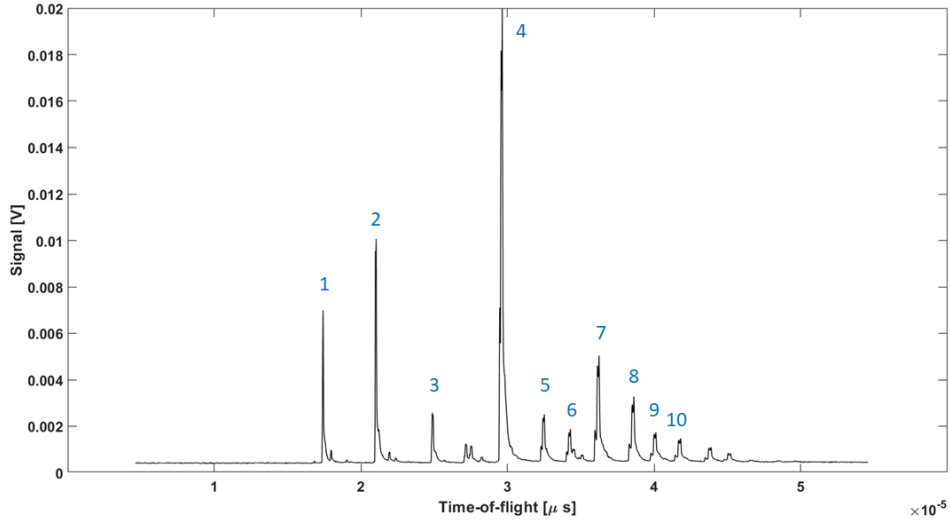


Figure 2.32 – Time-of-flight spectrum of an expansion of N_2O and H_2O .

Below in table 2.5 we can find a list of ten peaks with their corresponding time-of-flight t values. In order to calibrate one needs to find two peaks and attribute these peaks to two masses. In the example above (Figure 2.32), we can predict and assign the peak at $17.40 \mu s$ to NO^+ and the peak at $21.03 \mu s$ to N_2O^+ . If one made a mistake in assigning the two masses that will serve to calibrate the spectrum, it is easy to pick another two masses and keep trying to finally attribute all the peaks to logical masses. Now that we have these two masses we can start the calibration by numerically resolving the quadratic Equation 2.14 that gives the plot of the mass in function of time so we can find on this plot the mass of each corresponding time:

$$\frac{m}{z} = a(t - b)^2 \quad (2.14)$$

Peak number	TOF [μ s]
1	17.40
2	21.03
3	24.85
4	29.63
5	32.50
6	34.28
7	36.23
8	38.60
9	40.00
10	41.80

Table 2.5 – The important peak present in the spectrum of Figure 2.32 with their corresponding time-of-flight

As a result, we obtain the plot of the mass in function of time as follows (Figure 2.33):

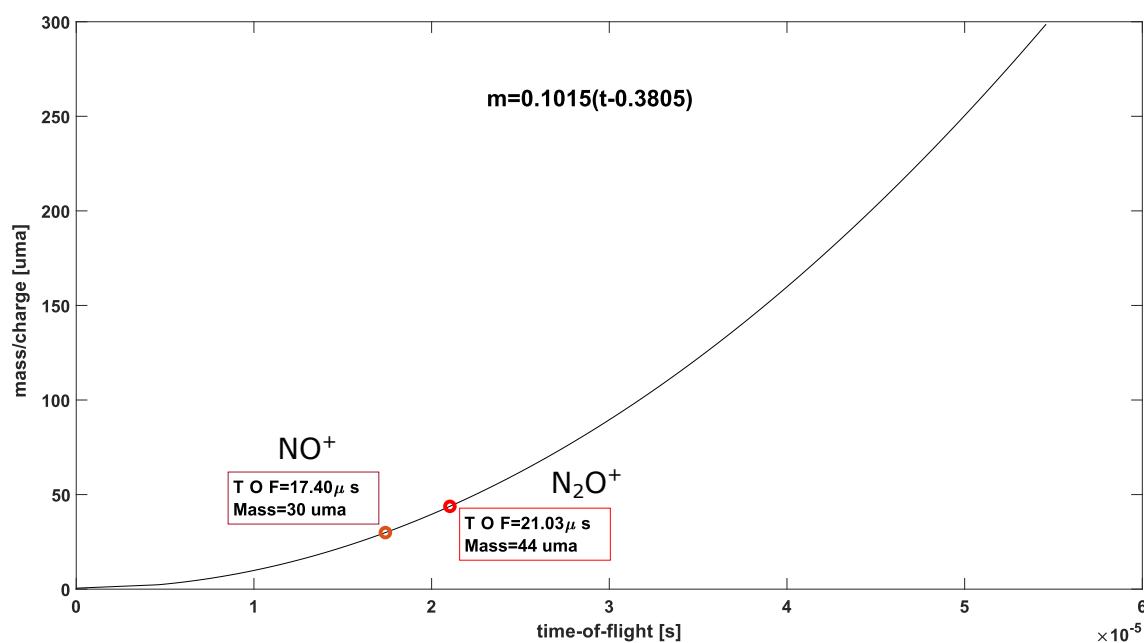


Figure 2.33 – Quadratic curve fitting of the mass-to-charge ratio with respect to the time of flight. The equation of the fitting is $m/z = 0.1015(t - 0.3805)^2$. The coefficient of determination of the fit is $r = 0.99908$. The two masses used to calibrate the spectrum are also presented with their corresponding TOF and mass.

Therefore, an accurate measurement of flight time will give an accurate mass value for a given energy and drift tube of length d . We can then attribute each peak to its mass value and identify the ten peaks in Table 2.6 as following:

Peak number	Chemical formula	T-O-F [μ s]	mass/charge [uma]
1	NO ⁺	17.40	30
2	N ₂ O ⁺	21.03	44
3	(N ₂ O)(H ₂ O) ⁺	24.85	62
4	(N ₂ O) ₂ ⁺	29.63	88
5	(H ₂ O)(N ₂ O) ₂ ⁺	32.50	106
6	(NO)(N ₂ O) ₂ ⁺	34.28	118
7	(N ₂ O) ₃ ⁺	36.23	132
8	(NO)(N ₂ O) ₃ ⁺	38.60	162
9	(N ₂ O) ₄ ⁺	40.00	176
10	(H ₂ O)(N ₂ O) ₄ ⁺	41.80	194

Table 2.6 – The assignment and the identification of the ten peaks to their corresponding mass/charge ratio.

2.4.2 Definition of the resolution for a time-of-flight mass spectrometer

In TOF-MS ions with the same ratio m/z are detected at the end of the drift tube with a spread Δt in arrival times [129]. That temporal distribution is mainly caused by the spatial distribution and kinetic energy distribution of the ions after their ionization. The spread limits the mass resolving power R_p that is defined by Equation 2.15 according to IUPAC [131].

$$R_p = \frac{m}{\Delta m} \quad (2.15)$$

With Δm the Full Width of the peak at Half its Maximum height (FWHM) associated to the ion of mass m in the mass spectrum. In order to express the resolution with respect to flight time t Equation 2.12 is used to obtain the time derivation of mass m , as yielded by Equation 2.16.

$$\frac{dm}{dt} = 2z \frac{2E_k t}{d^2} \quad (2.16)$$

By considering a finite variation of mass $dm = \Delta m$ and time $dt = \Delta t$ and substituting for Δm from Equation 2.16 into Equation 2.15, the mass resolution is given by Equation 2.17.

$$R_p = \frac{t}{2\Delta t} \quad (2.17)$$

Where t is the most probable time of flight of the distribution and Δt is the full width at half maximum (FWHM) of the peak measurement.

2.4.3 Ion separation, gating, bunching, and re-referencing

The photodissociation spectroscopy technique requires a high photofragments signal. The ion optics should be highly efficient to ensure an efficient interaction between the particles and the laser beam. Therefore, efficient overlapping requires a high resolution mass spectrometer coupled to an adapted ion optics to keep the beam aligned and collimated. C. J. Dedman, E. H. Roberts, S. T. Gibson, and B. R. Lewis [132] have proposed a new instrument able to produce well-defined ion packets having the smallest time spread Δt at the point of the interaction with the dissociative laser for a relatively simple scheme. The set-up consists of a single unit able to do multiple functions. It is able to accelerate the ions and to separate them according to their m/z ratio, and to gate the produced ions in order to select a dense and well defined single packet. The most important part is the bunching of the ions for a higher resolution. Finally, this unit is able to do a ground potential re-referencing of the ions before exiting the unit. This section describes the design that was developed and optimized in this thesis and which was inspired by the work of C. J. Dedman *et al.* [132]. The design was first modelled, the ions trajectory was then simulated to check the geometrical and operating parameters. Then the design was fabricated and then tested on the instrument. The unit is presented in Figure 2.34 and it is composed of a succession of electrodes made from aluminium. The unit is divided into two parts, the first is composed of six electrodes that apply a gradual acceleration to the ion beam, explained in section (**Acceleration, and ions separation**). The second part consists of two electrodes shaped as two cups able to gate bunch and re-reference the ion beam at ground potential explained later in section (**Ions gating**) and (**Ion beam re-referencing**).

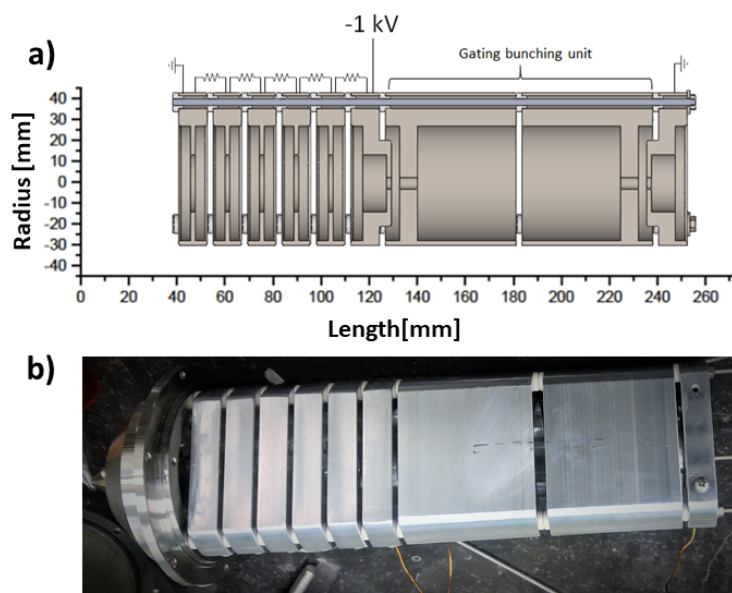


Figure 2.34 – a) The solidworks design of the TOF unit with the x and y dimensions, the acceleration electrodes are separated by resistors of 100 k Ω each. The first and the last electrodes are at ground potential. The ions are accelerated between the first and the 6 th electrodes, the latter have a potential of 1 kV. b) Photo of the unit attached to the stainless steel that hold the skimmer which is also in the photo

Acceleration, and ion separation

if we apply a difference of potential ΔV_a between two parallel electrodes, an electric field \vec{E}_a which direction is from the highest positive to the lowest negative potential is created. Ions of total electric charge $q = ze$ where e is the elementary charge exposed to this electric field parallel to the direction of their propagation will be accelerated. As illustrated in Figure 2.35 cations coming from the left electrode which is positively polarized will gain a kinetic energy $E_k = q\Delta V$ passing to the negative electrode. In order to introduce the ions and then to extract them after the acceleration, The two electrodes should have a hole in the middle. The hole will affect slightly the distribution of energies if the diameter is large as the higher potential will be in the middle and will slightly change when the ions are passing away from it. In our home-made spectrometer, the acceleration electrodes are assembled in a tube and connected

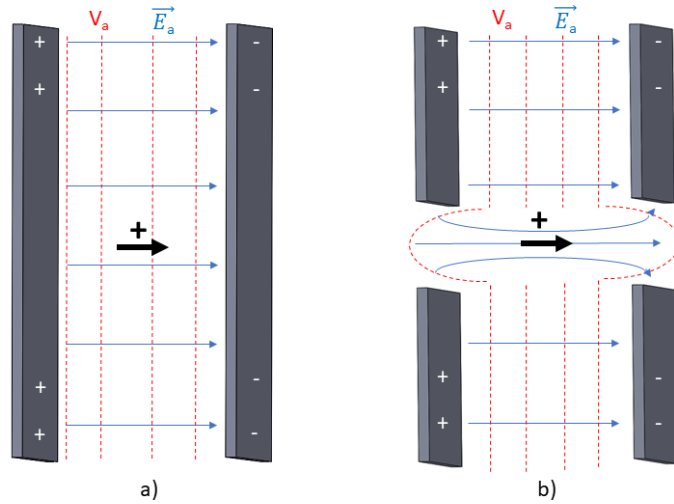


Figure 2.35 – a) Typical capacitor where equipotential lines of value V_a are represented by dashed red lines. Electric fields of value \vec{E}_a are represented by blue vectors. Cations inside the capacitor are accelerated in the direction of the black arrow which correspond also to the direction of the electric field. b) Two electrodes with a hole in the center. The only difference is that the potential lines and the electric field are slightly curved in the area of the hole. The electric field can accelerate the cations in the direction of the electric field through the two holes of the electrodes.

via resistors of $1\text{k}\Omega$ which play the role of potential dividers helping to produce a smooth gradient of potential. The electrodes present successive potentials of 0 V , -200 V , -400 V , -600 V , -800 V and -1000 V so the cations gain progressively a kinetic energy of $E_k = 200\text{ eV}$ from one electrode to the next one for a total kinetic energy of 1 keV exiting the final electrode. Ions of different mass-to-charge ratios m/z will gain the same energy. Therefore, they will gain different velocities v according to the Equation 2.18. The greater m/z , the smaller is v .

$$v = \sqrt{\frac{2E_k}{m/z}} \quad (2.18)$$

This assembly is placed at 4 cm after the grounded skimmer. Another design was implemented later

during this thesis and it will be described later in the perspectives section. The electrodes that were used in this unit are like the one represented in Figure 2.36 with its dimensions, and have these dimensions to allow them to be fixed in the tube after the skimmer and these electrodes have a triangular shape to allow a better pumping of the tube and the unit. In Figure 2.36 we can see the design of one electrode and then the acceleration scheme composed of the set of the six electrodes which are separated by ceramic insulators of 2 mm and connected via resistors (each having a resistance of 100 k Ω). The acceleration unit is represented in the schematic illustration in Figure 2.37, (the first six electrodes in red).

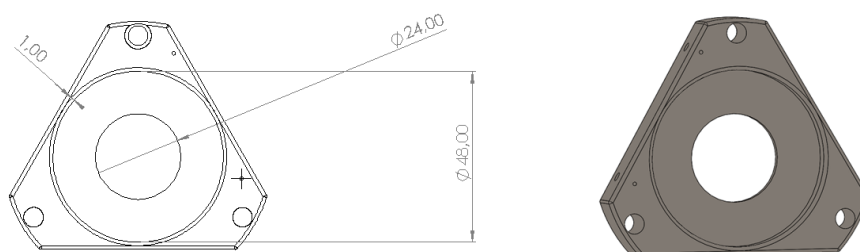


Figure 2.36 – The solidworks design of the electrodes used for the acceleration with its dimensions. The electrode is represented in red in Figure 2.37.

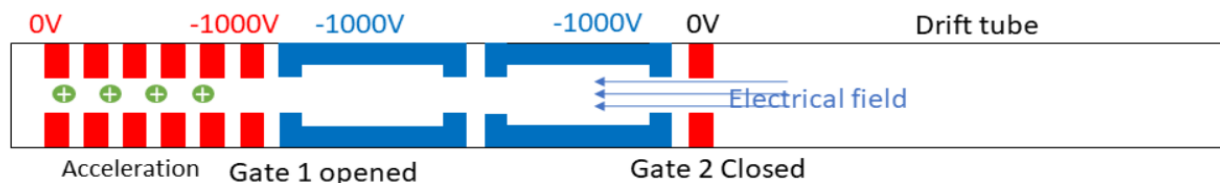


Figure 2.37 – The representation of the unit where we can find in red the acceleration electrodes and the positive ions in green. The ions gain gradually a kinetic energy to finally reach the electrode at -1000 kV. The rest of the unit is explained in the following sections

Ions gating

Following the acceleration, the ions enter the gating unit. It is composed of two electrodes shaped as two cups, and separated by insulators as presented in Figure 2.34 with all the dimensions. This unit is designed to select physically a defined packet of all species produced during the expansion and to define a starting time for the time-of-flight of the separated accelerated masses over the TOF drift tube length. The choice of the ionic source and its optimization are important, because the selected packet should contain as many ions as possible. Therefore, we maximize the number of photofragments later in the experiment, and the signal-to-noise ratio will be eventually improved. In addition we require that these ions have a limited lateral dispersion which is assured by the use of an electrostatic lens detailed in section 2.4.4.

As shown in Figure 2.39, gating is performed using two pairs of electrodes forming two gates. The first gate is located at the exit of the acceleration before entering the two cups and at the exit of the unit. When a pair is at the same potential as the beam, the gate is open. When one element of each pair is at a different potential, a strong electric field results in the deflection of all the ions from the beam axis and the gate is said closed. As shown in Figure 2.38, following the acceleration electrodes, the ions enters the gating electrodes represented in blue. Then, two high-voltage switches operate to (i) close the first door in order to select a packet of ions (ii) open the second gate to let the packet fly inside the drift tube. The two switches operations are simultaneous and operate at a time t_1 . t_1 is set as the start time for the time-of-flight of each m/z ion in the selected packet. The ions are finally detected at a time t_2 that is shorter for lower masses than higher masses. Therefore the TOF of each mass will be equal to $t_2 - t_1$ and a mass spectrum is obtained.

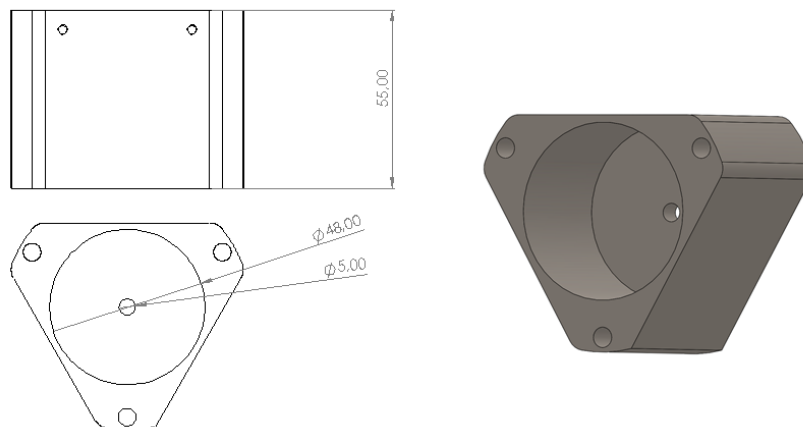


Figure 2.38 – The solidworks design of one gating electrode shaped like a cup with the relevant dimensions. The electrode is represented in blue in Figure 2.39

Practically we are using two fast high-voltage switches (Behlke HTS 61-01-GSM) in order to flip the potential of the two cups from -1 kV to ground potential or to a positive value. The characterization of the timing of the two switches is essential to know the limitations of our system. Therefore, we measure the voltage on the output of the switches that are connected each to one cup of the gating unit. Using an

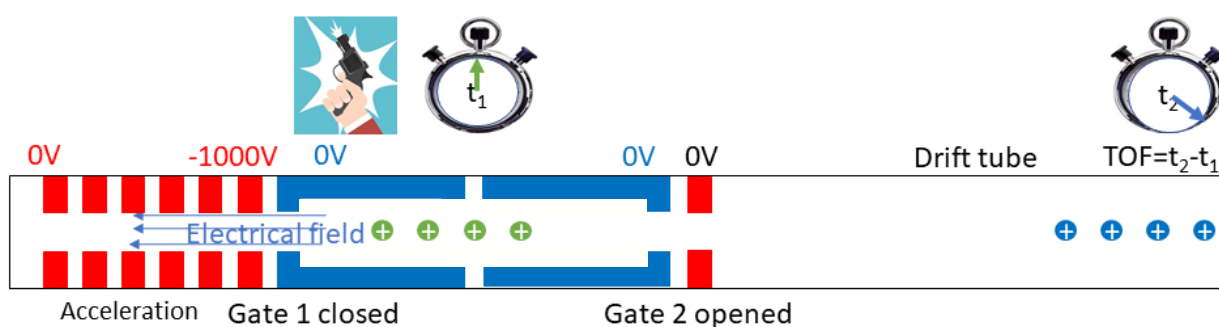


Figure 2.39 – The representation of the unit where we can find in blue the gating electrodes that each form a pair with the neighbour red electrode. Gating is performed when at t_1 the cations in green are inside the two cups and the potential of the two cups is switched to ground. The result is that the first gate is closed by creating an intense electric field with the electrode at -1kV , the second gate is opened and the selected packet of ions could travel to the detector to arrive at a time t_2 , the cations are in blue at this time. The time of flight is measured by calculating $t_2 - t_1$.

oscilloscope, we can measure the variation of the voltage of the switches output. The results are shown in Figure 2.40. We concluded that the rising time of the two switches is ≈ 200 ns. This value is higher than the one in the article of Dedman [132] because they used another home-made switch adapted to their experimental set-up. It allows to switch from a high positive/negative voltage to a negative/positive voltage. A resistor of 330Ω is added at the output to dump the overshoot and the ringing of the signal (LC circuit), at the cost of increasing the rising time (200 ns instead of 20 ns). A test was performed and there was no difference for the obtained resolution with or without the resistor.

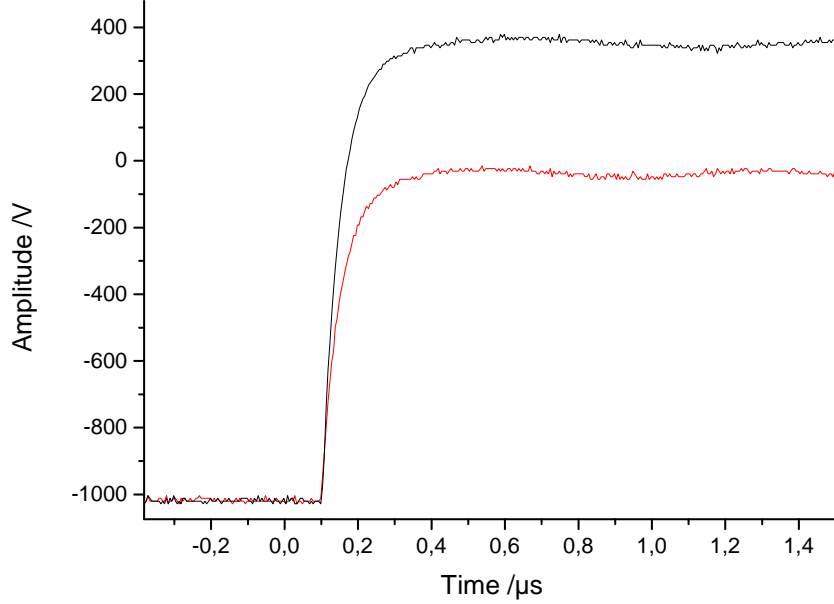


Figure 2.40 – The characterization of the rising time of the switches. In black the rising time of the switch that controls the voltage on the electrode of the first gate switching from a negative value of the potential (-1 kV) to a positive value (400 V). In red the second switch rising time is represented. It flips from -1 kV to 0 V. Both rising times are close to 200 ns.

Ion beam bunching and enhanced resolution results

As mentioned in the preceding section, in order to obtain a higher density of the ions when interacting with the laser, axial bunching and compressing (spatially and temporally) of the ions is crucial. Bunching is performed by creating a gradient of potential inside the two cup-shaped electrodes. Indeed, if we apply the gating to a selected packet of the jet but, instead of switching to 0 V both of the electrodes, the first one is switched to a certain tunable positive voltage to give a slight push to the ions having slightly lower energies and/or coming from further away from the exit of the bunching unit. These ions start to catch up with the ions ahead after exiting the unit. This tunable gradient is used to bunch the ions at the crossing point with the laser beam. Figure 2.41 explains the bunching process and show the voltages used in this thesis. Bunching the ions at a certain position and the choice of the difference of energy ΔE to compress a packet of ions of length l at energy E over a drift length L is given by Equation [132] :

$$\Delta E = \frac{2El}{L} \quad (2.19)$$

As discussed later in section 2.6.1 this bunching process introduces a small energy spread for the ions. If the distance between the TOF unit and the interaction with the laser beam is equal to $L = 1.72$ m and the length of the packet is $l = 86$ mm the difference of energy required is equal to $\Delta E = 100$ eV for a

beam energy of $E = 1000$ eV.

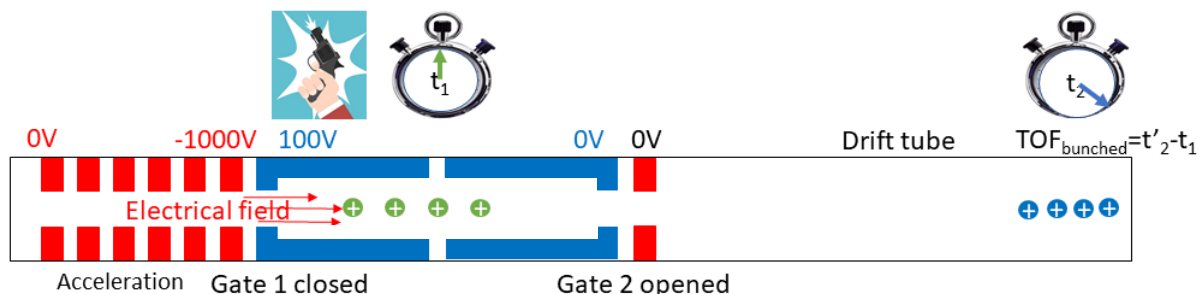


Figure 2.41 – The representation of the gating and bunching unit where we can find in blue the gating electrodes that each form a pair with the neighbour red electrode. Bunching is performed when at t_1 the cations in green are inside the two cups and the potential of the first cups is switched to a positive value (100 V in our case), the second cup is switched to ground potential to open the gate. The result is that at the position of the interaction with the laser, the cations represented in blue are axially bunched.

A comparison between the bunched and unbunched signals is presented in Figure 2.42 for N_2O^+ . Ions were produced from a pure expansion of N_2O (stagnation pressure $P_0 = 5$ bar) and an electric discharge ($V = 850$ V). The gating selects a time slice of the ion beam ($\Delta t = 1.25 \mu s$, i.e. the TOF of N_2O^+ through the gating unit) having a kinetic energy of 1 keV ($v_{N_2O^+} = 66$ km/s) which is compressed to $\Delta t = 80$ ns (FWHM), allowing observing the $^{14}N^{15}N^{16}O^+$ isotopologue present in natural abundance in the gaseous sample (0.8%). A resulting MRP of $R = 140$ was calculated in the time domain from $R = t_{N_2O^+} / 2\Delta t$. The bunching thus improves the MRP and the signal-to-noise by a factor 15 and 8, respectively. Our design comes with a loss of MRP of a factor 2 compared to the one reported by Dedman *et. al.* [132]. We can also see in Figure 2.42 that the bunched signal arrives faster than the unbunched one, as a result of the relative gain in velocity after using a voltage to push the slowest ions in the gated packet, which gives slightly more kinetic energy to all ions in the bunch.

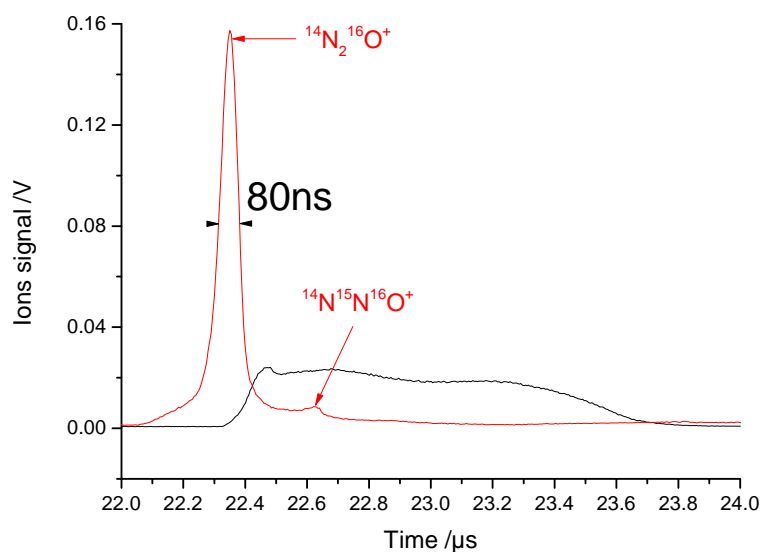


Figure 2.42 – Comparison between the N_2O^+ m/z bunched (red) and not bunched (black) spectra, the x-axis is the time of flight after the gating. The bunching and the associated improvement of the MRP allow the $^{14}\text{N}^{15}\text{N}^{16}\text{O}^+$ isotopologue to be observed.

Another advantage of this unit is the decoupling of the TOF calibration from the source initial conditions. In other words, the TOF of each ion will not change if we tune the opening time of the source or if we change the ionization voltage or the distance between the nozzle and the skimmer. It may influence the temperature and the selection of different products from the jet which will be discussed later in section 2.6.6.

Ion beam re-referencing

Following the gating and bunching, the ion beam should propagate inside the drift tube to finally reach the detector. To allow the propagation of the beam the drift tube should be maintained at the same potential of the beam, -1 kV in our case. To simplify the electrical design of the ion optics, it is more convenient to re-reference the ion bunch to ground potential. To do so, the potential switches to 0 V while the ions are inside the two electrostatic gates. In other words, by rapidly changing the potential the two cups from the beam potential to ground, ions within the two cups which have entered at the beam potential leave it at ground potential, but with unchanged kinetic energy.

SIMION[®] preliminary simulations

The voltages applied, the drift tube length and the timings are chosen according to preliminary simulations using SIMION[®] software. First we will start by representing the geometry of the unit, a SIMION[®] sectional view of the design is given in Figure 2.43:

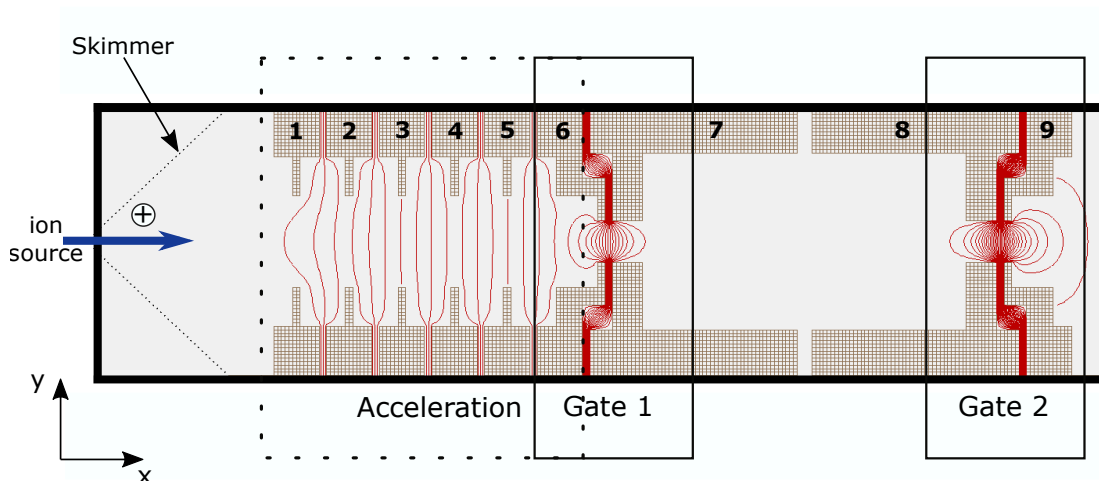


Figure 2.43 – SIMION[®] sectional view of the unit before switching. Electrodes are represented by brown squares and numbered from 1 to 9. The applied potential before and after the switching is described in the text. The red lines represent the equipotential lines. The oblique dashed line corresponds to the skimmer placed before the unit. The initial conditions of the ions are detailed in the text. The drift tube follows this unit and it is not represented in this figure.

The simulation details are given in the following:

1. **Particles initial conditions:** A beam of argon is considered, a packet of 500 particles of charge $q = 1$ and mass $m = 40$ amu, with a filled circular position distribution along the $+y$ -direction starts at $x=0$ (on the entrance of the skimmer) with a radius equal to 3 mm. The velocity of the ions is set to be equal to $v_x = 0.55$ mm/ μ s with a standard deviation $\sigma_x = 0.01$ mm/ μ s.
2. **Acceleration:** The electrodes responsible for the acceleration are numbered from 1 to 6. A gradient of potential is applied on these electrodes as represented in Table 2.8:

Number of electrode	Voltage
1	0 V
2	-200 V
3	-400 V
4	-600 V
5	-800 V
6	-1000 V

Table 2.7 – Potential applied on the acceleration’s electrodes.

- Before switching:** The two pairs of electrodes [6,7] and [8,9] form two electrostatic gates each. Before switching the first gate [6,7] should be open to allow the entrance of the ions inside the two cups formed by electrodes [7,8], so the potential of the electrode [7] is set to the same potential of electrode [6] which is equal to -1000 V. In addition the second gate [8,9] is said to be closed. Electrode [9] is grounded while electrode [8] has a potential equal to -1000 V.
- After switching:** Now that the ions are inside the two cups [7,8], the potential of these two electrodes is switched from [-1000 V,-1000 V] to [100 V,0 V]. Therefore the second gate is open and the first gate is closed. Switching electrode [7] to a positive potential [100 V] allows creating a gradient of potential inside the two cups to apply the bunching and to give a push to the ions that are a little late. Table 2.8 represents the applied voltages before switching (t_1) and after switching (t_2)

Number of electrode	Voltage t_1	Voltage t_2
7	-1000 V	0 V
8	-1000 V	0 V
9	0 V	0 V

Table 2.8 – Potential applied to the bunching electrodes.

The simulations helped to verify the working principle of the bunching and of the mass spectrometer. In the following we will show some results of various simulations. First we will start by representing in Table 2.9 the mass resolution of TOF distribution with and without bunching associated with different lengths of drift tube for different masses, with t the most probable time of flight and Δt the FWHM of the distribution.

	L = 1200 [mm]		L = 1300 [mm]	
	Bunching	No Bunching	Bunching	No Bunching
$m = 2[\text{amu}], v = 2500 [\text{m/s}]$	1857	335	3000	347
$m = 16[\text{amu}], v = 880 [\text{m/s}]$	525	111	679	114
$m = 17[\text{amu}], v = 860 [\text{m/s}]$	978	124	1557	118
$m = 18[\text{amu}], v = 830 [\text{m/s}]$	557	108	847	121
$m = 40[\text{amu}], v = 550 [\text{m/s}]$	587	69	708	72
	L = 1400 [mm]		L = 1500 [mm]	
	Bunching	No Bunching	Bunching	No Bunching
$m = 2[\text{amu}], v = 2500 [\text{m/s}]$	4233	358	3653	324
$m = 16[\text{amu}], v = 880 [\text{m/s}]$	1078	118	1446	122
$m = 17[\text{amu}], v = 860 [\text{m/s}]$	1447	73	1066	137
$m = 18[\text{amu}], v = 830 [\text{m/s}]$	1487	108	1394	130
$m = 40[\text{amu}], v = 550 [\text{m/s}]$	1371	92	453	92
	L = 1600 [mm]		L = 1700 [mm]	
	Bunching	No Bunching	Bunching	No Bunching
$m = 2[\text{amu}], v = 2500 [\text{m/s}]$	2928	356	1085	293
$m = 16[\text{amu}], v = 880 [\text{m/s}]$	1656	126	1096	130
$m = 17[\text{amu}], v = 860 [\text{m/s}]$	616	141	634	146
$m = 18[\text{amu}], v = 830 [\text{m/s}]$	1581	123	906	127
$m = 40[\text{amu}], v = 550 [\text{m/s}]$	584	79	667	79

Table 2.9 – Mass resolutions R_p of our simulated unit with and without bunching for different masses and lengths of drift tube.

As we can observe, the optimal length of the drift tube (i.e. the length that gives the highest enhancement of mass resolution with the bunching with respect to without the bunching) changes from one mass to another. Therefore, if we compare the ratio of the resolutions with and without the bunching for each mass and each length, $L = 1400$ mm seems to give the best result with a means of resolution ratio of 14.9 (for the mass of 40 amu).

An example is given in Figure 2.44 for Ar^+ ions with a length of a drift tube of 1600 mm. The length of the drift tube that was used in this thesis was 1600 mm, using what already existed in the laboratory, changing the drift tube length should be considered in future development to ensure that we are working with the highest resolution of the unit.

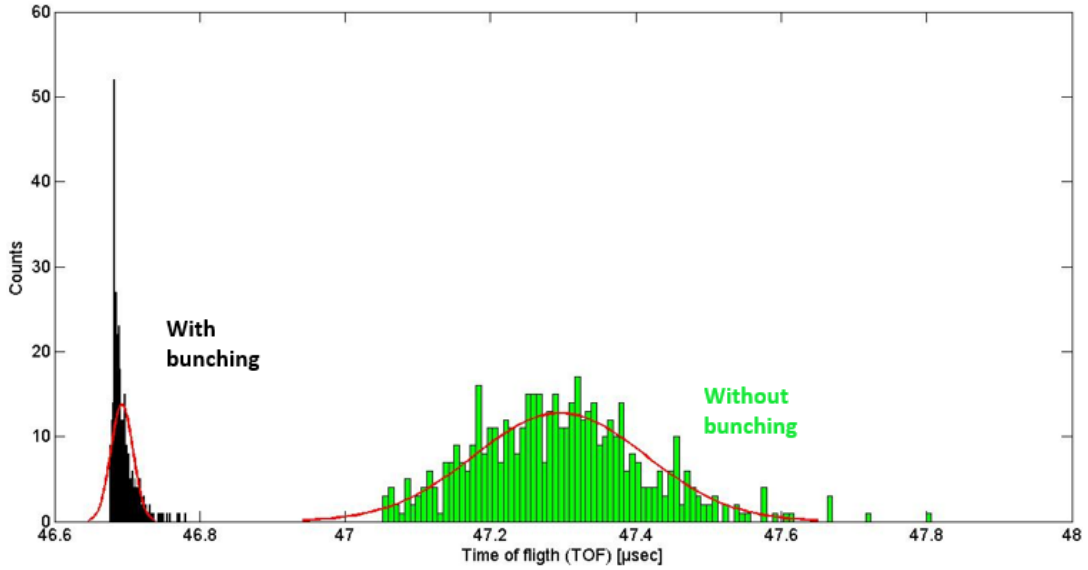


Figure 2.44 – TOF distribution of argon ions measured at the detector with bunching (black) and without bunching (green). The histograms are fitted in red with a Gaussian function enabling us to find the FWHM that can be used to find the resolution. FWHM without bunching $\approx 0.3 \mu\text{s}$. FWHM with bunching $\approx 0.03 \mu\text{s}$.

We can observe that the TOF for ions is longer without the bunching than with the bunching. That is explained by the additional energy gained by the bunched ions due to the potential gradient from 100 V to 0 V applied on the electrodes of the bunching unit. The mass resolution R can be calculated from Equation 2.17 for the two distributions. As a result, we obtain $R = 584$ and $R = 79$ with and without bunching, respectively. Therefore, the mass resolution is enhanced by a factor of 7.4 thanks to the bunching. The values of the potentials of the experimental setup and the length of the drift tube are chosen according to this preliminary simulation. The values are then adjusted in real time because it must be taken into account that SIMION[®] considers instantaneous switching which is not the case in our apparatus.

2.4.4 Electrostatic lens

An electrostatic lens is a system that assists the transport of charged particles [133]. It is analogous to an optical lens which can guide and focus the light in an optical instrument, the electrostatic lens is used to focus the charged particles and to ensure a maximum overlapping of the ionic beam and the laser for an efficient photodissociation. Different types of ion's guiding lenses exist. In this thesis a cylindrical electrostatic lens, also known as einzel lens, was used. It is composed of three electrodes with the same design as those used for the acceleration as shown in Figure 2.45. Thus, having three electrodes, the middle one is polarized using a voltage of 650 V and the two other electrodes are grounded. The electrodes are separated by ceramic insulators. This configuration gives rise to a symmetric lens (which is the case of a lens that does not change the energy of the beam [134]).

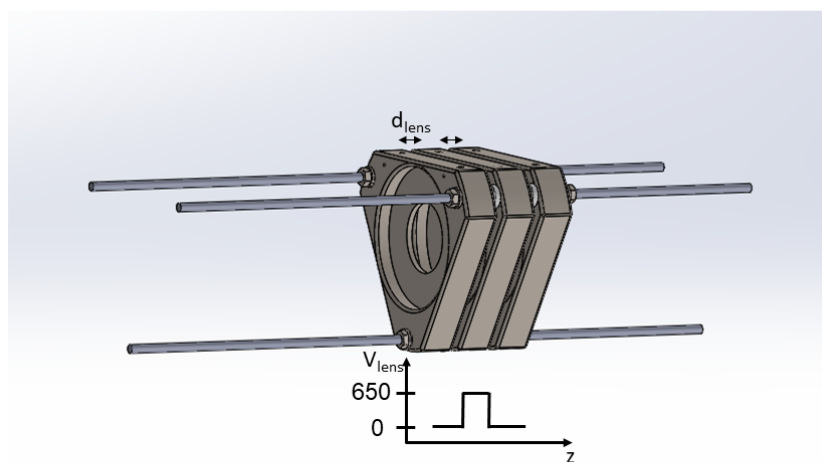


Figure 2.45 – The Solidworks© generated figure of the electrostatic lens used in the setup and the corresponding applied voltages.

2.4.5 Two dimensional deflector

Beam alignment

A proper beam alignment requires adding to the ion optics a 2D deflector to keep a good alignment of the propagation of the ions on the axis of the instrument. It is formed by two pairs of steering plates made of aluminium. On each pair, a voltage is applied to align vertically and horizontally the ion beam. In fact one of the plates of each pair is polarized and the corresponding applied voltage could be tuned, the second plate is grounded. The deflector conception is shown in Figure 2.46.

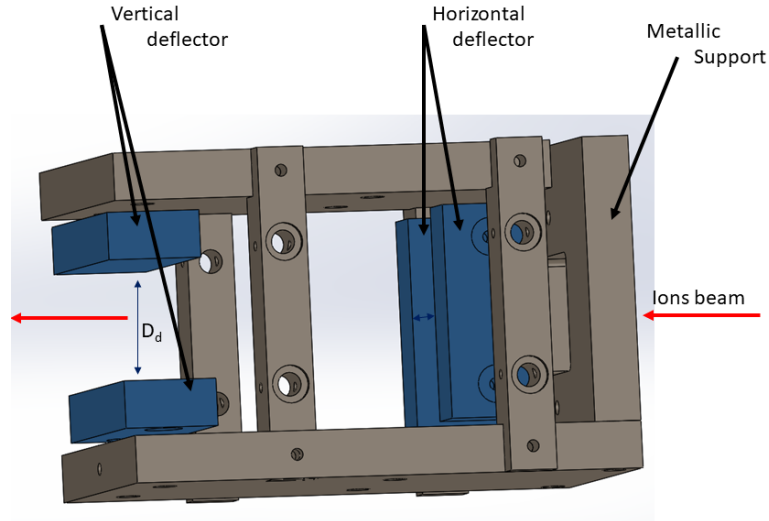


Figure 2.46 – The Solidworks© generated figure of the deflector. The blue plates are the active electrodes one of them is grounded and the second one is polarized. The voltage used is tuned during the experiment for a maximum signal.

To understand how the ions are deflected, we assume a two-dimensional deflector as illustrated in Figure 2.47.

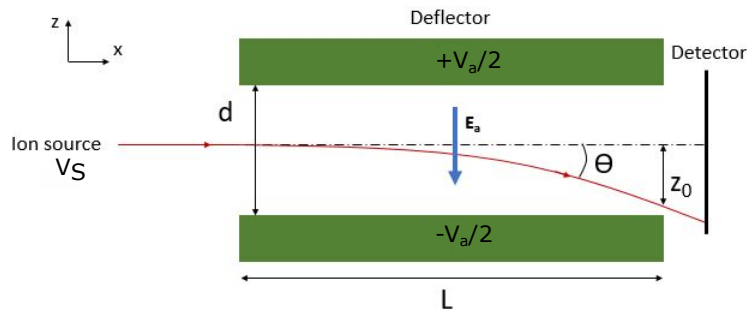


Figure 2.47 – Schematic representation of the deflector (left) that is composed of two parallel metal plates of length L between which a potential difference V_a is applied. The plates are separated by a distance d . Ions come from a source with an initial potential of V_s and the difference of potential V_a deflects their trajectory of an angle θ that gives a deflection vertical distance of z_0 .

The kinetic energy of an ion of a charge q at potential V_s is given by $E_k = \frac{1}{2}mv_x^2 = -qV_s$. v_x is the velocity of the ions in the x -direction having a mass m . Between the two electrodes the ions are accelerated in the z direction by the influence of the electric field E_a . Thus we can write :

$$m \frac{dv_z}{dt} = qE_a \quad (2.20)$$

By isolating dv_z and after integration of the Equation 2.20 we obtain the velocity v_z as following in the Equation 2.21:

$$v_z = \frac{q}{m} E_a t \quad (2.21)$$

Then in order to obtain the angle of deflection θ we replace time by $t = \frac{x}{v_x}$, so we can write:

$$\tan(\theta) = \frac{v_z}{v_x} = \frac{V_a}{2V_s} \frac{L}{D} \quad (2.22)$$

Therefore, the voltages applied to the plates and their dimensions are the factors that influence the direction of the ions and so the fact the ions can stay aligned along the instrument axis.

In this thesis the dimensions of the deflector are $L = 20$ mm and $D_d = 26$ mm and the ions have a positive charge. For example, for a deflection of 1 degree the energy of the particles before entering the potential zone is equal to 1 keV, thus the difference of potential which needs to be applied between the plates is $V_a = 480$ eV.

The first mass selection of ions

The same deflector is able to perform a first mass selection. In fact, by pulsing the potential value of the electrode of one of the pairs, the non-selected ions change direction and collide with the chamber. The mass selection is performed by time-gated deflection using short voltage pulses (typically $\simeq 1 \mu\text{s}$). 70 V is found to be sufficient to deviate the undesirable ions using a Behlke push pull high voltage (HV) switch (risetime of 20 ns) and the multi-channel digital delay generator. A second pair of plates ensures proper vertical alignment. A comparison of the full m/z spectrum obtained from pure N_2O gas injection with that measured with mass selection applied to select only N_2O^+ is presented in Figure 2.48.

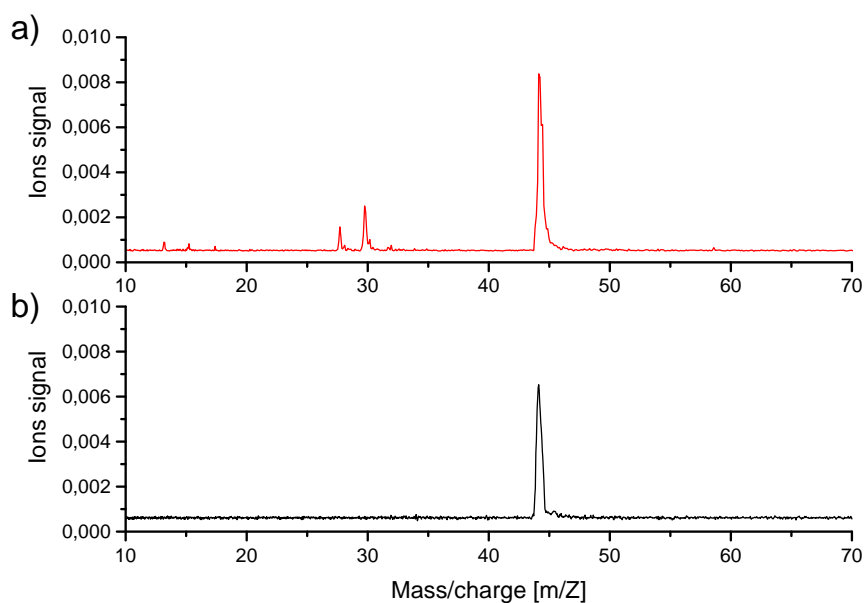


Figure 2.48 – a) The m/z spectrum measured with continuous deflection from N_2O gas injection and electric discharge (in red) is compared with b) the spectrum measured with a pulsed deflection of $1 \mu\text{s}$ to select only N_2O^+ (in black).

2.4.6 Pumping capacity

Skimmer

A skimmer is used in order to extract the molecules from the isentropic core of the free jet and inject them into a secondary chamber maintained at very low pressure. A detailed study of the effect of the skimmer geometry on the jet and on the extracted gas can be found in the literature [116]. Briefly, the skimmer should be long and thin enough in order to reduce or eliminate a reverse flow and which could interfere with the jet leading to the destruction of the expansion and heating up the gas. The external angle of the skimmer is also an important parameter to take into consideration. The angle should be calculated taking into account the Mach number of the flow. The ideal angle corresponds to the case where the oblique shock waves (the formation of which is induced by the presence of the skimmer) are attached to the lips of the skimmer. An overestimated angle leads to the detachment of the oblique wave. As a consequence, a detached shock wave is located upstream of the opening of the skimmer, causing the gas to heat up before it enters the skimmer. The internal angle showed no importance for low reservoir pressure. The ionized gas pulse expands towards a conical skimmer of 2 mm diameter. The skimmer allows the operator to select spatially part of the jet. Moreover the vacuum quality is ensured by using three turbo pumps (Pfeiffer ATH 2300M, Balzers 4306, Pfeiffer HiPace 700 Plus) and two stages of differential pumping using the skimmer and a pumping tube indexed as items (2) and (6) in Figure 2.1, respectively, to finally reach 10^{-7} mbar in the area of the interaction of the ion beam with the laser, the energy analyser and the MCP detector. This allows also to minimize the ion recombination or any warming up by colliding with the residual gas. A solidworks design of the skimmer and a detailed dimensions of skimmer are detailed in Figure 2.49

Differential pumping tube

A differential pumping tube is added before the interaction region. The main purpose of this tube is to maintain a constant low vacuum of 10^{-7} mbar inside the chamber. The dimensions of the tube are chosen in a way to ensure an optimum conductivity. the conductivity depends on the radius (Ra) and the length of the tube (L). The Poiseuille equation, is a physical law that gives the pressure drop in an incompressible and Newtonian fluid as following:

$$\Delta P = \frac{8\mu L Q_V}{\pi R a^4} \quad (2.23)$$

in which Δp is the pressure difference between the two ends, μ is the dynamic viscosity and Q_V is the volumetric flow rate. Indeed, in order to make the tube more effective, using a small radius is the solution. But, using a small radius limits the radius of transmission of the ionic beam that is why the solution is to use a longer tube of a length equal to $L = 50$ mm and a radius of $Ra = 8$ mm as shown in Figure 2.50

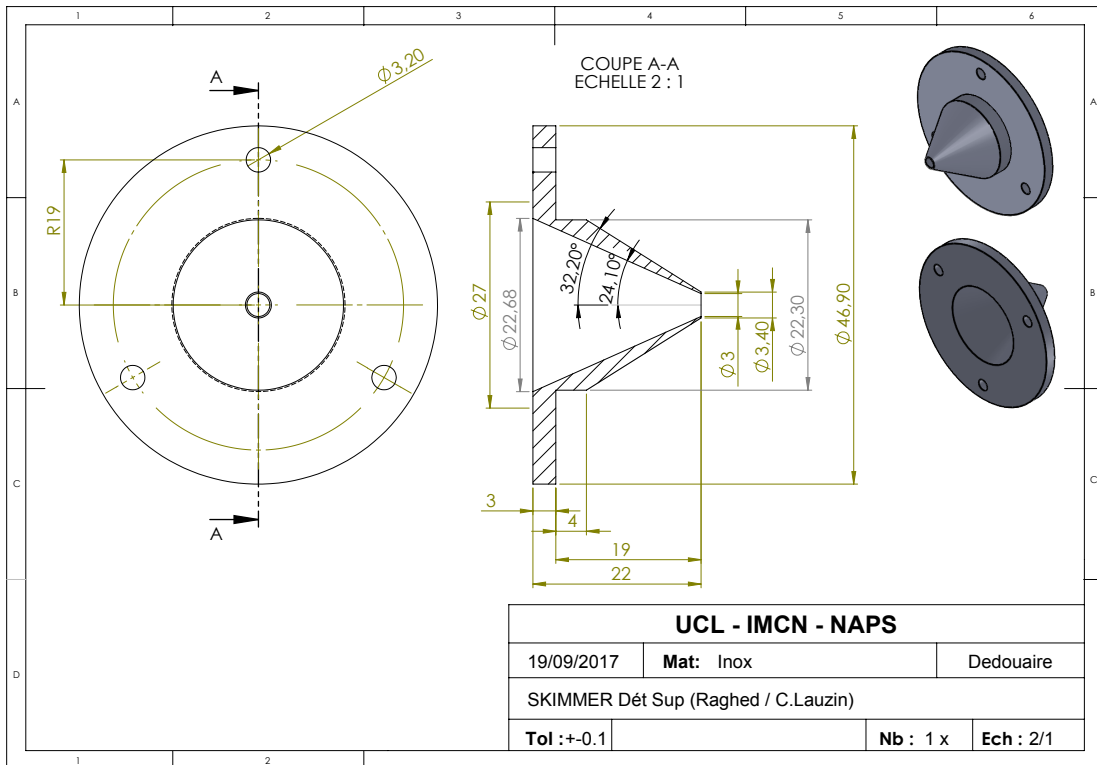


Figure 2.49 – The solidworks dimensions details of the skimmer.

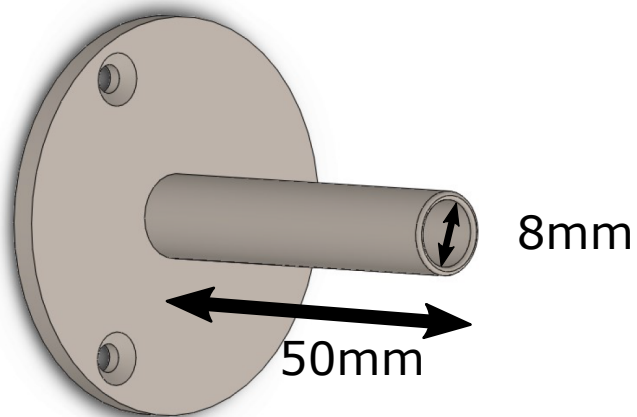


Figure 2.50 – Drawing representation of the differential pumping tube along with its dimensions.

2.5 Results of mass spectrometry

STARGate instrument is designed to produce different ionic species, negatively or positively charged. First we show that the production of different species can be controlled by changing different parameters, like the back-pressure, the gas mixture, the discharge voltage and the distance between the nozzle and the skimmer. Then, we will discuss the method used to measure experimentally the beam divergence. Finally, in section 2.5.3 we will discuss how each parameter influences the production of different ions.

2.5.1 Mean free path

The mean free path introduced in the first chapter is an important parameter. In fact, using the mean free path formula (Equation 1.7) we can estimate the percentage of the ions that will arrive at the detector. The probability ($Pr(n, l, \sigma)$) so the number of ions n_i arrives at the detector located at a distance l is equal to :

$$Pr(n_i, l, \sigma) = e^{-\sigma n_i l} \quad (2.24)$$

It is assumed that n_i for argon is equal to 2.7×10^{12} particles/mbar. The pressure in our drift tube is equal to 5×10^{-6} mbar so the number of ions is assumed to be equal to $n_i = 5.4 \times 10^{10}$ particles. σ is the cross-section, for an argon atom $\sigma = 6.33 \times 10^{-16}$ cm² and the length of the drift tube is equal $l \approx 2$ m. We obtain a probability of $Prob = 0.99$. We can conclude that the pressure in the chamber is low enough to have a good transmission of the particles through the drift tube to reach the detector. Figure 2.51 shows the logarithmic plot considering argon atoms for different chamber pressures.

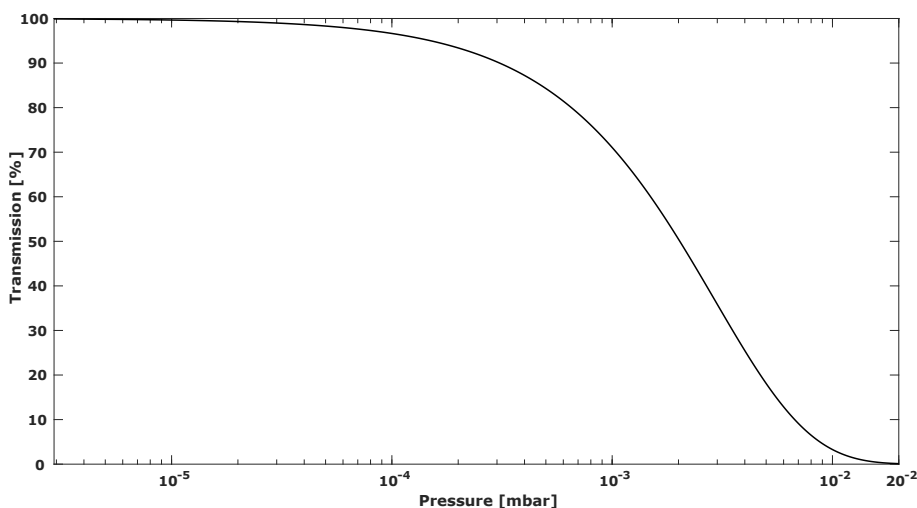


Figure 2.51 – The logarithmic plot of the transmission probability of the particles for a distance $l = 2$ m when considering argon ions for different chamber pressures.

2.5.2 Beam divergence

The ion beam diameter was evaluated by limiting the area of detection with a hole and placing the detector at the laser-beam interaction location. The deconvolution of the surface obtained by integrating the ion signal and deflecting the ion beam in the perpendicular directions (x and y) allowed to estimate the diameter to be equal to 10 ± 1 mm as shown in Figure 2.52. The differential pumping tube (8 mm)(section 2.4.6) placed just before the laser interaction area thus limits the ion beam diameter. This ion beam characterization was achieved with the first acceleration scheme. We could still be losing a small fraction of the ions at the tube locations but it did not prevent the observation of cold ions neither of a sufficiently large S/N ratio. In addition, the spatial size perpendicular to the TOF axis is optimized in real time by monitoring the ion signal and tuning the voltage of the electrostatic lens. Future improvements of the set-up could include a slightly larger tube diameter and/or the placement of the tube before the deflector and/or the improvement of the pumping capacity.

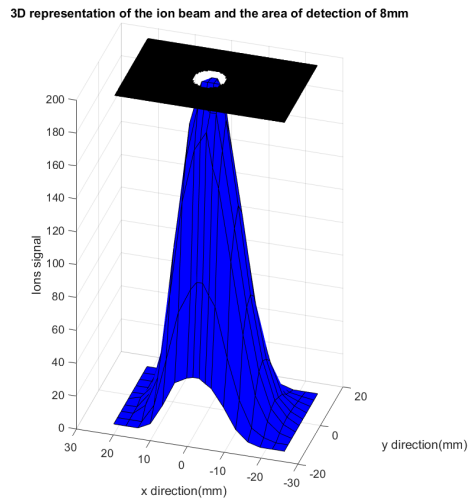


Figure 2.52 – The results of the test carried out to measure the beam spatial diameter. It is an important parameter to evaluate the overlap between the laser and the ion beam. The signal was recorded for different voltages of the deflector that made possible the scanning of the ionic beam.

2.5.3 Mass spectrometric analysis.

A supersonic expansion coupled to one of the ionization methods already explained in section 2.3.2, could give different products depending on many parameters of the source and initial conditions.

Pressure and nozzle diameter influence

The first two parameters are back-pressure and nozzle diameter. In fact, as explained by Morse [79], the total number of binary collisions occurring during the expansion is proportional to $P_0 D$ which could be a direct measurement of cooling. Meanwhile, the total number of three body collisions occurring during the expansion is proportional to $P_0^2 D$. Thus, the higher the pressure is, the more clustering effect could take place. We can choose to maintain a constant value of pressure, thus a larger diameter will mean more cooling and thus the promotion of chemistry and reactions could also give clusters or other complexes. Morse suggests that to enhance the cluster production the pressure should be increased while the diameter of the nozzle is maintained constant. We tried to verify the effect of these two parameters on the mass spectra and we obtained two results. The first result shows two spectra, both measured using a mixture of argon bubbling in water to carry a certain percentage of H_2O . The back-pressure of the first measurement was 2 bar and 3 bar for the second measurement. We can see in Figure 2.53, that an increase of pressure from 2 bar to 3 bar enhanced the production of larger masses of water protonated clusters. Not surprisingly, we observe that the monomer has almost the lowest percentage relative to higher masses for a high stagnation pressure. For both conditions the production of protonated water clusters with a number n between 4 and 6 is the most abundant in these source conditions.

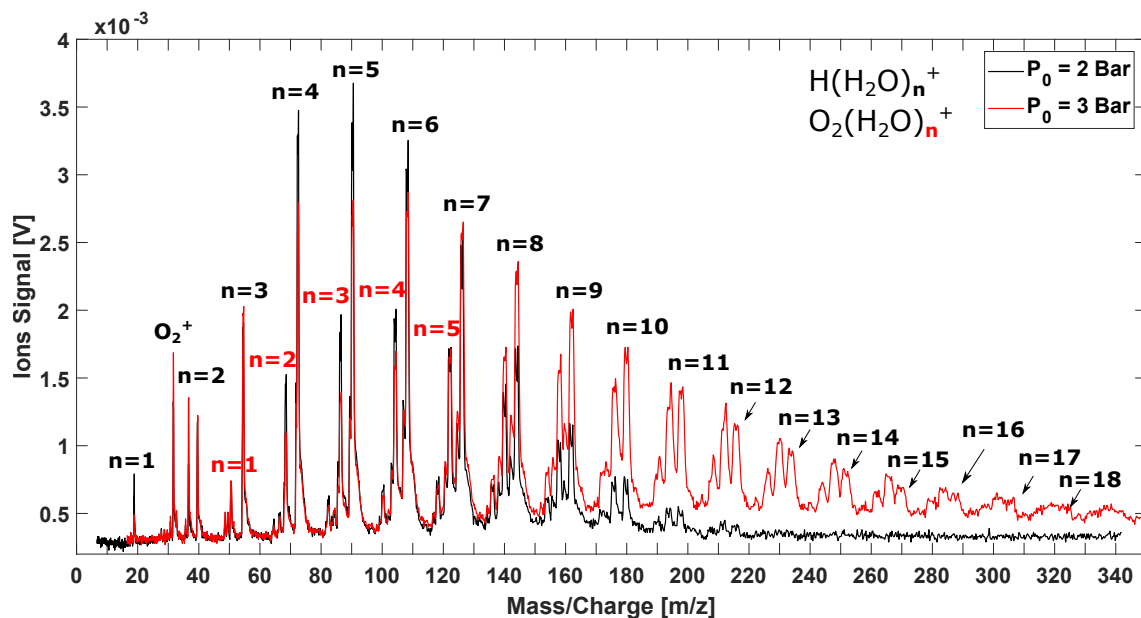


Figure 2.53 – A plot to show the difference between the products of a jet with a back-pressure equal to 2 bar (black) and 3 bar (red). The chamber pressure is maintained at 5×10^{-5} mbar, The discharge voltage is equal to -350 V.

Another experiment is done, but this time to characterize the nozzle diameter effect on the products of the expansion. By using the same mixture, the minimum voltage is used for the discharge for both measurement and by doing a measurement for two different diameters, the result is shown in Figure 2.54. As we can see from Figure 2.54, the higher the diameter, the higher the signal of the bigger masses

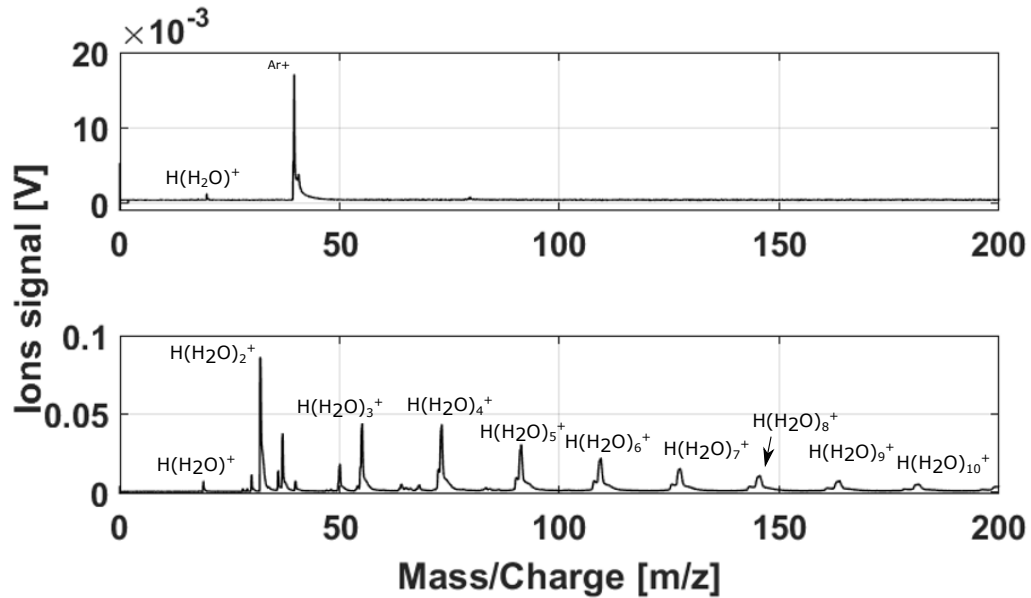


Figure 2.54 – Two plots showing on top the result of a jet using a nozzle of a diameter of 0.5 mm and on the bottom the result using a larger diameter of 1 mm.

(clusters/complexes). The most intense peak is the one of argon in the spectrum on top. A small peak at the mass of 80 m/z may correspond to the dimer of argon produced in small quantities. On the other hand, the formation of water clusters increased using a larger diameter.

Applied voltage

The voltage of the electric discharge has a direct influence on the production of clusters. As shown in Figure 2.55 the higher the voltage is (with no current limitation) the higher will be the current and the discharge will therefore heat up the source. In addition, the higher is the voltage, the higher is the energy of the electrons responsible for the ionization, which leads in some cases to the dissociation of the molecules/complexes. We observe better results in terms of clusters production using the lowest possible discharge voltage and a limitation of the discharge current. I have to mention that the discharge needs some time to stabilise. A higher voltage is required to ignite the discharge, then the user could observe in real time the products on the time-of-flight spectrum measured by the oscilloscope and tune the voltage accordingly. Higher voltage can be required, in particular: if helium is used as carrier gas instead of

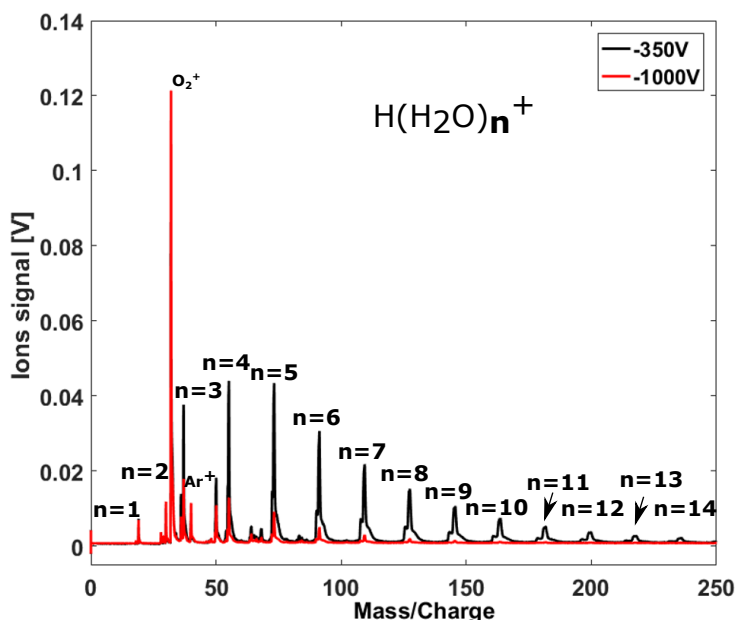


Figure 2.55 – Results of the test using two extreme voltage values. The result of applying a voltage of -350 V is shown in black and the result for applying a voltage of -1000 V is shown in red. A jet of Argon bubbling in water was used for a back-pressure of 3 Bar, a chamber pressure of 5×10^{-5} mbar and a nozzle diameter of 500 μm .

argon, the ionization potential of helium being higher than the one of argon, the energy of the electrons to ionize the gas, and hence the discharge voltage, should be higher. The result concerning the electron gun follows the same logic as the one of the electric discharge.

Seeding gas

As already explained in the first chapter, the seeding gas has a great effect on the products that result from the source. In order to verify the statement, an experimental measurement was carried out using a jet of a mixture of N_2O in argon, then in helium then a jet of pure N_2O . The result is shown in Figure 2.56 The figure shows that the seeding gas plays an important role and it could make great difference if

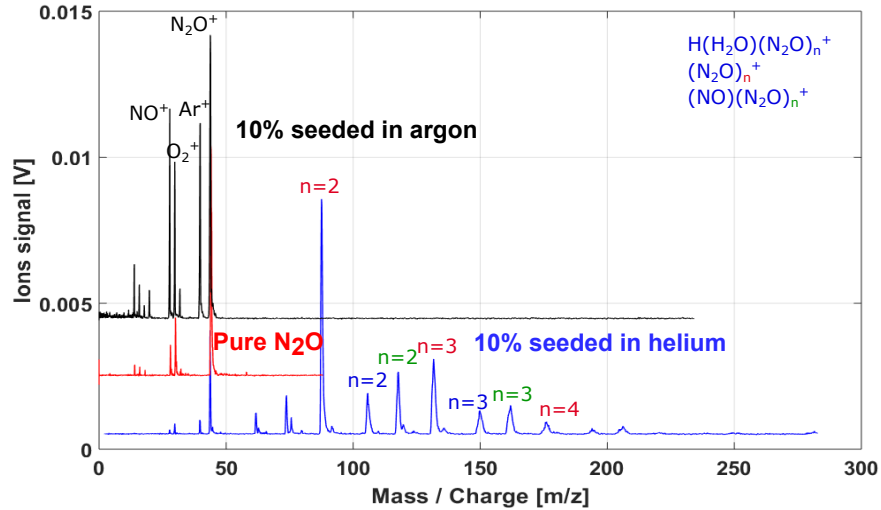


Figure 2.56 – The result of using a jet of 10% of N_2O seeded in argon (black), a jet of pure N_2O red and a jet of 10% of N_2O seeded in helium blue. Back-pressure = 3 bar, chamber pressure = 5×10^{-5} mbar and the diameter is about $500 \mu\text{m}$. The discharge voltage is equal to -350 V for the case of argon as a seeding gas and pure N_2O , and it is equal to -450 V in the case of helium as a seeding gas.

the production of clusters is desired or if the production of clusters is not desired. The decision depends on the species that we want to study in the end.

Distance nozzle-skimmer

Another important parameter that should not be neglected, is the distance between the nozzle and the skimmer. In the case of a supersonic expansion, the temperature of the jet evolves, decreasing with the increase of the distance from the nozzle (before the shock waves that heat up the jet again due to the large number of collisions and the repression of the jet). Therefore, it is believed that the products will change if the distance of the probing by the skimmer is changed. In later sections we show the dependence of the skimmer position on the rotational temperature of the molecules (section 2.6.6). A test was done to confirm the statement by measuring the mass spectrum of N_2O seeded in Helium for different nozzle-skimmer distances, and the results are shown in Figure 2.57.

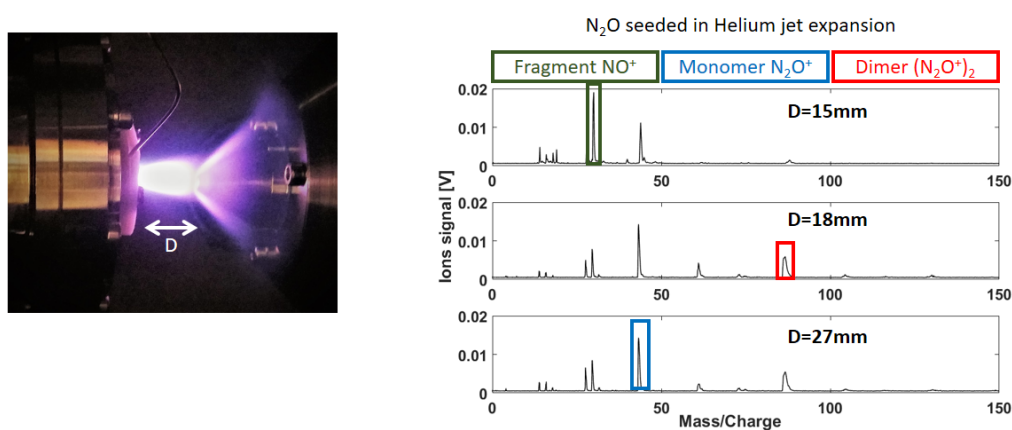


Figure 2.57 – The influence of changing the distance nozzle-skimmer on the products of a jet of N_2O seeded in Helium. The shorter distances (15 mm) enhance the production of lower masses (NO^+), while longer distances enhance the production of bigger masses (N_2O^+)/ $(\text{N}_2\text{O}^+)_2$.

We conclude from this last test that the distance nozzle-skimmer is important and one needs to control this distance to control the temperature and the production percentage of the desired charged complex/cluster. Other parameters could play an important role but will not be tested in this thesis, those are the nozzle temperature or the post ionization that could be done in the region behind the skimmer.

Production of clusters, cations and anions

large clusters of $\text{H}(\text{H}_2\text{O})_n^+$ up to $n = 38$ are depicted in the panel a). These complexes were produced by the expansion of argon bubbling in a water reservoir using a nozzle diameter of 1.5 mm, and are presented in Figure 2.58. This series stops at $n = 38$ but since the detection efficiency decreases with the mass (lower velocities), larger clusters could be present. Note that the MCP front was negatively biased to -2.1 kV, providing up to 3.1 keV kinetic energy at impact on the MCP. In panel b) we show the formation of pure N_2O_n^+ and mixed $[\text{H}_2\text{O}_m - \text{N}_2\text{O}_n]^+$ hydrated clusters formed from N_2O and water contamination in the gas injection pipes. The first steps of nucleation are clearly visible but also the competition between the different routes of nucleation. Anions have also been measured by switching the polarity of the ion optics using the electron gun for ionization of N_2O^+ and replacing the MCP stack with a channel electron multiplier (Sjuts KBL 25 RS) with its funnel at ground potential, and are presented in panel c) of Figure 2.58. These three panels illustrate the versatility of STARGATE in terms of molecular targets that could be studied. It also provides evidence of an efficient cooling which will be further demonstrated in Section 2.6.6.

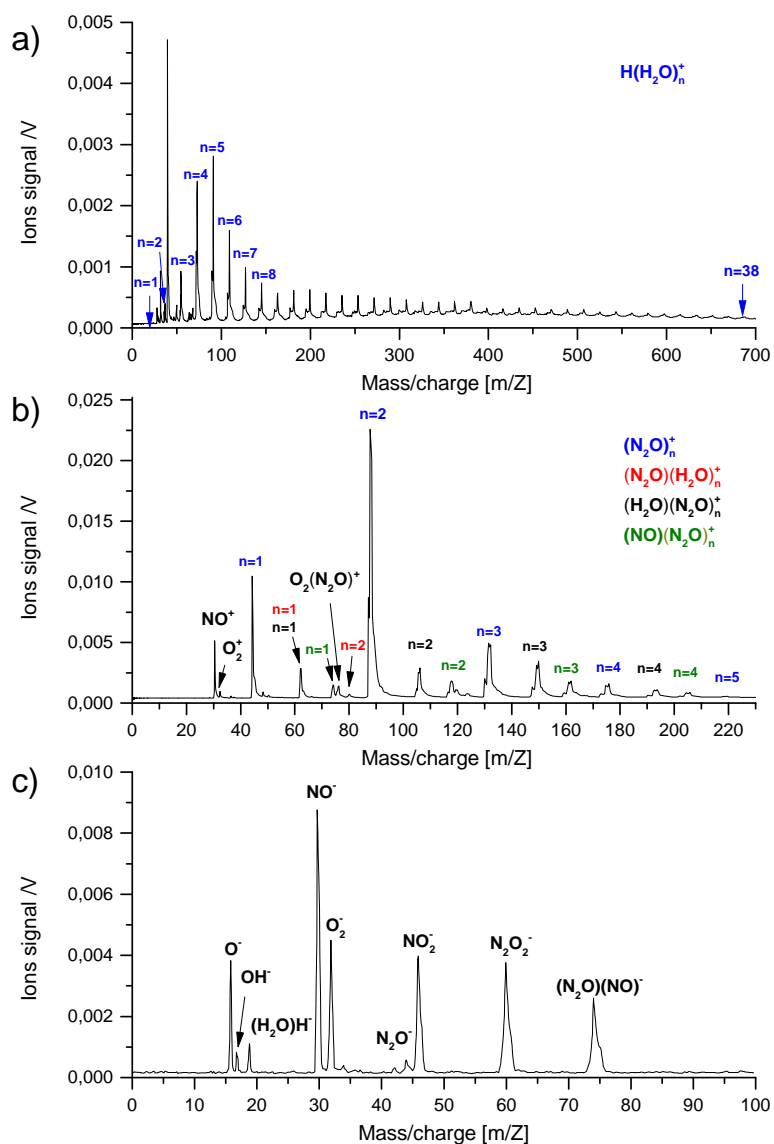


Figure 2.58 – a) Production of $\text{H}(\text{H}_2\text{O})_n^+$ ionic clusters up to $n = 38$ from argon bubbling in water with a backing pressure of 2 bar using a nozzle of 1.5 mm of diameter with an average pressure of 10^{-5} mbar in the jet chamber and the valve operating at 30 Hz. b) Production of $(\text{N}_2\text{O})_n^+$ ($n = 1 - 5$), $(\text{N}_2\text{O})(\text{H}_2\text{O})_n^+$ ($n = 1 - 2$), $(\text{H}_2\text{O})(\text{N}_2\text{O})_n^+$ ($n = 1 - 4$) and $(\text{NO})(\text{N}_2\text{O})_n^+$ ($n = 1 - 4$) ionic clusters from N_2O and residual water in the gas line. c) Production of anions using the electron gun with N_2O at a backing pressure of 3 bar.

Other interesting spectra were measured using different mixtures, for example, the spectra of a mixture of CO₂ seeded in helium and bubbling in water for a back-pressure of 4 bar and a discharge voltage equal to 400 V. The result is shown in Figure 2.59. The mass spectrum indicates that these conditions led to the formation of a large number of mixed clusters while injecting carbon dioxide. More attention is required to this result if a future target containing CO₂ is studied.

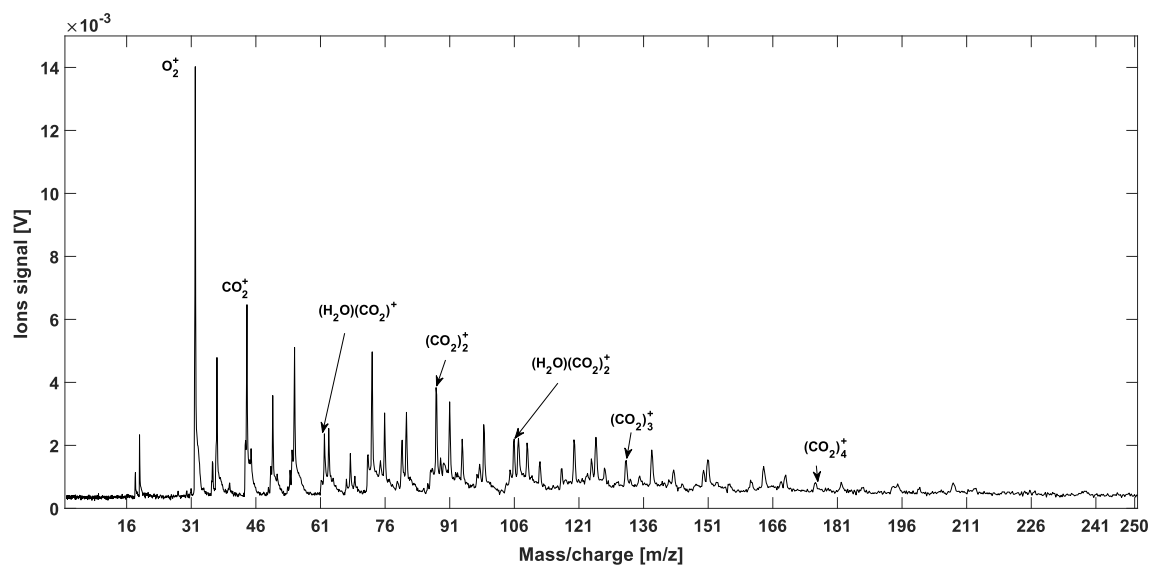


Figure 2.59 – The production of $[(\text{CO}_2)\cdot(\text{H}_2\text{O})]^+$, $(\text{CO}_2)_2^+$ and other interesting complexes using a jet of CO₂ seeded in helium.

2.6 Photodissociation spectroscopy

The guiding principle of photodissociation spectroscopy is that a spectrum is obtained by the measurement of the photofragment signal as a function of exciting wavelength [135]. Photodissociation spectroscopy is an action spectroscopy scheme. The action in this case is the dissociation of the ion by the photon. The photon needs then to be sufficiently energetic. In the UV/Vis region, absorption of a single photon can be sufficient to induce dissociation. This method takes then advantage of the sensitivity of the mass spectrometry techniques to record ion signal. Different mechanisms can occur as shown in figure 2.60:

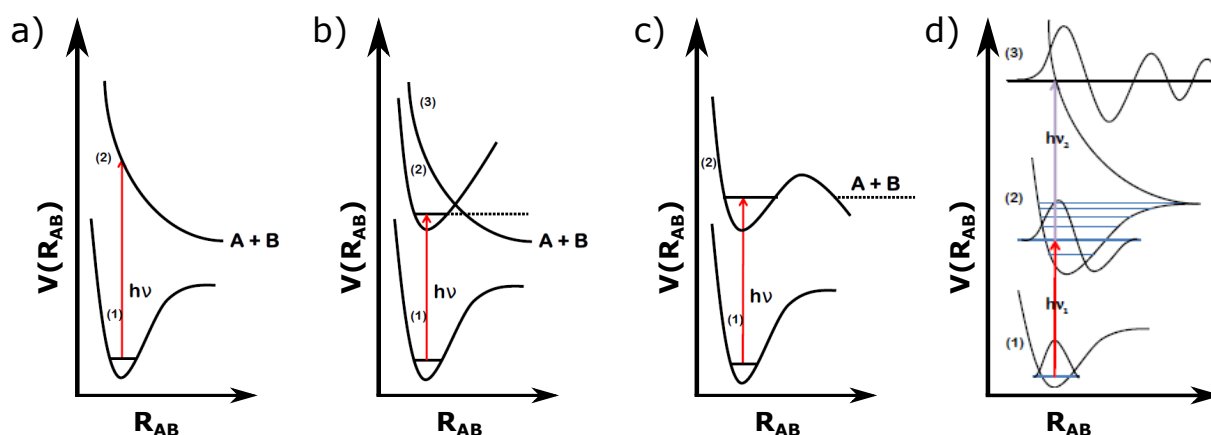


Figure 2.60 – Schematic representation of electronic dissociation through different mechanisms: a) direct dissociation, b) Herzberg type I predissociation c) Herzberg type II predissociation d) two photon dissociation process. This Figure is adapted from reference [136].

On the left of figure 2.60, panel a), the absorption of a photon in the UV/Vis couples the lower state to a dissociative state giving a broad unresolved spectrum. Panel b) represents a predissociation mechanism known as Herzberg type I predissociation. Indeed it corresponds to the case of the electronic spectrum of N_2O^+ observed in this thesis shown later in this section. A non-radiative transition occurs from state (2) to (3) which is a dissociative state. Another type of predissociation is shown in panel c) which corresponds to Herzberg type II predissociation. The molecule AB lies on the upper state higher than the dissociation threshold but a barrier exists. The molecule overcomes the barrier via tunnelling or redistribution of internal vibration energy. Panel d) corresponds to a schematic for a two-photon dissociation process. The energy transferred to the molecule by the first photon undergoes some form of redistribution before the arrival of the second photon. The second photon is then absorbed and initiates the dissociation. A direct transition from state (1) to state (3) would result in a unresolved broad band spectrum, using state (2) as an intermediate allows mapping the ro-vibrational levels of state (2) resulting in a more detailed spectrum [136].

Dissociation spectroscopy by multiple infrared photons has been extensively used as well to characterize vibrational transitions in a wide variety of molecules and ions [137]. In fact, when the laser photon is resonant with an IR transition of some mode of the ion, a photon absorption event will excite the ion to an upper state, if the ion is reasonably large (ei : $\text{H}_2\text{O}-\text{CO}_2^+$) rapid intramolecular vibrational relaxation

(IVR) disperses this energy among several low-frequency modes. A second photon can then excite again the same mode, and after a number of such absorptions with sufficient laser power, the ion will undergo dissociation. One IR photon dissociation (~ 0.1 eV) is sufficient to induce photodissociation in some cases of intrinsically weakly bounded ions [137]. One of the biggest advantages of UV/Vis/IR photodissociation spectroscopy lies in the fact that it is an essentially background free technique. Fragments are formed only when an absorption event occurs. In this work we optimised the instrument using N_2O^+ following the photodissociation mechanism illustrated in Figure 2.60. In the future the set-up will be considered to study ionic van der Waals complexes such as $\text{H}_2\text{O}-\text{CO}_2^+$ following the IRPD (single photon) photodissociation mechanism as illustrated in Figure 2.61.

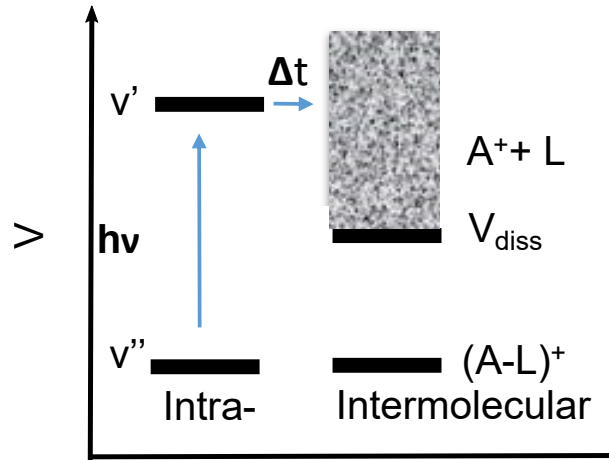


Figure 2.61 – Schematic representation of infrared dissociation. One or more infrared photon are absorbed exciting the ion to an upper state, after a certain duration the energy is redistributed and if this energy is higher than the binding energy, the complex is dissociated.

Practically, as mentioned before, photodissociation spectroscopy consists of integrating the ionic fragments signal generated by light absorption of a mass selected ion as a function of the wavelength of a light source, in our case a pulsed dye laser (30 Hz, 0.6 mJ/pulse and 5 ns duration from Continuum ND 6000) pumped by a Nd:YAG laser (Continuum Powerlite Precision II). For this kind of measurements to be background free, a selection on the ions has to be performed before and after interaction with the laser. In our case, we perform a mass selection, a kinetic energy shift at the location of the ion-laser interaction and an energy analysis. In section 2.4.5 we already detailed the pulsed deflection unit we implemented for the first mass selection. Section 2.6.1 presents the selective energy shifts of the ions produced by the photodissociation and the associated cylindrical energy analyser; and in section 2.6.2 we check the spatial and temporal overlap of the laser with the ions.

2.6.1 Kinetic energy selection

While the first mass selection selects species before the interaction with the laser, other species can result from the collisions of the selected ions with the residual gas in the drift tube. A second selection is performed by a 90° electrostatic deflector after the laser interaction to select the fragments of the

photodissociation and to exclude the remaining parent ions and fragments produced by collisions with residual gas. A double-focusing 90° electrostatic deflector adapted from the design of H. Kreckel *et al.* [138] has been implemented for the selection of the fragments depending on their kinetic energy. The deflector design is presented in Figure 2.62. It consists of two cylindrical electrodes which could be polarized and serve to deflect the trajectory of ions depending on the difference of potential that is applied on them. The potential difference ΔV that is necessary to guide an ion with energy E_{beam} on the designated center radius R_0 between the cylindrical electrodes can be calculated by equating the electrostatic force and the centrifugal force as :

$$\Delta V = \frac{2E_{beam}}{Ra_0} \times (Ra_2 - Ra_1) \quad (2.25)$$

In this equation $(Ra_2 - Ra_1)$ is the distance that separates the two electrodes of the deflector having respectively the two curvature radius $Ra_1 = 107.5$ mm and $Ra_2 = 89.5$ mm. An electric potential is additionally applied to the laser interaction region by a large cylindrical electrode surrounded by grounded electrodes. This bias cell represented in the left corner of Figure 2.62 a) aims at increasing the kinetic energy difference between fragments of the photodissociation process, and other fragments or parent molecules.

For example, if N_2O^+ has an energy of 1 keV before the bias cell, the fragments NO^+ produced by collisions in the TOF have the same velocity as N_2O^+ but a different mass, and their kinetic energy can be calculated to be 680 eV. By polarizing the central electrode (-250 V) of the electrostatic lens surrounding the laser interaction area (Figure 2.62 b)), the photodissociation fragments NO^+ are produced from accelerated N_2O^+ having an energy around 1250 eV. With an initial kinetic energy of 852 eV, these fragments are decelerated by leaving the electrostatic lens area to reach a kinetic energy of 602 eV in the 90° electrostatic deflector. This resulting energy is therefore lower than that of the fragments NO^+ (680 eV) generated outside the interaction region. These fragments can thus be differentiated by tuning the voltages applied on the 90° deflector accordingly. In Figure 2.62 b), trajectories of N_2O^+ , NO^+ produced by collisions outside the bias cell and NO^+ photofragments are represented in blue, red and black, respectively. One can notice in this simulation made using the SIMION® software that all species do not reach the detector except the NO^+ photofragments. We noticed that a similar effect can be observed by switching the voltage to +250 V and tuning the voltage applied on the deflector accordingly.

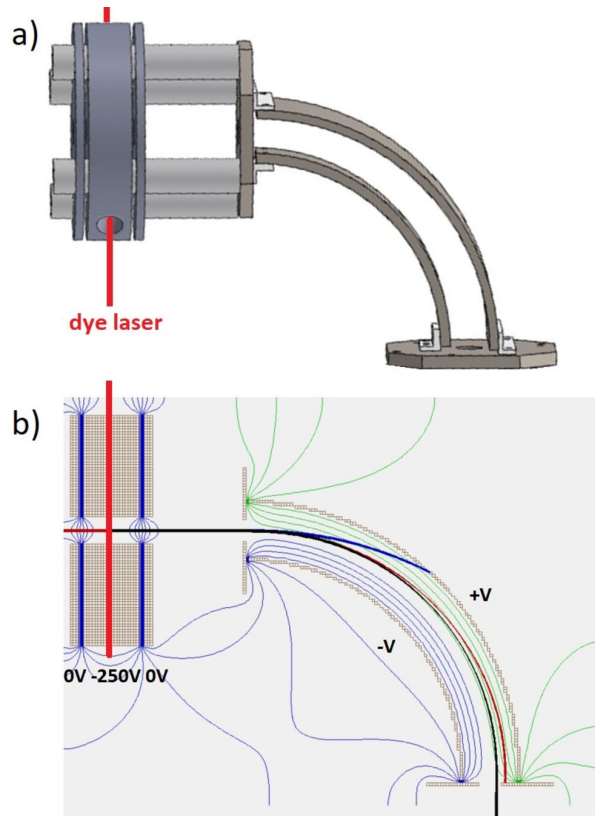


Figure 2.62 – a) The 90° electrostatic deflector is represented with the bias cell surrounding the laser interaction region. b) SIMION[®] simulation performed for the selection of the NO⁺ photo-fragments ($m = 30$ uma, $E_{NO^+} = 602$ eV) represented in black, by excluding the non-dissociated N₂O⁺ parent ions having a larger kinetic energy represented in blue ($m = 44$ uma, $E_{N_2O^+} = 1$ keV) and NO⁺ fragments resulting from collisions with the neutral residual gas in the drift tube represented in red ($m = 30$ uma, $E_{NO^+} = 680$ eV). The positive and negative electric equipotential lines are represented in green and blue, respectively, with an increment of 30 V. The voltages applied in the simulation are -250 V for the middle electrode and $\pm V = \pm 135$ V for each plate of the deflector. The initial energy of the photo-fragments is $E_{NO^+} = E_{N_2O^+} \times m_{NO^+}/m_{N_2O^+} = 852$ eV with $E_{N_2O^+} = 1250$ eV in the middle of the electrostatic field generated by the electrostatic lens.

Measurement of the energy spread of the beam

The 90° deflector is also able to measure the energy spread of the ionic beam. In fact, due to the influence of different values of the applied electric field while bunching and gating, the beam is assumed to have a certain distribution of energy. In order to find and calculate this spread and as explained before, the voltage applied to the two cylindrical electrodes can be used. The voltage applied on the two electrodes controls the ionic kinetic energy that is allowed to go through the deflector and to be finally detected (Equation 2.25). The method consists of scanning a certain range of voltages on the deflector while monitoring the signal of the ions on the detector. The result is shown in Figure 2.63

Using equation 2.25 and the voltages that we measured experimentally we can find the energy spread of the beam as shown in Figure 2.64 that was calculated to be 100 eV.

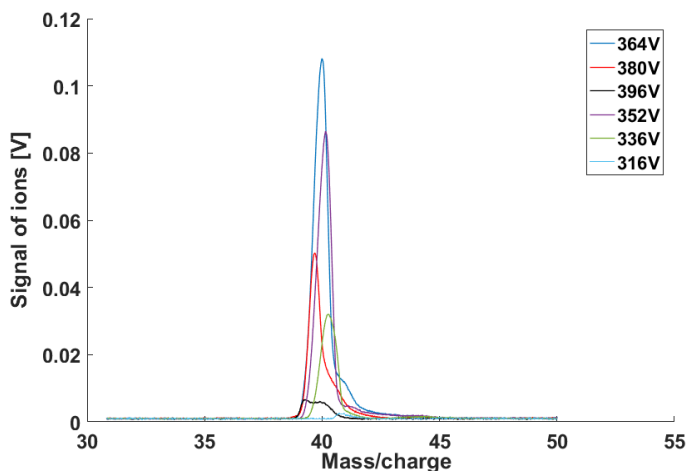


Figure 2.63 – Results of the test done to evaluate the energy dispersion of an argon ion beam. The test was done by measuring the signal on the detector for different voltages on the deflector.

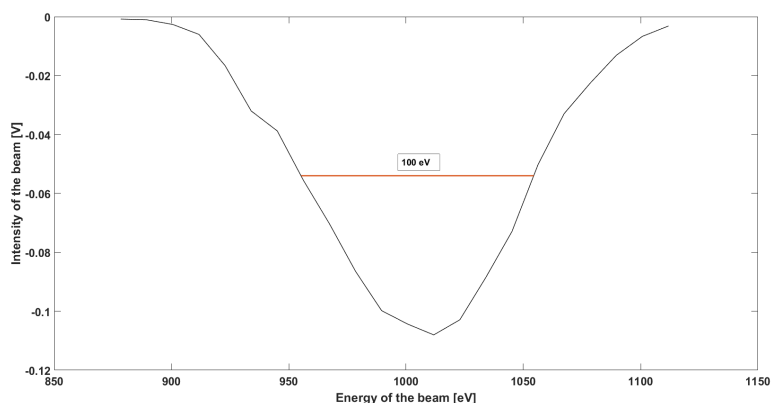


Figure 2.64 – The representation of the beam energy dispersion.

2.6.2 Temporal and spatial overlap of the N_2O^+ ion beam with the pulsed dye laser

The S/N of a photodissociation spectrum depends, for the S part, on the amplitude of the NO^+ signal which is integrated and averaged at each frequency step of the laser. The photodissociation signal thus requires maximizing the overlap of the mass-selected ions with the laser pulse in the time and spatial domain. The time delay of the pulsed gas injection is thus synchronized with the laser pulse by monitoring the photodissociation fragments on the MCP detector. The overlap of the pulsed laser with the bunched N_2O^+ beam has been evaluated in order to check if the MRP of the TOF-MS ($R=140$) is large enough, i.e. Δt small enough compared to the laser pulse duration ($\approx 5\text{ns}$). The time delay between the laser and the bunched ion beam has been scanned using the multi-channel digital delay generator. Figure 2.65 presents the NO^+ fragments generated from N_2O^+ as a function of this delay, with the laser tuned at the

Q branch frequency of the $\tilde{A}^2\Sigma^+(002) \leftarrow \tilde{X}^2\Pi_{3/2}(000)$ rovibronic band where the vibrational quantum numbers (μ_1, μ_2, μ_3) are indicated in parenthesis and the electronic states provided by the usual $\tilde{X}, \tilde{A}, \tilde{B}$ order followed by $^{2S+1}|\lambda|_{L+S}$. This scan displays a Gaussian profile of 105 ns FWHM, for a typical laser pulse duration of 5 ns. Nevertheless, most of the ions interact with the laser. Indeed, considering a speed of 66 km/s for an ion of 44 amu ($t_{TOF} \simeq 22 \mu\text{s}$, $E = 1 \text{ keV}$), a 105 ns dispersion corresponds to an ion bunch length of 6.9 mm which is very close to the diameter of the pulsed laser beam estimated to be $\simeq 6 \text{ mm}$ at the interaction region.

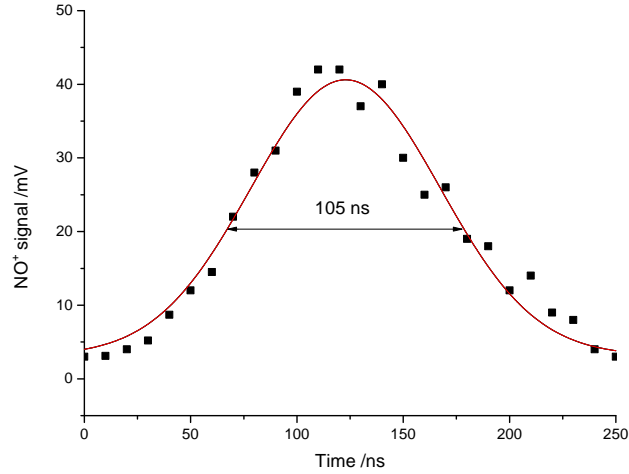


Figure 2.65 – Laser interaction time profile measured from the NO^+ photo-fragments by tuning the time delay between the N_2O^+ ion bunch and the laser pulse. The measurements are depicted in black squares and are fitted by a Gaussian profile presented in red. The laser frequency was fixed to the top of the Q branch frequency of the $\tilde{A}^2\Sigma^+(002) \leftarrow \tilde{X}^2\Pi_{3/2}(000)$ rovibronic band (30908.5 cm^{-1}). The origin of the x-axis is arbitrary.

2.6.3 Application to the high resolution spectroscopy of N_2O^+ , the $\tilde{A}^2\Sigma^+(002) \leftarrow \tilde{X}^2\Pi(000)$ vibronic band in N_2O^+

To evaluate the performances of our spectrometer in terms of frequency accuracy, measuring time, S/N ratio and rotational temperature, the rotationally resolved photodissociation spectrum of N_2O^+ corresponding to the $\tilde{A}^2\Sigma^+(002) \leftarrow \tilde{X}^2\Pi_{3/2}(000)$ rovibronic band (Figure 2.66) has been measured several times for different experimental conditions in the UV range by monitoring the appearance of ionic fragments (NO^+) as a function of the laser wavelength. This band has indeed been used to evaluate the performances of several spectrometers based on different action type of measurements [139, 140, 62]. To use refined molecular parameters of the $\tilde{A}^2\Sigma^+(002)$ state in the evaluation of our spectrometer, we started by measuring and analysing the $\tilde{A}^2\Sigma^+(002) \leftarrow \tilde{X}^2\Pi_{3/2}(000)$ and $\tilde{A}^2\Sigma^+(002) \leftarrow \tilde{X}^2\Pi_{1/2}(000)$ rovibronic bands of N_2O^+ .

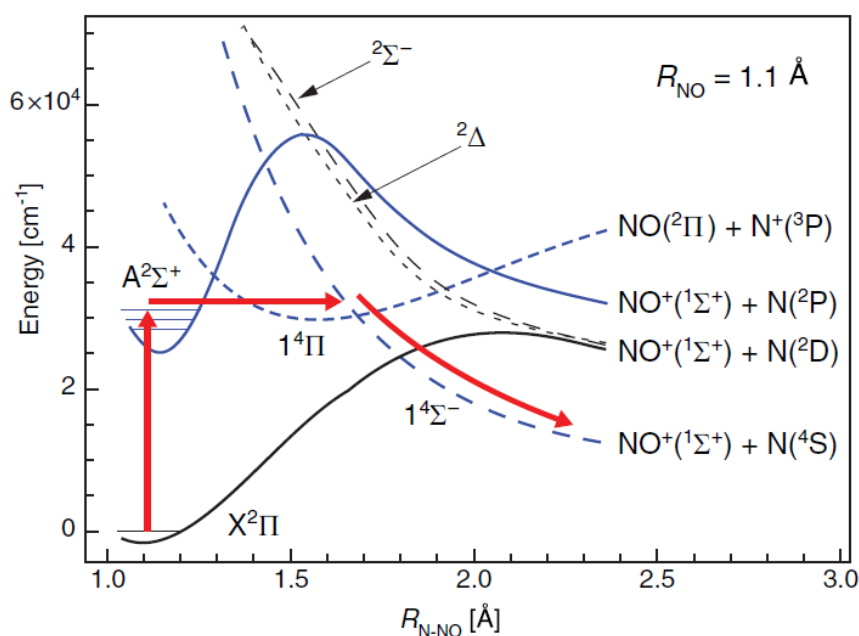
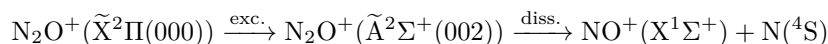


Figure 2.66 – Potential energy curves of N_2O^+ as a function of the N-NO distance $R_{\text{N-NO}}$ from reference [141]. The blue curves are the electronic states involved in the predissociation path shown by the red arrows.

We chose the N_2O^+ cation because it has been extensively investigated in the literature through lifetime measurements [142], optical emission [143, 144, 145, 146, 147, 148], photoelectron [149, 150] and photodissociation studies [151, 152, 153, 154, 155, 156, 157, 158, 159, 160]. The photodissociation of $\text{N}_2\text{O}^+(\tilde{A}^2\Sigma^+(002))$ in the 30885-30940 cm^{-1} range has been experimentally characterized in previous studies [143, 157, 161] with the following predissociation process :



The $\tilde{A}^2\Sigma^+(002) \leftarrow \tilde{X}^2\Pi_{3/2}(000)$ rovibronic band has already been recorded at high resolution [152, 143] and is one of the most intense in the 30500-32500 cm^{-1} (307-327 nm) spectral range covered by our frequency doubled pulsed dye laser operating with DCM.

We have used here the convention by Herzberg[148, 149], with v_1 corresponding to the higher frequency N-N σ^+ stretch, v_2 to the π bend and v_3 to the lower frequency N-O σ^+ stretch, and not that of Callomon *et al.* [143]. The spectroscopic parameters of the $\tilde{X}^2\Pi_{3/2}(000)$ ground state have been taken from the work of Fellows *et al.* [145] ($B'' = 0.411601(16) \text{ cm}^{-1}$, $D'' = 0.2072(61) \times 10^{-6} \text{ cm}^{-1}$, $A'' = -132.3551(11) \text{ cm}^{-1}$, $\gamma'' = -0.01424(22) \text{ cm}^{-1}$, $p = 0.1385(74) \times 10^{-2} \text{ cm}^{-1}$ and $q = -0.485(54) \times 10^{-4} \text{ cm}^{-1}$). Those of the $\tilde{A}^2\Sigma^+(002)$ upper state have been firstly taken from Frey *et al.* [152] and improved from analysis of the two intense bands presented in Figure 2.67. A total of 290 line assignments corresponding to 161 blended lines have been fitted with a standard deviation of 0.037 cm^{-1} by least squares methods with PGOPHER [162]. The fitted molecular constants are compared with previous studies in Table 2.10. Comparing with Callomon *et al.* [143], Frey *et al.*[152] and Herburger *et al.*[149], our study allowed to determine the vibronic energy transition $\tilde{A}^2\Sigma^+(002) \leftarrow \tilde{X}^2\Pi_{3/2}(000)$ instead of the band head position. A similar analysis also presented in Table 2.10 was published very recently by Igosawa *et al.* [140]. Although their measurements present an accuracy similar to ours, our molecular parameters determination is improved by using the merged blended lines option of PGOPHER. This option takes into account the relative intensities of the transitions in the frequency determination of the merged lines. This improved treatment allowed us to determine the quartic order centrifugal distortion term D' . As detailed hereafter, the $\tilde{A}^2\Sigma^+(002) \leftarrow \tilde{X}^2\Pi_{3/2}(000)$ band is used to test the absolute calibration of our measurements, to determine the rotational temperature of the ion beam and to infer the required measurement time to reach a specific signal-to-noise ratio. In the rest of the section, the spectra are compared with the rovibronic simulation calculated with PGOPHER software [162] using the parameters of Fellows *et al.* [145] for the ground state and of Table 2.10 for the $\tilde{A}^2\Sigma^+(002)$ state.

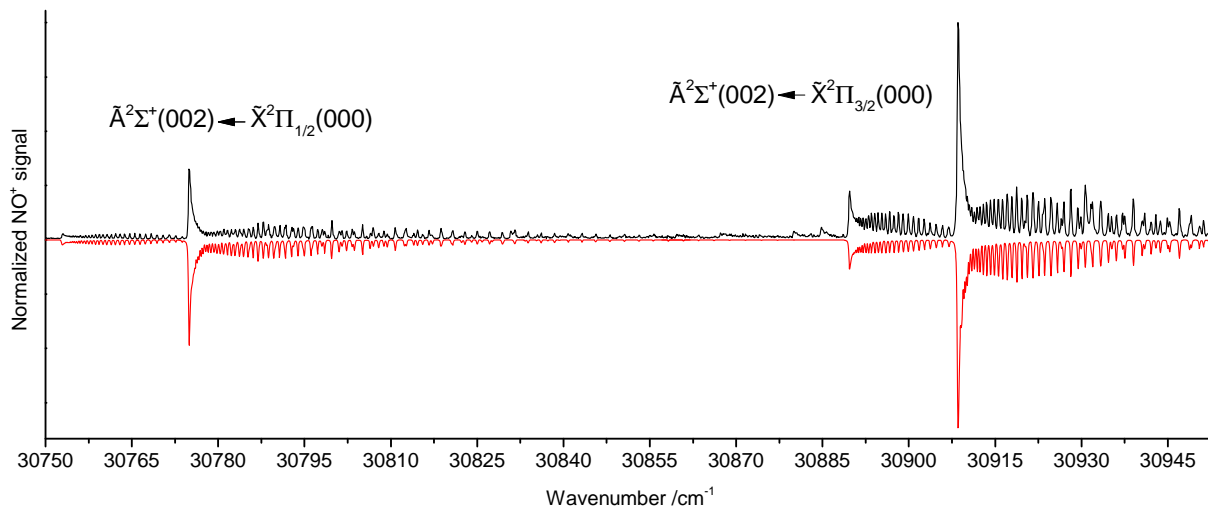


Figure 2.67 – The photodissociation spectrum (black) has been measured from the interaction of the N_2O^+ beam with a frequency doubled dye laser (0.6 mJ/pulse) for an average of 30 counts per laser step. The simulation (red) was performed with the PGOPHER software[162] using the parameters of Fellows *et al.* [145] for the $\tilde{X}^2\Pi_{1/2,3/2}(000)$ ground state and those of Table 2.10 for the $\tilde{A}^2\Sigma^+(002)$ state. A temperature of 300 K and a Voigt lineprofile have been considered for the simulation, with Gaussian and Lorentzian contributions of 0.2 cm^{-1} and 0.1 cm^{-1} (FWHM), respectively.

Table 2.10 – Rovibronic parameters (in cm^{-1}) for the $\tilde{A}^2\Sigma^+(002)$ excited state. The rotational constants of the $\tilde{X}^2\Pi$ ground electronic state have been fixed to the values of Fellows *et al.*[145]. Numbers in parentheses represent 1σ standard deviation in units of the last significant digits.

Parameters	Ref. [143]	Ref. [152]	Ref. [149]	Ref. [140]	This work
v_0				30844.3(1)	30844.27(10) ^a
B'	0.4290(5)	0.42893(10)	0.4279(8)	0.42891(2)	0.428883(24)
$D' \times 10^7$	1.69(38)	1.6	0.0	1.9	1.89(17)

^a Value subtracted by 0.1 cm^{-1} (Doppler shift) and standard deviation was calculated from the wavenumber calibration (section 2.6.5 for details).

2.6.4 Effect of the bias cell

The effect of the bias cell on the photodissociation spectrum of N_2O^+ has been studied. The improvement of the S/N by setting the central electrode of the bias cell to -250V (DC on) instead of 0V (DC off) is presented in Figure 2.68 a) for the $\tilde{A}^2\Sigma^+(002) \leftarrow \tilde{X}^2\Pi_{3/2}(000)$ band. The time-of-flight spectra, recorded for the same laser frequency are also presented in Figure 2.68, with the bias cell at 0 V in panel c) and -250 V in panel b). On these panels the black traces correspond to the absence of light and the green and blue traces are recorded with the laser on. One can clearly notices in panel b) the separation of the

photodissociation fragments from the other fragments produced from collisions in the drift tube. This results in a S/N improved by a factor 4 in the photodissociation spectrum and a removal of the collisional background. The presence of ions generated outside of the laser interaction, observable at $6.5 \mu\text{s}$, in panel b), is due to a still too large aperture at the exit of the 90° deflector (hole diameter of 12 mm). These residual ions can be rejected by the selection of a judicious integration time window. The combination of the bias cell and the choice of integration time window ensures thus a background free measurement.

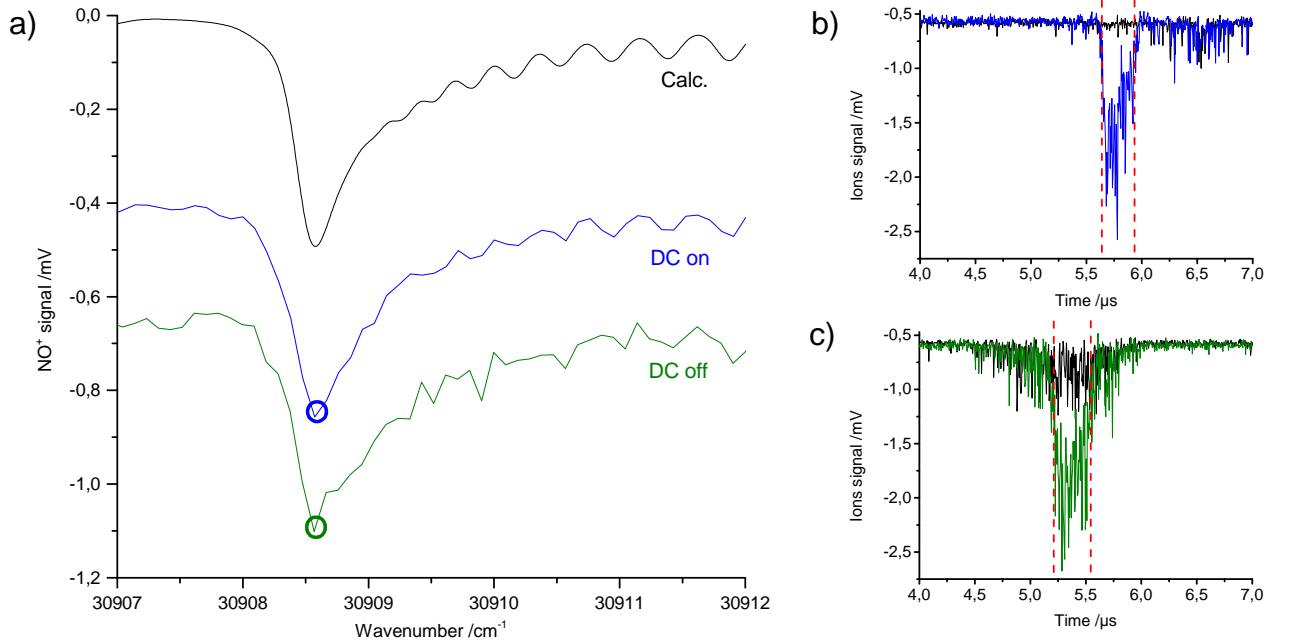


Figure 2.68 – (a) Q branch region of the $\tilde{A}^2\Sigma^+(002) \leftarrow \tilde{X}^2\Pi_{3/2}(000)$ photodissociation spectrum of N_2O^+ , from bottom to top measured with the bias cell at 0 V (DC off), at -250 V (DC on) and simulated using the PGOPHER software. Blue and green mass spectra of the panels b) and c) are the NO^+ fragments measured at the maximal intensity of the Q branch for the bias cell on and off, respectively. The mass spectra measured without UV laser are presented in black in panels b) and c).

The 2D pulsed mass selection allows to time select the peak of N_2O^+ , but the peak associated to the TOF of N_2O^+ still contains minor quantities of NO^+ and N_2^+ produced before the pulsed deflection and having the same velocity as N_2O^+ and so the same TOF. The voltage applied on the switched deflector (70 V) changes the trajectory of NO^+ and N_2^+ from the one of N_2O^+ , before entering the differential pumping tube. Experimentally, we have checked that decreasing the deflector voltage increases the NO^+ and N_2^+ signals and decreases the N_2O^+ one. This indicates that the combination of the pulsed deflection and differential pumping tube allows to exclude most of the NO^+ and N_2^+ but not entirely.

Another case, could be the production of NO^+ and N_2^+ in the area between the deflector and the differential pumping tube (pressure = 10^{-6} mbar) and before the last chamber (pressure = 10^{-7} mbar). These ions generated for a distance estimated to be 10 cm have the same direction of N_2O^+ , And they are not filtered prior to the differential pumping tube. The two cases are illustrated in Figure 2.69.

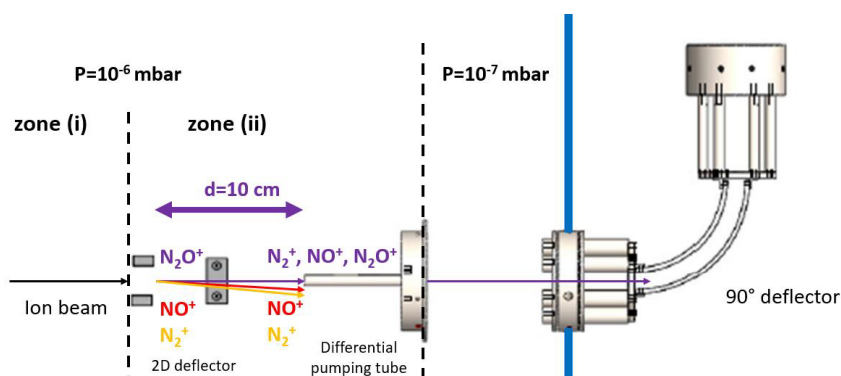


Figure 2.69 – Illustration of the two zones that are responsible of the apparition of NO^+ and N_2^+ in the photodissociation signal. In red and yellow we can observe the illustration of the trajectory of these ions from zone (i) and in purple the trajectory of these ions already produced in zone (ii).

Concerning the second energy selection, the hole of the end plate of the 90° deflector allows to select ions with a resolution of ± 35 eV (estimated from SIMION simulation). When the bias cell is off with the 90° deflector voltages tuned for 680 eV, ions with 680 ± 35 eV are selected, including NO^+ produced from photodissociation (680 eV) and collisions (680 eV), while N_2^+ is excluded (636 eV). When the bias cell is on with the 90° deflector voltages tuned for selecting ions with a kinetic energy of 602 eV, the ions with 602 ± 35 eV are selected, including NO^+ from photodissociation (602 eV modified with the bias cell) and some N_2^+ produced from collisions outside the bias cell (636 eV), NO^+ produced from collisions are excluded (680 eV). Which explains later the apparition of a parasite peak on the signal of photodissociation assigned to residual N_2^+ that follows a longer trajectory and arrives after the photo-fragments peak. We could check these hypotheses and decrease the N_2^+ signal for future measurements by adding the differential pumping tube before the 2D deflector. We could also increase the pumping capacity to decrease the residual pressure and also reduce the diameter of the differential pumping tube. The apparition of the parasite peak could be observed in Figure 2.68.

2.6.5 Calibration of the frequency scale

The absolute frequency of the photodissociation spectra was calibrated using Ne lines [163] measured from a hollow cathode. This optogalvanic spectrum and the photodissociation spectrum were simultaneously measured. While the photodissociation spectra have been measured with a frequency doubling BBO crystal in the 307-327 nm spectral range, the atomic Ne lines of the hollow cathode have been measured using the fundamental laser beam (614-654 nm). The absolute calibration of the frequency scale has been performed using three neon lines (640.40177 nm, 650.83255 nm, 653.46872 nm) with a standard deviation of 0.06 cm^{-1} .

In addition to the absolute calibration, a complementary Fabry Perot interferometer allowed to check the linearity of the laser frequency scanning using a solid state etalon presented in Figure 2.70. This interferometer has been designed using an *invar* ring of 1.99 mm separating two 50:50 beamsplitters enclosed in a thermostatically controlled vacuum chamber ($313.0 \pm 0.1 \text{ K}$). The resulting Fabry Perot cavity has also been characterized with the fundamental laser beam (614-654 nm) with a free spectral range of 2.507 cm^{-1} and a finesse of 4.4. The residuals of a linear fit performed on the interferences maxima allowed us to check the linearity of the laser frequency scanning with a standard deviation to linearity of 0.014 cm^{-1} and a maximum local deviation value of 0.04 cm^{-1} . To achieve this linearity, the etalon had to be placed in vacuum and its temperature stabilized. The stability in temperature is on the order of 0.1°C .

In addition, a Doppler effect arising from a slight deviation from the perpendicular arrangement between the laser and the ion beam has been estimated using a rooftop mirror for a double pass of the laser beam through the ion beam. The double pass spectrum has been reproduced with a linear combination of the single pass spectrum with itself shifted by 0.2 cm^{-1} . A frequency shift of $\pm 0.1 \text{ cm}^{-1}$ has been thus estimated for each path, this corresponds to a tilt of 0.9° from a perpendicular configuration. Besides this effect which can be corrected by subtracting 0.1 cm^{-1} to the frequency scale, the cumulative errors from relative ($\leq 0.04 \text{ cm}^{-1}$) and absolute (0.06 cm^{-1}) calibrations results in an estimated accuracy of 0.1 cm^{-1} on the calibrated frequency scale.

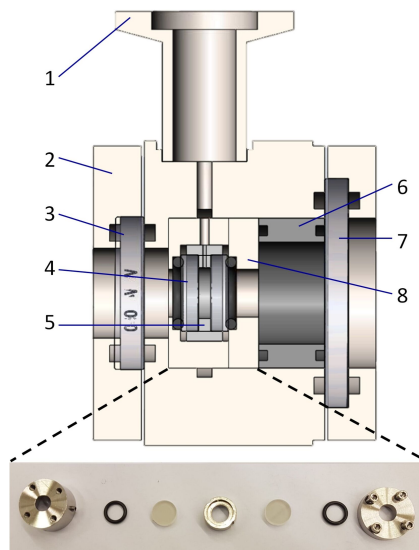


Figure 2.70 – Fabry Perot etalon composed of: 1) KF fitting for etalon evacuation, 2) external chamber diam. 2", 3) 1" wedged window, 4) 50:50 beamsplitters AR coated for 400-700 nm, 5) invar ring of 1.99 mm long, 6) PVC spacer to maintain the position of the stainless steel enclosure in the vacuum chamber, 7) 1.5" wedge windows and 8) stainless steel enclosure. The exploded view of the etalon and its content is presented below.

2.6.6 Rotational temperature

The background free measurement allowed us to measure the selected rovibronic band of N_2O^+ produced from the electric discharge in pure N_2O ($P_0 = 5$ bar) with a $S/N = 200$ and an acquisition average of 30 laser shots per frequency step (this represents one second per frequency step and a time of acquisition of $\simeq 10$ minutes for each spectrum presented in Figure 2.73).

The rotational temperature can be obtained from a fitting procedure using the PGO-PHER software, as well as the Gaussian linewidth and the baseline offset. Experimentally the rotational temperature can be tuned in a certain range by probing different parts of the ion beam using different ion extraction timings and distances between the nozzle and the skimmer. The lowest mean rotational temperature for a pure N_2O expansion ($P_0 = 3$ bar) is 110 ± 4 K and has been obtained using a distance of 1 cm between the skimmer and the nozzle. A maximum mean 305 ± 10 K has been obtained by adding a delay of 12 μs between the gas injection and the gating. The higher temperature can be obtained by selecting the start/late part of the jet. These two spectra are presented in Figure 2.73. It was possible to lower the rotational temperature down to 40 ± 3 K by using a gas mixture

of 1% N₂O with 99% Ar and a backing pressure of $P_0 = 5$ bar while probing the last part of the expansion. This spectrum presented in Figure 2.71 has been measured with a $S/N = 20$ for 30 shots per frequency step.

even for long trapping times. We were able to reach a higher S/N equal to 200 compared to 166 and a temperature lower by nearly one order of magnitude than the one they reported by Igosawa *et al.* for N_2O^+ using a cryogenic storage ring [140], even for long trapping time. In addition, the bias cell is only used by our team that allows a totally background free measurement which enhances the sensitivity of the detection.

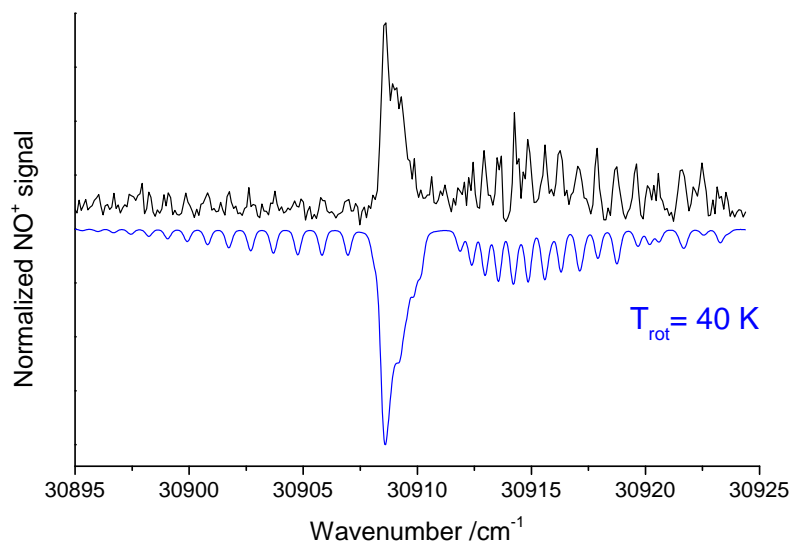


Figure 2.71 – Photodissociation spectrum (black) measured from a gas mixture of 1% N_2O with 99%Ar ($P_0 = 5$ bar). The simulation (blue) have been done using the PGOPHER software [162] for $T_{\text{rot}} = 40$ K.

2.7 Perspectives

2.7.1 Extraction scheme

First we have to mention that a lot of effort was spent during this thesis by A. Roucou a post-doctoral researcher in the same group, to ameliorate the instrument. One of the upgrades is the use of an extraction scheme directly after the skimmer. In fact, the first acceleration scheme inspired from Dedman *et al.* [132] consisted in a series of six aluminum ring electrodes connected via $100\text{ k}\Omega$ resistors to produce a smooth gradient of acceleration potential. In order to enhance the signal-to-noise ratio the ionic signal must be enhanced. For that purpose a different extraction scheme has been implemented that is composed of a conical electrode polarized at -700 V placed 1 cm after the aperture of the grounded skimmer in order to accelerate the ions immediately after the expansion. A succession of two pairs of electrodes at -2 kV and -1 kV allows accelerating the ions on a shorter distance and forming an electrostatic lens. This second design allowed us to improve the ion signal by at least a factor 30 while keeping a low rotational temperature. The second design has thus been set up permanently. The new design is shown in Figure 2.72 along with the associated SIMION[®] simulations.

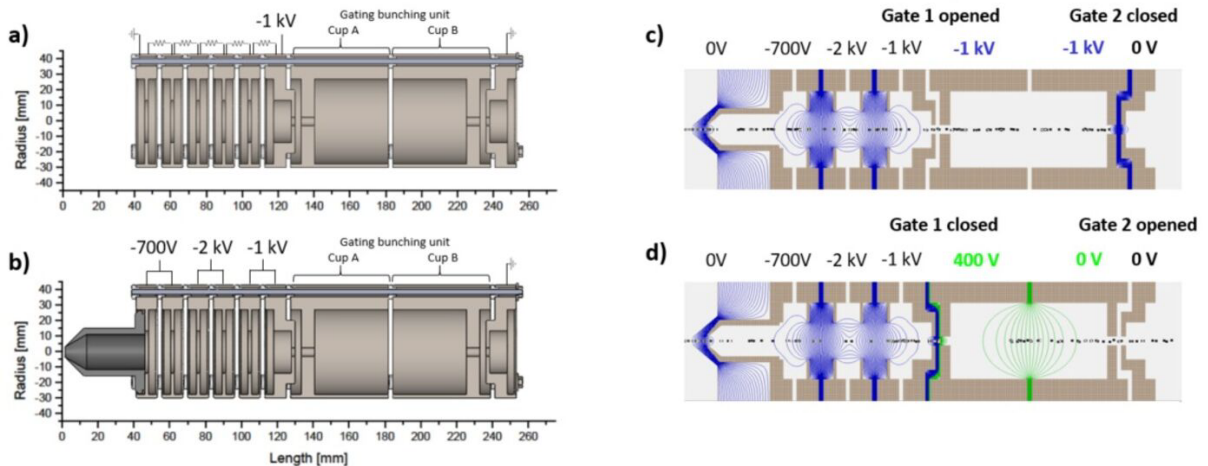


Figure 2.72 – a) The first acceleration scheme inspired from Dedman *et al.* [132] b) The second acceleration scheme. c) Before switching, the gating process simulation from SIMION[®] on the second acceleration scheme. d) After switching, the first part of the unit is at $+400\text{ V}$ to close the first gate and bunch the ions at the end of the TOF. The second part of the unit is switched to 0 V to let the ions enter the drifting tube.

The gating process and the second acceleration scheme is simulated using SIMION[®], using 150 particles of $m = 44$ amu with a charge $+e$ in an initial circular distribution (radius of 1.5 mm and $v = 550$ m/s). The two cup-like electrodes are initially at the acceleration voltage (-1 kV) and a last grounded electrode stops the ion beam reflected in the unit. Similar to the first design, the first part of the unit is switched to +400 V to close the first gate and bunch the ions at the end of the TOF. The second part of the unit is switched to 0 V to let the ions enter the drifting tube. This new design allowed the measurement of the spectra shown in Figure 2.73.

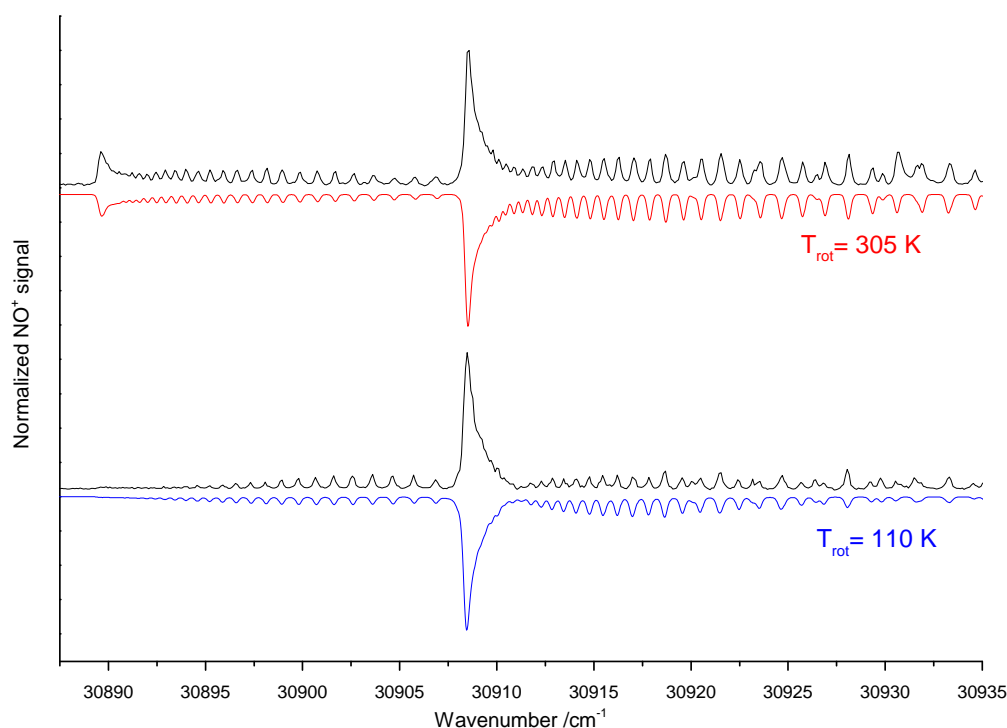


Figure 2.73 – The photodissociation spectra (black) have been measured from the interaction of the N_2O^+ beam with a doubled dye laser (0.6 mJ/pulse) by probing different parts of the ionic beam using different ion extraction timings and distances between the nozzle and the skimmer. An average of 30 counts per laser step allowed to reach a $S/N = 200$ for each spectrum. The simulations has been done for each measured spectrum using the PGOPHER software [162] for $T_{rot} = 305$ K (red) and $T_{rot} = 110$ K (blue)

Different temperature could be obtained by selecting starting or the ending of the jet as shown in Figure 2.74

We can thus map the temperature contour of the supersonic jet by probing different

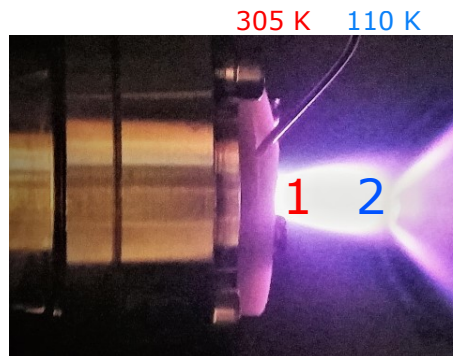


Figure 2.74 – Probing different zone of the jet giving two different temperatures (1 = 305 K 2 = 110 K) as shown in the spectra in previous Figure 2.73.

positions and this could be done in a few days.

2.7.2 Quadrupole mass filter

Another improvement could be the use of a quadrupole mass analyser to replace the TOF spectrometer. It consists of a set of four parallel conductive rods on which an RF and a DC voltage are applied in order to select the desired ion from the source. Figure 2.75 shows the quadrupole that we already have. The details on the functioning could be found in [164]. Efforts were done to simulate the same geometry and to find the necessary power supplies and RF generator to make this quadrupole functional. Using the quadrupole could result in a higher signal-to-noise ratio and it could be useful to detect higher masses with higher resolution than the TOF mass spectrometer, while working with slower ions.

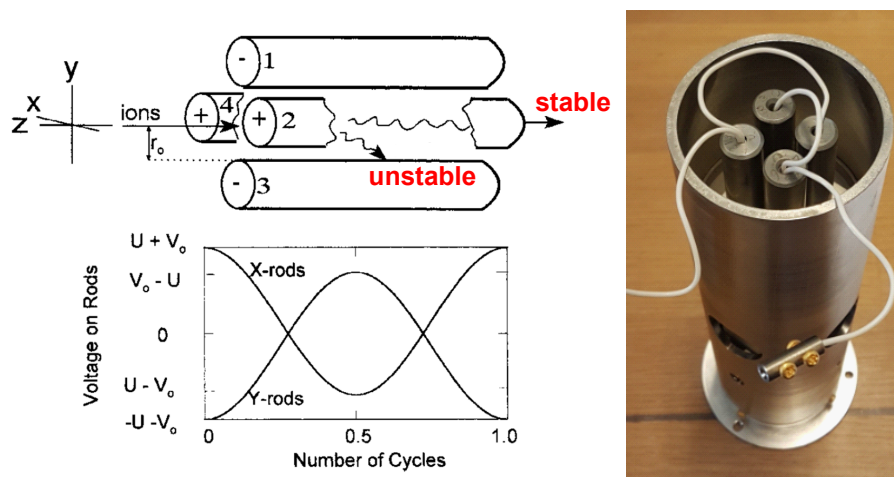


Figure 2.75 – A picture of the quadrupole filter available in our lab. A schematic of the rods is represented, along with the voltages applied and resulting in a stable trajectory and other unstable trajectories defined by the voltages applied (U is for the DC voltage and V_0 is the amplitude of the RF signal. Adapted from [122].

2.7.3 Photodissociation spectroscopy of $[\text{H}_2\text{O}-\text{CO}_2]^+$

Future work of STARGATE will be dedicated to the study of ionic clusters like $[\text{H}_2\text{O}-\text{CO}_2]^+$ by IR photodissociation (IRPD) spectroscopy. The plan is to measure the spectral signature of such complex in the near infrared, determine charge distribution and for larger species solvation structure. The charge distribution depends on physical and chemical properties of constituent molecules such as the ionization potential. Y. Inokuchi *et. al.* [13] measured the IRPD spectra of $[\text{H}_2\text{O}-(\text{CO}_2)_n]^+$ in the $1100\text{-}3800\text{ cm}^{-1}$ region at low resolution. Figure 2.76 shows the IRPD spectrum of this cluster. This spectrum was measured at low resolution using an IR pulsed laser. The appearance of an absorption band of CO_2 indicates that the $[\text{H}_2\text{O}-(\text{CO}_2)_n]^+$ ion has an ion-molecule form $\text{H}_2\text{O}^+ \text{---} \text{CO}_2$. The result is reasonable because the ionization potential of H_2O (12.62 eV) is lower than that of CO_2 (13.78 eV).

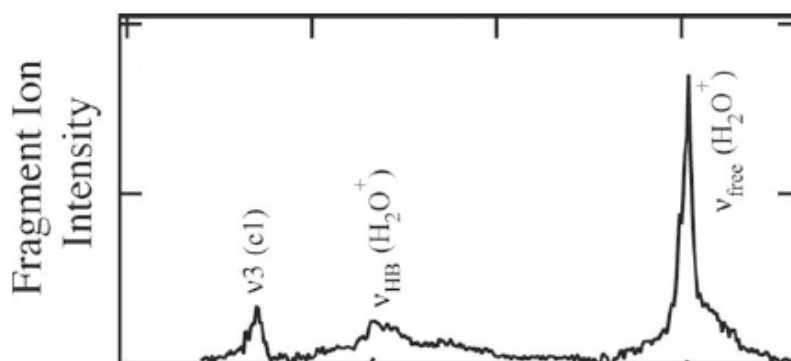


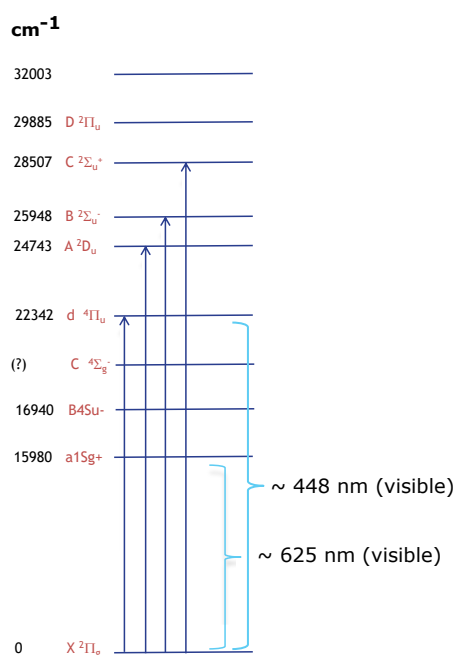
Figure 2.76 – IRPD spectrum of the $[\text{H}_2\text{O}-\text{CO}_2]^+$ ion, reproduced from [13].

THE FOURIER TRANSFORM INCOHERENT BROADBAND CAVITY ENHANCED ABSORPTION SPECTROSCOPY (FT-IBB-CEAS) INSTRUMENT

Astrophysicists have long suspected the presence of negative ions in interstellar space, their detection was made possible only recently [165], with the first spectroscopic characterization in the laboratory of several carbon chain anions [166] and subsequently their detection in various environments (black carbon star IRC+10216, the Taurus molecular clouds 1 TMC-1(CP), pre-stellar cloud L1544 and the protostellar object L1521F) through telescope observation [167]. Our incentive for studying anionic carbonic chains C_x^- ($x= 3, 4, 5, \dots$) has been their relevance to astrophysical observations after the detection of different molecular anions [168]: C_4H^- , C_6H^- , C_8H^- , C_3N^- , C_5N^- and CN^- . The astronomical detection of these anions was possible thanks to the laboratory characterization of their rotational spectra. Except for C_5N^- , whose identification in space was based on high-level ab initio calculations [169]. In the absence of permanent dipole moment, these carbon chain molecules remain inaccessible to detection methods based on rotational spectroscopy commonly used in radio-astronomy. Visible and near-infrared spectral domains, characteristic of rovibronic transitions, represent an alternative for the identification of such species. In this thesis new apparatus has been developed to record their near infrared absorption spectra. In the first part of this chapter we will explain the approach we used for the production of the molecular ions based on an electrical discharge in a uniform supersonic flow produced by a planar Laval nozzle. The planar geometry is chosen to increase the optical path in the probed absorption region by a factor of 10 compared to an axisymmetric geometry.

The second part of this chapter will focus on the Fourier transform incoherent broadband cavity enhanced absorption spectrometer (FT-IBB-CEAS) we have coupled to the supersonic flow to record the near infrared (NIR) spectrum of the produced ions. We are targeting electronic transitions of these anionic species. The electronic states of C_3^- and C_4^- are reproduced in figure 3.1 from NIST data [163]:

Electronic structure C_3^-



Electronic structure C_4^-

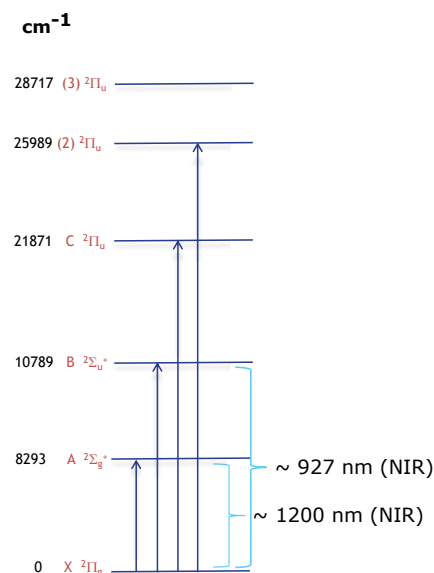


Figure 3.1 – Electronic structure of C_3^- and C_4^- produced using data from [163] .

Absorption experiments have been performed, both in matrices and in the gas phase to record the spectra of these species, but until now scientists couldn't record the rotational resolved spectra of these species. An example of an absorption spectrum of the $A \ ^2\Sigma_g^+ \leftarrow X \ ^2\Pi_g$ and $B \ ^2\Sigma_u^+ \leftarrow X \ ^2\Pi_g$ electronic transition of C_4^- in a 5 K neon matrix [170] (Figure 3.2):

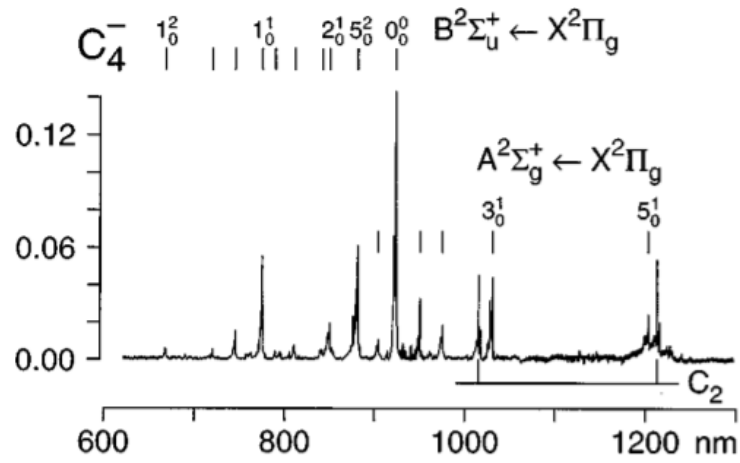


Figure 3.2 – Absorption spectrum of C_4^- in a 5 K neon matrix [152].

One of our objectives is therefore to record the absorption spectra covering the region from the visible to the near-infrared. First, we will start by validating the functioning of the instrument by measuring the spectrum of a neutral molecule like acetylene and methane that have relatively weak overtone transitions in this region. Then, spectra of radicals and ions will be measured to test the production of such species and the sensitivity of the whole instrument, and at the end we look forward to record the absorption spectrum of cold anions which will be a challenge due to the difficulty of their production and the need of ultra sensitivity for the detection.

3.1 Uniform planar discharge Nozzle

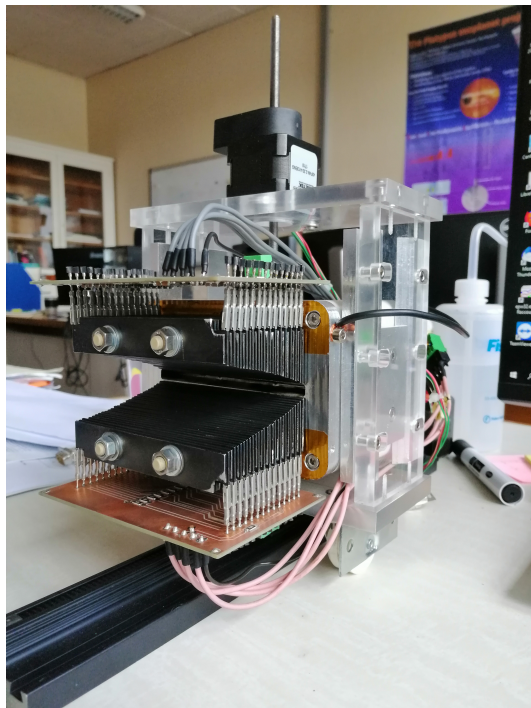


Figure 3.3 – Photo of the cold ionic source.

3.1.1 Conception of the Laval nozzle

Due to space charge effects, the density of anions produced in the laboratory is extremely low, even in a free supersonic jet expansion. In order to tackle this challenge, a novel ion source has been developed in IPR based on an electric discharge in a uniform supersonic flow. The gas flow is characterized by a planar geometry and expands through a slit throat where the discharge is initiated. The planar geometry is chosen so as to increase the optical path length through the cold gas by a factor of 10 compared to the more conventional axisymmetric geometry. This new planar nozzle is based on a convergent-divergent nozzle geometry so called Laval nozzle. It is shown in Figure 3.4. The calculation of the profile was performed by A. Benidar and the source is composed of (from right to left of the central drawing of Figure 3.4):

- A reservoir at high pressure having the dimensions of 60 x 100 x 45 mm.
- A converging section where the gas accelerates to reach a sonic speed at the nozzle slit throat and starts to cool down by the intermediate of two body collisions.

- At the very end of the converging part, three copper electrodes (brown), are installed to generate an electric field capable of ionizing the gas.
- A diverging part equipped with a set of polarized electrodes. These electrodes are arranged according to a precisely calculated geometric divergent profile. This set plays the role of a double guidance, aerodynamic for gas flow and electric Radio-frequency for the ionic particles.

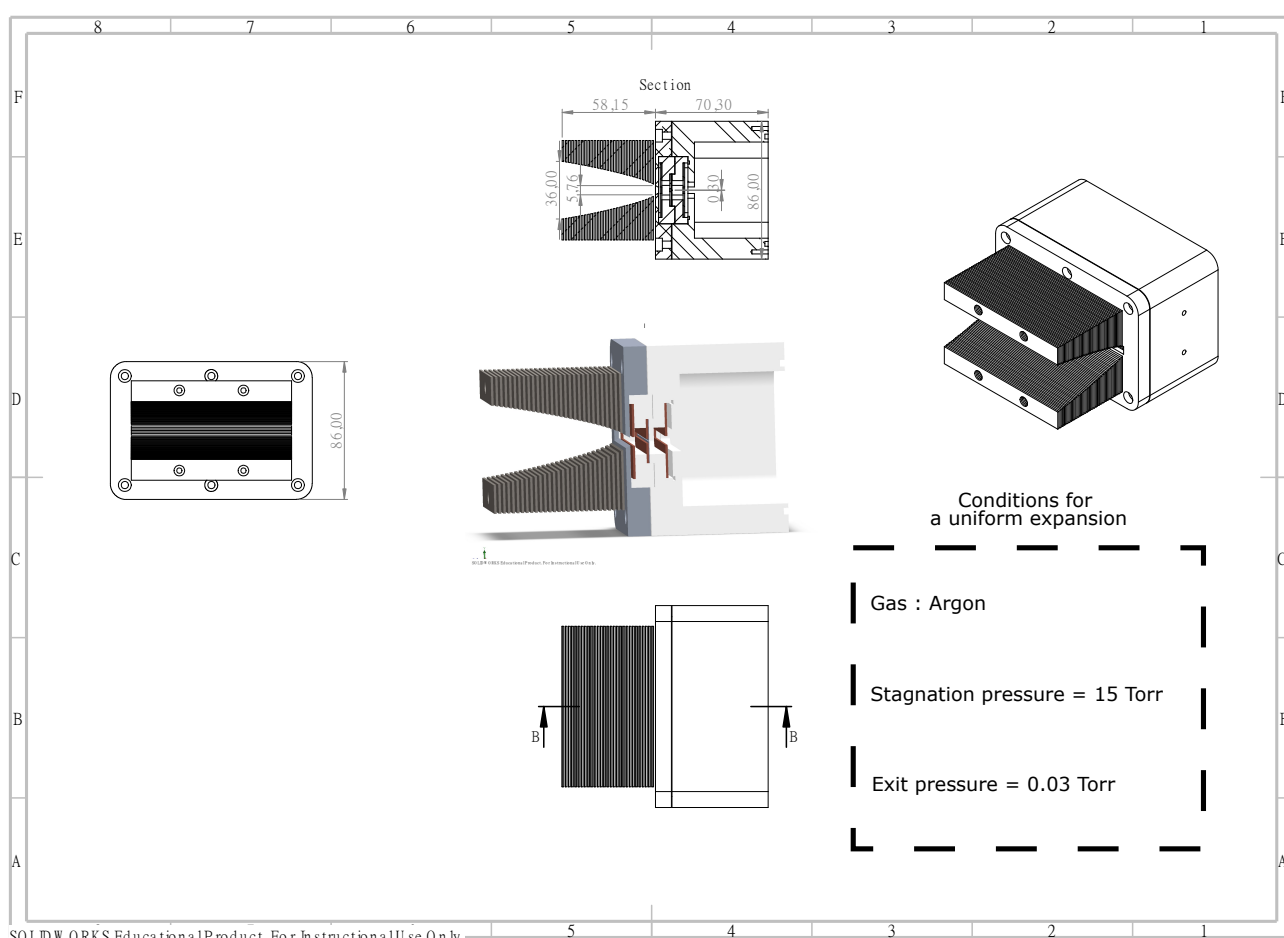


Figure 3.4 – Schematic of the source designed at IPR. The reservoir is made of polyoxymethylene(POM), the discharge electrodes are made of copper, the electrodes profiling the divergent part of the nozzle are made of aluminium, the surface of which is coated by a deposit of a carbon film in order to prevent the detachment of the electrons. The conditions to obtain a uniform expansion are also listed.

This source is mounted in a vacuum chamber evacuated by root pumps with a maximum pumping capacity of $15000 \text{ m}^3\text{h}^{-1}$. Using a thin slit throat aperture of about $100 \mu\text{m}$ yields to a stagnation pressure of about 300 torr. An efficient rotational/vibrational cooling of the molecules is expected. In one hand, such cooling is crucial to reduce the

spectral congestion caused by different species absorbing at wavelengths close to the absorbing wavelength of the ions of interest. On the other hand, cooling is necessary to magnify the recorded signal of the ions. This is particularly relevant for anions that are usually produced in low concentration. The Laval nozzle is a great tool to produce a uniform expansion over a certain range. Gas density being higher for a longer duration in a contained space promotes collisions could lead to promote chemistry and to form different species.

Planar versus axisymmetric geometry

In certain well defined pressure conditions corresponding to the so-called "adapted regime", a Laval nozzle produces a supersonic expansion characterized by a uniform temperature and density. The isentropic core is not divergent (absence of Doppler line broadening due to convective motion of the fluid) and the density remains stable and substantially greater than that of a free jet expansion. However the cold isentropic core is surrounded by warmer shear layers. The choice of a planar geometry for the nozzle aims at increasing the absorption path length of the probe laser beam through the cold part of the flow but also at reducing the relative contribution of the shear layers. Figure 3.5 shows the difference between a drawing of an axisymmetric Laval nozzle and a planar Laval nozzle. Calculations using Ansys Fluent fluid simulation software performed by A. Benidar,



Figure 3.5 – An example of two geometries, on the left an axisymmetric profiled Laval nozzle and on the right a planar profiled nozzle. Both require a convergent part and a divergent calculated profile to generate a uniform supersonic beam expansion.

as shown in Figure 3.6, are performed in order to compare the flow temperature trans-

verse profile of the two geometries. The axisymmetric geometry exhibits a strong radial temperature gradient while the planar geometry is characterized by an almost constant temperature in the perpendicular direction of the flow. Therefore, the use of a planar supersonic expansion reduces the gradient of temperature in the perpendicular direction of the flow.

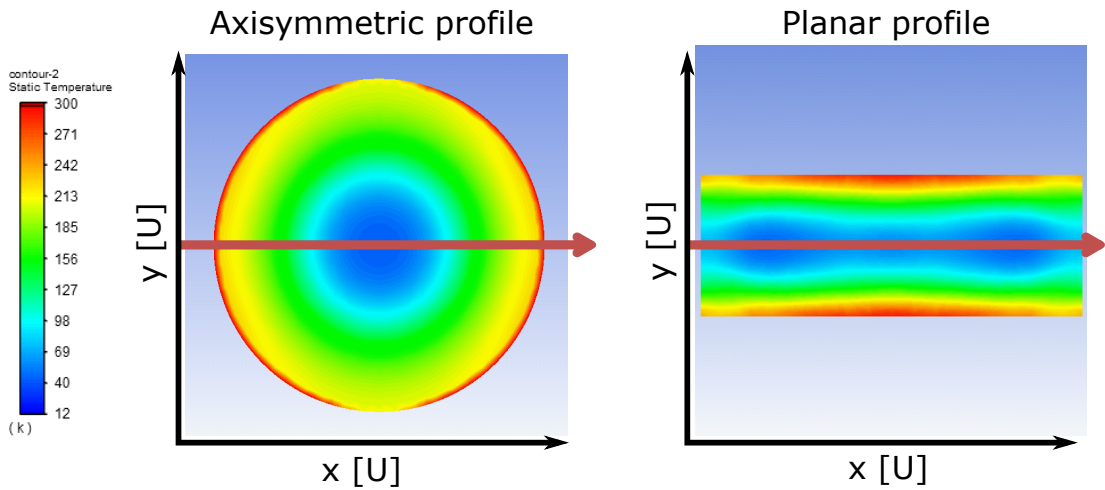


Figure 3.6 – CFD Contour plot of a cross section of the supersonic flow produced by a Laval nozzle working in its adapted regime. Left: axisymmetric Laval nozzle. Right: Planar Laval nozzle. The laser probing zone is indicated by a red arrow.

3.1.2 Computational Fluid Dynamics (CFD) simulations

In this section, analysis of the Laval nozzle performances is carried out numerically by computer simulation using the CFD software ANSYS FLUENT. The software solves numerically the Navier-Stokes equations. The processing, the initial conditions and the used equations are listed in Table (3.1). Velocity, temperature and pressure profiles of the nozzle are calculated with the help of this computer simulation approach. In a first step, a computational mesh is constructed from unstructured trigonal elements. In order to obtain a converging solution, a higher mesh density is adopted near the confining electrodes constituting the divergent part of the Laval nozzle, as well as near the area close to the thin nozzle throat. This is justified by the fact that flow gradients are more important in these areas. The meshing is presented in Figure 3.7. For the processing

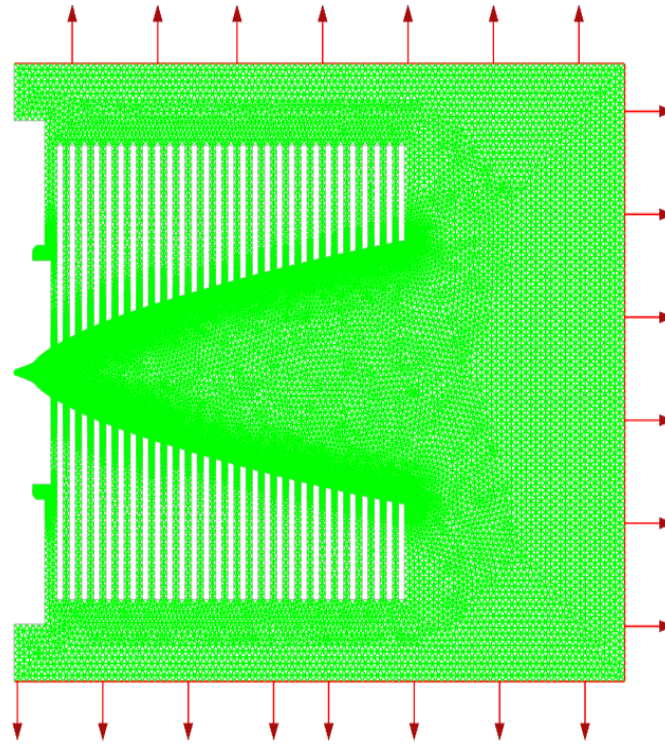


Figure 3.7 – Adopted meshing to run the CFD simulations. The red arrows indicate the outlet regions.

of the nozzle, 2D and double precision settings were used while reading the mesh. The solution parameters are presented in Table 3.2, while the residuals are presented in Figure 3.8. The solution is considered as converged after 1000 iterations and the corresponding order of scaled residuals was lower than 10^{-4} .

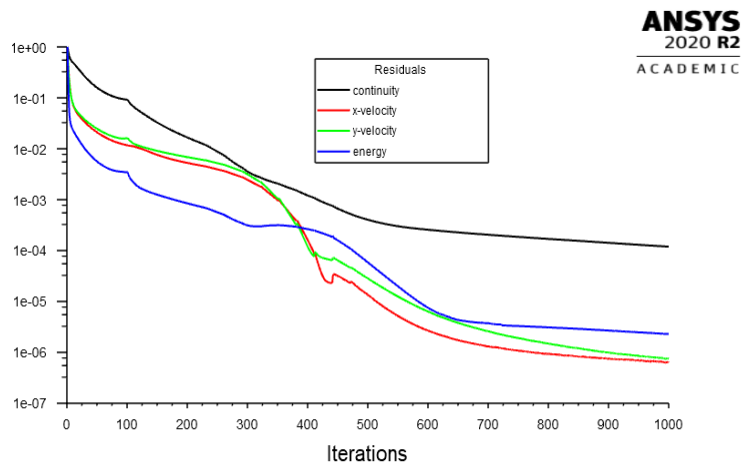


Figure 3.8 – Scaled residuals of the continuity, energy, x-velocity and y-velocity equations.

General	Solver type: Density-based
Models	Energy equation: On Viscous model: Laminar
Materials	Density: Ideal gas $c_p = 520.64$ J/kg.K Viscosity: Sutherland Thermal conductivity = 0.0158 w/m.K Molecular weight: Argon=39.948 g/mol
Boundary conditions	Inlet pressure = 14.2 torr Inlet temperature = 300 K Outlet pressure = 0.03 torr Outlet temperature = 300 K For initialization purpose only

Table 3.1 – Initial conditions used in the simulation.

Solution controls	Courant number = 5 Time: Steady Space: Planar Methods: Implicit least squares cell based
Solution initialization	Hybrid Relative to cell zone
Run calculation	No. of iteration 1000 Solution steering Supersonic + use FMG Initialization

Table 3.2 – Solution parameters used in the simulation.

Mach number, temperature and density profiles

In the following the contour plots that were obtained:

1. **Mach number:** As expected for a supersonic nozzle, the Mach number magnitude is equal to 1 at the throat section of the nozzle. This condition is known as choked flow condition, as discussed in chapter 1. The velocity at the nozzle exit is approximately equal to 525 m/s. Figure 3.9 shows the contour and the xy plots of the Mach number. Mach number reaches approximately 6 and remains constant for some centimetres to finally reach the outlet. A photo of an adapted jet of argon was recorded

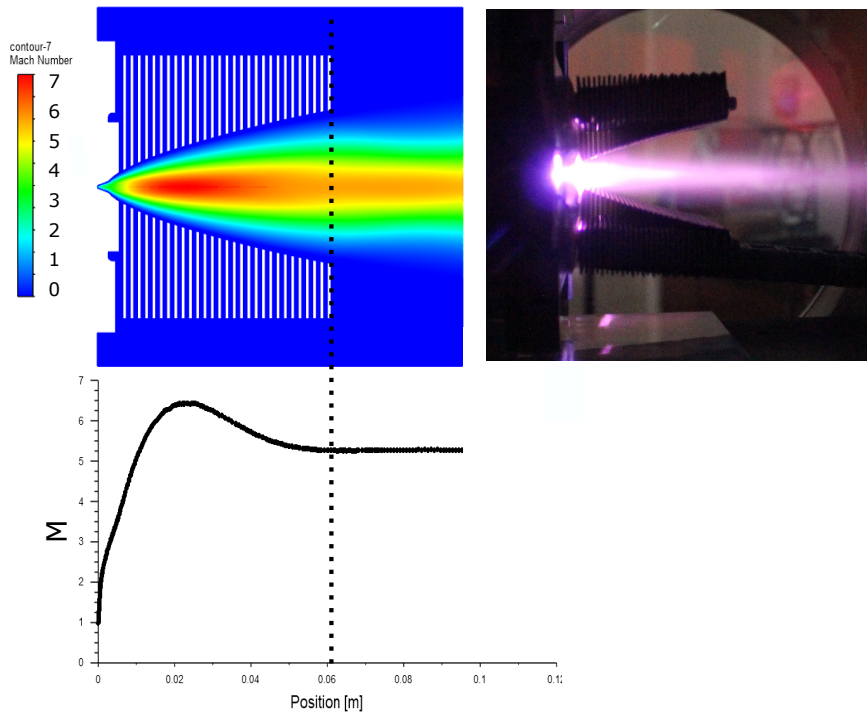


Figure 3.9 – Left top: Contours of the Mach number. Bottom left: Mach number evolution on the jet axis. Top right: photo of a plasma jet of argon obtained in adapted flow conditions.

using the electric discharge to visualise the jet. In fact, as already explained in the second chapter, when a discharge takes place the electronic excitation-de-excitation of the argon atoms results in a purple like color. The obtained light shows that the jet is well collimated and the uniformity persists over a long distance downstream the nozzle exit. This absence of divergence is interesting because it allows to obtain a higher density compared to a divergent free jet expansion.

- Temperature:** The temperature is maximum at the inlet, then decreases until the exit of the nozzle and remains constant (uniform) downstream the nozzle exit. This temperature distribution along the flow axis gives the possibility to probe different temperature inside the divergent part of the nozzle. The temperature magnitude is minimal inside the nozzle divergent part and is equal to 17.6 K then reaches 25 K at the exit of the nozzle and stays uniform.

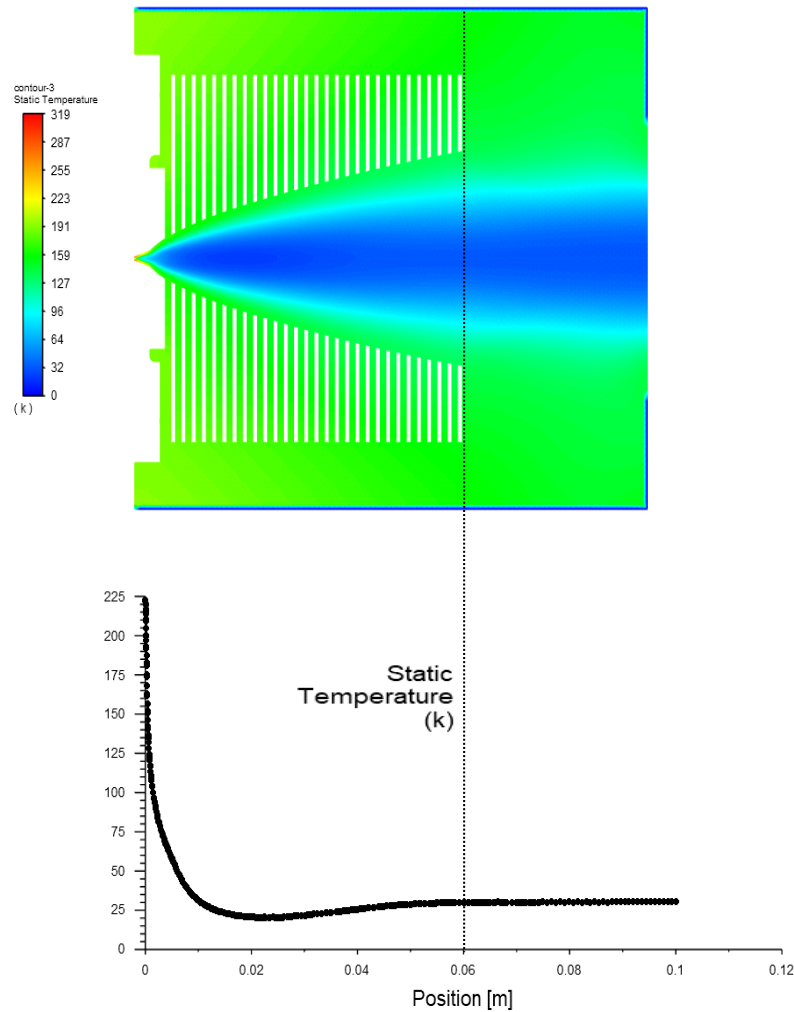


Figure 3.10 – Top panel: Temperature contour plot. Bottom panel: Temperature plot along the x direction.

- Density:** The density is maximum at the inlet, it decreases dramatically until the

exit of the nozzle and then remains relatively constant (uniform) downstream the nozzle exit. This density is higher than in a free jet expansion. The magnitude of density is around 0.001 kg/m^3 or $1.5 \times 10^{16} \text{ particle/cm}^3$ at the nozzle exit.

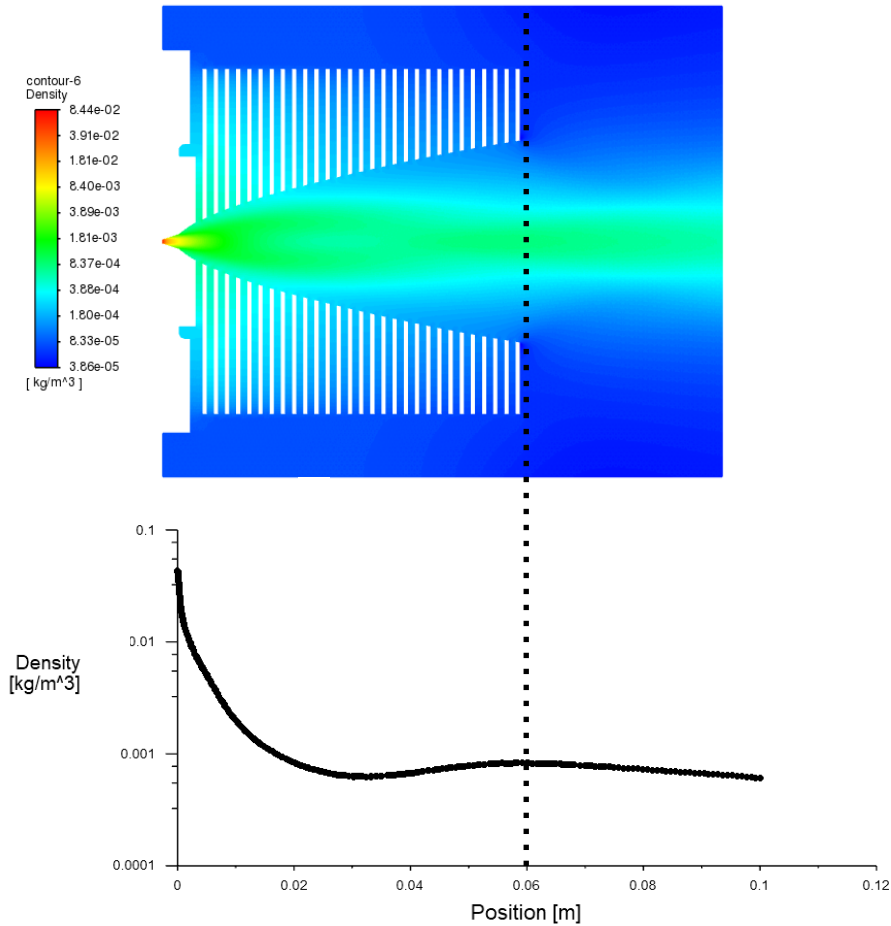


Figure 3.11 – Top panel: Density contour plot. Bottom panel: Density plot along the x direction. The density axis is in logarithmic scale in order to better visualise the density variation.

In conclusion, flow simulations corresponding to this new Laval nozzle design reveals the ability to produce a cold and uniform jet very different from free jet expansion:

1. Well defined jet temperature and density
2. Relatively high jet density (approx $10^{16} \text{ particle/cm}^{-3}$ for a low stagnation pressure (200 torr)

3. Physical parameters free of gradients

The simulations allow a clear visualisation of the isentropic core and the shear layers. The size of the isentropic core is about 3 mm which is larger than the probing laser spot (1-2 mm), we are therefore able to probe the isentropic core without being disturbed by the shear layers. Moreover, the laser beam can be positioned at different places in the divergent part, which is a convenient way to probe different flow temperature. Last but not least, the CFD simulations reveal that the discrete nature of the electrodes forming the divergent part of the nozzle does not deteriorate the quality of the flow. The CFD simulations confirm that the Laval nozzle produces uniform low temperature and high density flows. Fortunately, they do not reveal the presence of oblique shock waves which could heat up and re-compress the flow (see Chapter 1). The isentropic core is large enough to be probed by laser spectroscopy without being disturbed by the boundary layers. Finally, the electrodes of the divergent part of the nozzle do not seem to have an impact on the quality of the flow. These first conclusions must now be confirmed experimentally.

Non-adapted Laval nozzle.

The following figures (3.12 and 3.13) show what happens when helium or nitrogen is used as carrier gas in a Laval nozzle initially designed to be operated with argon. For these calculations, the pressure and the temperature were set at identical values at the nozzle throat regardless of the gas. However, due to different mass and/or specific heat ratio, the static pressure of the helium/nitrogen jet at the nozzle exit is higher than the one of the vacuum chamber. As a consequence, the jet expands further once reaching the vacuum chamber and never reaches a uniform regime. The flow is said non-adapted.

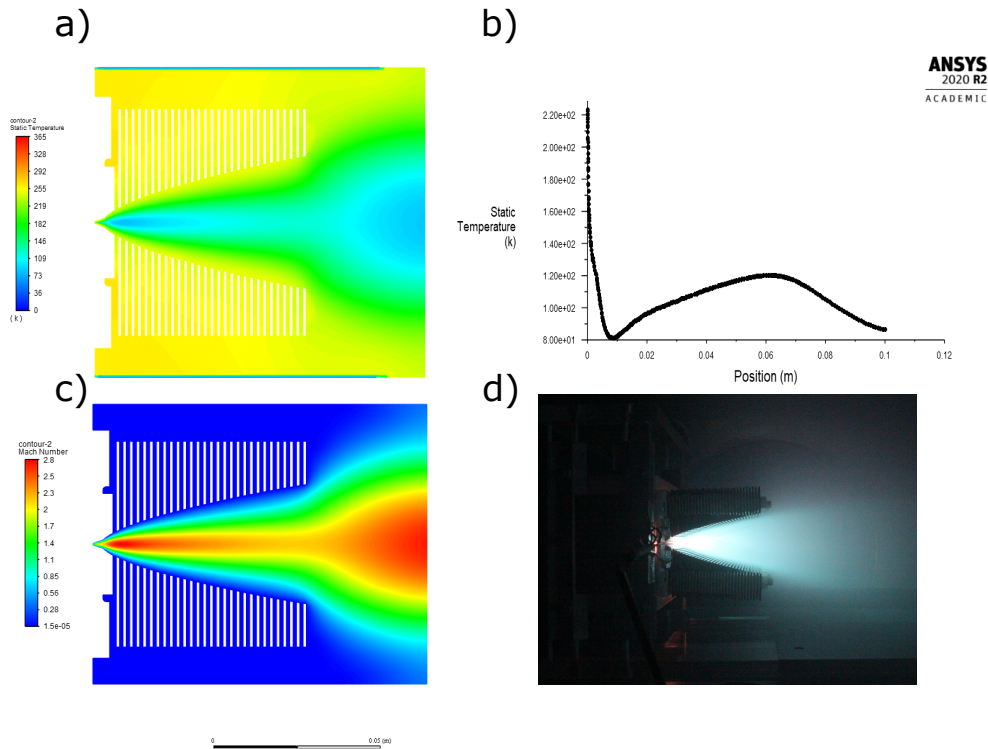


Figure 3.12 – a) CFD simulation showing the contour plot of the temperature of a jet of helium expanded in a nozzle designed to operate with argon. b) Static temperature plot along the nozzle axis showing a strong variation. c) CFD simulation of Mach number. d) Photo of the jet visualized with a plasma of helium which explains the light blue color. Helium has a different mass and viscosity producing a different jet structure than argon.

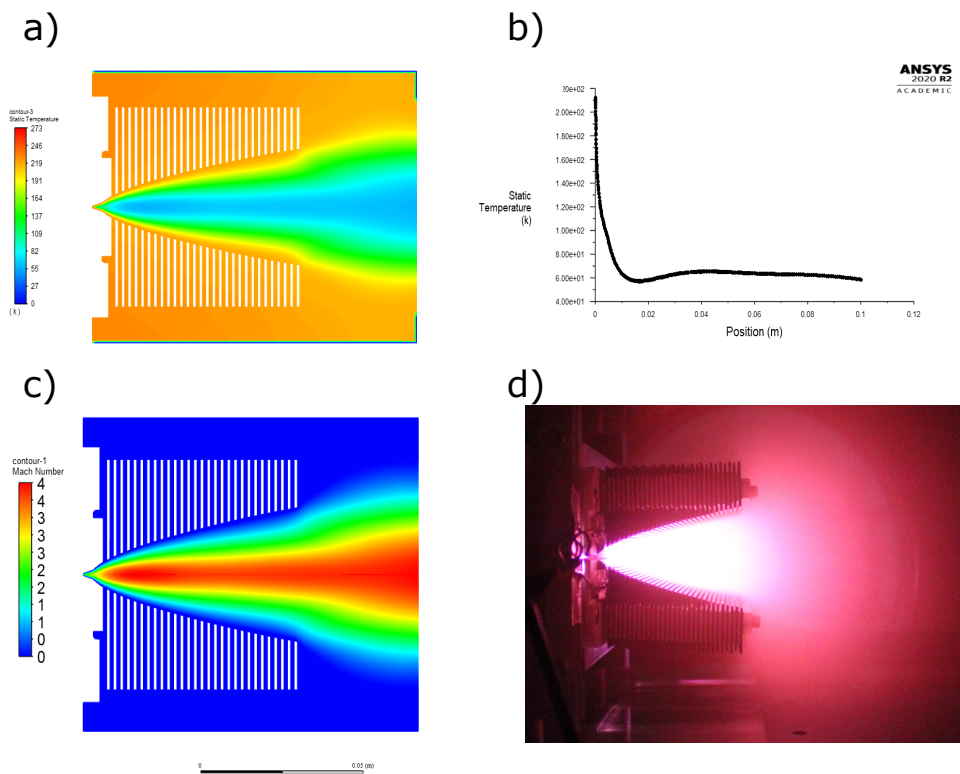


Figure 3.13 – a) CFD simulation showing the contour plot of the temperature of a jet of nitrogen expanded in a nozzle designed to operate with argon. b) Static temperature plot along the nozzle axis showing a strong variation. c) CFD simulation of Mach number. d) Photo of the jet visualized with a plasma of nitrogen which explains the red light color. Nitrogen has a different specific heat ratio, its molar mass is different from the one of argon and also its viscosity producing a different jet structure.

3.1.3 Ions optics

In order to increase the ion density in the interaction zone of the supersonic jet with the optical beam probe, we incorporated an ion guiding system in the divergent part of the nozzle. To this end, a series of electrodes has been distributed along the divergent part of the nozzle according to a geometric profile obtained from aerodynamic calculations (see Figure 3.14). As explained previously, such a profile was calculated as to produce a uniform supersonic flow.

A Radio-frequency (RF) and a direct current (DC) voltages are applied to the electrostatic system to manipulate and focus the charged species in the central part of the flow. The system is more efficient in the absence of a buffer gas, the ions can be handled with extreme precision and in a well understood manner using electric fields. In the case of a jet of higher pressure regime (0.1 to 10 torr), collisions with gas molecules increasingly dominate the behaviour of ion movement. It becomes much more difficult to control their movement over large distances, especially in the presence of strong dynamic gas effects. Under such pressure conditions, a multi-polar radio-frequency system is needed to ensure an efficient transmission and controlled guidance of the ions. The ions are produced in a high voltage (600-800 V) discharge at the nozzle throat and are then driven by the flow to be submitted to the electrostatic field created by the electrodes of the divergent part of the nozzle. Phase-shifted RF potentials are applied to adjacent electrodes, while a certain DC gradient is applied along the axis of the ion guiding system (Figure 3.14).

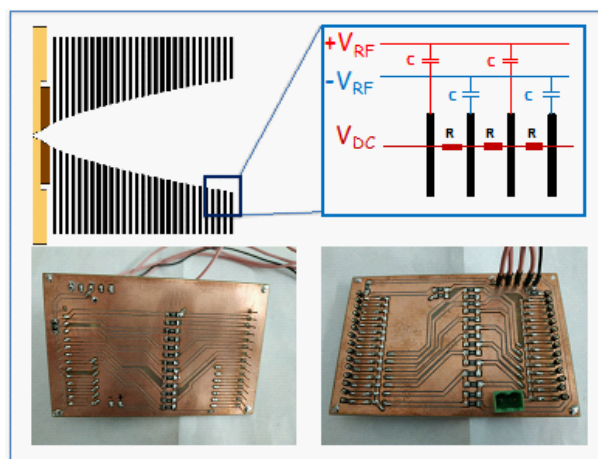


Figure 3.14 – Photo of the electronics controlling the polarisation of the electrodes, along with a schematic of the electrodes.

SIMION[®] simulation

A SIMION[®] simulation is essential to know exactly the values of the potentials and of the radio-frequency to be applied in order to obtain an optimal lensing of the ions, in what follows the details of the simulations are described. The simulation includes the two high voltage electrodes forming the ion source discharge. The voltage applied on the first electrode (1) on the left is set to -240 V and the second electrode (2) is set to ground potential (Figure 3.15). These two electrodes are separated by a distance of 4 mm. The set of equally spaced electrodes (3) is used to decelerate and to concentrate the ions on the axis of the flow. A DC voltage gradient of -28 V on the first electrode and 27 V on the last electrode of the series concentrates the ions at a point located 30 mm downstream from the electric discharge. This focal point can be changed by tuning the voltages applied on the electrodes of the set of electrodes (3). A RF voltage is also applied to the set (3). Following the testing of different frequencies, the optimal frequency is chosen to be equal to 1.1×10^6 Hz with a peak to peak voltage equal to 300 V. On the other hand the particles used in this simulation are divided into three groups: (i) positive ions with a mass of 40 UMA (argon) represented in blue, (ii) negative ions having a mass arbitrary fixed to 36 UMA represented in red, and (iii) electrons represented in black. All the particles have an initial circular distribution with a filled radius of 1 mm. The average speed is defined to be equal to 0.6 mm/ μ s (600 m/s) because the carrier gas is considered to be argon whose limit velocity is close to 600 m/s. All the ions are assumed to be produced between the two discharge electrodes (1) and (2). The result of the simulation is shown in Figure 3.15.

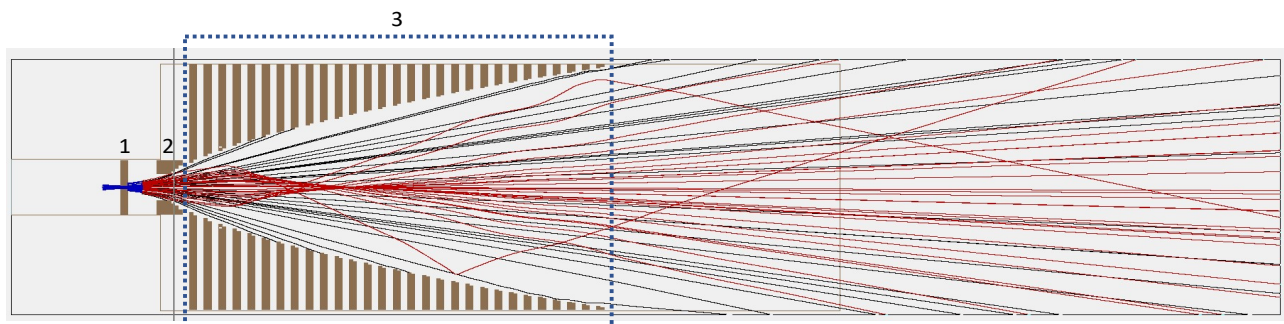


Figure 3.15 – SIMION[®] simulation of the trajectory of the ions. The anions are represented in red. The electrons in black and the protons in blue.

Comsol simulations

The previous simulation gives an idea about the electric fields that should be applied, but it does not take into account the action of the supersonic flow on the ion trajectories. For this, a more complex simulation is needed. To start, we present in the following table (table 3.3) the data used in the model:

Name	Value[unit]	Description
VD	200[V]	Discharge voltage
f0	1.2[MHz]	RF frequency
VPP	100[V]	RF peak-to-peak voltage
BGMM	0.04[Kg/mol]	Background gas molar mass
BGP	13.332[Pa]	Background gas pressure
BGT	80[K]	Background gas temperature
BND	1.2071e22[m ³]	Background number density
POT0	0[V]	Potential position 0
POT1	15[V]	Potential position 1
POT2	-15[V]	Potential position 2
POT3	-100[V]	Potential position 3
ICD	0.02[m]	Diameter of the isentropic flow
BGV	540[m/s]	Background gas velocity
CN	1[charge]	Charge number
ISP	0 [m/s]	Initial speed of particles
NPVS	3[particles]	number of particles in velocity space
Bias	200[V]	Bias potential

Table 3.3

The design of the ion guiding system was developed by computer modelling calculations using the Comsol software to evaluate the performance of this system and to optimize the different parameters. The Particle Tracing module was used to study the trajectory of the charged species in the flow. The electric fields resulting from the DC and RF electric potentials applied to the electrodes determine the trajectory of the ions.

Parameters such as temperature, jet velocity and density play an important role and are of course taken into account.

1. The **RF potential** of 100 Vpp at a frequency of 1.2 MHz is applied to the electrodes of the ion guiding system making it possible to produce in the flow a radial electric field able to confine the charged species on the axis of the flow and preventing the ions (positively or negatively charged) from recombining on the walls of the system. Figure 3.16 shows the design of the different electrodes, used for discharge and for the ion optics along with the values of the electric fields created by the application of the RF voltage.

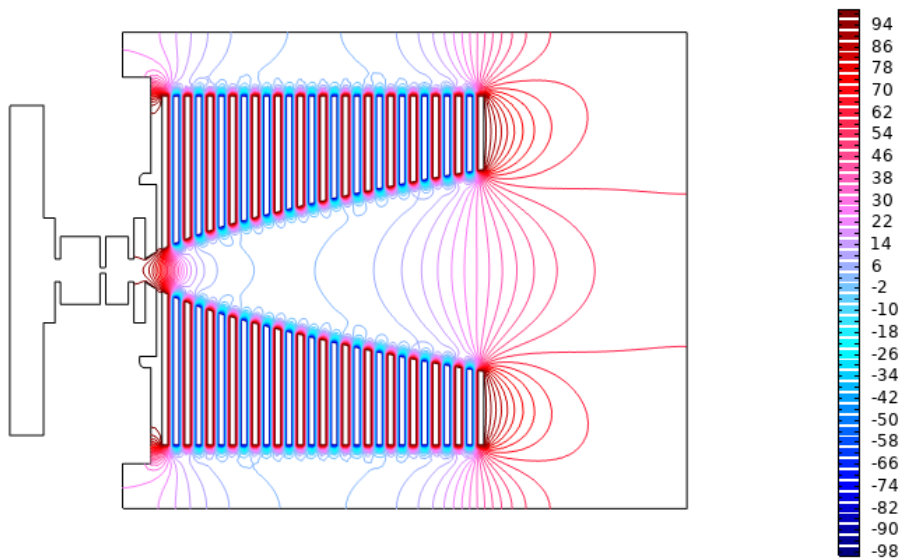


Figure 3.16 – Comsol representation of the electric fields and the value of the potential on the electrodes following the application of the RF voltage.

2. A tunable **DC potential** along the axis is also applied, allowing the creation of a potential well capable of slowing down the charged species and also to affect their trajectories. In our model, the applied DC voltage has a value of -15.65 V on the first electrodes and then changes gradually to reach 29.71 V on the last electrode. Electric fields resulting from the application of the DC voltages are shown in Figure 3.17.

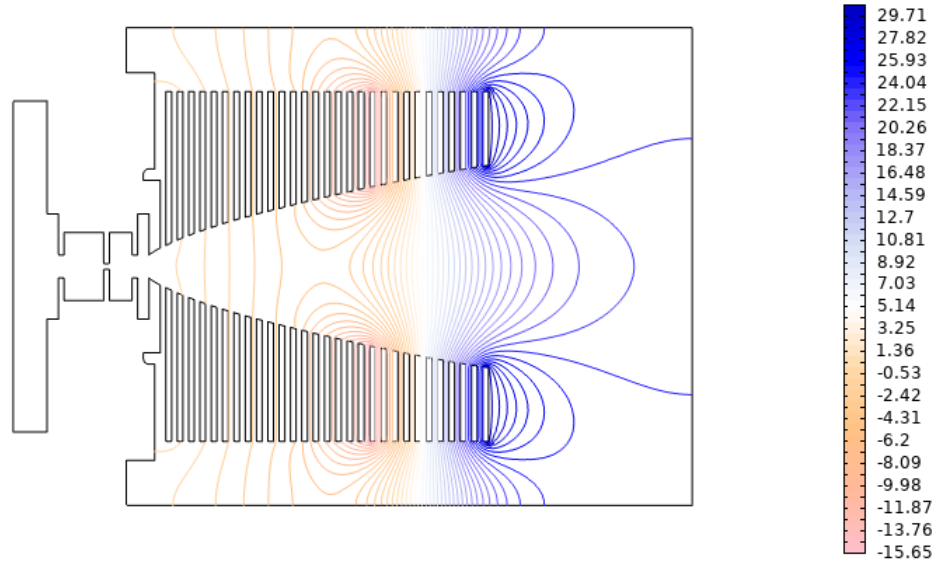


Figure 3.17 – Comsol representation of the electric fields and the value of the potential on the electrodes following the application of the DC voltages.

3. The combination of the two fields resulting from the DC and RF applied potential gives rise to one single field on the axis of propagation (x) of the flow. Figure 3.18 shows the potential on the electrodes in green and the resulting well of potential on the x-axis of propagation.

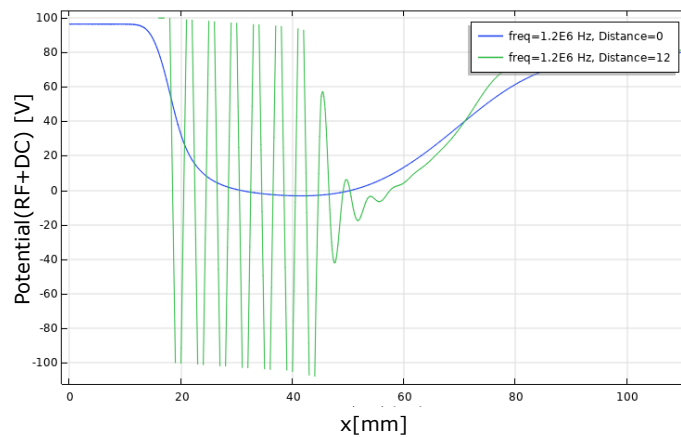


Figure 3.18 – Comsol representation of the plot of the potential resulting from the two applied DC and RF voltages. In blue, the profile of the total electric potential on the axis of the flow is represented. In green, the value of the electric potential on the level of the electrodes is represented.

4. Prior to the simulation, we define (i) the initial conditions of the ions (their mass, charge and distribution) and (ii) the conditions of the buffer gas (temperature, speed and density). The ion beam initial conditions (at the exit of the throat) are listed in Table 3.3 and the distribution of the initial velocity is set to be a hemispherical distribution. Figure 3.19 shows the result of the simulation without applying the electric potentials:

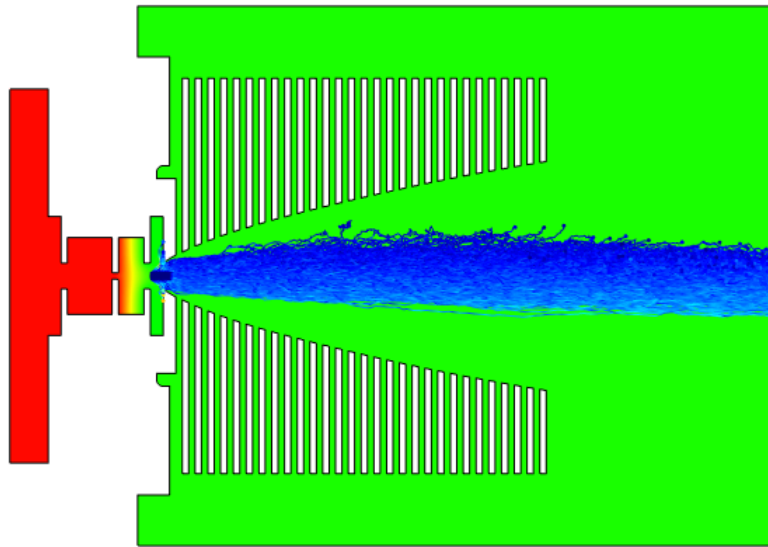


Figure 3.19 – Comsol simulation representation of the ions trajectory of Ar^+ ions seeded in argon gas in the absence of voltages on the electrodes.

5. The application of the RF and DC voltages results in the confinement of the trajectory of the ions by the electric fields created by the electrodes. The ions converge towards the axis of the propagation. The focal point could be then used as a probe axis for the laser beam. The size of this focal point must be as small as possible and be comparable to the diameter of the laser beam so that the interaction is optimized. This increases the local density of the charged species inside the optical cavity which in turn promotes the sensitivity of the spectroscopic instrument. The results are shown in Figure 3.20.

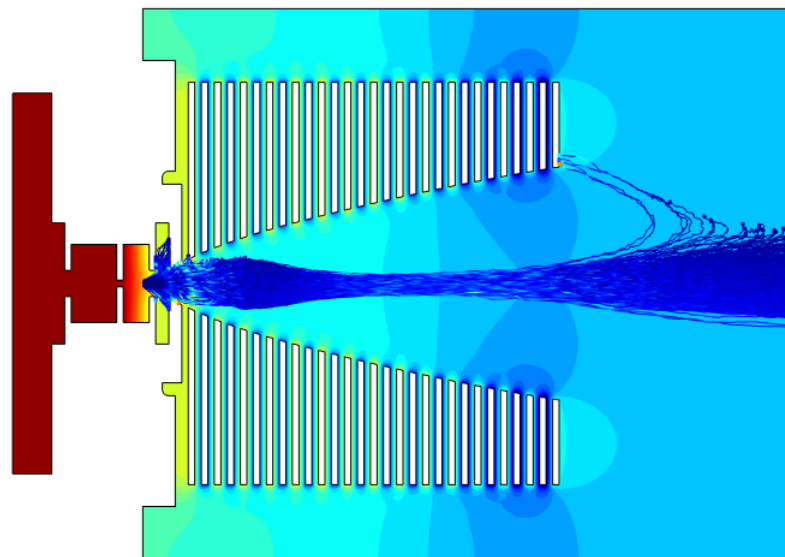


Figure 3.20 – Comsol trajectory simulation of Ar^+ seeded in argon after applying the DC and RF voltages on the electrodes. A focusing effect is obtained around 30 mm away from the nozzle throat.

3.2 High-sensitivity absorption techniques

The required sensitivity to achieve direct absorption spectroscopy of ions produced in low density can only be reached by increasing the pathlength of interaction between light and molecules through the use of resonant optical cavities. In particular, the development of cavity enhanced spectroscopic techniques led to several interesting studies of ions as reviewed by Linnartz [171]. Recently, the combination of Fourier-transform spectroscopy and incoherent broadband cavity-enhanced absorption spectroscopy in the near IR [172] demonstrates the usefulness of this approach for high resolution molecular spectroscopy, in particular when small sample volumes are required like the investigations of isotopic or dangerous samples, electric or plasma discharges (ions sample), flames, or chemical sources like flow tubes in a steady state. Before starting the detailed description of these techniques let us start with some basics. For years laser-based spectroscopy has been considered as a powerful means for the detection and the study of atoms and molecules. In particular absorption spectroscopy is widely used for the precise quantification of the concentration of atoms and molecules. Its basic principle is based on the Beer-Lambert law. Consider the spread of a monochromatic light beam of known intensity $I_0(\nu)$ in a isotropic homogeneous medium of length L . It is a question of measuring the transmitted light intensity $I(\nu)$ by a photodetector after crossing this medium for a certain frequency ν . Absorption is related to attenuation of light by Equation 3.1:

$$I(\nu) = I_0(\nu) \exp(-\alpha(\nu)L) \quad (3.1)$$

In which $\alpha(\nu)$ [cm^{-1}] is the absorption coefficient, it is also commonly expressed in molar quantities $\alpha(\nu) = C \times \epsilon(\nu)$, in which C is the concentration and ϵ is the molar extinction coefficient of the absorbing species. The product of α and the distance of interaction L is called "absorbance" expressed as $A(\nu) = \alpha(\nu) \times L$ and it is the normalized loss of light intensity per pass through the medium. $\alpha(\nu)$ is obtained using Equation 3.1 as follows:

$$\alpha(\nu) = -\frac{1}{L} \ln\left(\frac{I(\nu)}{I_0(\nu)}\right) \quad (3.2)$$

and it can also be expressed as a function of $\sigma(\nu)$ [$\text{cm}^2/\text{molecules}$] the absorption cross-section for a transition between two energy levels, N , the number of molecules per cm^3 , $S(T)$ is the intensity of the total absorption per molecule for a certain temperature T and

$\phi(\nu - \nu_0)$ which represent the normalised profile of the absorption line as follows:

$$\alpha(\nu) = N \times \sigma(\nu) = N \times S(T)\phi(\nu - \nu_0) \quad (3.3)$$

The absorption coefficient Equation 3.3 states that for a higher SNR we should have:

1. A high concentration.
2. A high absorption.
3. An important interaction length.

It is important to find the sensitivity of the measurement. Therefore, to assess the sensitivity, the minimum detectable absorption coefficient $\alpha_{min}(\nu)$ can be found by Equation 3.4:

$$\alpha_{min}(\nu) = \frac{I_0(\nu) - I(\nu)}{L \times I_0(\nu)} = \frac{\Delta I(\nu)}{L \times I_0(\nu)} \quad (3.4)$$

From Equation 3.4, increasing the sensitivity is equivalent to decreasing $\alpha_{min}(\nu)$. It can be achieved either by increasing the length of the optical path L or by reducing the noise level of the detected intensity $\Delta I(\nu)$. Many noise sources can contribute to the term $\Delta I(\nu)$, we can enumerate:

1. The fluctuations of the source $I_0(\nu)$
2. Electronic noise of the electronics of the detection
3. Interference fringes due to the formation of parasite cavities in the optical path

In order to find the detection limit one needs to find the minimum measurable concentration denoted as $n_{min}(\nu)$. From the Equation 3.3, $n_{min}(\nu)$ is written as:

$$n_{min}(\nu) = \frac{\alpha_{min}}{\sigma(\nu)} \quad (3.5)$$

In general, conventional absorption techniques use sources having a certain bandwidth so the spectrum contains several frequencies [173]. The principle of superposition [174] implies that each frequency of the spectrum of the source can be considered independent. Thus, after crossing the medium considered, the total intensity results from the sum of the intensities associated with each frequency. The absorption spectrum is obtained either by using a dispersive element (a diffraction grating or a prism) or by Fourier transform spectroscopy, the case of this thesis. This latter technique is called multiplexed because it allows the detection of a wide range of frequencies at the same time. Typical spectrometers using sources of incoherent light have a minimum detectable absorption coefficient varying

between 10^{-4}cm^{-1} to 10^{-5}cm^{-1} for an optical path varying between 10 cm to 100 cm [175]. To increase the length of the optical path, several techniques were developed. Initially appeared the optical multi-pass cells: like White cell [176] and Herriot cell [177]. Multi-pass cell allows an optical path length equal to a hundred times the physical length of the cell, up to several hundred meters. Coupled to a multi-pass cell, infrared Fourier transform spectrometers can reach a minimum detectable absorption coefficient of the order of 10^{-7}cm^{-1} [178]. Tests were done in the laboratory at IPR using a white cell scheme, the results and the details will be developed later in section 3.4.

After the development of high reflectivity dielectric mirrors (99.99%) the optical cavities start to appear. Through, compared to multi-pass cells, resonant cavities present two important advantages: a much higher interaction length which can be up to some hundreds of meters for medium finesse to ten kilometres, moreover using a cavity has the advantage of using a reduced sample volume. The light will enter the cavity through one of the cavity mirrors and exits through the other. The high reflectivity of the mirrors restrict the light from exiting and trap it in the cavity for a much longer time, thus for a much longer effective length. This is the basic concept behind cavity based methods and it can reach a much smaller detectable absorption coefficient relatively to the multi-pass cells. In this section we will start by describing two different techniques used and developed based on the augmentation of the optical path using high finesse cavities so called cavity absorption spectroscopy methods. The first method is time-dependent and called Cavity ring-down Spectroscopy (*CRDS*). The second method is intensity-dependent and called Cavity Enhanced Absorption Spectroscopy (*CEAS*) and their variants. In the following we will explain briefly the two methods, then we will develop the method used in this thesis which is intensity-dependent and based on using an incoherent broadband source and a Fourier transform detection. The method is called Incoherent Broadband Cavity Enhanced Absorption Spectroscopy (*FT-IBBCEAS*). Figure 3.21 shows the different techniques that lays on the cavity-enhanced absorption spectroscopy.

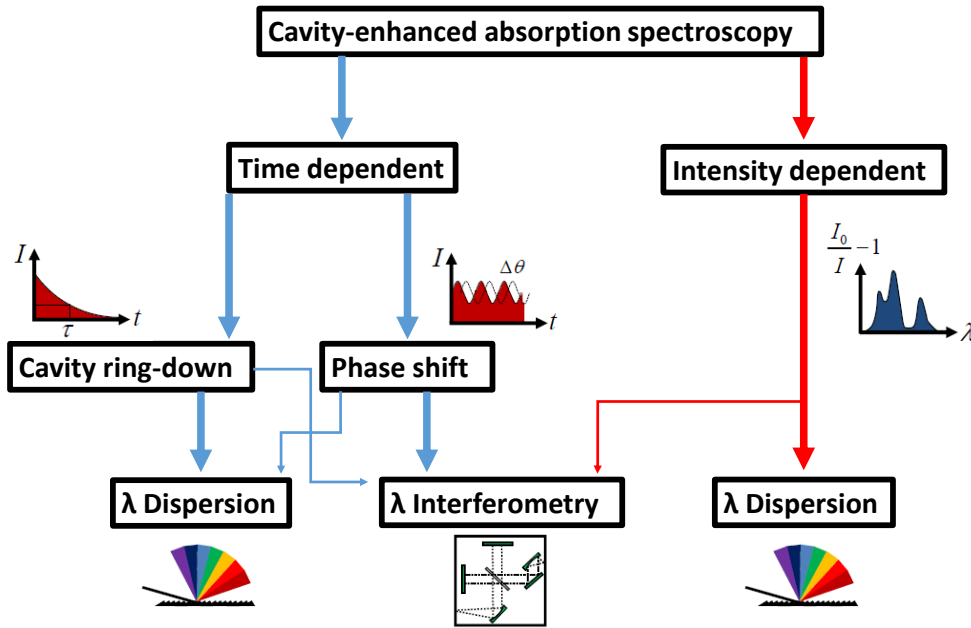


Figure 3.21 – Classification of cavity-enhanced absorption approaches and detection schemes, the size of the arrow indicates the weight of occurrences of type of approach in the literature (reproduced from [179]).

3.2.1 Cavity Enhanced Absorption Spectroscopy *CEAS*

CEAS is based on measuring the transmitted intensity through the optical cavity, the absorption is calculated directly from the losses of the intensity (see Figure 3.22). *CEAS* is experimentally less complicated than the techniques described in Appendix C. In fact, it requires a simpler optical alignment, it does not require fast electronics nor an acousto-optical modulator. Combined to a broadband light source, this method can measure with an important sensitivity the absorption spectrum of the gas inside the cavity. As for the *CW-CRDS*, the major difficulty in the *CEAS* lies in the injection of laser light into the narrowest cavity modes width (of the order of kHz). It is therefore essential to optimize the injection of the cavity, which requires different solutions depending on the characteristics of the laser source. In addition, the stability of the transmitted signal depends on the laser source, unlike *CRDS* where the decay time is in principle independent of source noise. Indeed, the signal is often affected by a larger level of noise caused by the frequency filtering of the cavity which converts the frequency fluctuations of the laser into amplitude fluctuations, which requires the accumulation of a higher number of scans [180]. The *CEAS* approach involves several steps. The first is the mode matching of

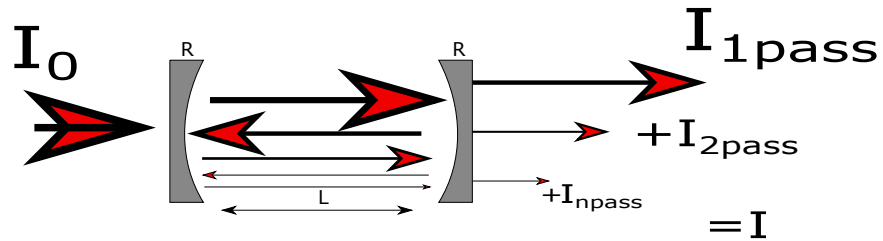


Figure 3.22 – Sketch of the IBB-CEAS principle, a schematic visualisation leading to understand the transmitted intensity I

the input laser to many different cavity modes, which means the TEM_{00} and also higher order transverse modes. The second is to record a series of laser frequency scans where the scan rate is rapid enough to suppress interference effects at any given frequency. Finally, slightly changing the mirror position during the scan, to shift the mode spectrum on successive laser scans [181]. Another difference from the *CRDS* scheme, is that to extract the absolute absorption, the cavity loss in the absence of the absorber must be known. Equation 3.6 gives the absorption coefficient at a given laser frequency (ν) and the intensity (I_0) in the absence and (I) in the presence of an absorber:

$$\alpha(\nu) = \frac{T}{L} \times \left(\frac{I_0(\nu)}{I(\nu)} - 1 \right) \quad (3.6)$$

The transmission in function of the finesse of the cavity is calculated using Equation 3.7

$$T = 1 - \frac{2F}{\pi} \alpha L \quad (3.7)$$

In which F is the finesse of the cavity and the effective length could be written as $L_{eff} = 2FL/\pi$. The Equation 3.7 states that in order to calibrate the absorption scale the finesse have to be found first. This calibration is done using a precise concentration of

the absorber gas in the cavity. Another technique is called *OF-CEAS*, it consists of re-injecting in a laser source a part of the constructive field of the high finesse cavity at each coincidence of the laser frequency and the TEM_{00} of the cavity. The optical retro-injection so-called Optical-Feedback, is possible in the case of a *V* cavity using three high reflective mirrors placed in *V* position. This technique is characterized by a high precision, a fast response time and a high sensibility [182].

3.2.2 Incoherent Broadband Cavity Enhanced Absorption Spectroscopy *IBB-CEAS*

The techniques described before, such as continuous wave absorption spectroscopy and cavity ring-down spectroscopy permit high resolution measurements with high sensitivity, but these techniques lack the ability to cover broadband spectral ranges in a relatively short acquisition time. Broadband cavity enhanced absorption spectroscopy is able to overcome this problem by measuring the broadband spectrum of a light source after the transmission through an optical high finesse cavity. In fact, an optical cavity is transparent for particular frequencies, even if excited with thermal, totally incoherent light. This is the superposition principle [183], the eigenmode structure of an optical cavity exclusively depends on its geometry, and is based on wave interference in the frequency domain (and not in the time domain), which are generally interpreted in terms of cavity resonances. The eigenmode structure is an inherent feature of the cavity and mode formation is independent of the coherence time of the excitation light. Practically, the measurement principles of *IBB-CEAS* could be described by considering the optical fields entering at different times into the cavity and interfering together after 1, 2, 3... round trips inside the cavity, resulting in uniformly spaced transmission resonance at frequencies $\nu = qc/2nL$ in which q is a positive integer.

These frequencies correspond to constructive interferences inside the cavity. If we consider a cavity of a certain length L with two high reflective mirrors that have the reflection r and transmission t amplitude coefficient, the corresponding transmitted field is written as following:

$$E(\nu) = E_0(\nu)t^2 \exp\left(-\frac{i\phi(\nu) + \alpha(\nu)L}{2}\right) \sum_{n=0}^{\infty} r^{2n} \exp(-i\phi(\nu) - \alpha(\nu)L)^n \quad (3.8)$$

In this Equation 3.8 $E(\nu)$ and $E_0(\nu)$ are respectively the transmitted field and the incident

field of the laser beam, n is an integer, α is the absorption coefficient of the species inside the cavity and $\phi(\nu)$ represents the phase shift of the field after a round trip in the cavity, given by Equation 3.9:

$$\phi(\nu) = 2Lk(\nu) = \frac{2\nu L}{c} \quad (3.9)$$

As mentioned before c is the speed of light and k is the wave vector amplitude.

The transmitted light

In the case of a high finesse cavity the transmission through the cavity is calculated using the cavity transmission function described in details in [174]. In order to find the transmitted intensity $I(\nu)$ through the cavity we start by calculating the modulus of the square of the field Equation 3.8: $I_0(\nu) = |E_0(\nu)|^2$ and by considering mirror transmission $T = |t|^2$ and the effective reflectivity $R = |r|^2$. $R_{eff}\nu = R(\nu)\exp(-\alpha(\nu)L)$ is introduced with the Airy function F_{airy} given by :

$$\frac{1}{F_{airy}(\nu)} = 1 + \frac{4R_{eff}(\nu)\sin^2(\phi(w)/2)}{(1 - R_{eff}(\nu))^2} \quad (3.10)$$

Using R_{eff} and airy Equation 3.10 we can find the equation for the transmitted intensity as following:

$$I(\nu) = I_0(\nu) \frac{T^2 \exp(-\alpha(\nu)L)}{(1 - R_{eff}(\nu))^2} F_{airy}(\nu) \quad (3.11)$$

The ratio $I(\nu)/I_0(\nu)$ defines the transfer function of the cavity $T_c(\nu)$. Which of a maximum of a mode the Airy function is maximum and equal to 1 and for weak absorption ($\alpha L \ll 1$) a first order development of the ratio gives :

$$T_c \simeq \frac{T^2}{(1 - R)^2} \left(1 + \alpha L \frac{R + 1}{R - 1}\right) \quad (3.12)$$

For this type of incoherent source, the transmitted intensity for a free spectral range(FSR) is the product of the integral of the transfer function (Equation 3.12) and the power density of the source. For frequencies in between resonances in which sine function is not close to 0, T_c drops and low transmission can occur. This is the case of destructive interferences of the circulating wave, a result for a non-resonant configuration of the cavity. On the other hand, at resonance ($\sin(kL) = 0$), the transmission is high due to the build up of a large intracavity field by constructive interference. For a broadband source it is

possible to calculate the low resolution cavity transmission, which can simply become the average transmission over several cavity modes. Therefore, the analytical solution of the transmission of the cavity is obtained by integrating the airy function (Equation 3.10) for a FSR that could be written as following:

$$T_{c,BB} = \frac{T^2 \exp(-\alpha L)}{1 - R \exp(-\alpha L)}^2 \times \frac{1}{2\pi} \times \int_0^{2\pi} \frac{1}{1 + m \sin(x)^2} dx \quad (3.13)$$

$T_{c,BB}$ is the transmission of the cavity, $m = 4R_{eff}(\lambda)/(1 - R_{eff}(\lambda))^2$ and $x = \phi(\nu)/2$ so the Equation 3.13 becomes:

$$T_{c,BB} = \frac{T^2 \exp(-\alpha L)}{1 - R^2 \exp(-2\alpha L)} \quad (3.14)$$

Again in the case of low absorption ($\alpha L \ll 1$) and with a high reflectivity coefficient the Equation 3.14 becomes:

$$T_{c,BB} \simeq \frac{T^2}{1 - R^2} \left(1 - \frac{1 + R^2}{1 - R^2} \alpha L\right) \simeq \frac{T^2}{2(1 - R)} \left(1 - \frac{F}{\pi} \alpha L\right) \quad (3.15)$$

F is the finesse (Appendix D). If we assume that $T \approx 1 - R$ which is the case of no losses due to diffraction or diffusion on the mirror, the Equation 3.15 becomes:

$$T_{c,BB} = \frac{T}{2} \left(1 - \frac{F}{\pi} \alpha L\right) \quad (3.16)$$

Equation 3.16 leads to finding the effective length L_{eff} in the case of a IBB-CEAS setup. It will be crucial later to find the absorption coefficient associated with the use of this setup also. So to start with the effective length, its is given by Equation 3.17 as following :

$$L_{eff} = \frac{FL}{\pi} = \frac{L}{1 - R} \quad (3.17)$$

So in this case the effect of the absorption is amplified by a factor equal to $\frac{F}{\pi}$

The injection of the cavity by a spatially incoherent source involves necessarily the excitation of several transverse modes. However, it does not affect the function of the transmission of the cavity (Equation 3.14). Indeed, for each transverse mode is associated a resonance comb quite similar to that associated with the TEM₀₀ mode, all these modes have the same FSR.

In order to have a precise calculation for the transmission we have to take in consider-

ation that the surface of the mirrors is not homogeneous, therefore not the same reflection coefficient $R(\nu)$ which is the case in this thesis as the used mirror has a reflectivity over a broad region of the spectrum (between 660 nm to 1250 nm) and the spectrum represents different values of R depending on the wavelength. As a result the transverse modes do not present the same losses. So for each transverse mode, we can associate the same expression of transmission of the cavity $T_{c,BB}$ but with using the different corresponding value of $R(\nu)$. So, the transmission through the cavity can be written as a sum of different functions $T_{c,BBm,n}$ (where (m, n) represents the order of the excited transverse modes) each associated with a different reflectivity value (Equation 3.18). We can not write a single cavity transmission function containing the effective reflectivity even for low absorptions.

$$T_{c,BB}(\nu) = \sum_{m,n} a_{m,n} T_{c,BBm,n}(\nu) = \sum_{m,n} \frac{T_{m,n}^2 \exp(-\alpha(\nu)L)}{1 - R_{m,n}^2 \exp(-2\alpha(\nu)L)} \quad (3.18)$$

in which $a_{m,n}$ are the projection of the incident beam on the different transverse modes. Therefore it is recommended to have a beam collimated with a small diameter inside the cavity, because the modes that are close to the center of the mirrors will have higher effective interaction length L_{eff} .

Equation 3.16 shows that the average cavity transmission could never be higher than $T/2$ which could be reached when there is no loss in the mirror and with the absence of the absorber inside the cavity. In fact the loss of the incident light intensity is one of the limitations in *IBB-CEAS* techniques. According to the transmission coefficient of the mirror T , a fraction T of the light is trapped inside of the cavity, which can partially be leaking in the forward direction and the other half in backward direction.

In figure 3.23, we compare the transmissions of a CEAS cavity (T_c) normalized to 1 for $\alpha = 0$ and the transmission calculated with the Beer-Lambert (BL) law for the same effective lengths. A minimal difference between BL and T_c is observed for small values of the absorption coefficient. The more the absorption becomes important, the more the gap increases between the curves reflecting the fact that the Beer-Lambert law is not suitable for the calculation of transmission of a *CEAS* cavity. Note also that for strong absorptions, the transmission signal of the *CEAS* decreases slower than that relating to the Beer-Lambert law. Which represents an interesting property for *CEAS* since it indicates that we have access to a wider range of the absorption coefficient values that could be measured. On the other hand, Fiedler *et al.*, recognized the existence of interference

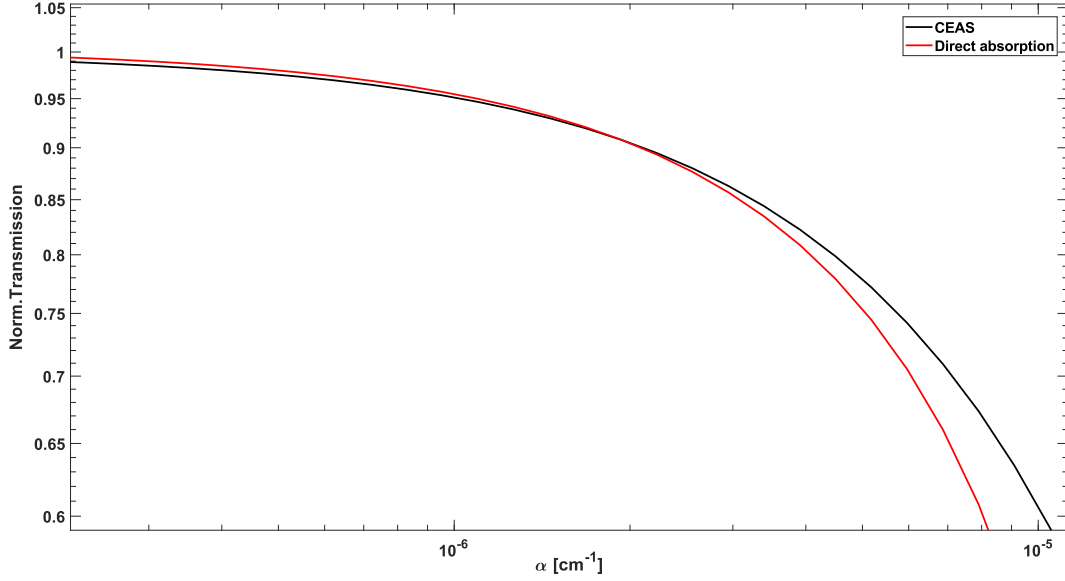


Figure 3.23 – Cavity transmission for a resonant *CEAS* in black and direct absorption over the same effective pathlength in red.

in the cavity produces transmission peaks at well defined resonance frequencies and the difference is that they based their derivation in the time domain. They considered simply a monochromatic light and they based the calculation on the superposition principle in the time domain in the cavity as illustrated in Figure 3.22. In addition, they assumed that the dielectric layers of the mirrors do not absorb light. $(1 - R)$ is due to imperfect mirror reflectivity and the cavity is subject to $(1 - Lo)$ losses per pass.

The intensity of the transmitted light through the cavity, I , can then be described by the sum of the intensities after an even number of reflections in the cavity. In this equation I_{in} is the intensity of the incident light.

$$\begin{aligned}
 I &= I_{in}(1 - R)(1 - Lo)(1 - R) && \text{First pass} \\
 &+ I_{in}(1 - R)(1 - Lo)R(1 - Lo)R(1 - L) \times (1 - R) + \dots + && \text{Second pass} \\
 &+ \dots \\
 &+ I_{in}(1 - R)(1 - R)R^n R^n (1 - Lo)^{2n+1} && n^{th} \text{ pass} \\
 &= I_{in}(1 - R)^2(1 - Lo) \sum R^{2n}(1 - Lo)^{2n}
 \end{aligned}$$

Since R and L are smaller than one this geometric series converges and the Equation 3.19

becomes:

$$I = I_{in} \frac{(1 - R)^2(1 - Lo)}{1 - R^2(1 - Lo)^2} \quad (3.19)$$

For an empty resonator the losses are equal to 0 therefore $Lo = 0$, thus we can define I_0 as $I_0 = I_{in}(1 - R)/(1 + R)$ (not to confuse I_0 with I_{in})

The absorption coefficient

Finding the absorption coefficient using *IBB-CEAS* technique consists of recording for the same experimental scheme the transmitted signal with then without the absorbing sample. We define s as the ratio between the two signal and it could be written as following:

$$s = \frac{T_{c,BB}(\alpha)}{T_{c,BB}(0)} = \frac{(1 - R)^2 \exp(-\alpha L)}{1 - R^2 \exp(-2\alpha L)} \quad (3.20)$$

This last equation, leads to find the absorption coefficient $\alpha(\nu)$ and it could be written as following:

$$\alpha(\nu) = -\frac{1}{L} \ln\left(\frac{R^2 - 1 + \sqrt{(R^2 - 1)^2 + 4s^2 R^2}}{2sR^2}\right) \quad (3.21)$$

After a Taylor development of the first order of the Equation 3.21 that is, taking $(1 - R)$ as a new variable for the expansion gives:

$$\alpha(\nu) = \frac{(1 - s)(1 - R)}{sL} \quad (3.22)$$

The error on finding α is relatively low for low absorptions and it could be around only about 10^{-3} as demonstrated by [173] so this equation is suitable for IBB-CEAS applications. Fiedler *et al* [184], obtained the absorption coefficient by using different approach in the the time domain as explained previously in section 3.2.2 and he obtained using Equation 3.19 the expression of losses which is equal to $(1 - L = \exp(-\alpha d))$ due to Lambert-Beer absorption which in turn is equal to the ratio of the measured intensities, without and with losses I_0/I :

$$(1 - L) = \pm \sqrt{\frac{1}{4} \left(\frac{I_0 (1 - R^2)}{I} \right)^2 + \frac{1}{R^2} - \frac{1}{2} \frac{I_0}{I}} \quad (3.23)$$

which if we apply the Lamber-Beer law we obtain the absorption coefficient α as following:

$$\alpha = \frac{1}{d} \left| \ln \left(\frac{1}{2R^2} \left(\sqrt{4R^2 + \left(\frac{I_0}{I} (R^2 - 1) \right)^2} + \frac{I_0}{I} (R^2 - 1) \right) \right) \right| \quad (3.24)$$

this expression of α in Equation 3.24 could be approximated for low losses and for high reflective mirror to give Equation 3.25

$$\alpha \approx \frac{1}{d} \left(\frac{I_0}{I} - 1 \right) (1 - R) \quad (3.25)$$

An example for α as a function of I_0/I is shown in Figure 3.24 for three different reflectivities R :

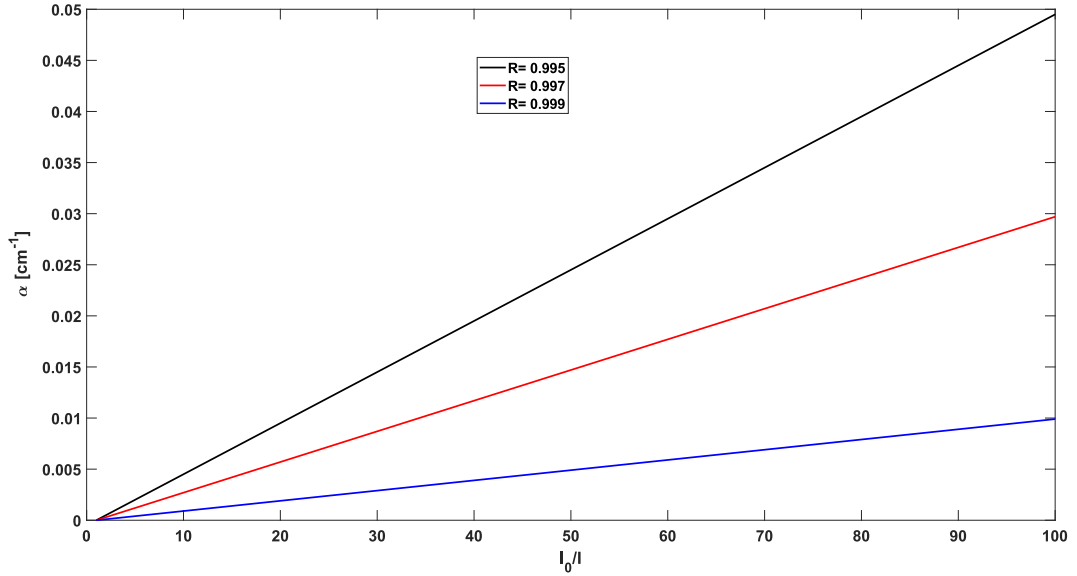


Figure 3.24 – Absorption coefficient α as a function of I_0/I for an optical cavity of length $d = 10$ cm and for different reflectivity.

Sensitivity of *IBB-CEAS*

According to Fiedler *et al.* the sensitivity of IBB-CEAS can be easily compared to that of a conventional single pass absorption spectroscopy. If we approximate that $\frac{I_0 - I}{I_0} \approx \frac{I_0 - I}{I}$ we can express the minimum absorption coefficient α_{min} by the following equation:

$$\alpha_{min} = \frac{1}{d} \left(1 - \frac{I_{min, single}}{I_{0, single}} \right) = \frac{1}{d} \left(1 - \frac{I_{min}}{I_0} \right) (1 - R) \quad (3.26)$$

In this equation, $I_{min, single}$ and I_{min} are respectively the minimum detectable intensities smaller than $I_{0, single}$ and I_0 . In addition, this equation indicates that this method is $(1 - R)^{-1}$ times more sensitive than a conventional single pass absorption method. For example if we consider a cavity having mirrors of reflectivity $R = 0.99$ this already corresponds to an enhancement factor equal to 100 in comparison to a conventional method.

Advantages, disadvantages of *IBB-CEAS*

A major limitation of the *IBB-CEAS* technique lies in knowing the precise reflectivity of the mirrors that determine the accuracy of absorption measurements of the target species. This precision could be limited also because of the contribution of the various transverse modes having different coefficients for different reflection intensity. Additionally, this technique offers a sensitivity 10 to 100 times lower than that reached with systems using *CRDS* and *CEAS* with monochromatic sources [185, 184, 173]. This sensitivity is achieved by averaging several spectra. Therefore, another inconvenience is that in order to achieve the best performance, the *IBB-CEAS* technique requires data acquisition times much longer than those offered by *CRDS* technique that could be done in seconds. However, systems employing this technique exhibit great simplicity, compactness, robustness and also a relatively low cost. Thus the *IBB-CEAS* method can compete with other techniques in certain applications where neither great sensitivity nor short measurement times are required. Furthermore, as mentioned in the introduction of this section, the absorption detection using *IBB-CEAS* technique is intensity dependant which exhibit different consequences cited as following:

- A calibration is required prior to the measurement in order to measure absolute absorption cross-sections.
- The mirror reflectivity for each wavelength is required over the entire range used for measurement.
- The measurement of I_{in} and I_0 should be measured to have ideal idea about the intensity fluctuation and eliminate it, but it is not always simple to do such measurement especially if a laser of high spectral power density is used.
- Longer integration time are required due to the limited detection sensitivity.

The spectral resolution is limited by the density of eigenmodes of the cavity which in the case of this technique is high, so the limitation comes from the detector we are using. The details are explained in the section 3.2.5. We have to note also that in *IBB-CEAS* spectroscopy, as opposed to *CRDS* there is no upper limit for strong absorptions,

saturation effects at very strong absorption are not considered [184]. However, some important practical advantages of *IBB-CEAS* which can be best described as a hybrid method between *CEAS* and conventional absorption spectroscopy, beside the advantages in term of sensitivity, compactness and robustness, the experimental setup is simple and does not requires much of the sophisticated electronics (feed-back loop, gates ... etc). This method could be also implemented over a broadband spectrum at one time which could be advantageous if we need to detect different bands for the same molecule or different molecules.

3.2.3 The light source choice

The choice of the light source is important because it will define the operating band of the spectrum, the light density, the spatial and temporal distribution in the cavity and whether the coupling can be effective or not. Listed hereafter are the different parameters of the light source that should be taken in consideration for a successful setup of a broadband cavity-enhanced spectroscopy technique.

1. *Broad unstructured emission spectrum*: A broadband source is of great interest to cover a wide spectral range in order to detect as many absorption bands as possible. However, rigorous filtering of the wavelengths outside the high reflectivity range of the cavity is essential to suppress the detection of unwanted frequencies contribution in the measured spectrum. It is preferable that the emission light is smooth and unstructured, so that the spectral intensity fluctuation will have less negative effects on the measurements.
2. *The source should have a high spectral brightness*: a large number of photons per unit area and time favours the coupling between a broadband source and high reflectivity mirrors. The smaller the emitting area for a specific output power the better are image properties but working on increasing the spatial coherence through spatial filtering is accompanied by a reduction in intensity [Wm^{-2}].
3. *A stable source with low spectral noise* is also of great importance. In fact, large spectral intensity gradients can be difficult to account for, even if the light source has only small fluctuations in intensity. The source needs a warm-up time before operating, otherwise the spectral potential will drift and the output intensity changes significantly.
4. And finally, *good mechanical an practical attributes* like robustness, compactness,

low maintenance, low cost and long life are key advantages for broadband *CEAS* and could influence the choice of the light source.

In the following section are summarized the most important light sources used in the literature to be coupled to *IBB-CEAS*.

Arc lamps

A xenon arc lamp is a type of gas discharge lamp. The light is produced by ionizing xenon gas at high pressure. Arc lamps produce a white light continuum covering the vacuum UV to the near infrared [172]. The most common Xenon arc lamps covers the region between 750 and 1000 nm and to a less extent around 475 nm. Most Xe-arc lamps have a diffuse distributed light emission which depends on the wattage rating of the bulb. Higher power lamps are not necessarily more appropriate for broadband cavity applications. Fiedler *et al.* 2013 [184] 'ISAS Berlin' used a xenon lamp with a luminosity of $18 \text{ W cm}^{-2}\text{sr}^{-1}\text{nm}^{-1}$ at 400 nm to measure the absorption spectrum of molecular oxygen at 1000 mbar in a static cell at room temperature and the absorption spectrum of gaseous azulene between 628 nm and 670 nm. The advantage cited by their article is the high spectral brightness. On the other side they encountered one disadvantage with the intensity fluctuations of their source. Another example is the one of Ashu-Ayem *et al.* 2012 [186]. They used *IBB-CEAS* to analyse the gas phase composition of their chamber, more precisely the absorption spectrum of I_2 (iodine) using a xenon arc lamp at 75 W. The advantage was the broad spectral region covering the visible region (400 nm to 800 nm), the disadvantage cited in their article was the high energy consumption of their light source. Different manufacturers are producing different arc lamps for different power, therefore, different brightness, and that could be couple to a collimation optics.

Halogen lamps

Halogen lamps are gas filled incandescent lamps containing a tungsten filament and a small amount of a halogen, such as iodine, that vaporize on heating and redeposits any evaporated tungsten particles back into the filament. Halogen lamps emit a smooth continuous spectrum from the near UV to the near IR. The advantage of halogen lamps over Xe lamps is the absence of lines and their price. However, the size of the emission and also their brightness make them less suitable for broadband *CEAS*. An example from the literature is the one of J. E. Thompson and H. D. Spangler [187]. They used a 250

W tungsten-halogen lamp (model TH-2). The technique was used to make quantitative measurements of Rayleigh scattering by carbon monoxide between 570 nm and 590 nm by integrated cavity output spectroscopy. A more related reference is the recent article of Prakash *et al.* 2018 [188], they used near-infrared incoherent broadband cavity enhanced absorption spectroscopy to measure the absorption spectra of methane, butane, ethane and propane in the wavelength region between 1100 nm and 1250 nm. They used a Tungsten-Halogen lamp from spectral products (ASBN-W-075B). Beside the advantage of low cost and easy use, this type of light sources requires a system of cooling to maintain the lamp at a certain temperature, beside the disadvantage of coupling efficiently the light to the cavity.

Light emitting diodes(LED)

Light-emitting diode (LED) is a semiconductor device that emits light when an electric current is applied and passes through it. High power color/white LEDs are efficient, compact, long lived and generally inexpensive. LEDs which are sufficiently bright for *CEAS* are available in the spectral range from the near infrared to the near UV. Being sensitive to temperature fluctuations they require an adequate temperature and current stabilization. LED spectra typically shift towards longer wavelength when the temperature increases [189]. The first application of LEDs for *IBB-CEAS* was demonstrated by Ball *et al.* [185], they used three different commercial LEDs as the light source: The ELJ-660-225B array and the similar SHPL-660-45 array (Roithner Lasertechnik, Austria) and the green LED (LXHL-LM3C, Lumileds Lighting, USA), each for different region of the spectrum. The light was first coupled into a 200 μm diameter, 0.22 NA fiber optic and then re-collimated and gently focussed into the cavity using a fiber collimator. Another example from the literature is the one of Wu *et al.* 2008 [190]. They used a high power blue LED (LXHL-LR3C, Lumileds Luxeon). It requires 3 W of electrical power and provide a radiometric power of 340 mW for the measurement of NO_2 absorption spectrum. In this article they mentioned the advantage of the high brightness and low power consumption of such light source.

Supercontinuum laser sources

In supercontinuum (SC) sources, the broadband spectrum is emitted by pumping a certain length of a highly non-linear micro-structured photonic crystal fiber (PCF) with short pulses from a seed laser having a high repetition rate. The advantage of using this

kind of sources is the high power density (up to several mW per nm due to high collimated fiber output). In addition, the spectrum is very broad; it typically extends from the blue region of the spectrum around 400 nm to the near-IR around $2.5 \mu\text{m}$ for a pump having a wavelength close to 1060 nm [191]. A major inconvenience is the optical feedback into the PCF, which makes the operation using an optical cavity difficult due to the strong back reflection on the back mirror of the cavity. The SC sources are known for their high power but also for their relatively high fluctuations. Langridge *et al.* were the first to use a SC source coupled to a broadband cavity in 2008 [192], for the quantitative measurement of NO_2 and NO_3 . Additionally, others like Ruth *et al.* 2005 implemented an interesting approach to create continuum radiation for the *IBB-CEAS*, which consists of generating supercontinuum radiation inside the cavity without the use of a PCF, this method is not simple to implement but it results in a notable enhancement of the coupling efficiency. Another example in the literature that has shown the importance of using this light source for the advantage of having a high power density and a broadband wavelength coverage was demonstrated by Chandran *et al.* 2016, [193], by using an open-path configuration explained in the following section 3.2.4 in order to measure NO_3 and aerosol extinction in northern china. The disadvantage they mentioned in their work was the instability of the source during long acquisition periods and its high cost. Figure 3.25 resumes the different used sources and the date of their implementation.

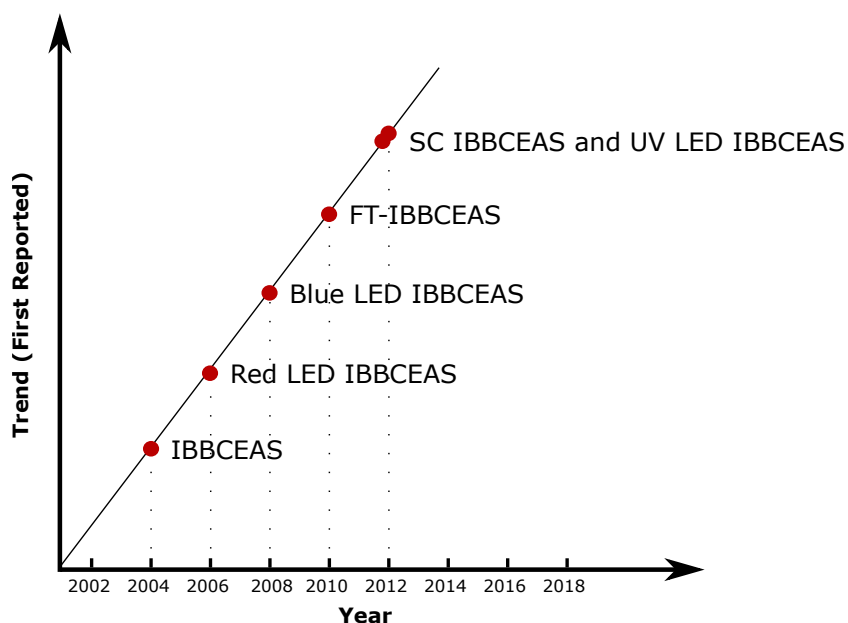


Figure 3.25 – Timeline of the different light sources used in the literature, reproduced from [194].

Comparative studies could be interesting to be discussed, a study done by C. Kaminski *et al.* 2009 [195] showed that the performance of a SC source is better in term of baseline noise and accuracy of the measurement compared to a white LED of 1 W, while the LED stayed advantageous in term of price and compactness. Other studies like the one of Denzer *et al.* 2011 [196], compare the performance of two near-IR superluminescent (SLEDs) that usually combine beam divergence and power density with the low temporal coherence of a conventional LED [197]. The latter study showed that the optical power from the SC source between 1600 nm and 1700 nm was four times higher than the total optical power incident on the cavity from the used SLEDs. In addition, a significant sensitivity improvement in a 4 min acquisition time was observed using the SC source. Table 3.4 summarize the different light sources along with the most important advantages and disadvantages. In conclusion, in this thesis the choice of the light source was a commercial supercontinuum laser described in details in section 3.3.

Source	Advantages	Disadvantages
Xenon lamp	High spectral brightness and a broadband emission	Intensity fluctuations and high energy consumption
LED	High brightness and low power consumption narrow full width at half maximum (FWHM)	Sensitive to temperature and current fluctuations
SC source	Ultra-high spectral brightness and a broader band emission	Unstable in a long acquisition periods and costly

Table 3.4 – Reported light sources used in IBCEAS, along with their advantages and disadvantages.

3.2.4 Cavity consideration

Optical resonators have acquired a growing interest since their invention, for their role as a key element for laser action, for the investigation of coherent radiation properties, and for all purposes that require control and enhancement of laser light. For almost all the electromagnetic spectrum, the physics of resonators has been well investigated with the experimental realization of very-high-quality-factor/finesse cavities, disclosing a large number of possible configurations [198, 199]. The most common reported geometry of

a cavity for *IBB-CEAS* measurement is the conventional linear mirror cavity formed by two highly reflective mirrors separated by a specific distance which is used in this thesis. Other interesting approaches could be found in the literature like the configuration of the V-shaped cavity used in *OF-IBB-CEAS*, created by folding a conventional linear cavity about its center with the addition of a third mirror. One major advantage is the possibility of using cavities of arbitrarily high finesse as needed to increase the sensitivity of physical measurements [200]. The term optical feedback (OF) describes the phenomenon whereby light entering the laser facet perturbs the free running condition of the laser, this could be used to couple efficiently the laser beam to the cavity [201]. Two other configurations are just to mention : the end-coated fiber cavity, or fiber Bragg gratings (FBGs) used as reflectors [202]. Another interesting approach is the use of prism cavity as explained hereafter.

Prism cavity

One of the most important parameters in *IBB-CEAS* is the bandwidth that it is able to cover. Using a broadband source and an adapted detection can help covering a broad spectrum region. The only limiting experimental factor of the spectral coverage is the high reflectivity range of the mirrors. Lehmann and Johnston [203] introduced in 2008 in case a supercontinuum source is available, a high finesse cavity based on retroreflector prisms with Brewster angle alignment. These prisms are made from fused silica with a reflectivity higher than 99.99% at 1064 nm. Depending on the prism material, large regions can be covered with high effective reflectivity. The experiment was carried out by recording the transition of molecular oxygen at 14529 cm^{-1} and the fifth overtone of the acetylene C-H stretch at 18430 cm^{-1} . The reader can find the experimental details and how the two prisms are aligned in their published work [203]. These prisms are designed so that the beam is incident to the air interface at an angle greater than the critical angle. The implementation is well described but still difficult to put in place because of the need of precise angles based on specially designed mechanical holders. Another inconvenient is the high price of these prisms.

Off-axis linear cavity used in IPR

The high-reflectivity mirrors (HRMs) are mounted on an optical breadboard placed inside a large vacuum chamber. The chamber is isolated using rubber to minimize the vibrations coming from the roots pumps. The two plano-concave HRMs have a radius

of curvature of 1 m and a reflectivity higher than 99.85% on the range of wavelengths extending from 620 nm to 1120 nm (Laser mirrors 153136 from the Layertec catalog). The mode matching was not done properly but the signal was maximized as described in the following section 3.3. Two alignment modes can be used for optical cavities. The first one is the on-axis alignment. Indeed, like a Fabry–Perot, the cavity acts as a spectral filter with transmission peaks spaced by the free-spectral-range (FSR). However, fixing the laser wavelength at the exact transmission peak requires complicated active-locking techniques. In our case we used the off-axis alignment. It is often introduced to suppress coupling noise when narrow-linewidth lasers are used. The reason of this off-axis geometry results in the excitation of an extremely dense mode spectrum so that the interaction between the laser and the cavity can be considered always resonant. This dramatically reduces the typical amplitude noise associated with the resonant behaviour of optical cavities. This can be adjusted by slightly changing the incident angle of the input beam. More information on on-axis and off-axis configurations are given in reference [204].

3.2.5 Detection using a Fourier Transform (FT) spectrometer

In terms of detection, the transmitted light can be either directly focused onto a monochromator with a CCD detector or can be injected into an interferometer. In the case of using a dispersive approach [205, 206], the light leaking out of the cavity can be injected into a monochromator. A reflective grating is used to disperse the light. Its slit width, the groove density of the grating and the distance between the injection point and the CCD detector, determine the spectral resolution that could be between 0.1 nm and 1 nm in the UV-VIS range. Although the detection over a wide wavelength range is rapid, the resolution and the sensitivity are still limited in comparison with the detection using an interferometric approach. In our case we use an interferometric approach [172, 207]. In fact, the light transmitted through the cavity is imaged into a Fourier-transform spectrometer. The latter relies on the use of a Michelson interferometer to measure the light spectrum. Light then undergoes constructive or destructive interferences depending on the relative distance travelled by the light in the two sides of the interferometer. The result is the apparition of interference pattern on the output. The interference signal is converted into an electrical signal by a single-channel detector, and a digital interferogram is obtained by means of an analog-to-digital (A/D) converter. Finally, the spectrum information is reconstructed after performing the Fourier transform on the recorded interferogram. The spectral resolution is determined by the maximum path length difference

caused by the two interfering beams, and limited by the size of the aperture. The intensity at the detector is the sum of the interference patterns of all the spectral components. For more information on the working principle the reader could refer to the article of A. Libert *et al.* [208]. The advantage of using this approach is the high sensitivity and resolution that could be reached. IPR is equipped with a Bruker IFS 125 HR interferometer whose maximum resolution is around 0.00185 cm^{-1} . The disadvantages are the long acquisition time required to record the spectra and the instrument is not compact and it is costly.

3.3 IBB-CEAS using a supercontinuum laser coupled to a high finesse cavity and a Fourier transform spectrometer, for the characterization of cold acetylene and cold methane

3.3.1 Experimental setup

In this section, we describe in details the experimental setup consisting of the cold source of molecules described in the first section 3.1 coupled to the optical technique *IBB-CEAS*. A preliminary result was obtained, we were able to measure the spectra of acetylene and methane at both ambient and low temperatures. The experimental apparatus of *IBB-CEAS* is schematically shown in Figure 3.26. The choice of our light source is a supercontinuum laser (YSL Photonics SC-Pro) shown in Figure 3.27

Laser's most important feature is its broadband spectrum that extends from 400 nm to 2400 nm. The laser power is tunable with a maximum power of 6 W, the manual advices to work using 90% to 100% of the total power to insure a relatively stable signal. A simple experimental test done in the laboratory showed that the fluctuation of the laser is minimal for higher power used which verifies the manual. The laser operates with an internal repetition rate that goes from 0.1 MHz to 25 MHz. In fact the modulation depends on the region that we want to study, each modulation rates is beneficial to study different frequency ranges. Figure 3.28 shows the emission spectrum of the supercontinuum laser given by [209] and the different emission spectra for different modulations measured in the lab. Figure 3.28 is the result of a test done to characterize the effect of the modulation on the emission spectrum of the laser beam. As we can see for a modulation ≈ 5 MHz we have a better signal in the visible area. On the other side, using a modulation of 25 MHz enhances the signal close to the pumping laser wavelength (around 1064 nm). The choice depends on the spectral region of the absorber.

The light is injected into the vacuum chamber using the original micro structured fiber optic so called photonic-crystal fiber (PCF). The fiber has a length of 1.5 m with a built in collimator at its end. The colimated supercontinuum light passes through an adapted sealed window. It is a commercial window sold by *wThorlabs* shown in Figure 3.29. The wedged aspect is chosen to insure that the light will not interfere due to parallel faces. The window is B-coated for a maximum transmission of wavelength between 650 nm and

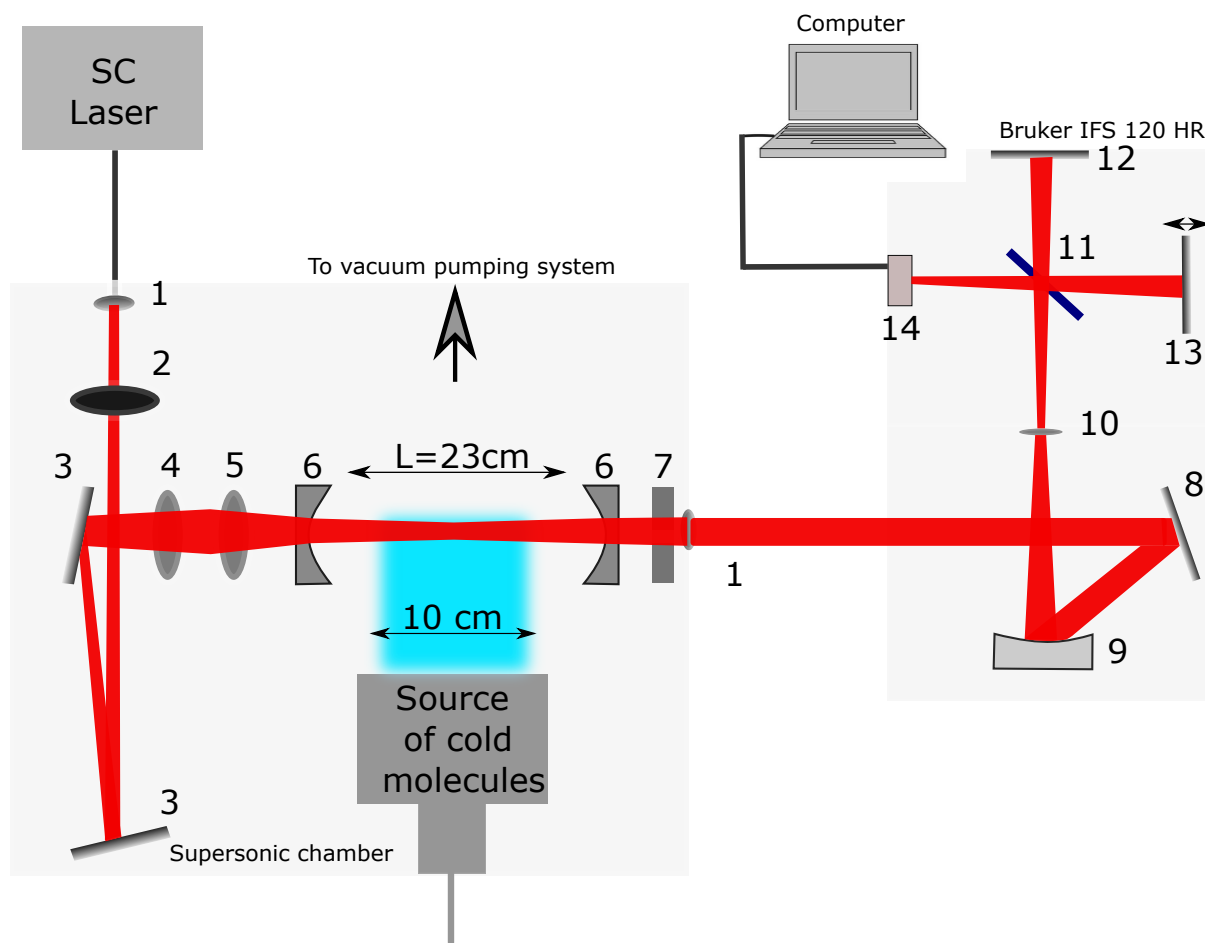


Figure 3.26 – Experimental setup of the *FT-IBB-CEAS*. It consists of a supercontinuum laser injected into the vacuum chamber using a fiber optic with a built in collimator at the end. The basic elements of this setup are: (1) adapted window, (2) optical filter, (3) two planar mirrors, (4) and (5) two achromatic lenses, (6) optical cavity, (7) iris. The transmitted light is coupled to the Fourier transform spectrometer. (8) planar mirror, (9) concave mirror, (10) spectrometer aperture, (11) beam splitter, (12) fixed mirror, (13) moving mirror and (14) detector. The signal is then analysed using a computer. The cavity length is $L = 23$ cm, and the supersonic expansion diameter is 10 cm which correspond to the interaction length for a single passage of the light. The planar cold jet of molecules is represented in blue.

1050 nm corresponding to our region of study. Figure 3.30 shows the reflectance of the window (devoted as number 1 in Figure 3.26) in function of the wavelength. The average reflectance corresponding to the relevant spectral region marked in grey is $\approx 0.05\%$ in average. In order to have a stable injection of the laser light to maintain the vacuum inside the chamber, a small stainless steel optical feedthrough was fabricated and sealed using a KF-40 hinge clamp. The mirror was fixed and sealed using an o-ring and six screws to press the mirror on it (Figure 3.31).

The bandwidth of the light is narrowed using an optical filter to correspond to the

3.3. IBB-CEAS using a supercontinuum laser coupled to a high finesse cavity and a Fourier transform spectrometer, for the characterization of cold acetylene and cold methane



Figure 3.27 – YSL Photonics SC-Pro

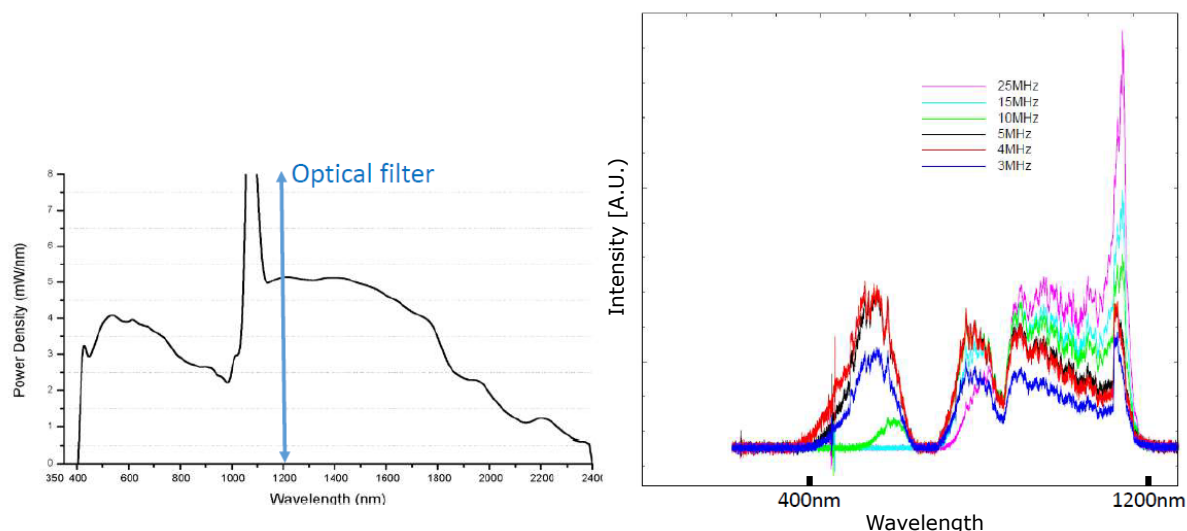


Figure 3.28 – On the left, the emission spectrum given by the product manual sheet and on the right the emission spectrum of the laser with a power set to 50% for different modulation values.

bandwidth of the optical cavity. It is difficult or even impossible to find a single optical filter capable of covering more than 100 nm and at the same time completely suppressing wavelengths outside its range. For this reason, a series of filters were used depending on the spectral range of interest. By using two conventional plane mirrors we were able to direct the laser light and center it on the optical axis of the cavity. The first optical alignments showed that we slightly lost the signal after pumping the chamber. The reason was clear, when the chamber is pumped the optics slightly change their position. Therefore, two controlling steering motors (Figure 3.32) were added to one of the mirrors. The x and y

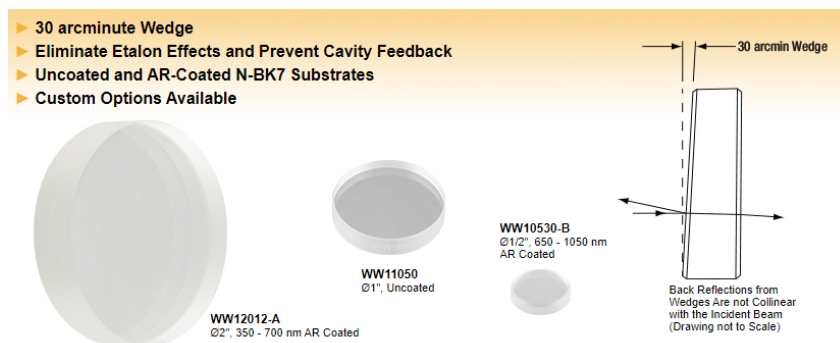


Figure 3.29 – Photo of the wedged window used for the injection of the laser light into the vacuum chamber, taken from *Thorlabs*

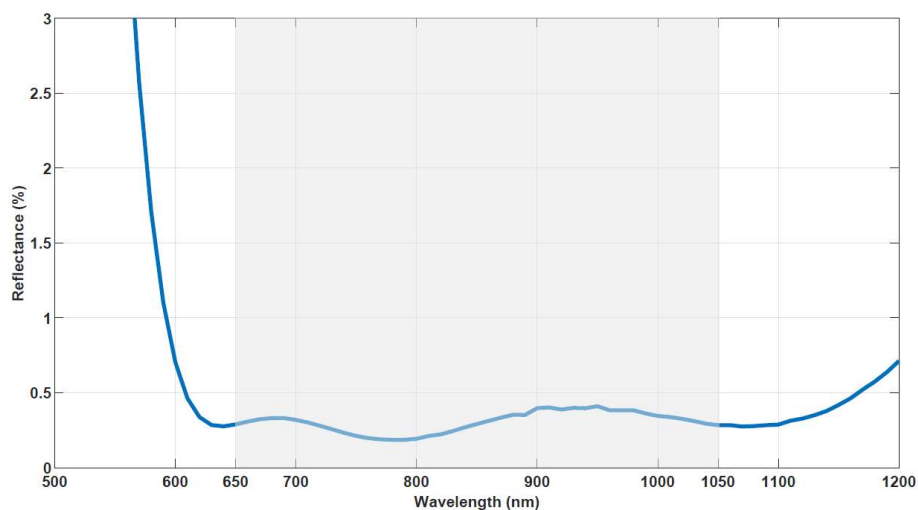


Figure 3.30 – The reflectance of the window given by *Thorlabs* and reproduced.

positions of the mirror can thus be modified from the outside after that the vacuum has been established inside the chamber.

Two achromatic doublets lenses were used, with respectively a focal length of $f_1 = 150$ mm and $f_2 = 30$ mm, both operating in the range between 650 nm and 1050 nm. These two lenses are designed to limit the chromatic and aberration effects. In fact, as our laser source is broadband and presents different wavelengths, the achromatic lenses are able to

3.3. IBB-CEAS using a supercontinuum laser coupled to a high finesse cavity and a Fourier transform spectrometer, for the characterization of cold acetylene and cold methane

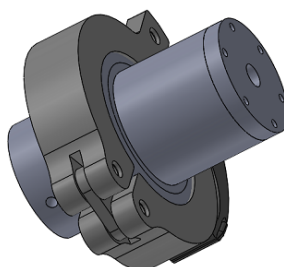


Figure 3.31 – The conception assembly of the mechanical part used to introduce the light into the vacuum chamber and the KF-40 hinge clamp attached to it.



Figure 3.32 – Photo of the two motors fixed on the mirror, making it easy to control and steer the mirror in the x and y direction with a simple controller outside of the chamber

focus all the wavelengths on the same plane. The position and the focal lengths of the two lenses were chosen precisely to ensure a maximum coupling of the light with the cavity.

The following element which is the most important is the cavity, explained in the following section 3.3.2.

3.3.2 Mode matching

To achieve a good signal-to-noise ratio (S/N), it is important to match the first order mode of the laser beam, that is supposed to be Gaussian, with the one of the cavity. The laser mode is directly linked to the shape of its propagating ray which is characterised by two parameters as described in Appendix D. As a reminder, the parameter are w and R , the half width of the beam and the radius of curvature of the wavefront of the beam, respectively. Mode matching consists to adapt these two parameters to the cavity resonant modes. The cavity is characterized by its waist size, its position, and its Rayleigh range. Our objective is to have a minimum divergence of the laser beam to couple the light effectively to the Fourier transform spectrometer. In the following, we will start characterizing the laser beam at the output of the fiber optic (Section 3.3.2). Following this first step we will characterise our cavity and finally using the ABCD formalism we will find the approximative position of the lenses, their focal lengths and the position of the laser beam relatively to the cavity position.

Laser beam properties

First we will start by finding an approximation of the beam waist position $z(waist)$ relatively to the output of the optical fiber and diameter w_0 . Therefore, a simple experimental setup has been installed. As a reminder, the laser source being a supercontinuum laser with a broadband spectrum, each wavelength leads to a specific waist $w_0(\nu)$ and waist position $z(waist(\nu))$ which make the mode matching a little challenging because we need to couple a maximum of light for a certain range of wavelengths (in our case between 650 nm and 1050 nm). The advantage using a supercontinuum laser is that the beam is well collimated and the diameter at the exit is approximatively equal to 3 mm at 70% power of the laser beam. The characterization method consists of measuring the beam power using a power-meter for different positions from the laser beam. In fact, we first measured the beam maximum power. To this end, we gradually obscure the beam using a razor and with a conventional millimeter-scale ruler we measured the power difference between the initial position (x_i) of the razor at maximum power and the final position (x_f) for which the power is divided by two. Therefore, the physical quantity $(x_f - x_i)_{position}$ represents the beam half diameter for different positions relatively to the exit of the fiber. Figure 3.33 represents, in red, the quantity $x_{f_{x_i}}$, symmetrical sketch models the complete profile of the beam, and in blue, the extrapolation of the two rays using a linear fit. The

3.3. IBB-CEAS using a supercontinuum laser coupled to a high finesse cavity and a Fourier transform spectrometer, for the characterization of cold acetylene and cold methane

two lines meet at a point considered to be the laser waist position. Therefore the position

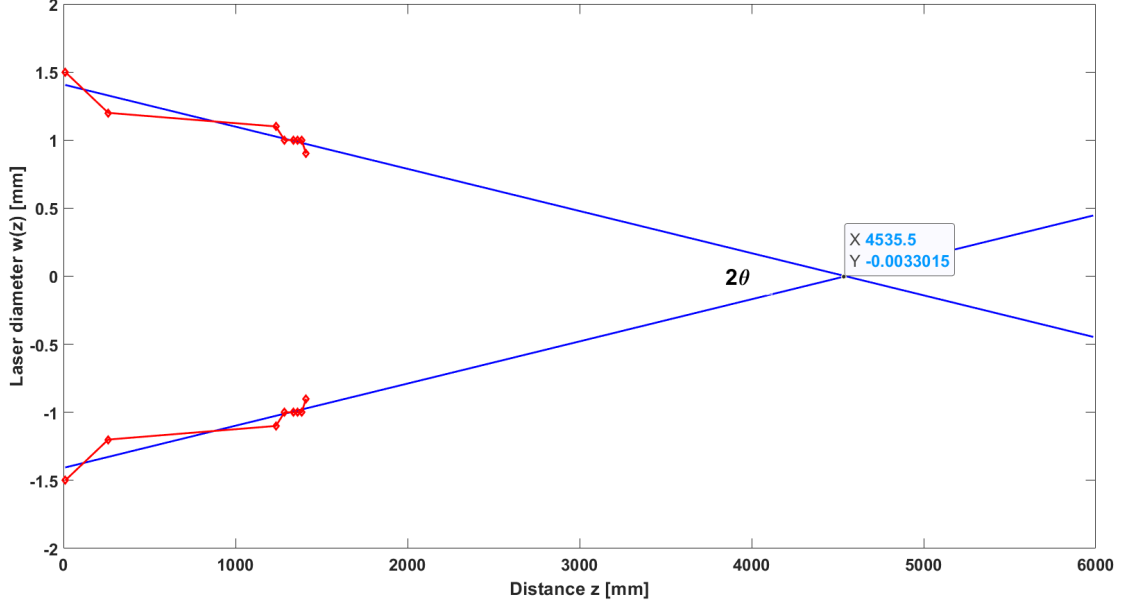


Figure 3.33 – The beam diameter relatively to the distance from the fiber output. The details are explained in the text and the diamonds markers correspond to the different testing positions. The beam divergence θ is also presented in the figure.

of the waist is at $z(w_0) = 4535.5$ mm. The next step is to find the beam divergence θ , for this, we can simply resolve the equation :

$$\frac{\theta}{2} = \text{Arctan}\left(\frac{w(z=0)}{z(w_0)}\right) = 3.307 \times 10^{-4} \text{rad} \quad (3.27)$$

The divergence of the beam and its waist (w_0) are related via Equation 3.28:

$$\theta = \frac{\lambda}{\pi w_0} \quad (3.28)$$

Therefore the waist is calculated using Equation 3.28 and it is found to be equal to $w_0 = 0.5775$ mm. using the beam waist we can find $z_r = 1.7462 \times 10^3$ mm and we can finally use z_r and w_0 to model the laser beam using a Gaussian profile (from Appendix D). Figure 3.34 shows the gaussian fit modelling our laser beam profile. We can conclude and consider the laser as low divergent, and this is an advantage because it requires less complicated optical alignment. Now the next step consists on calculating the different positions of the two lenses for an approximation of the best optical configuration for an

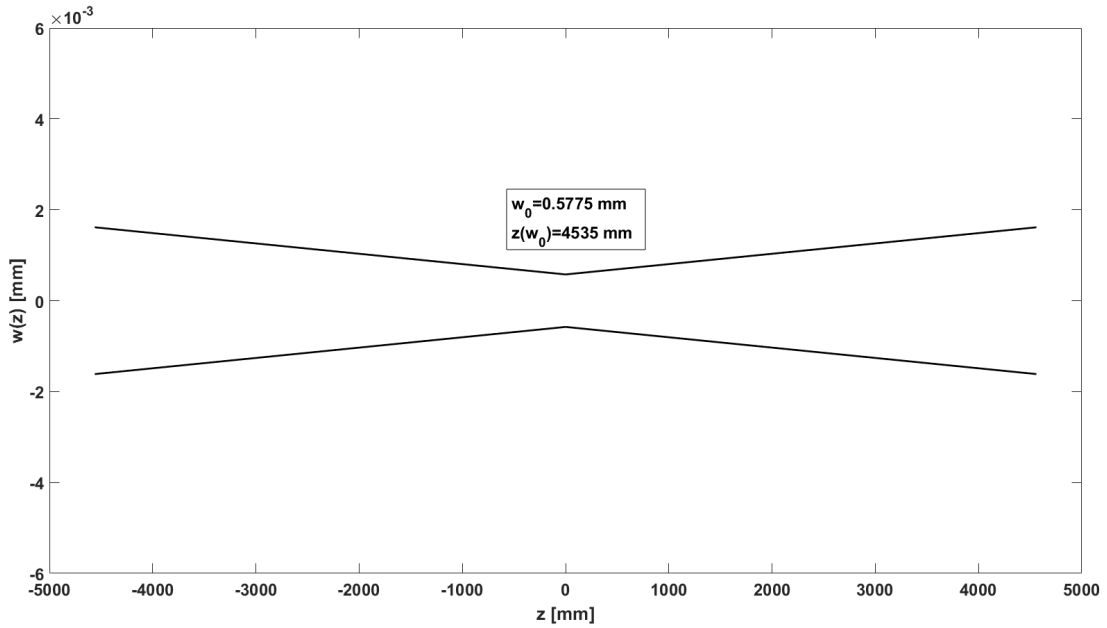


Figure 3.34 – Gaussian profile of the laser beam where the diameter at the output of the laser is ~ 3 mm and the waist w_0 is approximately equal to 0.5775 mm positioned at ~ 4535 mm from the laser output.

optimal coupling of the laser beam and the cavity.

Cavity characteristics

The cavity considered in this thesis is composed of two spherical mirrors with the same radius of curvature, $R = 1000$ mm separated by a distance of 23 cm. The cavity stability is verified using Equation D.24 from Appendix D which gives:

$$0 \leq 0.5929 \leq 1 \tag{3.29}$$

The resonant mode of a cavity is a Gaussian mode corresponding to a stationary wave inside the cavity. For each stationary wave there are several resonant transverse modes of different orders. In the calculations we tried to 'match mode' the less divergent mode which is the TEM_{00} mode. If we assume a gaussian beam travelling along the z-axis with a wave number k and an electric field of amplitude E_0 , the evolution of the electric field

along the z-axis can be described by the Equation 3.30 [210]:

$$E(x, y, z) = E_0 \left[\frac{w_0}{w(z)} \exp\left(\frac{-r^2}{w(z)^2}\right) \right] \exp\left[-i\left(kz - \arctan\left(\frac{z}{z_r}\right)\right)\right] \exp\left[-i\frac{kr^2}{2R(z)}\right] \quad (3.30)$$

In this equation, w_0 is the beam waist of the resonant mode. It corresponds to the minimum half width of the beam inside the cavity and it is located at the center because the mirrors have the same radius of curvature. The quantity z_r is the Rayleigh length characterizing the divergence of the gaussian beam. The detailed equations can be found in the Appendix D. Using equation $z_r = \sqrt{(R - \frac{d}{2})\frac{d}{2}}$ and $w_0 = \sqrt{z_r \frac{\lambda}{\pi}}$. The waist inside the cavity is $w_0 = 0.251$ mm.

ABCD formalism and mode matching

As already shown in the previous sections, the laser beam has a low divergence, which is advantageous and allows the experimentalist not to worry about the coupling of the laser beam to the cavity or to the Fourier Transform spectrometer. Thus, by adapting the beam waist to the waist of the cavity while keeping the beam divergence low, we can efficiently couple the first order mode of the laser beam to that of the optical cavity without worrying for other wavelength that should also be somehow coupled because the laser beam has high spatial coherence. The ABCD formalism is used to describe the effect of each optical device on a gaussian beam and it is based on the q parameter (see Appendix D). The propagation of the beam is studied by fixing a position for the first lens relatively to the laser output which is chosen to be 200 mm. Then the q factor is calculated taking into consideration the focus parameters of the first lens. To do so we recall the Equation D.16 from the Appendix D:

$$q(z) = z + iz_r \quad (3.31)$$

The q-parameter of the laser is first calculated to be equal to:

$$q_{laser} = i \frac{\pi w_{(0,laser)}^2}{\lambda} \quad (3.32)$$

And the final q-parameter which corresponds to the one of the cavity is equal to:

$$q_{final} = i \frac{\pi w_{(0,cavity)}^2}{\lambda} \quad (3.33)$$

The thickness of the high reflective mirrors is equal to $te = 6.35 \times 10^{-3}$ and the refractive index of the material of the mirrors is $n_m = 1.457$ which allows to calculate the ABCD matrix of the output of the first mirror of the resonator.

Therefore, we obtained the transfer matrix by multiplying the matrices that correspond to (i) a refraction of the flat surface of the HR mirror, (ii) a propagation inside the HR mirror, (iii) a refraction on the curved side of the mirror, and finally a free propagation reaching the middle of the cavity to match its waist. The matrices are written from the right to the left and multiplied to obtain the ABCD matrix of this transfer as following:

$$\begin{bmatrix} 1 & \frac{l}{2} \\ 0 & 1 \end{bmatrix} \begin{bmatrix} 1 & 0 \\ n_m - 1 & n_m \end{bmatrix} \begin{bmatrix} 1 & te \\ 0 & 1 \end{bmatrix} \begin{bmatrix} 1 & 0 \\ 0 & \frac{1}{n_m} \end{bmatrix}$$

Afterwards, we can find the q-parameter, q_{left} before entering the cavity by applying Equation D.17 from Appendix D to q_{final} . The lengths L_1 and L_2 respectively (see Figure 3.35) between the first lens ((4) in Figure 3.26) and the second one ((5) in Figure 3.26) and between the second lens and the first cavity mirror L_3 , are then calculated, by resolving the two obtained equations for the q-parameter that correspond to the ray after the first lens and the ray just before entering the cavity. The details of the calculation algorithm is given in the Appendix D Equation D.6 which finally gives the result below as illustrated in Figure 3.35.

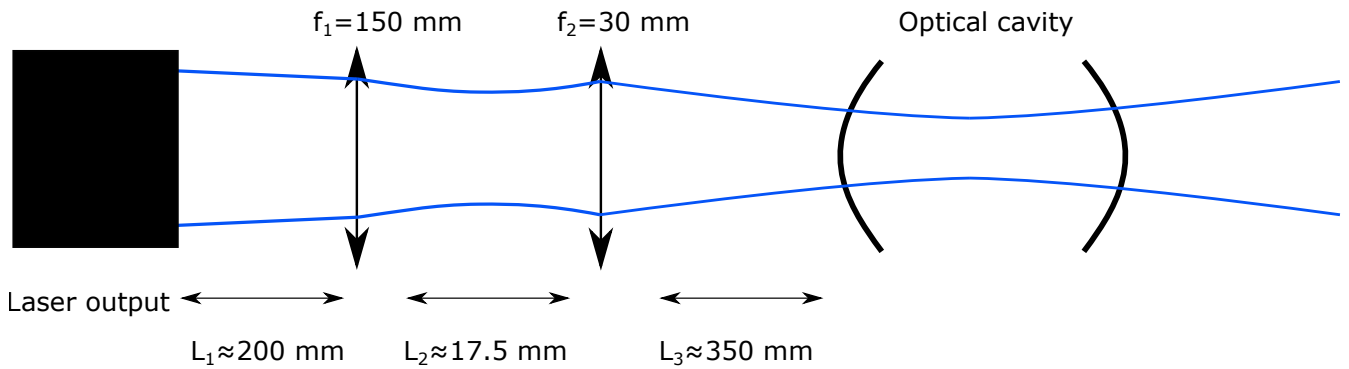


Figure 3.35 – The representation of the different calculated lengths between different optical components starting from the output of the laser beam to the exit of the cavity. This figure also illustrates the width of the beam in the optical system represented by a blue color.

Practically, we started by fixing the optics at the same exact positions that we calculated. Then by monitoring the signal in real-time, we managed to enhance the signal, hence the coupling to the cavity, by moving the lenses finding the optimal distances ex-

3.3. IBB-CEAS using a supercontinuum laser coupled to a high finesse cavity and a Fourier transform spectrometer, for the characterization of cold acetylene and cold methane

perimentally. Hopefully, the experimental positions were not that far from the calculated ones.

3.4 Results and perspectives

Calibrating the instrument and characterizing its properties is done by measuring the transmitted spectra through the optical setup. A **preliminary measurement** was done using a multi-pass cell (White-cell scheme) and the description of this method is well known since 1942 [211]. Briefly it consists on coupling the light source to a system of mirrors as illustrated in Figure 3.36, and then to inject the output of the mirrors into spectrometer which is a commercial Fourier transform spectrometer (Bruker IFS 125 HR) in our case. This measurement helped us to validate the coupling of the laser to the spectrometer.

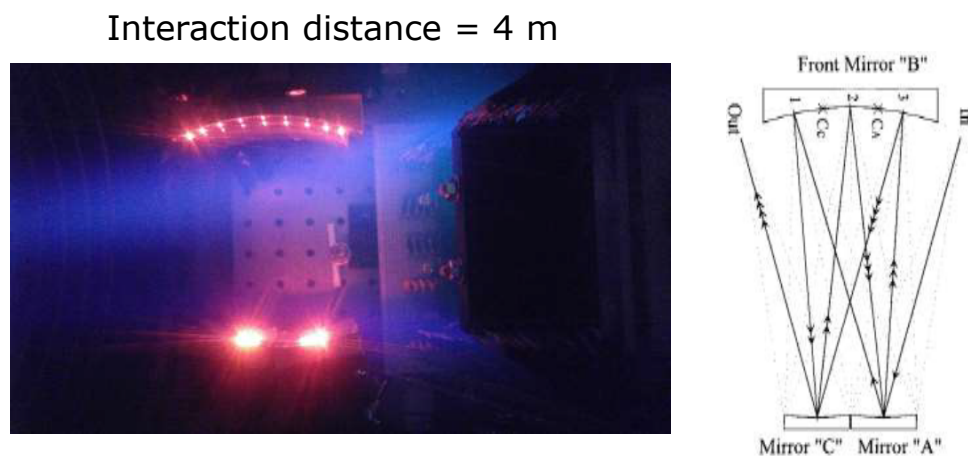


Figure 3.36 – On the left, a photo of the white cell scheme while operating, the glowing goes to the discharge of a portion of methane seeded in argon (50%), the parallel mirrors are separated by 10 cm. The dots on the mirrors corresponds to the laser light. On the right a simple illustration of the path of the laser light on the mirrors, in this illustration the light undergoes seven reflections before getting out. In our case the light was able to undergo 39 reflections which correspond to 4 m of interaction with the cold molecules.

We recorded the absorption spectrum of methane at ambient temperature; by injecting 20 torr of methane into the chamber. Then, using the Laval nozzle, which supposed to produce molecules at low temperature we recorded the spectrum of the same gas by injecting methane seeded in argon (50% - 50%). The obtained spectrum (see Figure 3.37 validates the coupling between the supercontinuum light source and the FTs. However, due to the modest absorption pathlength of 4 m, the S/N is relatively poor. Highlighting the necessity of using a high finesse optical cavity.

In experimental spectroscopy, researchers developing an instrument should pay attention to three essential parameters: (1) the spectral bandwidth, (2) the resolution and the

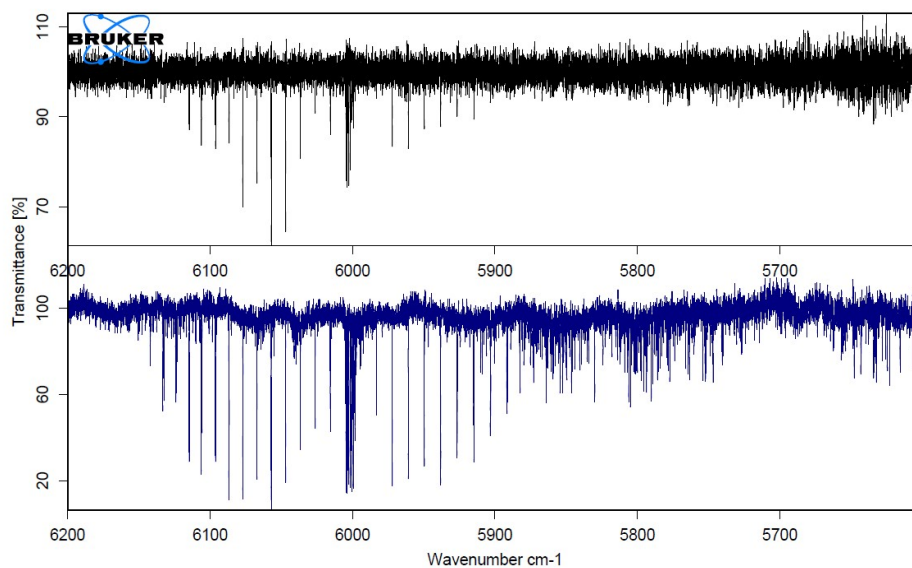


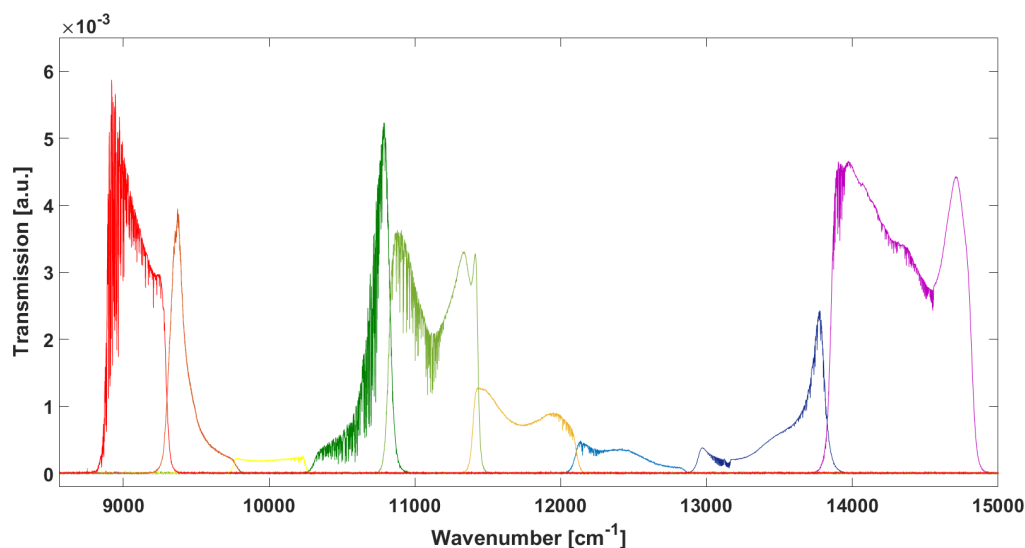
Figure 3.37 – Top panel: Spectrum of cold methane recorded using the Laval nozzle. Bottom panel: Spectrum of the same band of methane at ambient temperature. These spectra were recorded using the White cell scheme and a relatively high gas pressure.

acquisition speed which are related and finally (3) the sensitivity of the instrument.

3.4.1 Spectral bandwidth of the instrument

In our case we are using a cavity that covers wavelengths from 650 nm to 1200 nm. Two different experimental approaches have been used to record the transmitted signal through the cavity. The first approach consists in using different **optical filters** to cover all the spectrum of the cavity. As already shown in the previous section, the mirrors reflectivity bandwidth determinates the transmitted spectrum that could be used to record the absorption of different molecules inside this region. We show in Figure 3.38 the result of using different filters covering a total bandwidth from approximatively 670 nm to 1130 nm. To our knowledge, there is no filter that can both cover the whole spectral range of the cavity with a high transmittance and reflect efficiently the filtered wavelengths. Each filter covers a total bandwidth of 50 nm, for this reason different filters are installed in the setup and can be switched easily. The reader should keep in mind that the laser should be tuned differently for visible wavelengths and for the near infrared wavelengths.

The second approach consists in using a **Pellin-Broca prism** at the exit of the cavity and prior to the injection into the Fourier transform spectrometer. The prism allows the spatial separation of the wavelengths that are transmitted throughout the cavity. Indeed,



88

Figure 3.38 – Transmitted broadband spectrum using different optical filters represented by different colors covering the region of the reflectivity of cavity mirrors.

each wavelength will take a specific direction. An aperture is located at the entry of the spectrometer as shown in Figure 3.26 and its diameter could be used for different values. The latter helps selecting one bandwidth of the transmitted light by playing the role of an iris and stopping the undesired areas. Figure 3.39, shows the transmitted spectrum using an adapted Pellin broca prism. The latter is fixed on a rotating support. By rotating the prism different areas of the spectrum could be selected manually and it is adapted in real time by examining the signal on the spectrometer.

3.4.2 Resolution and acquisition speed

The resolution is an important parameter that is fixed by the spectrometer and limited by the absorption linewidth of each molecule. A number of factors are responsible for the broadening of the spectral lines. Briefly, homogeneous line broadening are well described by Lorentzian profiles, whereas inhomogeneous line broadening are described by Gaussian profiles. However, inhomogeneous as well as homogeneous broadenings are both present in normal experimental conditions in laser spectroscopy. A spectral line undergoing homogeneous and inhomogeneous broadening effects is usually well represented by a "Voigt" profile, which is a convolution of a Lorentzian and a Gaussian profile and it will be used in this work to fit the measured absorption lines.

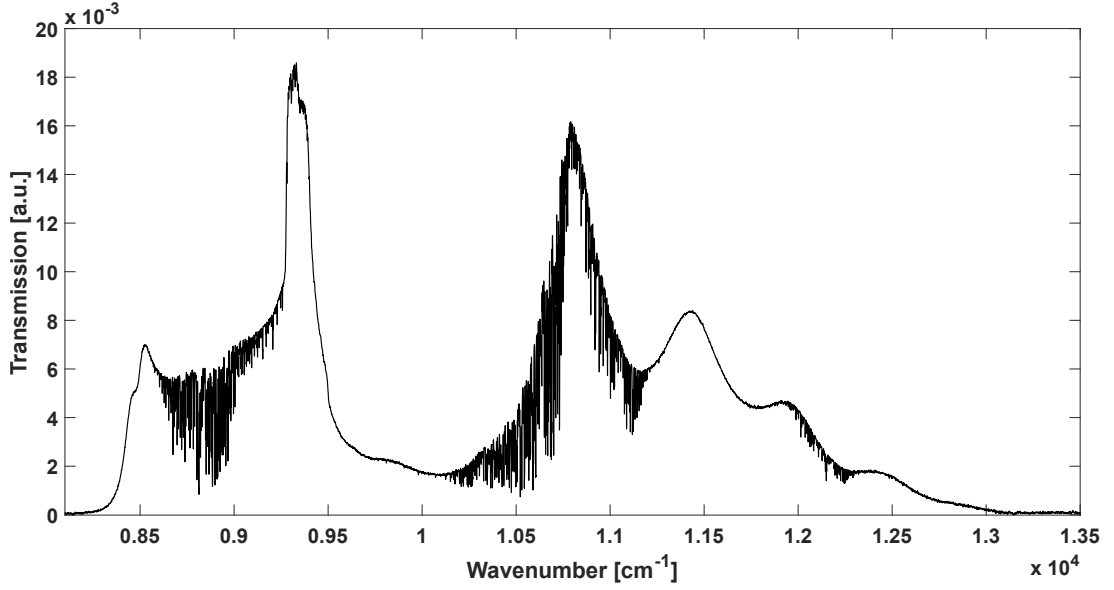


Figure 3.39 – Transmitted broadband spectrum using a Pellin-Broca prism that also covers the region of the reflectivity of the mirrors.

The full width at half maximum of Doppler broadened line ($\delta\nu_D$) is given by [212]:

$$\delta\nu_D = 7.16 \times 10^{-7} \nu_0 \sqrt{T/Mn} \quad (3.34)$$

ν_0 is the atomic transition frequency in cm^{-1} , $\delta\nu_D$ is proportional to $\sqrt{T/Mn}$ so it is reduced for heavy molecules at low temperatures.

For acetylene, chosen as test molecule, the FWHM Doppler broadening is equal to 0.0235 cm^{-1} at 300 K and 0.0096 cm^{-1} at 50 K. A first test consisted of recording the infrared spectrum of a mixture of 2% of acetylene seeded in argon using two different instrumental resolutions of 0.01 and 0.02 cm^{-1} . The gas mixture was injected into the vacuum chamber through the planar Laval nozzle. The two recorded spectra are shown in Figure 3.40. The linewidth is about 0.02 cm^{-1} , making useless a higher instrumental resolution. Such a broad absorption line is unexpected at low temperature and somewhat confusing. This seems to indicate that a large amount of hot gas is unfortunately being probed.

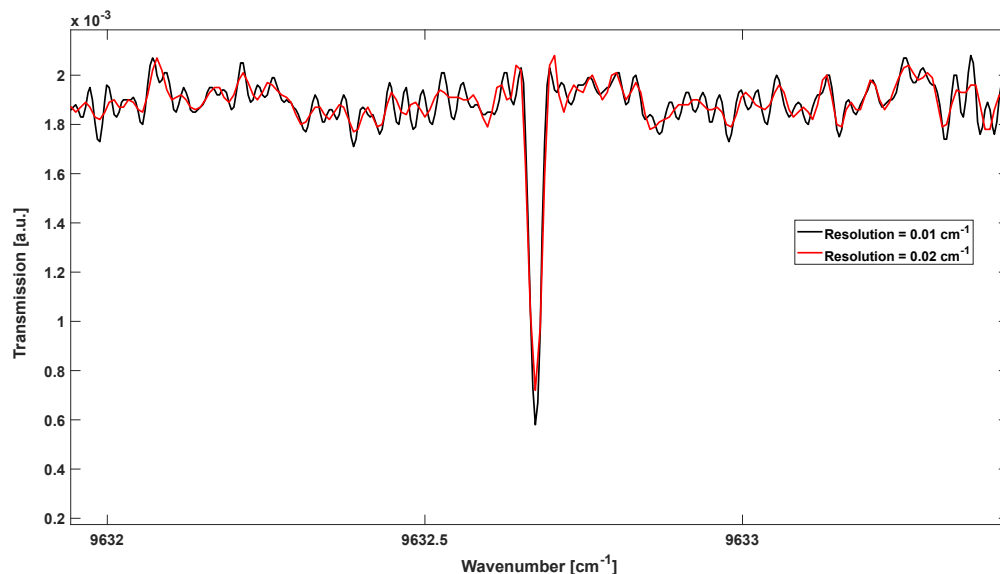


Figure 3.40 – Absorption line of jet-cooled acetylene around 9632 cm^{-1} recorded with an instrumental resolution of 0.02 cm^{-1} (red curve) and a resolution of 0.01 cm^{-1} (black curve).

A second test was carried out to study the effect of the velocity of the FT spectrometer scanner on the recorded spectra. The scanner velocity is directly related to the acquisition rate and working in jet conditions requires increasing the acquisition rate as much as possible in order to limit gas consumption. Several acquisition rates of 5, 7.5, 10, 15 and 20 kHz were tested. For 15 and 20 kHz the signal is deformed and its amplitude is weaker than the one recorded at lower acquisition frequencies. The acquisition rate was then set at 10 kHz, which is a compromise between the amplitude of the signal and the time of acquisition. The detector used in this thesis is apparently slow and can be replaced in the future for faster scans. The different detectors that are given in the data sheet are represented in Figure 3.41, in our case we used *SiD510*.

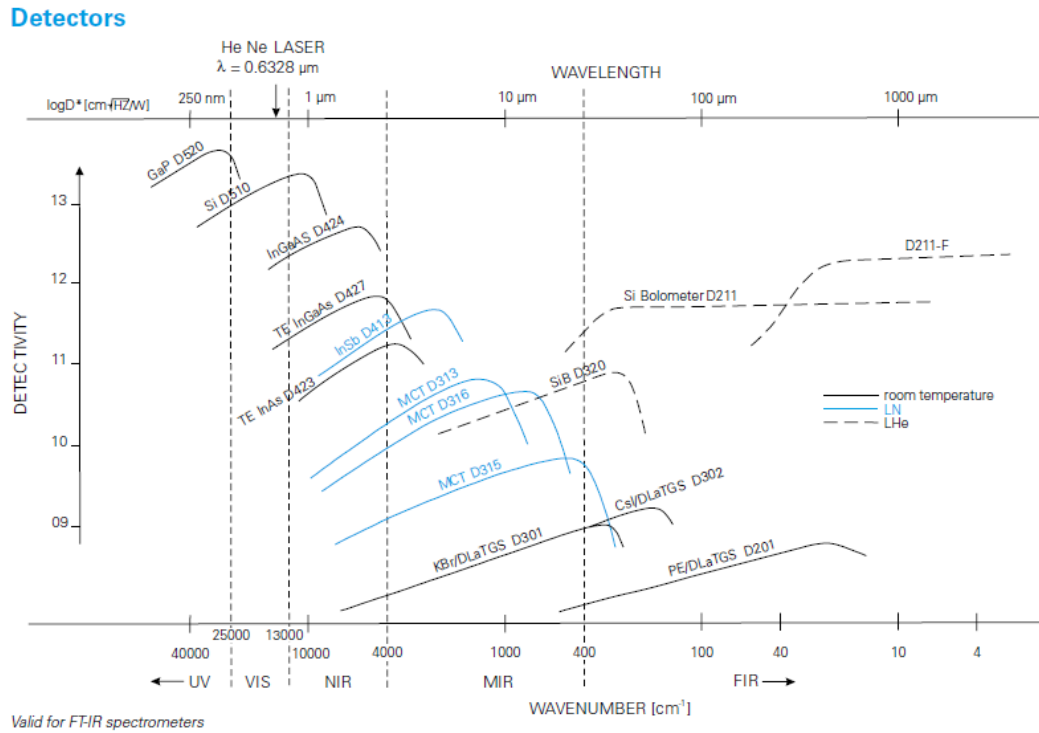


Figure 3.41 – Representation of the different detectors, giving their efficiency for different region in the electromagnetic spectrum.

A third test was devoted to the influence of the number of co-added scans on the S/N . The S/N was extracted from the acetylene jet spectrum recorded at 0.02 cm^{-1} resolution and plotted in function of the number of co-added scans (see Figure 3.42). As expected, the S/N increases approximately as the square root of the number of scans and remains constant after approximately 700 scans. This limit corresponds to the influence of non-random spectral fringes which cannot be eliminated by accumulation of spectra. About 16 hours are needed to record 700 scans with an acquisition rate of 10 kHz, which is not realistic in jet conditions. Here again, a compromise will be necessary between S/N and recording time.

We add that from the list of the beam splitters given by the FT manufacturer and shown in Figure 3.43 we were using the CaF₂ which is the most efficient for the UV/VIS/NIR regions.

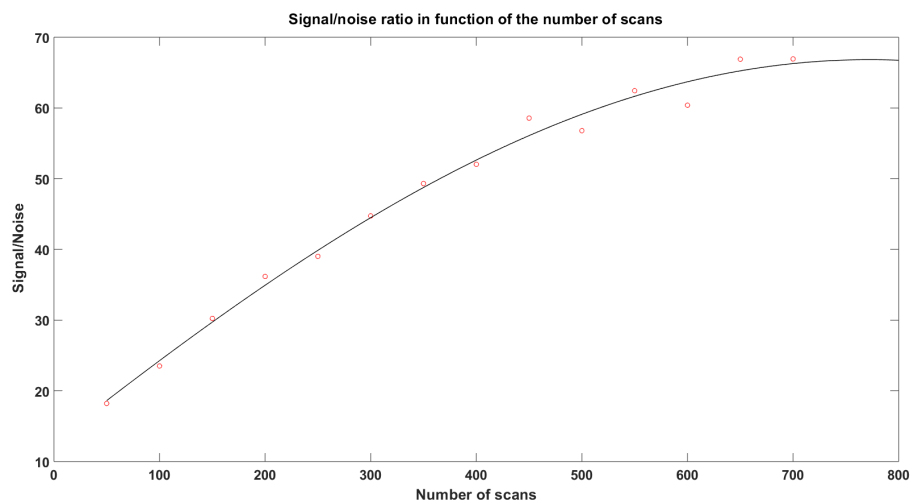


Figure 3.42 – Evolution of the signal-to-noise ratio versus the number of co-added scans measured in jet conditions with an instrumental resolution of 0.02 cm^{-1} and a scanning velocity of 10 kHz. Each point corresponds to the evaluation of the S/N for a certain number of measurements. The result was fitted using \sqrt{N} function.

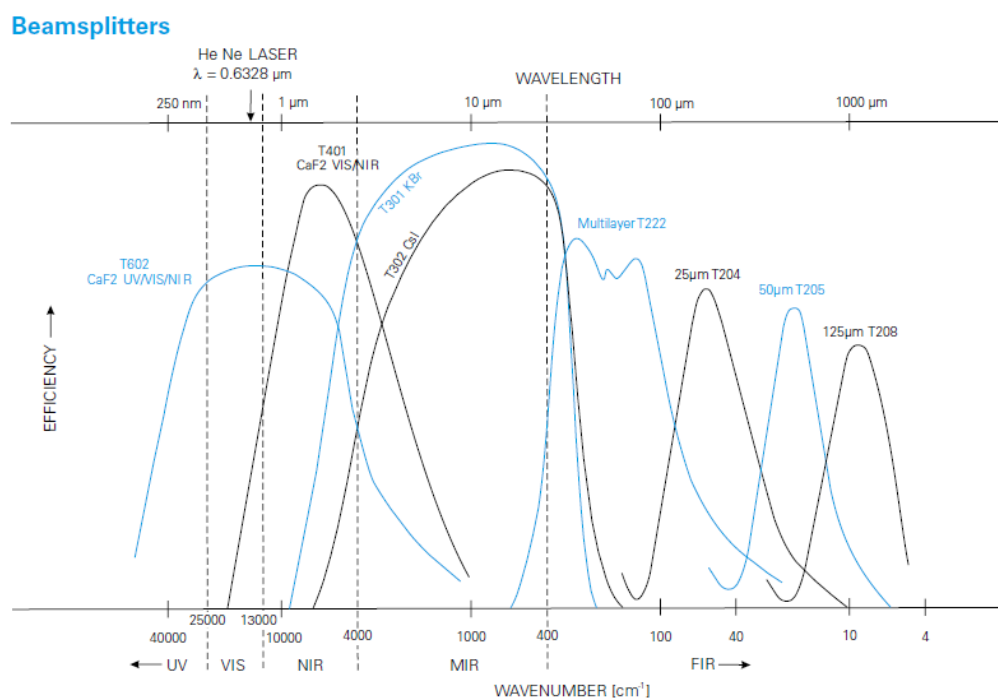


Figure 3.43 – Beam splitters table, giving the efficiency of different beam splitters for different region in the electromagnetic spectrum.

3.4.3 Interference fringes feature and their elimination

A fringing effect is present in the resulting spectrum blurring away spectral lines (see Figure 3.44). It is caused by the multiple reflections in the optics (not all the optics used are wedged). Therefore it is important to eliminate these parasitic centerbursts from the interferogram. Setting these centerbursts to zero in the interferogram suppresses the fringing effect on the spectrum.

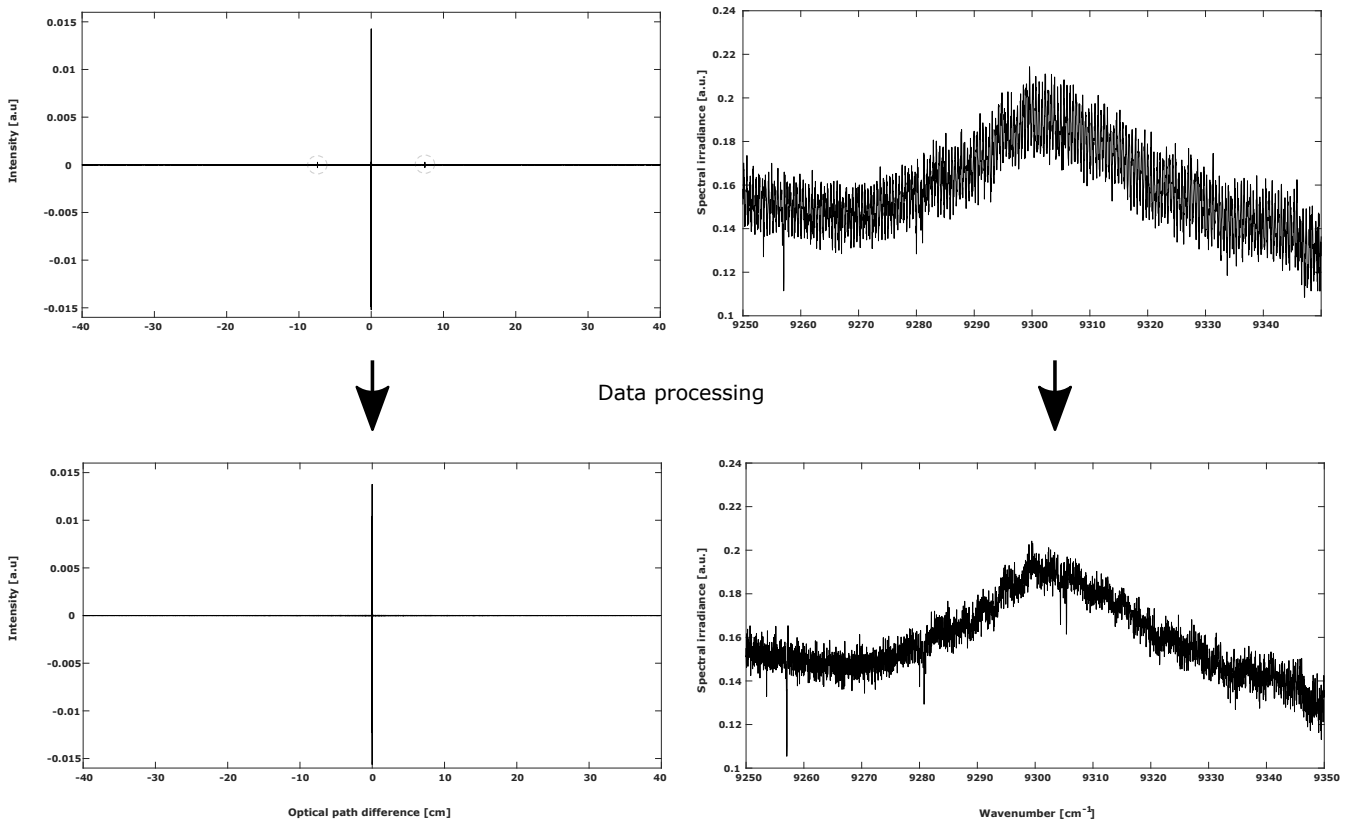


Figure 3.44 – Fringing effects from both the interferogram (on the left) and spectrum perspective (on the right). The data processing consists of the removal of the parasitic centerbursts marked by two circles on the top interferogram. Absorption lines of CH₄ molecules are distinguished after the data processing.

3.4.4 Sensitivity of the instrument

Absorption spectroscopy relies on the measurement of the frequency-dependent attenuation of light after its interaction with the sample. As already discussed earlier in section 3.2.2, when working with optical cavities illuminated by a broadband light source it is not possible to just use the conventional Beer-Lambert law, but we have to use a complicated equation which takes into consideration the transmission spectrum of the optical cavity where the need to recall Equation 3.26

$$\alpha_{min} = \frac{1}{d} \left(1 - \frac{I_{min,single}}{I_{0,single}}\right) = \frac{1}{d} \left(1 - \frac{I_{min}}{I_0}\right) (1 - R) \quad (3.35)$$

In this equation, R is the cavity mirrors reflectivity provided by the manufacturer and its value is given in the plot in Figure 3.45. Knowing the theoretical minimum reflectivity

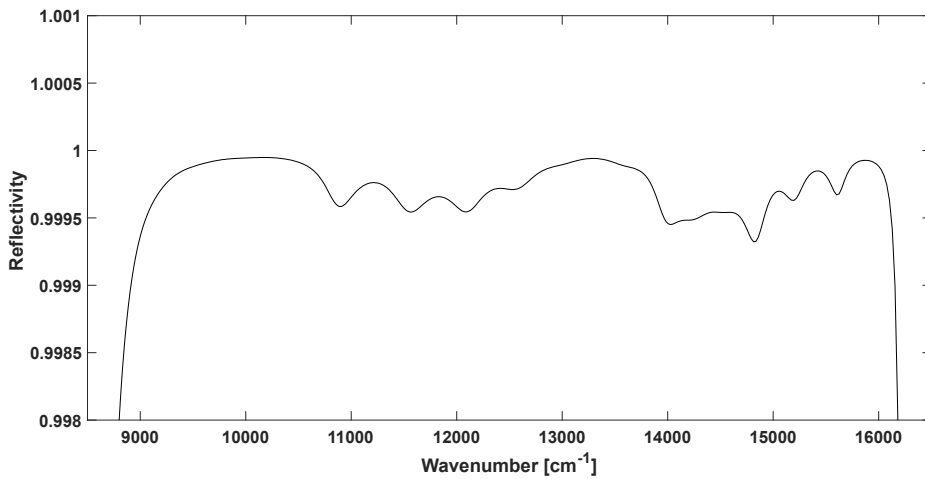


Figure 3.45 – Plot of the calculated reflectivity of the cavity mirrors.

($R_{min} = 0.9993$) and maximum reflectivity ($R_{max} = 0.9999$) the minimum and maximum theoretical finesse could be therefore calculated as following:

$$\begin{aligned} Finesse_{min} &= \pi \frac{\sqrt{R_{min}}}{1 - R_{min}} = 4486.4 \\ Finesse_{max} &= \pi \frac{\sqrt{R_{max}}}{1 - R_{max}} = 31414 \end{aligned} \quad (3.36)$$

Which gives a theoretical effective length L_{eff} equal to $\frac{Finesse \times 2d}{\pi}$ between $L_{eff,min} = 656.9101$ m and $L_{eff,max} = 45991$ m which depends on the absorption region.

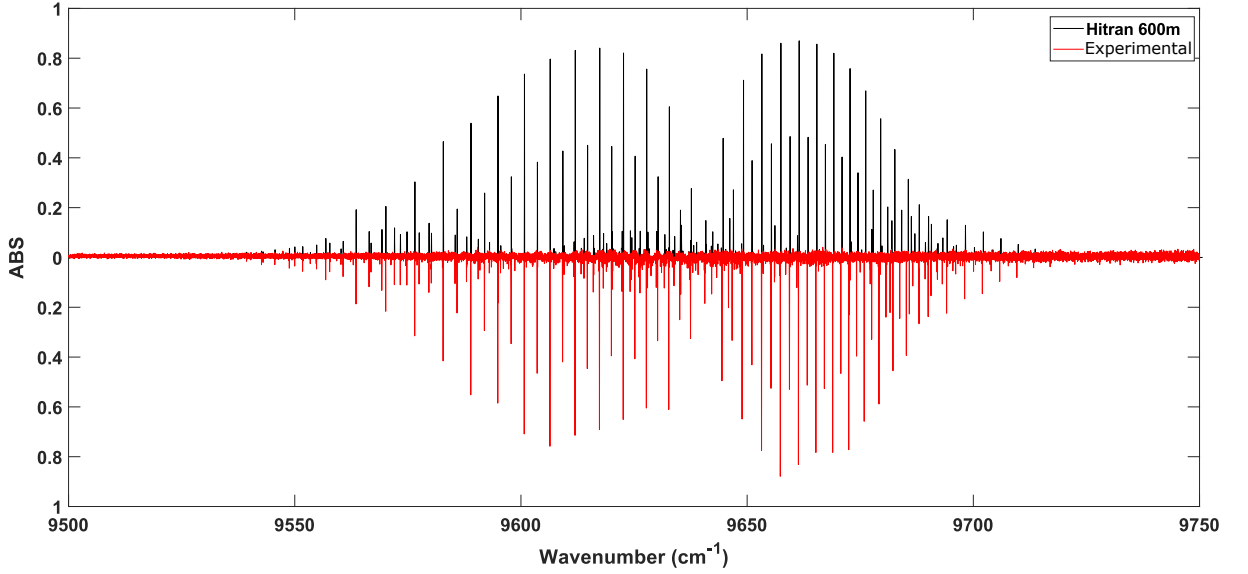


Figure 3.46 – Comparison between the simulation of the absorption band at 9650 cm^{-1} of 0.1 torr of acetylene at room temperature for an interaction length of 600 m and the corresponding measured spectrum. Number of scans is equal to 600.

In order to determine the experimental sensitivity of the instrument, it is therefore necessary to determine experimentally the reflectivity of the mirrors. To this end, we recorded the absorption spectrum at room temperature of a well known amount of acetylene (0.1 torr) (Figure 3.46), for a resolution of 0.02 cm^{-1} , after 600 scans using a filter and at ambient temperature. This band lines intensities i_H are known from the HITRAN database and by employing the following equation used by O’Leary *et al.*, [213]:

$$R = 1 - \frac{Ndi_H}{\int \left(\frac{I_0(\tilde{\nu})}{I(\tilde{\nu})} - 1 \right) d\tilde{\nu}} \quad (3.37)$$

In this equation N is the density ($\text{molecule} \times \text{cm}^{-3}$) of acetylene in the cavity. it could be calculated via the ideal gas relation giving $3.2 \times 10^{15} \text{ molecule/cm}^3$.

$d = 23 \text{ cm}$ is the cavity length, i_H is the HITRAN 2008 database lists line intensities [$1/(\text{cm} \cdot \text{molecule} \cdot \text{cm}^{-2})$] as the integral of the absorption cross-sections at a temperature of 296 K.

Finally taking into consideration the most intense absorption peaks the experimental determination of the mirror reflectivity is given in Figure 3.47. The mean value of the mirrors reflectivity is calculated to be equal to $R = 0.9957$. The calculated reflectance corresponds to the manufacturer data but showed an important local fluctuation, more

measurements are needed if this data will be used to correct the final obtained spectra which is not our case in this thesis.

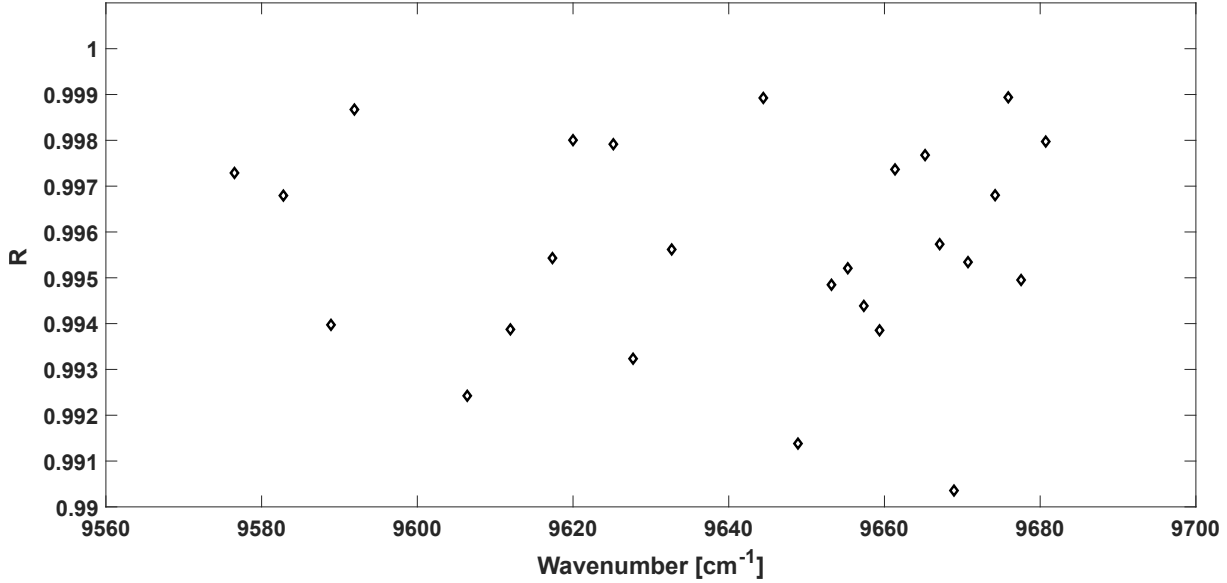


Figure 3.47 – Mirrors reflectivity between 9550 cm⁻¹ and 9720 cm⁻¹.

From this recording, a minimum experimental absorption coefficient of α_{min} equal $4.1 \times 10^{-8} \text{ cm}^{-1}$ was obtained by considering an interaction length of 600 m, a reflectivity of 0.9957 and an acquisition time of 12 hours. For a relevant comparison, the obtained sensitivity of our spectrometer is only compared with instruments based on the combined use of a supercontinuum laser and a Fourier transform spectrometer. To our knowledge, only three groups used these two techniques. A. Ruth *et al.* [172] reported a 10 hours measurement at 688 nm (14500 cm^{-1}) and at a resolution of 0.05 cm^{-1} using a longer cavity length of 89 cm than the one we used (23 cm), covering a small spectral region ($662 \pm 50 \text{ nm}$), unfortunately they don't provide any value of α_{min} . In a second article, the same group [214] mentions a spectrum recorded at a resolution of 0.12 cm^{-1} during 60 min leading to a value of α_{min} equal to $6.45 \times 10^{-8} \text{ cm}^{-1}$ at 7000 cm^{-1} , which is comparable to our instrumental sensitivity (α_{min} equal to $4.1 \times 10^{-8} \text{ cm}^{-1}$ measured at a resolution of 0.02 cm^{-1} , recording time was 12 hours). W. Denzer *et al.* [215] recorded spectra between 1.5 and 1.7 μm using both supercontinuum laser and superluminescent LED (SLED). In the former case, they reported a sensitivity of α_{min} equal to $4 \times 10^{-9} \text{ cm}^{-1}$ for an acquisition time of 4 min for a cavity length of 25 cm. Using the SLED, they reported a sensitivity of α_{min} equal to $2 \times 10^{-8} \text{ cm}^{-1}$, but at much lower resolution of 4 and 16 cm^{-1} . The third setup is reported by A. Libert *et al.* [208], they were able

to obtain a sensitivity of α_{min} equal to $6.5 \times 10^{-8} \text{ cm}^{-1}$, cavity length was set to 88 cm, they used a resolution of 0.015 cm^{-1} to record a spectrum between 12600 cm^{-1} and 13600 cm^{-1} during 10 hours, which is slightly better sensitivity than the one of our experimental setup. For comparison, Venable *et al.* [216] reported the highest sensitivity of $5 \times 10^{-10} \text{ cm}^{-1}$ using a longer optical cavity of 4.5 m with 1 min acquisition time and a resolution of 0.3 cm^{-1} but using a CCD spectrometer and measuring a single spectral point at 662 nm. Considering the full absorption spectrum would provide a lower detection limit.

The same study was performed using room temperature methane in the range between 1100 cm^{-1} and 1140 cm^{-1} where the mirrors reflectivity is slightly lower (see Fig. methane), therefore giving a smaller interaction length of 500 m (versus 600 m for the former region investigated using acetylene).

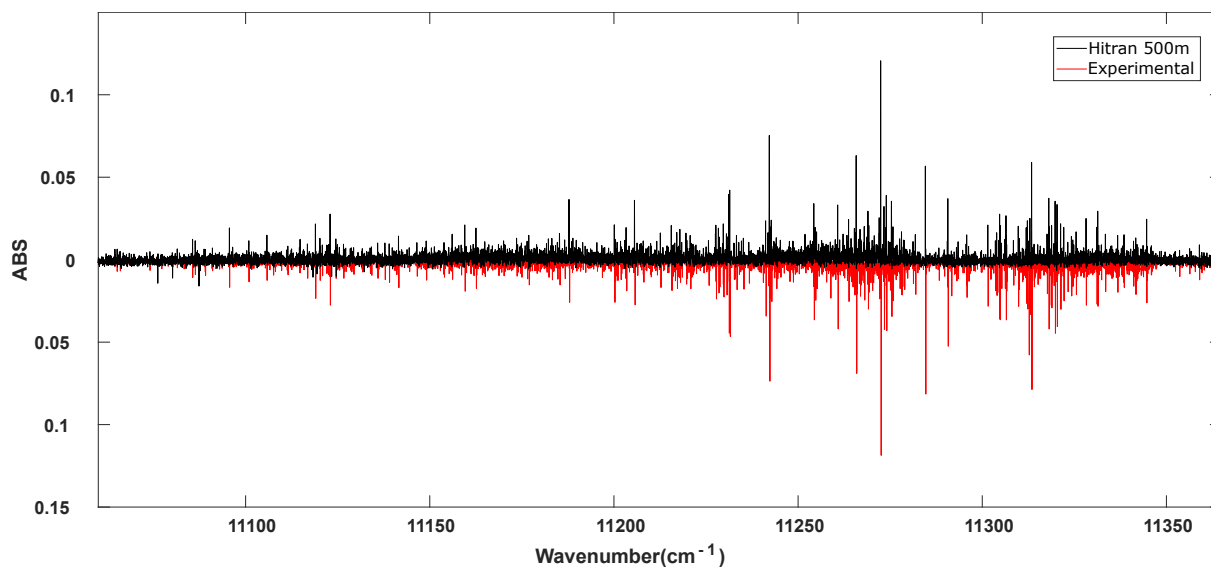


Figure 3.48 – Comparison between the simulation of the absorption band at 11250 cm^{-1} of a concentration of 0.3 torr of methane for an interaction length of 500 m and the corresponding measured spectrum. The number of scans is equal to 600 scans.

3.4.5 Jet cooled spectra of acetylene and methane

Our initial objective was to record the cold spectra of molecules using the home-made planar Laval nozzle. However, due to a lack of time and for the sake of simplicity, we decided to operate the Laval nozzle in non adapted conditions. The stagnation conditions were chosen so as to produce a strong expansion of argon just downstream of the nozzle throat, similar to the expansion formed by a slit jet nozzle not equipped with a divergent section. An injection of 1.5 slm of acetylene seeded in 15 slm of argon fixed the pressure in the reservoir at 226 torr and the pressure in the chamber at 0.095 torr. The nozzle throat width was chosen to be $80 \mu\text{m}$. The position of the laser beam was set to 30 mm from the nozzle throat.

Figure 3.49 shows the results for three different pressures in the expansion chamber while keeping the back pressure constant. A mixture of 10 % of acetylene seeded in argon was used with a back pressure of 230 torr. The absorption band between 9500 cm^{-1} and 9800 cm^{-1} was recorded.

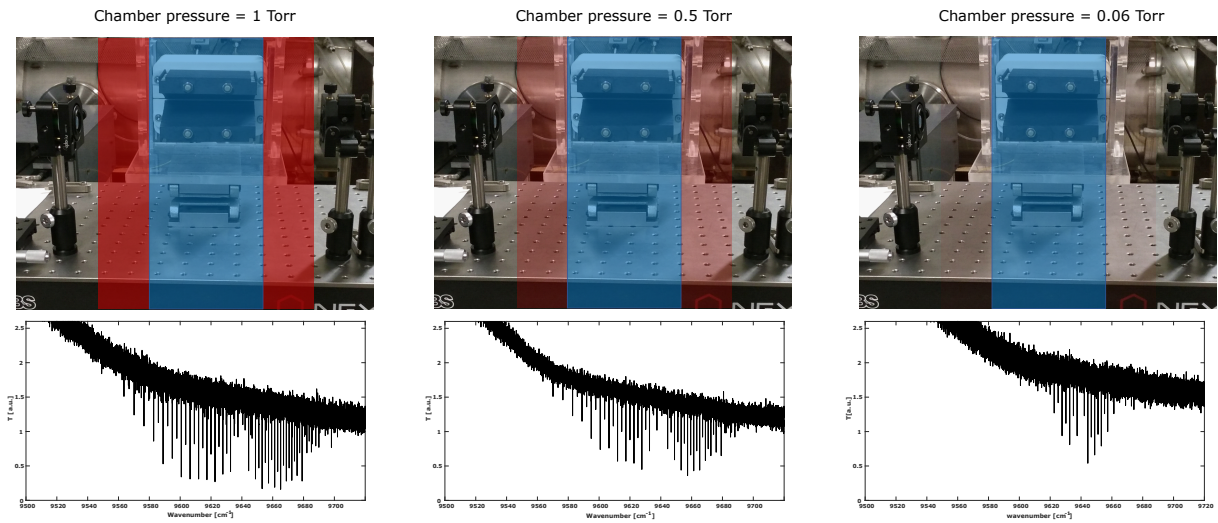


Figure 3.49 – On the top a photo of the source and the cavity showing the areas of hot gases in red and cold gases in blue. The lower is the pressure of the chamber, the lower is the concentration of hot gases. On the bottom the corresponding spectrum for each case is presented. We can see clearly the contribution of hot gases because of the absorption of higher rotation energy states that are depopulated at lower temperatures.

In order to evaluate the performances of our optical system we recorded the weak absorption bands, according to Hitran vibrational notations $(0\ 0\ 0\ 0\ 0\ 0+g) \rightarrow (2\ 0\ 1\ 0\ 0\ 0+u)$ and $(0\ 0\ 0\ 0\ 0\ 0+g) \rightarrow (1\ 1\ 1\ 2\ 0\ 0+u)$ of jet cooled acetylene which are located between 9500 and 9800 cm^{-1} . The absorption lines of these bands are characterized

by integrated absorption cross sections of 5×10^{-24} cm.molecule⁻¹, typically. The best simulation based on the HITRAN database was obtained for a temperature of 40 K and a partial jet pressure of acetylene of 0.0022 torr (Figure 3.51). The effective length corresponding to the length of interaction through the jet flow is equal to 260 m, calculated by dividing the effective length at ambient temperature by a factor of 2.3 corresponding to the ratio of the interaction length at ambient temperature and using the nozzle (see Figure 3.50). From this recording, a minimum experimental absorption coefficient of 7.3×10^{-7} cm⁻¹ was obtained.

The relevant experimental parameters are summarized hereafter:

1. Chamber pressure = 0.095 torr
2. Reservoir pressure = 226 torr
3. Slit width = 80 μ m
4. Gas mixture : 1.5 Slm C₂H₂ + 15 Slm Ar
5. Probed distance from the throat = 30 mm
6. Resolution = 0.02 cm⁻¹
7. Number of scans = 150 scans

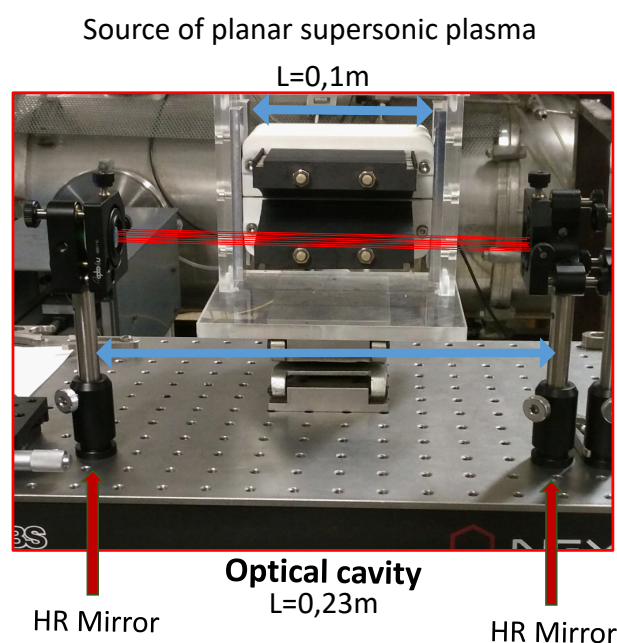


Figure 3.50 – Photo of the cavity and the nozzle showing the difference in the interaction length between a static measurement that corresponds to 0.23 m and a cold jet measurement with 0.1 m of interaction.

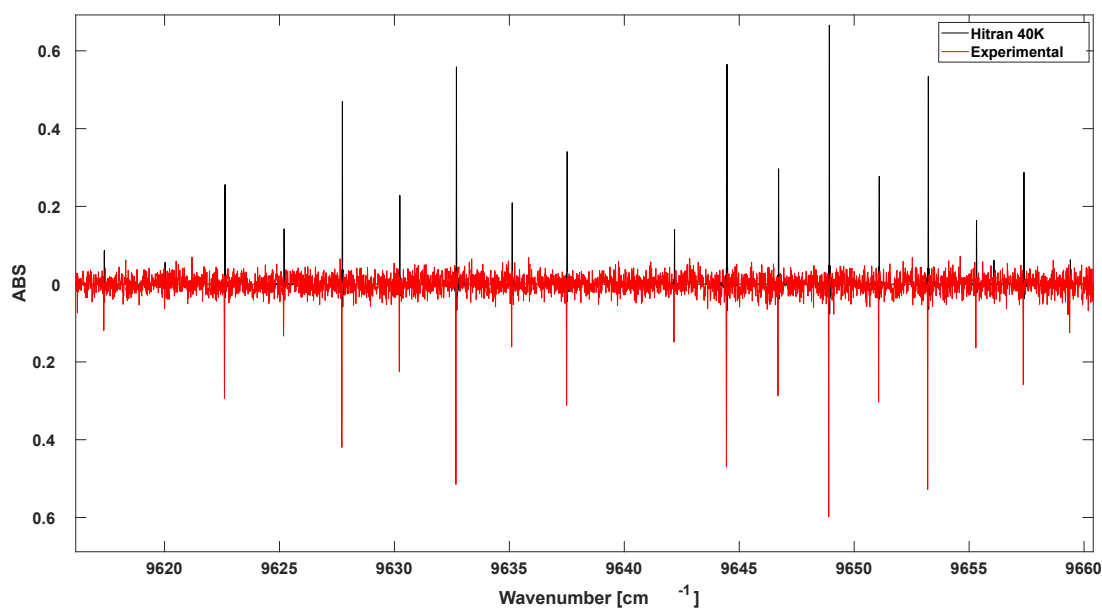


Figure 3.51 – Absorbance spectrum of cold acetylene recorded using the nozzle in non adapted conditions (red). Simulated spectrum using the HITRAN database (black).

Figure 3.52 shows the comparison between the spectrum at low and room temperatures of acetylene. The lines intensities cannot be compared because of the lower density during the expansion relatively to the static measurement. One should measure a static spectrum at the same density for a relevant comparison.

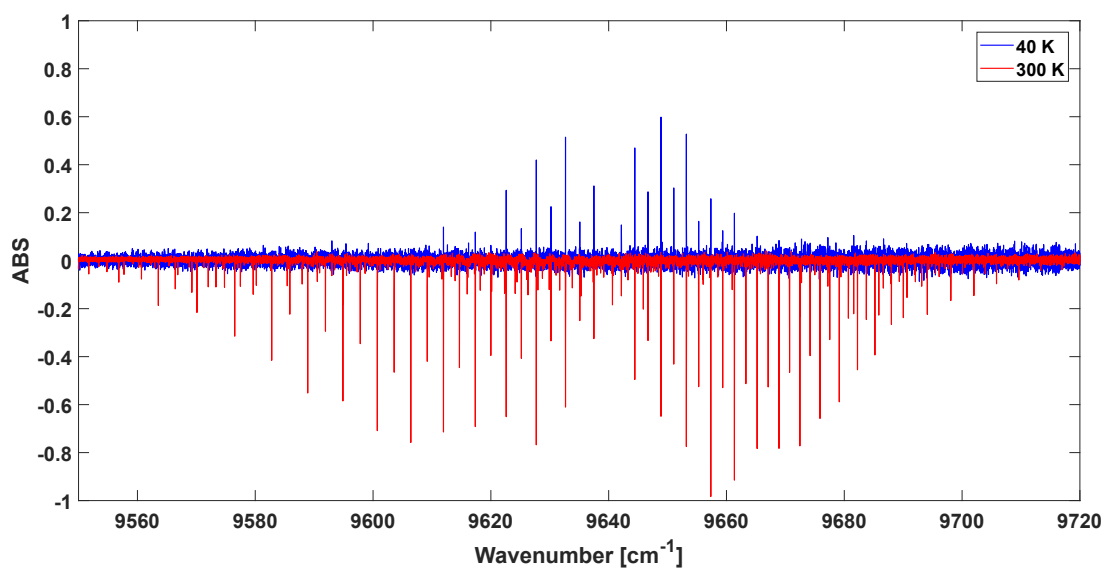


Figure 3.52 – Absorbance spectrum of acetylene recorded at low and room temperatures.

Another measurement (Figure 3.53) of the weak overtone band of methane at 11285 cm^{-1} was performed using the following experimental parameters, these bands are not yet assigned and, the absorption lines of these bands are characterized by integrated absorption cross sections of $5 \times 10^{-26}\text{ cm.molecule}^{-1}$, typically:

1. Chamber pressure = 0.14 torr
2. Reservoir pressure = 318 torr
3. Slit width = $80\text{ }\mu\text{m}$
4. Gas mixture : 1.8 Slm CH_4 + 20 Slm Ar
5. Probed distance from the throat = 30 mm
6. Resolution = 0.02 cm^{-1}
7. Number of scans = 100 scans

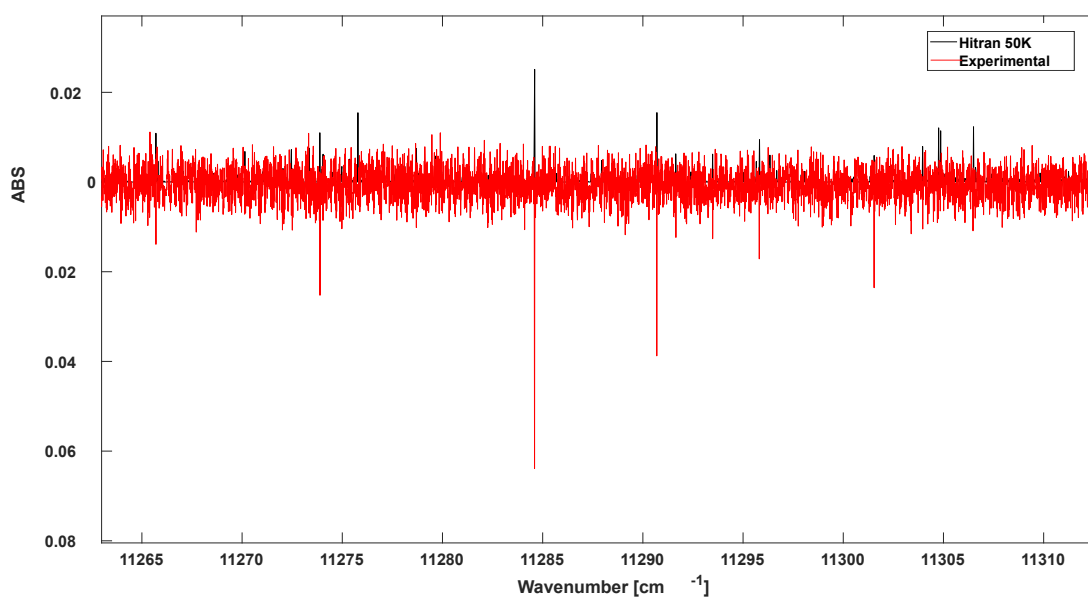


Figure 3.53 – Absorbance spectrum of cold methane recorded using the nozzle in non adapted conditions (red). Simulated spectrum using the HITRAN database and a temperature of 50 K (black).

The recorded spectrum is not well reproduced by the HITRAN database, therefore demonstrating the interesting potential of our experimental approach to investigate the highly excited overtones of methane which are still poorly studied. Another comparison with a simulation at 100 K (Figure 3.54) showed that the experimental spectrum presents a lower number of absorption peaks which still need to be understood.

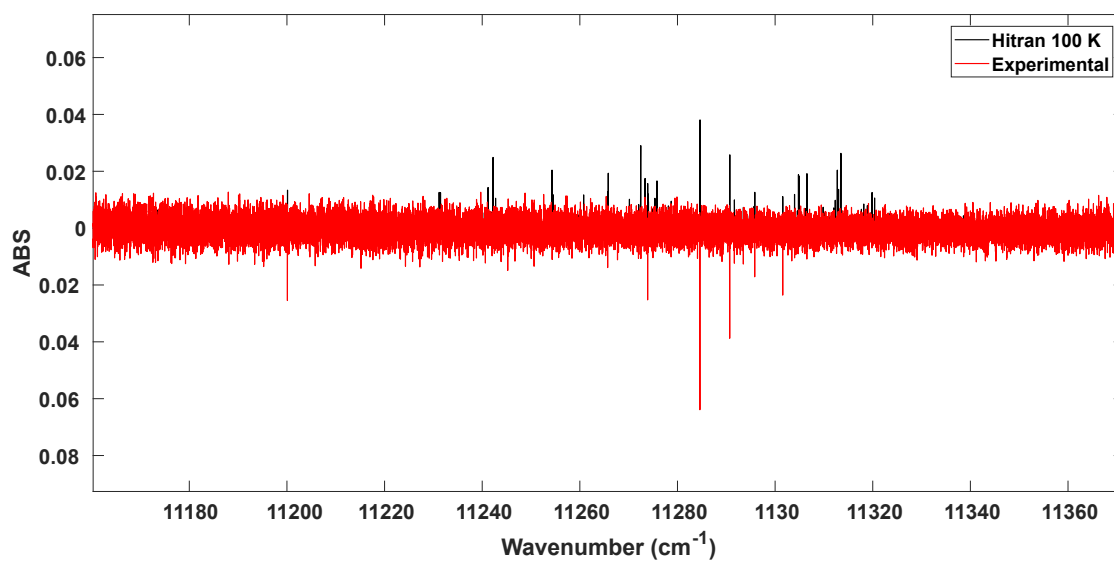


Figure 3.54 – Absorbance spectrum of cold methane recorded using the nozzle in non adapted conditions (red). Simulated spectrum using the HITRAN database and a temperature of 100 K (black).

CONCLUSION

This thesis has been devoted to the development of two different instrumental systems. The first part focuses on the development of STARGATE capable of performing photodissociation spectroscopy. The second part concerns the instrumentation development of the incoherent broadband cavity enhanced absorption spectroscopy coupled to a Fourier transform spectrometer. Concerning the versatile instrument STARGATE, the gas injection valve inspired from the work of Proch and Trickl [84] has been associated with a skimmer and an electric discharge or an electron gun to produce isolated molecular ions and cationic complexes. The extraction, acceleration, bunching/gating and re-referencing of the ionic beam associated with a TOF of $L = 1.5$ m allowed us to reach a mass resolution of 140. Two ion mass selections were performed first by a pulsed parallel plate deflector and secondly by a 90° toroidal field deflector, which, when associated with an energy tagging of the photodissociation fragments, allowed to perform background free rovibronic spectral measurements of N_2O^+ ($S/N = 200$). The molecular constants in the $\tilde{A}^2\Sigma^+(002)$ upper state have been improved from the analysis at 300 K of the $\tilde{A}^2\Sigma^+(002) \leftarrow \tilde{X}^2\Pi_{3/2}(000)$ and $\tilde{A}^2\Sigma^+(002) \leftarrow \tilde{X}^2\Pi_{1/2}(000)$ rovibronic bands. We have demonstrated that the rotational temperatures can be tuned from 40 K to 305 K. The lowest temperature has been obtained using a gas mixture of N_2O (1%) with argon (99%) as a carrier gas, and by gating the beginning of the ion beam pulse. The higher temperature has been obtained with a pure N_2O gas injection and by delaying gating with respect to the beginning of the gas pulse. This result opens up many perspectives. The lowest temperatures simplify dense rovibronic spectra and increase the S/N by populating fewer quantum states. The ability to produce higher temperature ions allows to observe transitions associated with larger total angular momentum J values and hot vibrational bands for small molecular ions (3-4 atoms). Thus, additional information on the dynamics of the molecule can be extracted and additional lines can be assigned to help detecting molecular ions in relatively hot environments.

Concerning the possible improvements of this setup, the pulsed supersonic expansion could be improved by reducing the residual pressure in the extraction unit and in the drift tube, thereby limiting the number of detrimental collisions of the ions with the

residual gas. Moreover we have noticed a lack of stability in the design of Proch and Trickl [84] after a few hours of operation with an electric discharge. We thus plan to build a faster valve based on the design of A. Catanese *et al.* [217] in a near future, preferably used in combination with the electron gun. Shorter pulses are promising in terms of density, temperature and also since only $1.25 \mu\text{s}$ of the ion beam pulse duration (for 1 keV N_2O^+) is selected by the gating bunching unit compared to $200 \mu\text{s}$ of pulsed gas injection. Furthermore, following the results of preliminary SIMION[®] simulations, the MRP of our simplified TOF set-up could be improved by using shorter cups. The sensitivity of the spectrometer can be improved further by using a post acceleration of the ions [218] between the 90° energy analyser and the MCP detector as to increase the MCP detection efficiency [219].

Concerning the second part of this work, the primary motivation was to produce low temperature data (10-20 K) of anionic carbon chains of astrophysical interest. For this purpose, we have developed a new experimental setup that consists of a planar Laval nozzle source. The source was coupled to a highly sensitive spectroscopic technique, known as incoherent broadband cavity enhanced absorption spectroscopy (IBB-CEAS). We used acetylene and methane as test molecules. In order to recapitulate:

1. The cold ionic Laval source was capable of generating a cold (20 - 60 K) and uniform gas flow with a maximum Mach number equal to 6, with a planar geometry (10 cm) to increase the interaction length, thus improve the (S/N).
2. The set of electrodes placed at the divergent part of the nozzle, were able to focus the produced ions at different distances from the throat. It was demonstrated by numerical simulations.
3. Experimentally, we successfully coupled a broadband source to a high finesse cavity and a Fourier transform spectrometer. The cavity was used to measure the absorption spectra of gases at ambient as well as at cold temperature.
4. We measured the overtone absorption spectrum of acetylene, around 9540 cm^{-1} at ambient temperature to determine the effective interaction length (600 m), the effective mirrors reflectivity in this region (0.9957) and the sensitivity of the instrument ($\alpha_{min} = 4.1 \times 10^{-8} \text{ cm}^{-1}$). We also measured the absorption spectrum of jet-cooled acetylene in the same region. The rotational temperature was evaluated to be around 40 K. From this recording, a minimum experimental absorption coefficient of $7.3 \times 10^{-7} \text{ cm}^{-1}$ was obtained. The result is encouraging and we can enhance the sensitivity by replacing the detector by a faster one allowing a higher

number of scans. Our spectrometer is among the best worldwide FT-IBBCEAS in terms of sensitivity, spectral broadband, and moreover it can be coupled to a supersonic Laval nozzle to record spectra of species at low temperature (40 K).

5. We also recorded the overtone absorption spectrum of methane at ambient and low temperature around 11285 cm^{-1} .

For these measurements the resolution was limited to 0.02 cm^{-1} . The reasons behind these limitations still need to be investigated, it could be due to the radial velocity of the jet and the thermal agitation of the molecules. In addition, improving the coupling between the laser and the Fourier transform spectrometer, might be a way to lift up this limitation.

In terms of perspectives, this experimental instrument will make it possible, in the near future, to perform spectroscopy of anionic carbon chains. Discharge using a DC voltage on the electrodes at the throat level of the nozzle is already installed and ready to be tested. In addition, working in adapted conditions of the Laval nozzle besides using the ion guiding system will enhance the density of the produced ions in the area of the jet.

APPENDIX: FLUID DYNAMICS

There are various mathematical models that describe the motion of fluids. However, the most complete and accurate description comes from partial differential equations. For instance, a flow is characterized by the balance in mass, momentum, and total energy described by the continuity and conservation equations, beside kinetic and internal energy variation. Navier-Stokes equations are used among others to describe compressible viscous flows (and in particular high speed compressible flows), while Euler equations are adapted to model non viscous compressible flows. These equations are recalled to be able to describe the physics behind the supersonic jet expansion. We will start with some assumption, considering the fluid volumes that are neither too large (macroscopic) nor too tiny (microscopic). It is therefore a question of studying a mesoscopic volume dV . Two approaches allow us to go back to the properties of a flow. The first one is the Lagrangian approach, which consists of studying the evolution of a fluid particle. More precisely, the fluid is described at each moment by all the physical properties of the fluid particles that compose it. The velocity is equal to $\vec{v}(t)(\vec{r}_0, t)$ where \vec{r}_0 is the initial position of the particle and t is the time. Rather than describing the velocity of a fluid particle, which provides characteristics of the flow as a function of time but never at the same places (the position of the particle keeps varying). The second is the Eulerian description, which consists in studying the fluid movement at fixed locations. This time the velocity depends only on the chosen point \vec{r} and it could be written as $\vec{v}(\vec{r}, t)$ where \vec{r} is the position of the particle in Cartesian coordinates and t the corresponding time. These two methods lead to the same results but the Eulerian approach is more suitable and easier for fluid mechanics calculations because we can start by taking in consideration the boundary conditions. We therefore consider for the next sections a volume of fluid fixed in a Cartesian coordinate system: $dV = dx dy dz = dS dl$.

A.1 Mass conservation, continuity equation

The basis of the conservation-of-mass principle for fluid mechanics is that mass can neither be created nor destroyed within the volume or system of interest. In a supersonic expansion the mass is conserved if we consider the absence of a certain percentage of condensation of the gas under expansion. The interpretation of the continuity equation for mass is the following: For a given closed surface in the system, the change in time of the mass enclosed is equal to the mass that traverses the surface, positive if matter goes in and negative if matter goes out.

This equation is one of the master equations used by the CFD calculation software used in this thesis (*Ansys-Fluent*). This software is used to simulate the flow produced by a coaxial free jet expansion (Chapter 2) and the Laval nozzle specially designed for this thesis (Chapter 3).

$$\boxed{\frac{d\rho}{dt} + \text{div}(\rho\vec{v}) = 0} \quad (\text{A.1})$$

This equation is also known as the continuity equation. In a jet expansion the mass is conserved, the velocity increases at the expense of the volumetric mass density. This equation is used by the program used to simulate the jet as we will be shown in chapter 2 and 3.

A.1.1 Momentum conservation

The procedure for finding the conservation equation as for momentum p follows the same logic for expressing the continuity equation. The variation of the momentum per unit of time is equal to the sum of the external forces applied to its section S to which we add a source term that derives from the Fundamental Principle of Dynamics : $\frac{d\vec{p}}{dt} = \sum \vec{F}_{ext}$.

$$\vec{p} = m\vec{v} \quad (\text{A.2})$$

This momentum comes from external forces applied to the volume of the fluid. Thus, in the integral form, the momentum conservation equation is written as:

$$\begin{aligned} \frac{d\vec{p}}{dt} &= \sum \vec{F}_{ext} \\ \frac{\partial}{\partial t} \iiint \rho \vec{v} dV &= -\frac{\partial}{\partial t} \int \rho \vec{v} (\vec{v} \cdot \vec{n}) dS + \sum \vec{F}_{ext} \end{aligned} \quad (\text{A.3})$$

There are two types of forces acting on our system:

- surface forces \vec{f}_S : contact actions applied by the surrounding fluid, manifested by (i) the fluid in the reservoir at high pressure that apply a force in the direction of the jet and (ii) the fluid in the chamber at low pressure that applies a force in the opposite direction of the jet.

$$\vec{f}_S = \bar{\sigma} d\vec{S} \text{ with } \sigma \text{ the stress tensor.}$$

- volume's forces \vec{f}_V : actions from a distance which is linked to external forces; it is essentially the sum of weight due to gravity, pseudo-forces of inertia and electrical forces (that could result from ionized gas).

Which gives the equation for conservation of momentum in its Eulerian form that can be written as:

$$\boxed{\frac{\partial \rho \vec{v}}{\partial t} = -div(\rho \vec{v} \vec{v}) + div(\bar{\sigma}) + \rho \vec{f}_V} \quad (\text{A.4})$$

A.1.2 Energy conservation

Following the first principle of thermodynamics, the total energy conservation for a closed system is written as :

$$\boxed{\frac{\partial \rho E}{\partial t} + div(\rho E \vec{v}) = div(\vec{v} \sigma \cdot \vec{v}) - div(\vec{q}) + \rho \vec{f} \cdot \vec{v}} \quad (\text{A.5})$$

For a steady flow in a nozzle, the enthalpy H is the sum of the internal energy U and the work due to external pressure forces that are responsible for the gas motion PV . We can express the enthalpy per unit of mass h by the sum of internal energy u and energy per unit of mass $\frac{P}{\rho}$ which gives:

$$h = u + \frac{p}{\rho} \quad (\text{A.6})$$

In order to express the variation of the internal energy, we can write:

$$\frac{du}{dt} = \frac{dh}{dt} - \frac{1}{\rho} \frac{dp}{dt} + \frac{p}{\rho} \frac{d\rho}{dt} \quad (\text{A.7})$$

By using the conservation of mass Equation A.1 we obtain:

$$\frac{du}{dt} = \frac{dh}{dt} - \frac{1}{\rho} \frac{dp}{dt} - \frac{p}{\rho^2} \text{div}(\vec{v}) \quad (\text{A.8})$$

If we consider a non-viscous flow and by neglecting the term related to heat in the energy conservation equation A.5 from Appendix A, we are able to write:

$$\frac{\delta(\rho U)}{\delta t} + \text{div}(\rho U \vec{v}) = -\rho \text{div}(\vec{v}) \quad (\text{A.9})$$

In order to simplify the operation we can use the Lagrangian's description as follows:

$$\rho \frac{du}{dt} = -p \text{div}(\vec{v}) \quad (\text{A.10})$$

Thus, the variation of the enthalpy could be written:

$$\rho \frac{dh}{dt} = \frac{dp}{dt} \quad (\text{A.11})$$

knowing that $\frac{d}{dt} = \frac{\delta}{\delta t} + \vec{v} \cdot \vec{\text{grad}}$

$$\rho \frac{\delta h}{\delta t} + \vec{v} \cdot \vec{\text{grad}} h = \frac{\delta p}{\delta t} + \vec{v} \cdot \vec{\text{grad}} p \quad (\text{A.12})$$

Assuming a stationary unidirectional flow and that $h = c_P T = cte$

$$\begin{aligned} \rho v_x c_P \frac{dT}{dx} &= v_x \frac{dp}{dx} \\ \rho c_P \frac{dT}{dx} &= \frac{dp}{dx} \end{aligned} \quad (\text{A.13})$$

Comparing Equation A.13 to the equation of the conservation of momentum A.4 we obtain:

$$\rho c_P \frac{dT}{dx} = -v_x \frac{dv_x}{dx} \quad (\text{A.14})$$

which gives after integration:

$$\underbrace{c_P T_0}_{[1]} = \underbrace{c_P T}_{[2]} + \underbrace{\frac{1}{2} v^2}_{[3]} \quad (\text{A.15})$$

A.1.3 Navier-Stokes model, compressible real fluid

The Navier-Stokes equations mathematically result from the conservation of momentum, the conservation of mass, and the conservation of energy. They arise from applying Newton's second law to fluid motion, together with the assumption that the stress in the fluid is the sum of a diffusing viscous term (proportional to the gradient of velocity) and a pressure term describing viscous flow. The main difference between them and the simpler Euler equations is that Navier–Stokes equations model viscosity while the Euler equations are only valid for inviscid flows.

According to the conservation equations, the laws underlying the Navier-Stokes model and the approximations inherent to our problem, Navier-Stokes equations are used in the *Fluent* modeller that we have used in this thesis to simulate our flows. In the case of a compressible Newtonian fluid, The Navier-Stokes equation relating pressure P , temperature T and density ρ is given by:

$$\underbrace{\rho \left(\frac{\partial v}{\partial t} + v \cdot \nabla v \right)}_1 = \underbrace{\nabla P}_2 + \underbrace{\nabla \cdot (\mu (\nabla v + (\nabla v)^T) - \frac{2}{3} \mu (\nabla \cdot v) I)}_3 + \underbrace{\sum F_{ext}}_4 \quad (\text{A.16})$$

The different terms correspond to the inertial forces (1), pressure forces (2), viscous forces (3), and the external forces applied to the fluid (4). This equation is always solved together with the continuity equation by *Fluent* modelling software. Solving them, for a particular set of boundary conditions (such as inlets, outlets, and walls), predicts the fluid local velocity, temperature, and pressure for a given geometry.

APPENDIX: STATISTICAL PHYSICS

We consider a system in which the particles considered are discernible. The volume V of the reservoir containing N particles of an ideal gas is fixed and the particles are assumed to be non-interacting. The system is isolated, thus the number of particles N and the internal energy E of the gas are fixed. In the absence of interaction the internal energy of the gas is simply the sum of the internal energies ϵ_k of the molecules.

$$E = \sum_{k=1}^N \epsilon_k \quad (\text{B.1})$$

In the case of monoatomic gases, the degrees of freedom are limited to the translation. Thus E is the sum of the translational kinetic energies of the particles in the system. The particles could occupy different discrete energy states with equal probabilities. Each state i having an energy ϵ_i is degenerated g_i times and occupied by n particles.

We can write:

$$N = \sum_{i=1}^r n_i \quad (\text{B.2})$$

and

$$E = \sum_{i=1}^r n_i \epsilon_i \quad (\text{B.3})$$

The Maxwell-Boltzmann distribution corresponds to the most probable distribution. We therefore look for the values of n_i to obtain at the well-known Maxwell-Boltzmann expression:

$$n_i = g_i e^{\alpha + \beta \epsilon_i} = g_i e^{\alpha} e^{\beta \epsilon_i} \quad (\text{B.4})$$

We define e^{α} that could be expressed in function of the number of particles N :

$$N = \sum_i n_i = e^{\alpha} \sum_i g_i e^{-\frac{\epsilon_i}{kT}} = e^{\alpha} Z \quad (\text{B.5})$$

so we obtain:

$$e^\alpha = \frac{N}{Z} \quad (\text{B.6})$$

For state i the number of particles is equal to:

$$n_i = N \frac{g_i e^{-\epsilon_i/kT}}{\sum g_i e^{-\epsilon_i/kT}} \quad (\text{B.7})$$

The partition function for a system is simply an exponential function of the sum of all possible energies for that system. It is expressed by:

$$Z = \sum_i g_i e^{-\epsilon_i/kT} \quad (\text{B.8})$$

The quantities $g_i e^{-\epsilon_i/kT}$ of this sum are proportional to the number of particles in the corresponding energy states as Z/N is a constant. Therefore we can write for a temperature T :

$$g_i e^{-\epsilon_i/kT} = \frac{Z}{N} n_i \quad (\text{B.9})$$

The partition function is important because it permits to find how the particles are spread over the different energy states at equilibrium. It is important to notice that the distribution B.7 depends only on the temperature.

If we refer to the last paragraph and if we consider $g(\epsilon)$ the density of the energetic states and $n(\epsilon)$ the occupied states density we can write:

$$n(\epsilon) = \frac{N g(\epsilon) e^{-\epsilon/kT}}{Z} \quad (\text{B.10})$$

with

$$Z = \int_0^\infty g(\epsilon) e^{-\epsilon/kT} d\epsilon \quad (\text{B.11})$$

Finding $n(\epsilon)$ requires the knowledge of the density of accessible states $g(\epsilon)d\epsilon$. We can calculate $g(\epsilon)d\epsilon$ if we consider a six dimensional space (x, y, z, p_x, p_y, p_z) of a volume θ composed of the volume of the reservoir V and a volume of a sphere having a radius p_0 such as $\frac{p_0^2}{2m} = \epsilon$ where m is the mass of the particle, thus the volume is:

$$V' = \frac{4}{3} \pi p_0^3 = \frac{4}{3} \pi (2m\epsilon)^{3/2} \quad (\text{B.12})$$

We derive the volume of the total space which is the product of the volume of the reservoir

V and the elementary volume of the sphere dV' :

$$d\theta = VdV' = V2\pi(2m)^3/2\epsilon^{1/2}d\epsilon \quad (\text{B.13})$$

The number of the accessible states $g(\epsilon)d\epsilon$ is proportional to the elementary volume $d\theta$. The factor of proportionality is $\frac{1}{h^3}$ where h is the Planck constant.

$$g(\epsilon)d\epsilon = \frac{1}{h^3}2\pi V(2m)^{3/2}\epsilon^{1/2}d\epsilon \quad (\text{B.14})$$

From this last equation we can find the partition function:

$$\begin{aligned} Z &= \int_0^\infty \frac{2\pi V}{h^3}(2m)^3 2\epsilon^{1/2} \times e^{-\epsilon/kT} d\epsilon \\ Z &= \frac{V}{h^3}(2\pi mkT)^{3/2} \end{aligned} \quad (\text{B.15})$$

And finally we can obtain the expression of the density of the occupied states as following:

$$n(\epsilon) = \frac{2\pi N}{(\pi kT)^{3/2}}\epsilon^{1/2} \times e^{-\epsilon/kT} \quad (\text{B.16})$$

As we are dealing with a monoatomic gas the energy is equal to the translational kinetic energy. So the one dimension Maxwell-Boltzmann velocity distribution $f_{\mathbf{v}}$ gives the velocity distribution for identical molecules of molar mass m [kg] of an ideal gas at temperature T [k].

$$\begin{aligned} n(\epsilon)d\epsilon &= f(v)dv \\ \epsilon &= \frac{1}{2}mv^2 \implies d\epsilon = mv \times dv \\ f(v) &= mv \times n(\epsilon) \end{aligned} \quad (\text{B.17})$$

which gives

$$f(v) = 4\pi N \left(\frac{m}{2\pi kT}\right)^{3/2} v^2 e^{-mv^2/2kT} \quad (\text{B.18})$$

$f(v)$ is the distribution of the norm of the velocities of an ideal gas placed in a reservoir at a certain temperature T . Figure B.1 shows the different distributions of velocities of two different gases for two different temperatures. In fact, the distributions get narrower proportionally to the lowering of the temperature. In other words, if we find a way to narrow or to have a uniformity of the velocities of the molecules, we can lower their

temperature. This is the advantage of the supersonic jet expansion used in this thesis which has the effect of reducing the thermal agitation of the molecules thanks to the multiple collisions which take place during the expansion of the gas through a small orifice. Another important parameter is the most probable velocity \vec{v}_p , it is defined as the most common velocity of a certain gas and could be obtained by solving the equation $\frac{df(v)}{dv} = 0$. We find that

$$v_p = \left(\frac{2kT}{m}\right)^{1/2} \quad (\text{B.19})$$

We can also find the mean velocity \bar{v} by solving the following equation:

$$\bar{v} = \frac{\int_0^\infty v f(v) dv}{\int_0^\infty f(v) dv} \quad (\text{B.20})$$

Which gives:

$$\bar{v} = \left(\frac{8kT}{\pi m}\right)^{1/2} \quad (\text{B.21})$$

Finally the mean square speed which is the second-order raw moment of the speed distribution. It is the square root of the mean square speed, corresponding to the speed of a particle with median kinetic energy:

$$\frac{mv^2}{2} = \frac{3}{2}kT \quad (\text{B.22})$$

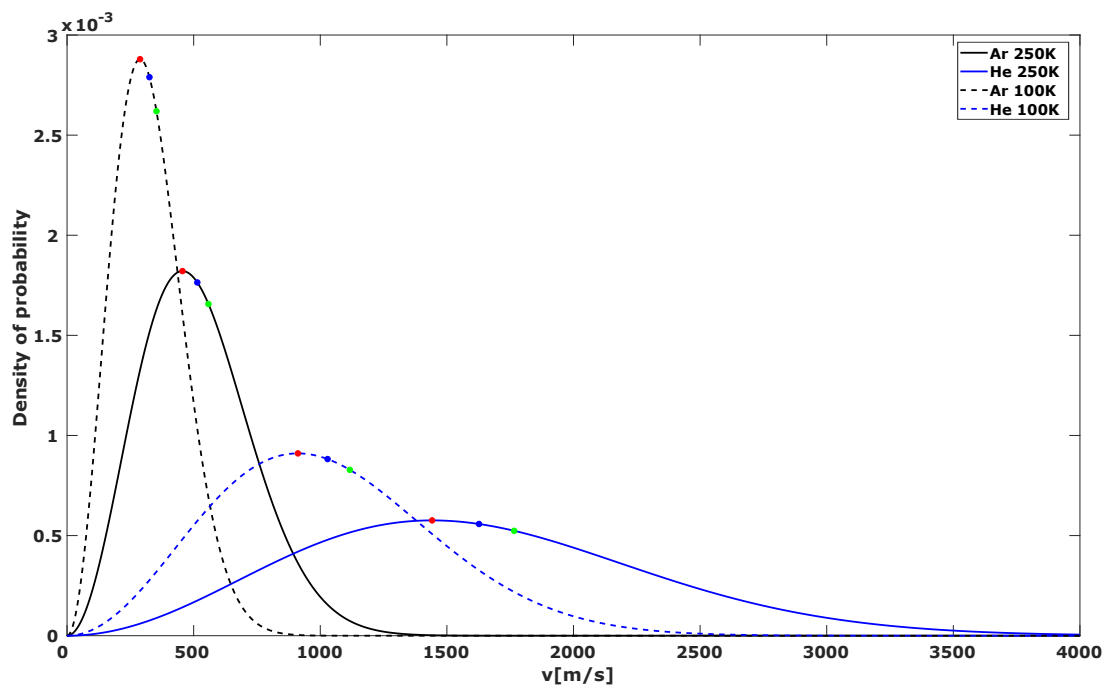


Figure B.1 – Distribution of the modulus of velocities for argon and helium for two different temperatures (250K and 100K). We notice that a lowering of the temperature is accompanied by a reduction in the width of the distributions and a reduction in the most probable velocity v_p which is also presented in this figure in *red*. also with the mean velocity \bar{v} in *blue*. and The mean square speed \bar{v}^2 in *green*.

APPENDIX: ADDITIONAL PULSED SUPERSONIC SOURCE

We have developed in Louvain-la-Neuve a pulsed valve and a nozzle (general valve Series 9) same as the one used in Canada, in the university of Calgary [220]. In order to increase the length of the jet's interaction with the laser, a slotted orifice is used. This distributes the expansion of gas along the laser beam. The length of the slit is equal to 30 mm, and the width is of 25 μ m. In order to evenly distribute the gas expansion along the laser beam, a multi-channel block was used. A diagram of this block is shown in figure C.1 The diameter of the holes is different to ensure the uniform distribution of the expanding gas along the orifice. The slot is formed by a pair of adjustable blades that could be screwed to the block.

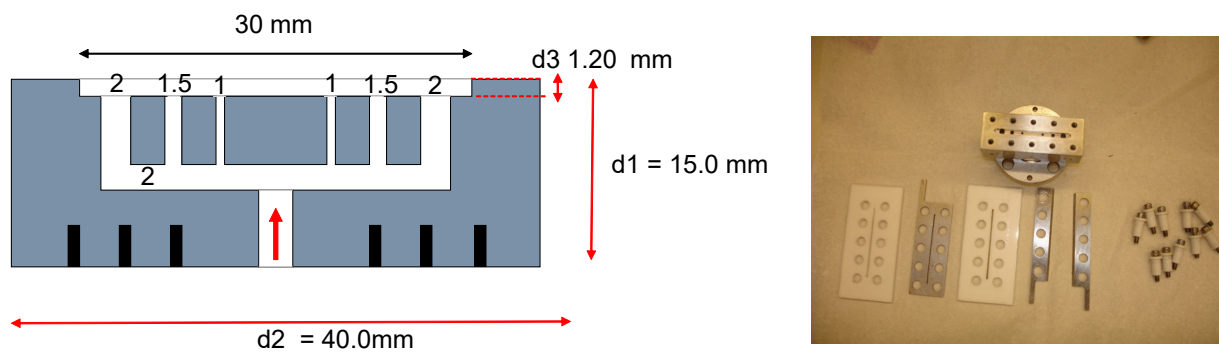


Figure C.1 – On the left, a schematic design of the nozzle. On the right a photo showing the nozzle and the teflon/ stainless steel pieces used to initiate a discharge and to insure a planar geometry at the exit of the nozzle.

RING-DOWN SPECTROSCOPY CRDS

Cavity ring-down Spectroscopy aka *CRDS* is the name for a highly sensitive method for direct absorption measurements [221]. This technique is based on the observation of the exponential decay of the light inside the optical cavity, which can lead to measure the absorption of the studied species. A typical Cavity ring-down Spectroscopy setup consists of a cw laser diode, a high finesse optical cavity (length L) and a detection system.

The experimental principle is based on the measurement of a rate rather than a magnitude of an intensity change, this approach is then advantageous and virtually eliminates the problem of light intensity fluctuations, which are common in conventional absorption spectroscopy. This combined with the ability of using very long effective lengths gives *CRDS* its high sensitivity. Therefore the finesse is an important parameter to be taken in consideration, it is explained in Appendix D, the higher the finesse is the higher the interaction length with the studied gas inside the cavity is. Another parameter is the pulse duration, if it is small compared to the time to return to the cavity which could be calculated via $2L/c$, there is no light interference with it in the cavity. The fraction of the laser pulse trapped in the cavity will be reflected alternately on each mirror losing at each reflection a part of its energy. The temporal profile of the observed transmitted signal is then formed by a succession of pulses whose intensity gradually decreases as shown in Figure C.2. Furthermore, the spectrum of the laser pulse will decompose into several modes of resonance of the cavity as discussed in Appendix D. The most important in this technique is the measurement of the decay time which allows the determination of the coefficient molecular absorption as a function of frequency ν . To do so we will start by finding the first fraction of light of intensity I_1 transmitted by the cavity and it is written as following:

$$I_1 = T^2 \exp(-\alpha L) I_0 \quad (\text{C.1})$$

In this equation T is the transmission coefficient of the mirrors and α is the absorption coefficient of the species inside the cavity. In fact, after each round trip inside the cavity the measured intensity will decrease by a factor of $\exp(-2\alpha L)$, so after a number n of

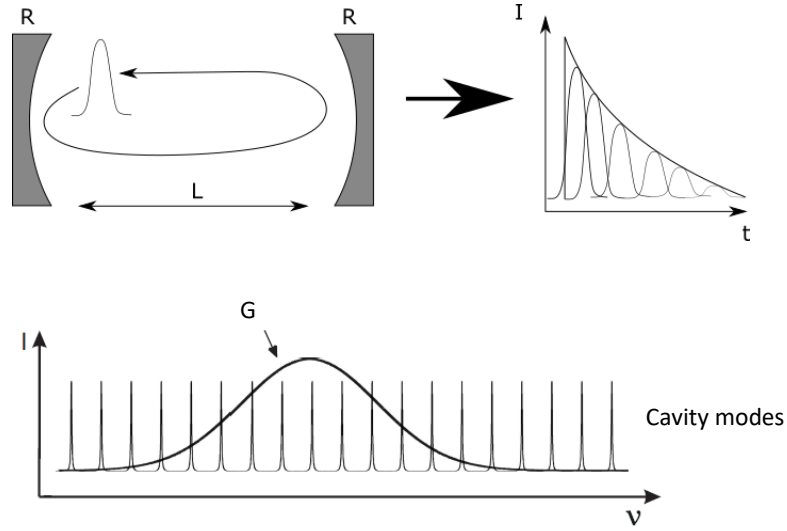


Figure C.2 – Time profile of the transmission of a laser pulse after several round trips in a high-finesse optical cavity. G is the spectral profile of the laser pulse that extends over the cavity modes.

round trips the detected intensity is written as:

$$I_n = [R \exp(-\alpha L)]^{2n} I_1 = I_1 \exp(-2n(-\ln R + \alpha L)) \quad (\text{C.2})$$

The reflection coefficient R is close to 1 as we are dealing with high reflectivity mirrors, $\ln R$ could be replaced by $-(1 - R)$. The variable n can be also changed to a temporal variable as $t = 2nL/c$ which corresponds to the time for one round trip of the light inside the cavity. Which can give:

$$I(t) = I_1 \exp\left(-\frac{t}{\tau}\right) \quad (\text{C.3})$$

τ is equal to:

$$\tau = \frac{L}{c[(1 - R) + \alpha L]} \quad (\text{C.4})$$

This quantity represents the exponential decay time of the light inside the cavity. More precisely it represents the duration for which the initial intensity I_1 is divided by e . The measurement of this duration is the principle parameter in *CRDS* setup known as the

ring-down time. To better understand the physics behind this quantity illustrated in Equation C.4 another more common representation is given by Equation C.5

$$\frac{1}{\tau} = \frac{(1 - R) + \alpha L}{L/c} \quad (\text{C.5})$$

In this equation $\frac{1}{\tau}$ represents the total losses inside the cavity per time unit. The two terms $(1 - R)$ and αL represent respectively the losses on the mirror surface and the losses due to the absorption of the gas inside the cavity for one round trip. Which leads to the determination of the absorption coefficient as following:

$$\alpha = \frac{1}{c\tau} - \frac{1 - R}{L} \quad (\text{C.6})$$

Other important parameters in *CRDS* setup are the effective length L_{eff} which is equal to $L_{eff} = c\tau$ and it could be presented in function of the finesse as following:

$$L_{eff} = \frac{2F}{\pi} L \quad (\text{C.7})$$

In addition, the minimal absorption coefficient that varies between 10^{-6} cm^{-1} and 10^{-10} cm^{-1} . Note that the *CRDS* setup using a pulsed laser presents different and many inconveniences due to the large emission spectrum and the relatively bad spatial profile of the beam. Indeed, it represents different longitudinal and transverse modes which can influence the decay time relatively to a perfect exponential [222]. A new technique was then implemented by coupling a monochromatic cw-laser to the high finesse cavity and the technique is called *CW-CRDS*. The latter brings an additional difficulty compared to *CRDS* with pulsed lasers because it is necessary to inject effectively for a sufficient time the fine spectrum of the laser (for example of the order of MHz for a laser diode in the even finer mode of the cavity ($\approx 10 \text{ kHz}$)). Briefly, the principle [223] is similar to the one of the typical *CRDS* as it consists of using a cavity and two highly reflective mirrors. The injection of the cavity is obtained simply using an acousto-optic modulator which deflects the beam towards the entrance to the cavity. Thus the modulator plays the role of an interrupter. The length of the cavity is modulated by applying an electrical voltage on a piezoelectric fixed on one of its mirrors. The signal is detected by a photodiode. Typically, *CW-CRDS* allows a detection dynamic covering 3 to 4 orders of magnitude (varying from 10^{-5} cm^{-1} to 10^{-9} cm^{-1}). For example, a minimum detectable absorption coefficient of the order of $2 \times 10^{-11} \text{ cm}^{-1}$ [224] was obtained by averaging 30000 ring-down

events per point of the absorption spectrum.

The repetition rate of the decay times is limited by the frequency of modulation of the cavity in *CW-CRDS* while in the *CRDS* with pulsed lasers it depends on the laser used. The reproducibility of the values of the ring-down times is much better with *CW-CRDS* relatively to *CRDS* with pulsed lasers. This difference is directly related to the stability of the laser source. Indeed, in the *CW-CRDS*, the laser is spectrally and spatially stable whereas a pulsed laser exhibits fluctuations in spectral distribution. Therefore, it's not always the same transverse modes and longitudinal that are excited and which induce different values of time of decline. The spectral width is generally determined by the width of the laser. The *CW-CRDS* allows a gain in spectral resolution compared to the *CRDS* with pulsed lasers. In the first case, it is of the order of MHz and in the second case it is of the order of GHz. However, a disadvantage of the *CW-CRDS* is the limited availability of laser sources, especially laser diodes in certain spectral regions therefore limiting the scanning range.

APPENDIX: GAUSSIAN BEAMS AND OPTICAL CAVITIES

In this Appendix, we will briefly recall some theoretical basic elements for the treatment and description of the coupling of the light beam into an optical cavity considered symmetric.

D.1 Transverse cavity modes

To introduce the notion of cavity modes, we need to solve the Maxwell equation in the framework of the paraxial approximation, considering the propagation of the light in an isotropic, unloaded and non-magnetic medium. Following these assumptions, we have the wave equation:

$$\nabla^2 E = \frac{1}{c^2} \frac{\partial^2 E}{\partial t^2} \quad (\text{D.1})$$

In this equation E is the electric field and c is the speed of light in vacuum ≈ 299792 km/s. Considering a monochromatic wave propagating in the z direction and the field polarisation n . We can write the solution of the wave equation as:

$$E(x, y, z, t) = \frac{1}{2} E(x, y, z) e^{i\omega t} n \quad (\text{D.2})$$

In which $E(x, y, z)$ is the scalar field associated to E . The equation D.1 can then be written as a scalar equation as following :

$$(\nabla^2 + k^2)E = 0 \quad (\text{D.3})$$

in which the value of the wave vector k is given by $k = 2\pi/\lambda$. If we then take in consideration the transverse structure of the electric field and its propagation along the

z axis a solution of the equation D.3 could be written in the form :

$$E(x, y, z) = \psi(x, y, z)e^{-ikz} \quad (\text{D.4})$$

By combining both equations D.3 and D.4 and if the second order terms are neglected because of the paraxial approximation, the equation D.4 becomes:

$$\frac{\partial^2 \psi}{\partial x^2} + \frac{\partial^2 \psi}{\partial y^2} - 2ik \frac{\partial \psi}{\partial z} = 0 \quad (\text{D.5})$$

The solutions of this equation D.5 depends on the choice of the coordinates. If we consider Cartesian coordinates, the equation D.4 could be written as:

$$E_{m,n}(x, y, z) = E_0 \frac{w_0}{w(z)} H_m\left(\sqrt{2} \frac{x}{w(z)}\right) H_n\left(\sqrt{2} \frac{y}{w(z)}\right) \exp\left(-\frac{r^2}{w^2(z)} - i\phi(r, z)\right) \quad (\text{D.6})$$

in this equation $r = \sqrt{x^2 + y^2}$ and $\phi(r, z) = kz - (m + n + 1)\arctan\left(\frac{z}{z_0}\right) + \frac{kr^2}{2R(z)}$. Equation D.6 expresses the distribution of the electric field as the product of two Hermite polynomials (H_m and H_n), a Gaussian function and a phase term defining the Hermite–Gauss modes. The indices m and n define the order of the mode, more practically the shape of the profile in the x and y direction.

Figure D.1 illustrates the distribution of the intensity of the first modes with m nodes for the horizontal direction and n nodes for the vertical direction. For $m = n = 0$, we get a purely Gaussian profile. This mode is noted TEM₀₀) and called fundamental transverse mode or beam at the diffraction limit. All the others modes (TEM _{m,n}) are higher order transverse modes.

We distinguish three important parameters which characterize the beam :

1. w_0 : The minimum size of the beam at $z = 0$ so called waist and calculated via equation D.9. The beam waist is located where the wavefront is plane.
2. $w(z_r)$: The size of the beam at $1/e^2$ of the maximum intensity calculated using equation D.7 and we note that the divergence of the beam is characterised by the variation of $w(z)$ with respect to z
3. $R(z)$: The radius of curvature of the wavefront calculated using equation D.10

These parameters are written as following:

$$w(z) = w_0 \sqrt{1 + \left(\frac{\lambda z}{\pi w_0^2}\right)^2} = w_0 \sqrt{1 + \left(\frac{z}{z_r}\right)^2} \quad (\text{D.7})$$

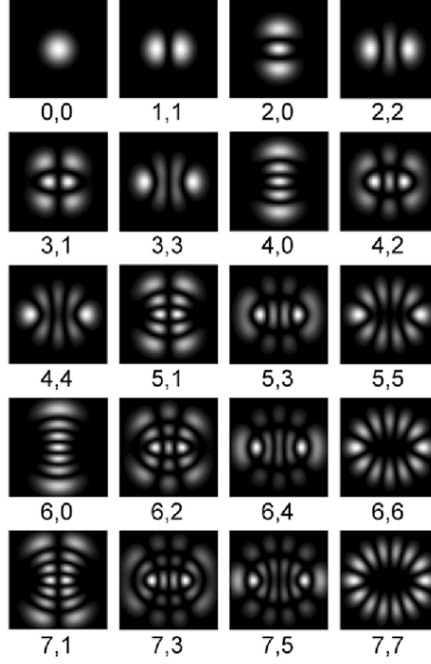


Figure D.1 – Distribution of the transverse mode of the intensity of the first Hermite-Gauss modes $TEM_{m,n}$ under each photo the value of m, n is indicated. This photo is reproduced from reference [225].

Where z_r is the Rayleigh length expressed by:

$$z_r = \frac{\pi w_0^2}{\lambda} \quad (\text{D.8})$$

with w_0 the waist of the laser beam written as :

$$w_0^2 = \frac{\lambda}{2\pi} \sqrt{L(2R - L)} \quad (\text{D.9})$$

$$R(z) = z \left[1 + \left(\frac{z_r}{z} \right)^2 \right] \quad (\text{D.10})$$

A Gaussian beam can be characterized by the complex parameter q which can be written in function of $R(z)$ and $w(z)$ as following:

$$\frac{1}{q(z)} = \frac{1}{R(z)} - i \frac{\lambda}{\pi w^2(z)} \quad (\text{D.11})$$

We characterize the divergence of the beam by θ , which we obtain by taking the asymptotic value of $w(z)$; $\theta = \lambda/\pi w_0$. In equation D.6, the amplitude term indicates that the energy of the intracavity light is concentrated around the optical z axis and the wave front is

spherical at great distances (parabolic when approaching the origin, plane in $z = 0$ and there is an inversion of the sign of the radius of curvature on both sides of the origin). This implies that the light overlap perfectly with itself after each round-trip. An example, is the calculation of the distance required to have an increase of 1% of the half width of the laser beam $w(z)$ by assuming a He:Ne laser of :

1) Wavelength $\lambda = 633nm$

2) The width of the beam at the output of the laser is $2w = 2\text{ mm}$

$z_r = \frac{\pi w_0^2}{\lambda} = 4.96\text{ m}$ The distance is then computed and it is $z = 0.7\text{ m}$. The laser is thus considered to be linear and non-divergent as long as short distances are considered.

The resonant frequencies $\nu_{m,n,q}$ for each mode can be defined as follows:

$$\nu_{m,n,q} = \frac{c}{2L} \left[q + \frac{1}{\pi} (m + n + 1) \left(\arctan \sqrt{\frac{z_2}{R_2 - z_2}} - \arctan \sqrt{\frac{z_1}{R_1 - z_1}} \right) \right] \quad (\text{D.12})$$

The frequency difference between two modes of the same order (m, n) , is called Free Spectral Range (denoted FSR) is then given by:

$$\delta\nu = FSR = \frac{c}{2\eta L} \quad (\text{D.13})$$

η is the refraction index of the intra-cavity medium. In the case of a symmetrical cavity ($R_1 = R_2 = R$), the frequency difference between two different order modes is written :

$$\nu_{m',n',q} - \nu_{m,n,q} = \frac{c}{L\pi} \arctan \sqrt{\frac{L}{2R - L}} \Delta(m + n) \quad (\text{D.14})$$

Moreover the light in an optical cavity will interfere with itself when it overlaps. Which is possible by imposing on the phase of being a multiple of 2π after a round trip in the cavity. So the length L separating the two mirrors must be equal to an integer of half the wavelength. Any frequency being a multiple of this FSR can resonate within the cavity and therefore will be then transmitted through the cavity. The cavity is thus characterized by a set of transverse modes of propagation associated with multiple longitudinal orders (indicated by q). Each order being associated with a certain frequency. Note that there are several possible distributions of the spread of the electric field in a free space. However, an advantage with Hermite-Gauss modes is that they preserve their profiles when propagating. As long as the propagation of the field remains dominant in one direction, any other distribution can be constructed as a superposition of these modes. Obviously, the phases

would change and therefore the intensity profile would also differ from a superposition to another. Note also that there are other types of modes called Laguerre-Gaussian modes and which are obtained by using the cylindrical coordinate system.

D.2 Quality factor M^2

A real laser beam, having several transverse modes, has a waist and a divergence wider than those relating to an ideal Gaussian beam characterized by a single mode TEM₀₀. To quantify this difference, a factor denoted M^2 can be defined in the following equation using the divergence θ :

$$M^2 = \frac{\pi w_0 \theta}{\lambda} \quad (\text{D.15})$$

D.3 Ray transfer matrices

As explained above, a Gaussian beam can be characterised by the radius of curvature of its wavefront and by the half width of the beam along its propagation axis. The q-parameter of a Gaussian beam is a complex parameter that gathers these two quantities to ease the study of the influence of optical devices on the beam. This parameter is defined by the equation D.11 and we can also write:

$$q(z) = z + iz_r \quad (\text{D.16})$$

Where z is the position along the propagation axis, the origin of this axis is set at the beam waist position. The ABCD formalism is used to describe the effect of each optical device on a Gaussian beam and it is based on the q-parameter. Each optical device has its own ABCD matrix, that represents its influence on the beam. The ones that will be used in this thesis in order to do the mode matching between the laser and the cavity are the ones of a free propagation along a distance L in a medium of refractive index n , the one of a convex lens of a focal length f and the one at the output of the resonator. This third element is characterised by its thickness te , the radius of curvature of the concave mirror R and the refractive index of the medium constituting the mirror n_m . These matrices are the ones given in table D.1. If a beam of parameter q goes through an optical device

described by the ABCD matrix

$$\begin{bmatrix} A & B \\ C & D \end{bmatrix}$$

the beam will have a new beam parameter q' given by

$$q' = \frac{Aq + B}{Cq + D} \quad (\text{D.17})$$

D.4 Stability of the optical cavity

It is crucial to study the stability of an optical cavity before injecting a light beam into it, since it reflects the conditions that allow the beam to remain confined as long as possible inside the cavity. In addition, it is necessary to ensure proper cavity dimensions to guarantee its stability. This is obtained thanks to the formalism of the matrices ABCD which was explained above. So the spread of a light beam through several optical elements becomes simply a multiplication of several matrices. We can then represent an optical cavity by the matrices describing the trajectory of the light starting from the reflection on the first mirror characterised by the radius of curvature R_1 , then a free propagation d inside the cavity, another reflection on the second mirror characterised by the radius of curvature R_2 and finally another free propagation d and the matrices are multiplied from the last element to the first element as following:

$$\begin{bmatrix} A & B \\ C & D \end{bmatrix} = \begin{bmatrix} 1 & d \\ 0 & 1 \end{bmatrix} \begin{bmatrix} 1 & 0 \\ -\frac{2}{R_2} & 1 \end{bmatrix} \begin{bmatrix} 1 & d \\ 0 & 1 \end{bmatrix} \begin{bmatrix} 1 & 0 \\ -\frac{2}{R_1} & 1 \end{bmatrix} \quad (\text{D.18})$$

We consider r_1 and r_2 the distance separating a light beam and the optical axis and θ_1 and θ_2 the angular direction of propagation with respect to this same axis before(1) and after(2) a passage through the cavity:

$$\begin{bmatrix} r_2 \\ \theta_2 \end{bmatrix} = \xi \begin{bmatrix} r_1 \\ \theta_1 \end{bmatrix} = \begin{bmatrix} A & B \\ C & D \end{bmatrix} \cdot \begin{bmatrix} r_1 \\ \theta_1 \end{bmatrix} \quad (\text{D.19})$$

Optical element	ABCD matrix
Free propagation	$\begin{bmatrix} 1 & d \\ 0 & 1 \end{bmatrix}$
Refraction at a flat interface	$\begin{bmatrix} 1 & 0 \\ 0 & \frac{n_1}{n_2} \end{bmatrix}$
Refraction at a curved interface	$\begin{bmatrix} 1 & 0 \\ \frac{n_1-n_2}{Rn_2} & \frac{n_1}{n_2} \end{bmatrix}$
Reflection from a flat mirror	$\begin{bmatrix} 1 & 0 \\ 0 & 1 \end{bmatrix}$
Reflection from a curved mirror	$\begin{bmatrix} 1 & 0 \\ -\frac{2}{R} & 1 \end{bmatrix}$
Thin lens	$\begin{bmatrix} 1 & 0 \\ -\frac{1}{f} & 1 \end{bmatrix}$
Thick lens	$\begin{bmatrix} 1 & 0 \\ \frac{n_2-n_1}{R_2n_1} & \frac{n_2}{n_1} \end{bmatrix} \begin{bmatrix} 1 & t \\ 0 & 1 \end{bmatrix} \begin{bmatrix} 1 & 0 \\ \frac{n_1-n_2}{R_1n_2} & \frac{n_2}{n_1} \end{bmatrix}$
Single prism	$\begin{bmatrix} k_n & \frac{d}{nk_n} \\ 0 & \frac{1}{k_n} \end{bmatrix}$

Table D.1 – ABCD transfer matrices of different optical elements. d is the distance, n_1 and n_2 the initial and final refractive index, R the radius of curvature of a curved surface, f is the focal length, θ is the mirror angle of incidence in the horizontal plane, t the center thickness of lens, k_n is the beam expansion factor.

in which ξ is a constant that relate the ray (r_2, θ_2) to the initial ray (r_1, θ_1) , the equation D.19 gives:

$$\xi^2 - \xi(A + D) + (AD - BC) = 0 \quad (\text{D.20})$$

It is given that $(AD - BC) = 1$ and if we assume that $a = \frac{1}{2}(A + D)$ the equation D.20 becomes:

$$\xi^2 - 2a\xi + 1 = 0 \quad (\text{D.21})$$

Two possible solutions for this equation :

1. $e^{\pm i\phi}$ if $|a| \leq 1$
2. $e^{\pm\phi}$ if $|a| \geq 1$

if we choose the second solution and after a certain number N of round trip inside the cavity, we obtain:

$$\begin{bmatrix} r^N \\ \theta^N \end{bmatrix} = \xi^N \begin{bmatrix} r_1 \\ \theta_1 \end{bmatrix} = e^{\pm N\phi} \begin{bmatrix} r_1 \\ \theta_1 \end{bmatrix} \quad (\text{D.22})$$

Therefore the condition for the stability of the cavity is :

$$|A + D| \leq 2 \quad (\text{D.23})$$

Which finally gives:

$$0 \leq \left(1 - \frac{d}{R_1}\right)\left(1 - \frac{d}{R_2}\right) \leq 1 \quad (\text{D.24})$$

In the figure D.2 we introduce the stability parameter g which can lead to plot $g_2 = 1 - \frac{L}{R_2}$ against $g_1 = 1 - \frac{L}{R_1}$ to show graphically the stability of different configuration of the cavity

D.5 Optical cavity finesse

The finesse of a Fabry-Perot type optical cavity is mathematically defined by:

$$F = \frac{FSR}{\Delta\nu} = \frac{\pi\sqrt{R}}{(1 - R)} \quad (\text{D.25})$$

where $\Delta\nu$ is the Full Width at Half-Maximum (FWHM) of the transmission peaks of the cavity. We can define finesse as the number of bounces a beam makes before leaking out or being absorbed inside the cavity. It is therefore a way to quantify the performance of the cavity. One of the main factors affecting the smoothness is the reflectivity of the mirrors, beside other factors like the scattering effect mainly due to the presence of dust

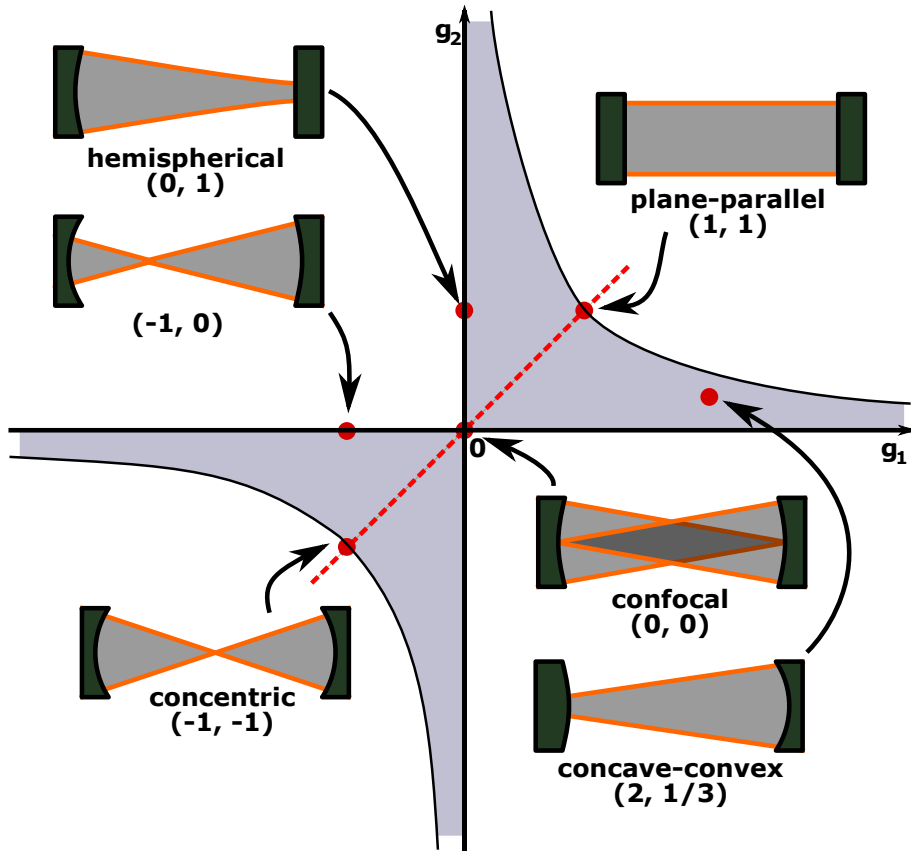


Figure D.2 – Stability diagram for a two-mirror cavity. Shaded areas corresponds to a stable configuration. Cavities at points exactly on the line are marginally stable, reproduced from [226].

particles, the microroughness, coating non-uniformity and the transmission of the input mirror. Moreover, other elements that can affect the finesse like mechanical vibrations and thermal stability of the cavity. These factors directly influence the number of back and forth movements of the light inside the cavity. The greater the number of round trips, the more effects of constructive or destructive interference that a beam will undergo will be high. The greater the finesse, the greater the intracavity intensity. With dielectric mirrors having a reflection coefficient $R = 99.99\%$, a finesse of the order of a few tens of thousands can be achieved. The quality factor Q is given by the resonance frequency over its linewidth and it is expressed in the following form:

$$Q = \frac{\nu}{FSR} \times F \quad (\text{D.26})$$

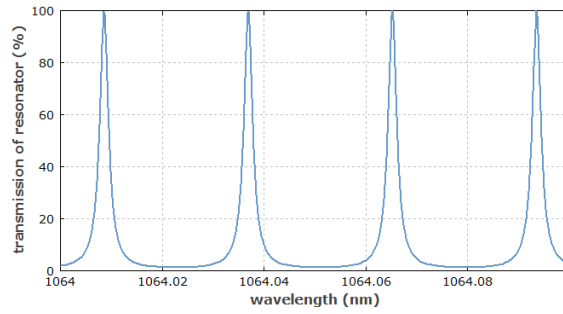


Figure D.3 – An example of calculated transmission of a cavity having mirror reflectivity equal to 80% and the finesse equal to 14, assuming a perfect spatial and frequency mode-matching.

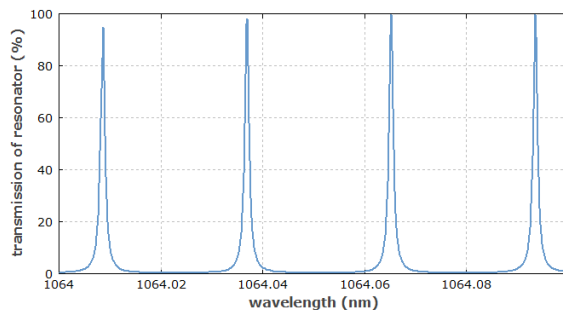


Figure D.4 – An example of calculated transmission of a cavity having mirror reflectivity of 90% and finesse equal to 29.8.

D.6 Mode matching calculation

The script below compute the position of the lens and the laser relatively to the first high reflective mirror:

```
1 %this script is to mode match the laser and the cavity and by
   taking the
2 %mirror as a medium that changes the beam waist
3 %
4 % This script calculates a modematching network (made of two
   lenses)
5 % between two beam waists (output beam from the laser and beam
   matched to the cavity)
6 %
7 %
8 % Input parameters:
9 %
10 %
11 % lambda — wavelength
12 % f1, f2 — focal lenght of lenses
13 % w0_laser — laser beam waist radius
14 % L — distance from the laser output
15 % L1 — distance from laser waist to the first (f1) lens.
16 % w0 — beam waist radius of beam that matches to the cavity (
   FSR and ROC of mirrors are requied to calculate it)
17 %
18 %
19 % [laser beam waist radius] <-----L1-----> [f1]
   <-----L2-----> [f2] <-----L3-----> [cavity
   beam waist radius]
20 %
21 % returned parameters:
22 % L2 — distance between f1 and f2 lenses
23 % L3 — distance from f2 lens do the cavity's waist
24 %
```

```

25
26
27 lambda = 600e-9; % wavelength in m
28 w0_laser = 0.55e-3;% waist in m
29
30
31 f1= 0.15; %focal length for first lens in m
32 f2= 0.03; %focal length for second lens in m
33
34
35 L0 = 4.552; %beam waist position in m
36 L=2*10^-2; %distance from the laser output
37 L1= L-L0; %distance from input waist to first lens in m
38
39 %calculate q for the laser
40 qlaser=1i*pi*w0_laser^2/lambda;
41
42 %place here the beam parameters for the cavity
43 %[q0,w0,zR,z]=getBeamParameters(w1,w2,x,lambda);
44
45 % waist size of the cavity
46 R = 1; % in m
47 L_m = .25; % distance between cavity mirror in m
48 z0 = sqrt((R-L_m/2)*L_m/2); % Rayleigh range for the cavity
49 w0 = sqrt(z0*lambda/pi) ;% ;cavity waist, in the middle of the
    cavity or at the mirror
50
51 qfinal=(-1i*lambda/(pi*w0^2))^(-1);
52 te =6.35e-3;%Thickness of the output mirror [m]
53 n=1.457;%Refractive index of the medium in the output mirror
54 Aout=[1 0 ; 0 L_m/2]*[1 0 ; n-1 n]*[1 te ; 0 1]*[1 0 ; 0 1/n];%
    ABCD matrix of the output of the first mirror of the
    resonator

```

```

55 qlleft =(Aout(1,1)*qfinal + Aout (1 ,2))/(Aout(2,1 )*qfinal +
    Aout( 2,2)) ;%q before the input mirror
56
57
58 q0 = i*pi*w0^2/lambda;
59
60 %fprintf('The input beam has parameters w0=%f mm, z=%f mm.\n',w0
    *1000,z*1000);
61
62 %calculate the focus parameters of the first lens
63 LInt1 = -f1*(f1*L1-L1^2+qlaser^2)/(f1^2-2*L1*f1 + L1^2 - qlaser
    ^2);%by knowing L1 we can find L1
64 qInt1 = f1^2*qlaser/(f1^2-2*L1*f1 + L1^2 - qlaser^2);
65
66 %now we run the one lens modeMatching using the intermediate
    waist and
67 %the second lens
68
69 [LInt2 ,L3]= GetModeMatchLength(qInt1 ,q0 , f2) ;
70
71 %fprintf('LInt1 %f \n',LInt1+L1);
72
73
74 if (LInt2==0)
75     fprintf('I'm sorry , we found no solution.\n')
76     return ;
77 end
78
79 L2=LInt1+LInt2;
80
81 fprintf('\n\nThe mode matching network with lenses of f1=%f m,
    f2=%f m\n' ,...
82     f1 , f2) ;
83 fprintf('has L1=%f m, L2=%f m, and L3=%f m.\n\n',L1 ,L2 ,L3) ;

```

```

84 fprintf('Total length L1+L2+L3: %f m\n\n',L0+L1+L2+L3);
85
86
87
88 fprintf(' [Waist=%gmm] <-----L1-----> [ f= %gm] <-----L2
      -----> [ f= %gm] <-----L3-----> [Waist=%gmm]\n',
      w0_laser*1000,f1 , f2 ,w0*1000);

1 function [L1,L2] = GetModeMatchLength(q1,q2,f)
2
3
4 %This function returns the two lengths L1 and L2 needed to
      modematch the
5 %two beams q1,q2 with a single lens of focal length f.
6 %q1 and q2 are purely imaginary parameters.
7
8
9
10 rad=sqrt(f^2*q1*q2 + q1^2*q2^2);
11
12 %does a solution exist?
13 if (f^2<abs(q1*q2))
14     L1=0;
15     L2=0;
16     fprintf('No solution exists. The minimum f is %f mm.\n',...
17         1000*sqrt(abs(q1*q2)));
18     return
19 end
20
21 %calculate the root, taking the positive root.
22 L2 = real(f - q2 - (f^2*q2) / (f*q2+q1*q2 - (f*q2+rad)));
23
24 %find L1 in terms of L2
25 L1=((f*q2 + rad)./q2);

```


BIBLIOGRAPHY

- [1] AGGM Tielens, « The molecular universe », *in: Reviews of Modern Physics* 85.3 (2013), p. 1021.
- [2] Nicholas S Shuman, Donald E Hunton, and Albert A Viggiano, *in: Chem. Rev.* 115.10 (2015), pp. 4542–4570.
- [3] Holger SP Müller et al., « The Cologne Database for Molecular Spectroscopy, CDMS: a useful tool for astronomers and spectroscopists », *in: Journal of Molecular Structure* 742.1-3 (2005), pp. 215–227.
- [4] H Gupta et al., « Rotational spectra of the carbon chain negative ions C₄H⁻ and C₈H⁻ », *in: The Astrophysical Journal Letters* 655.1 (2007), p. L57.
- [5] Andrew J Coates et al., « Heavy negative ions in Titan’s ionosphere: Altitude and latitude dependence », *in: Planetary and Space Science* 57.14-15 (2009), pp. 1866–1871.
- [6] Thomas J Millar, Catherine Walsh, and Thomas A Field, *in: Chem. Rev.* 117.3 (2017), pp. 1765–1795.
- [7] F Postberg et al., « The E-ring in the vicinity of Enceladus: II. Probing the moon’s interior—the composition of E-ring particles », *in: Icarus* 193.2 (2008), pp. 438–454.
- [8] Lennart G Björn and Frank Arnold, « Mass spectrometric detection of precondensation nuclei at the arctic summer mesopause », *in: Geophysical Research Letters* 8.11 (1981), pp. 1167–1170.
- [9] Jasper Kirkby et al., « Role of sulphuric acid, ammonia and galactic cosmic rays in atmospheric aerosol nucleation », *in: Nature* 476.7361 (2011), pp. 429–433.
- [10] Katrianne Lehtipalo et al., « The effect of acid–base clustering and ions on the growth of atmospheric nano-particles », *in: Nature communications* 7.1 (2016), pp. 1–9.
- [11] J Curtius, ER Lovejoy, and KD Froyd, « Atmospheric ion-induced aerosol nucleation », *in: Space Science Reviews* 125.1 (2006), pp. 159–167.

-
- [12] Jozef Lengyel et al., « Electron-triggered chemistry in HNO₃/H₂O complexes », *in: Physical Chemistry Chemical Physics* 19.19 (2017), pp. 11753–11758.
- [13] Yoshiya Inokuchi et al., « Structures of water-CO₂ and methanol-CO₂ cluster ions:[H₂O • (CO₂)_n]⁺ and [CH₃OH • (CO₂)_n]⁺(n= 1–7) », *in: The Journal of chemical physics* 130.15 (2009), p. 154304.
- [14] Alan Van Orden and Richard J Saykally, « Small carbon clusters: spectroscopy, structure, and energetics », *in: Chemical reviews* 98.6 (1998), pp. 2313–2358.
- [15] F Salama, « Carbon-Carbon in the Universe », *in: Science* 282.5397 (1998), pp. 2204–2210.
- [16] Y. Endo, H. Kohguchi, and Y. Ohshima, « PDN–FTMW spectroscopy of open-shell complexes », *in: Faraday Discussions* 97 (1994), pp. 341–350.
- [17] G Bazalgette Courrèges-Lacoste et al., « Vibrationally excited state spectroscopy of radicals in a supersonic plasma », *in: Chemical physics letters* 335.3–4 (2001), pp. 209–214.
- [18] D. L. Osborn et al., « Photodissociation spectroscopy and dynamics of the N₂O₂ anion », *in: The Journal of chemical physics* 104.13 (1996), pp. 5026–5039.
- [19] Yuexing Zhao et al., « Spectroscopy and electron detachment dynamics of C⁻₄, C⁻₆, and C⁻₈ », *in: The Journal of chemical physics* 105.12 (1996), pp. 4905–4919.
- [20] P Barletta, J Tennyson, and P F Barker, « Towards sympathetic cooling of large molecules: cold collisions between benzene and rare gas atoms », *in: New Journal of Physics* 11.5 (2009), p. 055029, DOI: 10.1088/1367-2630/11/5/055029, URL: <https://doi.org/10.1088/1367-2630/11/5/055029>.
- [21] K.-K. Ni et al., « A High Phase-Space-Density Gas of Polar Molecules », *in: Science* 322.5899 (2008), pp. 231–235, ISSN: 0036-8075, DOI: 10.1126/science.1163861, eprint: <https://science.sciencemag.org/content/322/5899/231.full.pdf>, URL: <https://science.sciencemag.org/content/322/5899/231>.
- [22] Eddy Timmermans et al., « Feshbach resonances in atomic Bose–Einstein condensates », *in: Physics Reports* 315.1–3 (1999), pp. 199–230.
- [23] Dipak K Basu, *Dictionary of Material Science and High energy physics*, CRC Press, 2018.

-
- [24] Arron B Wolk et al., « Cryogenic ion chemistry and spectroscopy », *in: Accounts of chemical research* 47.1 (2014), pp. 202–210.
- [25] Thomas R. Rizzo and Oleg V. Boyarkin, « Cryogenic Methods for the Spectroscopy of Large, Biomolecular Ions », *in: Gas-Phase IR Spectroscopy and Structure of Biological Molecules*, ed. by Anouk M. Rijs and Jos Oomens, Cham: Springer International Publishing, 2015, pp. 43–97, ISBN: 978-3-319-19204-8, DOI: 10.1007/128_2014_579, URL: https://doi.org/10.1007/128_2014_579.
- [26] P Bryan Changala et al., « Rovibrational quantum state resolution of the C60 fullerene », *in: Science* 363.6422 (2019), pp. 49–54.
- [27] Ronald GJ Fraser, *Molecular rays*, Cambridge University Press, 2015.
- [28] Richard E Smalley, Lennard Wharton, and Donald H Levy, « The fluorescence excitation spectrum of rotationally cooled NO₂ », *in: The Journal of Chemical Physics* 63.11 (1975), pp. 4977–4989.
- [29] Donald H Levy, « Laser spectroscopy of cold gas-phase molecules », *in: Annual Review of Physical Chemistry* 31.1 (1980), pp. 197–225.
- [30] *L. de Broglie (1929), O. Stern (1943), I.I. Rabi (1944), C.H. Townes (1964), A. Kastler (1966), P. Kusch (1955) and W.Lamb (1955), N.F. Ramsey (1989), D. Herschbach and Y.T. Lee and J. Polanyi (1986).*
- [31] LK Randeniya and MA Smith, « A study of molecular supersonic flow using the generalized Boltzmann equation », *in: The Journal of chemical physics* 93.1 (1990), pp. 661–673.
- [32] APJ Voncken and ATAM De Waele, « Adiabatic expansion of 3 He in 4 He at very low temperatures », *in: Journal of low temperature physics* 100.5 (1995), pp. 463–499.
- [33] P.W. Atkins, M. Mottet, and P. Depovere, *Éléments de chimie physique*, Chimie physique, De Boeck Supérieur, 1998, ISBN: 9782744500107, URL: <https://books.google.be/books?id=Ydh2QUWXLr8C>.
- [34] Robert Georges et al., « Nuclear spin symmetry conservation in 1H216O investigated by direct absorption FTIR spectroscopy of water vapor cooled down in supersonic expansion », *in: The Journal of Physical Chemistry A* 121.40 (2017), pp. 7455–7468.

-
- [35] Hylton R. Murphy and David R. Miller, « Effects of nozzle geometry on kinetics in free-jet expansions », *in: The Journal of Physical Chemistry* 88.20 (1984), pp. 4474–4478.
- [36] Erwin Franquet et al., « Free underexpanded jets in a quiescent medium: A review », *in: Progress in Aerospace Sciences* 77 (2015), pp. 25–53.
- [37] R. Georges, *La conservation de l'énergie, notes de cours*, ULB, 2001.
- [38] Salvador Montero, « Temperature and entropy in supersonic free jets », *in: Physics of Fluids* 25.5 (2013), p. 056102.
- [39] Belén Maté et al., « Inelastic collisions in para-H₂: Translation-rotation state-to-state rate coefficients and cross sections at low temperature and energy », *in: The Journal of chemical physics* 122.6 (2005), p. 064313.
- [40] Totaro Imasaka, David Moore, and TUAN VO-DINH, « Critical assessment: Use of supersonic jet spectrometry for complex mixture analysis (IUPAC Technical Report) », *in: Pure and Applied Chemistry - PURE APPL CHEM* 75 (Jan. 2003), pp. 975–998, DOI: 10.1351/pac200375070975.
- [41] F.B. Dunning and R.G. Hulet, *Atomic, Molecular, and Optical Physics: Atoms and Molecules*, Experimental Methods in the Physical Sciences, Elsevier Science, 1996, ISBN: 9780080860183, URL: <https://books.google.be/books?id=0chPSpRpjo0C>.
- [42] O. F. Hagena and W. Obert, « Cluster Formation in Expanding Supersonic Jets: Effect of Pressure, Temperature, Nozzle Size, and Test Gas », *in: The Journal of Chemical Physics* 56.5 (1972), pp. 1793–1802, DOI: 10.1063/1.1677455.
- [43] Ghassen Saidani et al., « High temperature reaction kinetics of CN ($v=0$) with C₂H₄ and C₂H₆ and vibrational relaxation of CN ($v=1$) with Ar and He », *in: The Journal of chemical physics* 138.12 (2013), p. 124308.
- [44] Michel Herman et al., « High resolution Fourier transform spectroscopy of jet-cooled molecules », *in: International Reviews in Physical Chemistry - INT REV PHYS CHEM* 19 (Apr. 2000), pp. 277–325, DOI: 10.1080/01442350050020905.
- [45] Alexander Golombek, Lisa Danzig, and Andreas Wucher, « Characterization of a supersonic gas jet via laser-induced photoelectron ionization », *in: Nuclear Instruments and Methods in Physics Research Section B: Beam Interactions with Materials and Atoms* 480 (2020), pp. 1–9.

-
- [46] M. Herman et al., « High resolution Fourier transform spectroscopy of jet-cooled molecules », *in: International reviews in physical chemistry* 19.2 (2000), pp. 277–325.
- [47] Richard Courant and Kurt Otto Friedrichs, *Supersonic flow and shock waves*, vol. 21, Springer Science & Business Media, 1999.
- [48] Richard T Driftmyer, « A correlation of freejet data », *in: AIAA journal* 10.8 (1972), pp. 1093–1095.
- [49] AL Addy, « Effects of axisymmetric sonic nozzle geometry on Mach disk characteristics », *in: AIAA Journal* 19.1 (1981), pp. 121–122.
- [50] David H Huang and Dieter K Huzel, *Modern engineering for design of liquid-propellant rocket engines*, American Institute of Aeronautics and Astronautics, 1992.
- [51] G Dupeyrat, JB Marquette, and BR Rowe, « Design and testing of axisymmetric nozzles for ion-molecule reaction studies between 20° K and 160° K », *in: The Physics of fluids* 28.5 (1985), pp. 1273–1279.
- [52] BR Rowe, « Studies of Ion-Molecule Reactions at $T < 80\text{k}$ », *in: Rate Coefficients in Astrochemistry*, Springer, 1988, pp. 135–152.
- [53] Dean B Atkinson and Mark A Smith, « Design and characterization of pulsed uniform supersonic expansions for chemical applications », *in: Review of scientific instruments* 66.9 (1995), pp. 4434–4446.
- [54] Kuno Foelsch, « The analytical design of an axially symmetric Laval nozzle for a parallel and uniform jet », *in: Journal of the Aeronautical Sciences* 16.3 (1949), pp. 161–166.
- [55] HJ Andrä, *in: Progress in Atomic Spectroscopy*, Springer, 1979, pp. 829–953.
- [56] M Carré et al., *in: Mol. Phys.* 40.6 (1980), pp. 1453–1480.
- [57] Harold A Schwarz, *in: J. Chem. Phys.* 67.12 (1977), pp. 5525–5534.
- [58] M Okumura, LI Yeh, and Yuan-Tseh Lee, *in: Laser Spectroscopy VII*, Springer, 1985, pp. 122–125.
- [59] M Okumura et al., *in: J. Chem. Phys.* 85.4 (1986), pp. 2328–2329.
- [60] James M Lisy, *in: J. Chem. Phys.* 125.13 (2006), p. 132302.

-
- [61] Otto Dopfer, Doris Roth, and John P Maier, *in: J. Chem. Phys.* 114.16 (2001), pp. 7081–7093.
- [62] Evan J Bieske and Otto Dopfer, *in: Chem. Rev.* 100.11 (2000), pp. 3963–3998.
- [63] Evan J Bieske, *in: J. Chem. Soc. Faraday T* 91.1 (1995), pp. 1–12.
- [64] Mark A Boyer et al., *in: J. Phys. Chem. A* (2020).
- [65] P Löffler et al., *in: Chem. Phys. Lett.* 252.5-6 (1996), pp. 304–310.
- [66] Matthew F Bush et al., *in: J. Am. Chem. Soc.* 129.6 (2007), pp. 1612–1622.
- [67] Andreas Osterwalder et al., *in: J. Chem. Phys.* 121.13 (2004), pp. 6317–6322.
- [68] Oskar Asvany et al., *in: J Chem. Phys.* 127.15 (2007), p. 154317.
- [69] Satrajit Chakrabarty et al., *in: J. Phys. Chem. Lett.* 4.23 (2013), pp. 4051–4054.
- [70] Ewen K Campbell et al., *in: Nature* 523.7560 (2015), pp. 322–323.
- [71] Oskar Asvany et al., *in: Science* 347.6228 (2015), pp. 1346–1349.
- [72] Caroline EH Dessent and Klaus Müller-Dethlefs, *in: Chem. Rev.* 100.11 (2000), pp. 3999–4022.
- [73] Clément Lauzin, Ugo Jacovella, and Frédéric Merkt, *in: Mol. Phys.* 113.24 (2015), pp. 3918–3924.
- [74] Ugo Jacovella et al., *in: Phys. Chem. Chem. Phys.* 20.2 (2018), pp. 1072–1081.
- [75] Daniel M Neumark, *in: Accounts Chem. Res.* 26.2 (1993), pp. 33–40.
- [76] Himansu S Biswal et al., *in: J. Am. Chem. Soc.* 133.11 (2011), pp. 3931–3942.
- [77] Irina Dyukova et al., *in: Anal. Chem.* (2020).
- [78] Christopher J Gray et al., *in: Anal. Chem.* 89.8 (2017), pp. 4540–4549.
- [79] M. D. Morse, « Supersonic beam sources », *in: Experimental methods in the physical sciences* 29 (1996), pp. 21–47.
- [80] W. R. Gentry and C. F. Giese, « Ten-microsecond pulsed molecular beam source and a fast ionization detector », *in: Review of Scientific instruments* 49.5 (1978), pp. 595–600.
- [81] R.M. Jordan, *PSV pulsed supersonic valve C-211*, 2016.
- [82] U. Even, « The Even-Lavie valve as a source for high intensity supersonic beam », *in: EPJ Techniques and Instrumentation* 2.1 (2015), p. 17.

-
- [83] Parker[®], *Pulse Valve, Ultra Low Leak Extreme Performance Valve, Fiche technique, Miniature Solenoid Valves*, 2016.
- [84] D Proch and T Trickl, *in: Rev. Sci. Instrum.* 60.4 (1989), pp. 713–716.
- [85] D. Irimia et al., « A short pulse (7 μ s FWHM) and high repetition rate (dc–5kHz) cantilever piezovalve for pulsed atomic and molecular beams », *in: Review of Scientific Instruments* 80.11 (2009), p. 113303.
- [86] J. B. Cross and J. J. Valentini, « High repetition rate pulsed nozzle beam source », *in: Review of Scientific Instruments* 53.1 (1982), pp. 38–42.
- [87] A. Flettner et al., « High harmonic generation at 1 kHz repetition rate with a pulsed valve », *in: Applied Physics B: Lasers and Optics* 73.2 (2001), pp. 129–132.
- [88] W. K. Schomburg, *Introduction to microsystem design*, Springer, 2015.
- [89] Anthony L Peratt, « Plasma and the universe: Large scale dynamics, filamentation, and radiation », *in: Plasma Astrophysics and Cosmology*, Springer, 1995, pp. 97–107.
- [90] Francis F Chen et al., *Introduction to plasma physics and controlled fusion*, vol. 1, Springer, 1984.
- [91] Willard W Harrison et al., « Glow discharge mass spectrometry », *in: Analytical Chemistry* 58.2 (1986), 341A–356A.
- [92] E Sili, F Koliatene, and JP Cambronne, « Pressure and temperature effects on the paschen curve », *in: 2011 Annual Report Conference on Electrical Insulation and Dielectric Phenomena*, IEEE, 2011, pp. 464–467.
- [93] Michael A Lieberman and Alan J Lichtenberg, *Principles of plasma discharges and materials processing*, John Wiley & Sons, 2005.
- [94] Frank Gunzer, Sascha Krüger, and Jürgen Grotemeyer, « Photoionization and photofragmentation in mass spectrometry with visible and UV lasers », *in: Mass spectrometry reviews* 38.2 (2019), pp. 202–217.
- [95] MD Shirk and PA Molian, « A review of ultrashort pulsed laser ablation of materials », *in: Journal of Laser Applications* 10.1 (1998), pp. 18–28.
- [96] Yu-Ju Lu, Julia H Lehman, and W Carl Lineberger, « A versatile, pulsed anion source utilizing plasma-entrainment: Characterization and applications », *in: The Journal of chemical physics* 142.4 (2015), p. 044201.

-
- [97] Huan Yu and Shan-Hu Lee, « Chemical ionisation mass spectrometry for the measurement of atmospheric amines », *in: Environmental Chemistry* 9.3 (2012), pp. 190–201.
- [98] Richard Knochenmuss et al., « The matrix suppression effect in matrix-assisted laser desorption/ionization: application to negative ions and further characteristics », *in: Rapid communications in mass spectrometry* 12.9 (1998), pp. 529–534.
- [99] Hua Wang et al., « Desorption corona beam ionization source for mass spectrometry », *in: Analyst* 135.4 (2010), pp. 688–695.
- [100] WW Harrison and CW Magee, « Hollow cathode ion source for solids mass spectrometry », *in: Analytical Chemistry* 46.3 (1974), pp. 461–464.
- [101] Na Na et al., « Development of a dielectric barrier discharge ion source for ambient mass spectrometry », *in: Journal of the American Society for Mass Spectrometry* 18.10 (2007), pp. 1859–1862.
- [102] Douglas C Duckworth and R Kenneth Marcus, « Radio frequency powered glow discharge atomization/ionization source for solids mass spectrometry », *in: Analytical Chemistry* 61.17 (1989), pp. 1879–1886.
- [103] S Dobrea et al., « Optical and mass spectrometry diagnosis of a CO₂ microwave plasma discharge », *in: Romanian Reports in Physics* 66.4 (2014), pp. 1147–1154.
- [104] Edward B Noel, *Electric discharge device*, US Patent 2,568,459, 1951.
- [105] L. Biennier et al., « Pulsed discharge nozzle cavity ringdown spectroscopy of cold polycyclic aromatic hydrocarbon ions », *in: The Journal of chemical physics* 118.17 (2003), pp. 7863–7872.
- [106] S. Davis et al., « Jet-cooled molecular radicals in slit supersonic discharges: Sub-Doppler infrared studies of methyl radical », *in: The Journal of chemical physics* 107.15 (1997), pp. 5661–5675.
- [107] A. Bogaerts et al., « Gas discharge plasmas and their applications », *in: Spectrochimica Acta Part B: Atomic Spectroscopy* 57.4 (2002), pp. 609–658.
- [108] National Institute of Standards and Technology, *Security Requirements for Cryptographic Modules*, tech. rep. Federal Information Processing Standards Publications (FIPS PUBS) 140-2, Change Notice 2 December 03, 2002, Washington, D.C.: U.S. Department of Commerce, 2001, DOI: 10.6028/nist.fips.140-2.

-
- [109] N. J. Braithwaite, « Introduction to gas discharges », *in: Plasma sources science and technology* 9.4 (2000), p. 517.
- [110] TN Kitsopoulos et al., « High resolution threshold photodetachment spectroscopy of negative ions », *in: Chemical physics letters* 159.4 (1989), pp. 300–306.
- [111] M. Hosseinzadeh and A. Sadighzadeh, « Design and numerical simulation of thermionic electron gun », *in: arXiv preprint arXiv:1509.06363* (2015).
- [112] G. S. Settles, *Schlieren and shadowgraph techniques: visualizing phenomena in transparent media*, Springer Science & Business Media, 2012.
- [113] A. Ben-Yakar, « Experimental investigation of mixing and ignition of transverse jets in supersonic crossflows », PhD thesis, stanford university, 2000.
- [114] K. Stein et al., « Undergraduate Studies of Supersonic Flow From a Converging-Diverging Nozzle », *in:* (2005).
- [115] J. Winckler, « The Mach interferometer applied to studying an axially symmetric supersonic air jet », *in: Review of Scientific Instruments* 19.5 (1948), pp. 307–322.
- [116] R Campargue, « Progress in overexpanded supersonic jets and skimmed molecular beams in free-jet zones of silence », *in: The Journal of Physical Chemistry* 88.20 (1984), pp. 4466–4474.
- [117] G. Settles and M. Hargather, « A review of recent developments in schlieren and shadowgraph techniques », *in: Measurement Science and Technology* 28 (2017), p. 042001.
- [118] J. Shamir, *Optical Systems and Processes*, SPIE Press monograph, Spie, 1999, ISBN: 9780819432261.
- [119] Joseph J Thomson, « XIX. Further experiments on positive rays », *in: The London, Edinburgh, and Dublin Philosophical Magazine and Journal of Science* 24.140 (1912), pp. 209–253.
- [120] AJ Dempster, « A new method of positive ray analysis », *in: Physical Review* 11.4 (1918), p. 316.
- [121] Francis William Aston, « LXXIV. A positive ray spectrograph », *in: The London, Edinburgh, and Dublin Philosophical Magazine and Journal of Science* 38.228 (1919), pp. 707–714.

-
- [122] RA Yost and CG Enke, « Selected ion fragmentation with a tandem quadrupole mass spectrometer », *in: Journal of the American Chemical Society* 100.7 (1978), pp. 2274–2275.
- [123] E. De Hoffmann and V. Stroobant, *Mass spectrometry: principles and applications*, John Wiley & Sons, 2007.
- [124] WE Stephens, « A Pulsed Mass Spectrometer with Time Dispersion », *in: Phys. Rev.* 69 (1946), p. 691.
- [125] AE Cameron and DF Eggers Jr, « An Ion“Velocitron” », *in: Review of Scientific Instruments* 19.9 (1948), pp. 605–607.
- [126] WC Wiley and Ii H McLaren, « Time-of-flight mass spectrometer with improved resolution », *in: Review of scientific instruments* 26.12 (1955), pp. 1150–1157.
- [127] VI Karataev, BA Mamyrin, and DV Shmikk, « New method for focusing ion bunches in time-of-flight mass spectrometers », *in: SPTP* 16 (1972), p. 1177.
- [128] JHJ Dawson and M Guilhaus, « Orthogonal-acceleration time-of-flight mass spectrometer », *in: Rapid Communications in Mass Spectrometry* 3.5 (1989), pp. 155–159.
- [129] Robert J Cotter, *in: ACS Publications*, 1994.
- [130] Agilent Technologies[®], *Time-of-Flight Mass Spectrometry Technical Overview*, 2011.
- [131] Alan D McNaught, Andrew Wilkinson, et al., *Comp. Chem. Term.* Vol. 1669, Blackwell Science Oxford, 1997.
- [132] CJ Dedman et al., *in: Rev. Sci. Instrum.* 72.7 (2001), pp. 2915–2922.
- [133] Orloff Jon, *Handbook of Charged Particle Optics*, 2009.
- [134] F H Read, « A symmetric electrostatic lenses of three apertures », *in: Journal of Physics E: Scientific Instruments* 3.2 (1970), pp. 127–131, DOI: 10.1088/0022-3735/3/2/310, URL: <https://doi.org/10.1088/0022-3735/3/2/310>.
- [135] Francis O Talbot et al., « Photodissociation spectroscopy of trapped protonated tryptophan », *in: The Journal of chemical physics* 122.7 (2005), p. 074310.
- [136] Satrajit Chakrabarty, « Electronic Spectroscopy of Cold Cations in a 22-Pole Trap by Indirect Methods », *in: PhD thesis* (2013).

-
- [137] Tomas Baer and Robert C Dunbar, « Ion spectroscopy: where did it come from; where is it now; and where is it going? », *in: Journal of the American Society for Mass Spectrometry* 21.5 (2010), pp. 681–693.
- [138] H Kreckel et al., *in: Rev. Sci. Instrum.* 81.6 (2010), p. 063304.
- [139] Anatoly Dzhonson et al., *in: J. Mol. Struct.* 795.1-3 (2006), pp. 93–97.
- [140] R Igosawa et al., « Photodissociation spectroscopy of N₂O⁺ in the ion storage ring RICE », *in: The Journal of Chemical Physics* 153.18 (2020), p. 184305.
- [141] A Hirota et al., « Radiative cooling dynamics of isolated N₂O⁺ ions in a cryogenic electrostatic ion storage ring », *in: Physical Review A* 102.2 (2020), p. 023119.
- [142] Dieter Klapstein and John P Maier, *in: Chem. Phys. Lett.* 83.3 (1981), pp. 590–593.
- [143] John H Callomon and Frederik Creutzberg, *in: Philos. Tr. R. Soc. S.-A.* 277.1266 (1974), pp. 157–189.
- [144] Carlos E Fellows and Michel Vervloet, *in: Chem. Phys.* 264.2 (2001), pp. 203–209.
- [145] CE Fellows, *in: J. Chem. Phys.* 138.16 (2013), p. 164316.
- [146] LL Lessa, AS Martins, CE Fellows, et al., *in: J. Chem. Phys.* 143.16 (2015).
- [147] LL Lessa, SD de Cândido, and CE Fellows, *in: J. Chem. Phys.* 140.21 (2014), p. 214311.
- [148] Mohammed A Gharaibeh and Dennis J Clouthier, *in: J. Chem. Phys.* 136.4 (2012), p. 044318.
- [149] Holger Herburger et al., *in: J. Chem. Phys.* 151.14 (2019), p. 144302.
- [150] Wenwu Chen, Jianbo Liu, and CY Ng, *in: J. Phys. Chem. A* 107.40 (2003), pp. 8086–8091.
- [151] Robert G Orth and Robert C Dunbar, *in: J. Chem. Phys.* 66.4 (1977), pp. 1616–1620.
- [152] R Frey, R Kakoschke, and EW Schlag, *in: Chem. Phys. Lett.* 93.3 (1982), pp. 227–231.
- [153] M Larzilliere and Ch Jungen, *in: Mol. Phys.* 67.4 (1989), pp. 807–837.
- [154] Timothy F Thomas, Fred Dale, and John F Paulson, *in: J. Chem. Phys.* 67.2 (1977), pp. 793–800.

-
- [155] M Larzillière et al., *in: Chem. Phys. Lett.* 119.1 (1985), pp. 55–60.
- [156] Haifeng Xu et al., *in: J. Chem. Phys.* 119.22 (2003), pp. 11609–11614.
- [157] Haifeng Xu et al., *in: J. Chem. Phys.* 121.7 (2004), pp. 3069–3073.
- [158] S Abed et al., *in: Chem. Phys.* 74.1 (1983), pp. 97–112.
- [159] Michel Larzilliere et al., *in: J. Chim. Phys.* 77 (1980), pp. 689–693.
- [160] Zhengfang Zhou et al., *in: J. Chem. Phys.* 150.22 (2019), p. 226101.
- [161] Hua Wang et al., *in: J. Chem. Phys.* 132.24 (2010), p. 244309.
- [162] Colin M Western, *in: J. Quant. Spectrosc. Ra.* 186 (2017), pp. 221–242.
- [163] *NIST Atomic Spectra Database*, https://physics.nist.gov/PhysRefData/ASD/lines_form.html.
- [164] Philip E Miller and M Bonner Denton, « The quadrupole mass filter: basic operating concepts », *in: Journal of chemical education* 63.7 (1986), p. 617.
- [165] MC McCarthy et al., *in: Astrophys. J. Lett.* 652.2 (2006), p. L141.
- [166] S Brünken et al., « Detection of the carbon chain negative ion C₈H⁻ in TMC-1 », *in: The Astrophysical Journal Letters* 664.1 (2007), p. L43.
- [167] FA Gianturco et al., *in: Astrophys. J.* 830.1 (2016), p. 2.
- [168] D McElroy et al., « The UMIST database for astrochemistry 2012 », *in: Astronomy & Astrophysics* 550 (2013), A36.
- [169] Peter Botschwina and Rainer Oswald, « High-level ab initio calculations for (potential) interstellar anions: Structures, spectroscopic properties and energetics », *in: AIP Conference Proceedings*, vol. 1504, 1, American Institute of Physics, 2012, pp. 458–460.
- [170] Patrick Freivogel et al., « Electronic absorption spectra of C 4- and C 6- chains in neon matrices », *in: The Journal of chemical physics* 107.1 (1997), pp. 22–27.
- [171] Harold Linnartz, *Cavity Ring-Down Spectroscopy of Molecular Transients of Astrophysical Interest*, Wiley-Blackwell: Chichester, United Kingdom, 2009.
- [172] Albert A Ruth, Johannes Orphal, and Sven E Fiedler, « Fourier-transform cavity-enhanced absorption spectroscopy using an incoherent broadband light source », *in: Applied optics* 46.17 (2007), pp. 3611–3616.

-
- [173] M. Triki et al., « Cavity-enhanced absorption spectroscopy with a red LED source for NO_x trace analysis », *in: Applied Physics B-lasers and Optics - APPL PHYS B-LASERS OPT* 91 (Apr. 2008), pp. 195–201, DOI: 10.1007/s00340-008-2958-x.
- [174] Kevin K. Lehmann and Daniele Romanini, « The superposition principle and cavity ring-down spectroscopy », *in: The Journal of Chemical Physics* 105.23 (1996), pp. 10263–10277, DOI: 10.1063/1.472955, eprint: <https://doi.org/10.1063/1.472955>.
- [175] James D Ingle Jr and Stanley R Crouch, « Spectrochemical analysis », *in:* (1988).
- [176] John U White, « Very long optical paths in air », *in: JOSA* 66.5 (1976), pp. 411–416.
- [177] Ying He et al., « Ultra-high sensitive light-induced thermoelastic spectroscopy sensor with a high Q-factor quartz tuning fork and a multipass cell », *in: Optics Letters* 44.8 (2019), pp. 1904–1907.
- [178] M-R De Backer et al., « The CW-CRDS spectra of the 16O/18O isotopologues of ozone between 5930 and 6340 cm⁻¹—Part 3: 16O18O18O and 18O16O18O », *in: Journal of Quantitative Spectroscopy and Radiative Transfer* 127 (2013), pp. 24–36.
- [179] Albert A Ruth, Sophie Dixneuf, and R Raghunandan, « Broadband cavity-enhanced absorption spectroscopy with incoherent light », *in: Cavity-enhanced spectroscopy and sensing*, Springer, 2014, pp. 485–517.
- [180] Jérôme Morville et al., « Effects of laser phase noise on the injection of a high-finesse cavity », *in: Appl. Opt.* 41.33 (2002), pp. 6980–6990, DOI: 10.1364/AO.41.006980, URL: <http://ao.osa.org/abstract.cfm?URI=ao-41-33-6980>.
- [181] Steven Brown, « Absorption Spectroscopy in High-Finesse Cavities for Atmospheric Studies », *in: Chemical reviews* 103 (Jan. 2004), pp. 5219–38, DOI: 10.1021/cr020645c.
- [182] J. Morville et al., « Fast, low-noise, mode-by-mode, cavity-enhanced absorption spectroscopy by diode-laser self-locking », *in: Applied Physics B* 80 (June 2005), pp. 1027–1038, DOI: 10.1007/s00340-005-1828-z.
- [183] M. Article citationsMore» Born and E. Wolf, *Corpuscular Point of View to Explain Light's Properties*, Optics and Photonics Journal, Vol.8 No.5, May 31, 2018, 19980.

-
- [184] Sven E. Fiedler, Achim Hese, and Albert A. Ruth, « Incoherent broad-band cavity-enhanced absorption spectroscopy », *in: Chemical Physics Letters* 371.3 (2003), pp. 284–294, ISSN: 0009-2614, DOI: [https://doi.org/10.1016/S0009-2614\(03\)00263-X](https://doi.org/10.1016/S0009-2614(03)00263-X), URL: <http://www.sciencedirect.com/science/article/pii/S000926140300263X>.
- [185] Stephen M. Ball, Justin M. Langridge, and Roderic L. Jones, « Broadband cavity enhanced absorption spectroscopy using light emitting diodes », *in: Chemical Physics Letters* 398.1 (2004), pp. 68–74, ISSN: 0009-2614, DOI: <https://doi.org/10.1016/j.cplett.2004.08.144>.
- [186] Enowmbi R. Ashu-Ayem et al., « Coastal Iodine Emissions. 1. Release of I₂ by *Laminaria digitata* in Chamber Experiments », *in: Environmental Science & Technology* 46.19 (2012), PMID: 22934673, pp. 10413–10421, DOI: 10.1021/es204534v, eprint: <https://doi.org/10.1021/es204534v>, URL: <https://doi.org/10.1021/es204534v>.
- [187] Jonathan E. Thompson and Heather D. Spangler, « Tungsten source integrated cavity output spectroscopy for the determination of ambient atmospheric extinction coefficient », *in: Appl. Opt.* 45.11 (2006), pp. 2465–2473, DOI: 10.1364/AO.45.002465, URL: <http://ao.osa.org/abstract.cfm?URI=ao-45-11-2465>.
- [188] Neeraj Prakash et al., « Near-infrared incoherent broadband cavity enhanced absorption spectroscopy (NIR-IBBCEAS) for detection and quantification of natural gas components », *in: Analyst* 143 (14 2018), pp. 3284–3291, DOI: 10.1039/C8AN00819A, URL: <http://dx.doi.org/10.1039/C8AN00819A>.
- [189] AbdulAziz Al-Jalal et al., « Measurement of low concentrations of NO₂ gas by differential optical absorption spectroscopy method », *in: Measurement* 146 (2019), pp. 613–617, ISSN: 0263-2241, DOI: <https://doi.org/10.1016/j.measurement.2019.07.022>, URL: <http://www.sciencedirect.com/science/article/pii/S0263224119306517>.
- [190] Tao Wu et al., « Incoherent broadband cavity enhanced absorption spectroscopy for in situ measurements of NO₂ with a blue light emitting diode », *in: Appl. Phys. B* 94 (Nov. 2008), pp. 85–94, DOI: 10.1007/s00340-008-3308-8.

-
- [191] S J Jia et al., « Flat supercontinuum generation from 1028–2804 nm in an all-solid fluorotellurite fiber », *in: Laser Physics Letters* 15.11 (2018), p. 115104, DOI: 10.1088/1612-202x/aae040, URL: <https://doi.org/10.1088/1612-202x/aae040>.
- [192] J. M. Langridge et al., « Cavity enhanced absorption spectroscopy of multiple trace gas species using a supercontinuum radiation source », *in: Opt. Express* 16.14 (2008), pp. 10178–10188, DOI: 10.1364/OE.16.010178, URL: <http://www.opticsexpress.org/abstract.cfm?URI=oe-16-14-10178>.
- [193] K. Suhail et al., « Open path incoherent broadband cavity-enhanced measurements of NO₃ radical and aerosol extinction in the North China Plain », *in: Spectrochimica Acta Part A: Molecular and Biomolecular Spectroscopy* 208 (2019), pp. 24–31, ISSN: 1386-1425.
- [194] Kaiyuan Zheng et al., « Review of incoherent broadband cavity-enhanced absorption spectroscopy (IBBCEAS) for gas sensing », *in: Sensors* 18.11 (2018), p. 3646.
- [195] JM Langridge et al., « Cavity enhanced absorption spectroscopy of multiple trace gas species using a supercontinuum radiation source », *in: Optics Express* 16.14 (2008), pp. 10178–10188.
- [196] Wolfgang Denzer et al., « Trace species detection in the near infrared using Fourier transform broadband cavity enhanced absorption spectroscopy: Initial studies on potential breath analytes », *in: The Analyst* 136 (Feb. 2011), pp. 801–6, DOI: 10.1039/c0an00462f.
- [197] Anthony L. Gomez et al., « Integrated fiber optic incoherent broadband cavity enhanced absorption spectroscopy detector for near-IR absorption measurements of nanoliter samples », *in: Appl. Opt.* 51.14 (2012), pp. 2532–2540.
- [198] G Rempe et al., « Measurement of ultralow losses in an optical interferometer », *in: Optics letters* 17.5 (1992), pp. 363–365.
- [199] Luigi Consolino et al., « Bow-tie cavity for terahertz radiation », *in: Photonics*, vol. 6, 1, Multidisciplinary Digital Publishing Institute, 2019, p. 1.
- [200] J Morville et al., « Fast, low-noise, mode-by-mode, cavity-enhanced absorption spectroscopy by diode-laser self-locking », *in: Applied Physics B* 80.8 (2005), pp. 1027–1038.

-
- [201] Katherine M Manfred et al., « ICL-based OF-CEAS: a sensitive tool for analytical chemistry », *in: Analytical chemistry* 89.1 (2017), pp. 902–909.
- [202] Manish Gupta, Hong Jiao, and Anthony O’Keefe, « Cavity-Enhanced Spectroscopy in Optical Fibers », *in: Optics letters* 27 (Dec. 2002), pp. 1878–80, DOI: 10.1364/OL.27.001878.
- [203] Paul Johnston and Kevin Lehmann, « Cavity enhanced absorption spectroscopy using a broadband prism cavity and a supercontinuum source », *in: Optics express* 16 (Oct. 2008), pp. 15013–23, DOI: 10.1364/OE.16.015013.
- [204] Xing Chao et al., « Cavity-enhanced absorption spectroscopy for shocktubes: Design and optimization », *in: Proceedings of the Combustion Institute* 37.2 (2019), pp. 1345–1353.
- [205] Ravi M Varma et al., « Long optical cavities for open-path monitoring of atmospheric trace gases and aerosol extinction », *in: Applied optics* 48.4 (2009), B159–B171.
- [206] Anton Walsh et al., « Optomechanical Shutter Modulated Broad-Band Cavity-Enhanced Absorption Spectroscopy of Molecular Transients of Astrophysical Interest », *in: The Journal of Physical Chemistry A* 117.39 (2013), pp. 9363–9369.
- [207] Johannes Orphal and Albert A Ruth, « High-resolution Fourier-transform cavity-enhanced absorption spectroscopy in the near-infrared using an incoherent broadband light source », *in: Optics express* 16.23 (2008), pp. 19232–19243.
- [208] A Libert et al., « Design and characteristics of a cavity-enhanced Fourier-transform spectrometer based on a supercontinuum source », *in: Review of Scientific Instruments* 91.11 (2020), p. 113104.
- [209] www.yslphotonics.com.
- [210] Geoffrey Brooker, *Modern Classical Optics*, Oxford Master Series in Physics, July 2003.
- [211] John U. White, « Long Optical Paths of Large Aperture », *in: J. Opt. Soc. Am.* 32.5 (1942), pp. 285–288.
- [212] Wolfgang Demtröder, *Laser spectroscopy: vol. 2: experimental techniques*, vol. 2, Springer Science & Business Media, 2008.

-
- [213] Deirdre M. O’Leary et al., « The near infrared cavity-enhanced absorption spectrum of methyl cyanide », *in: Journal of Quantitative Spectroscopy and Radiative Transfer* 113.11 (2012), Three Leaders in Spectroscopy, pp. 1138–1147, ISSN: 0022-4073, DOI: <https://doi.org/10.1016/j.jqsrt.2012.02.022>, URL: <http://www.sciencedirect.com/science/article/pii/S0022407312000866>.
- [214] Titus Gherman et al., « Incoherent broadband cavity-enhanced absorption spectroscopy in the near-ultraviolet: Application to HONO and NO₂ », *in: Environmental science & technology* 42.3 (2008), pp. 890–895.
- [215] Wolfgang Denzer et al., « Trace species detection in the near infrared using Fourier transform broadband cavity enhanced absorption spectroscopy: initial studies on potential breath analytes », *in: Analyst* 136.4 (2011), pp. 801–806.
- [216] Stephen M Ball and Roderic L Jones, « Broad-band cavity ring-down spectroscopy », *in: Chemical reviews* 103.12 (2003), pp. 5239–5262.
- [217] Anthony Catanese et al., *in: Rev. Sci. Instrum.* 89.10 (2018), p. 103115.
- [218] JA Gibbard et al., *in: Rev. Sci. Instrum.* 89.12 (2018), p. 123304.
- [219] Ranran Liu, Qiyao Li, and Lloyd M Smith, *in: J. Am. Soc. Mass. Spectr.* 25.8 (2014), pp. 1374–1383.
- [220] Mehdi Dehghany, « High resolution infrared spectroscopy of Van der Waals clusters of nitrous oxide and carbon dioxide », *in:* (2010).
- [221] K.W. Busch and M.A. (Eds.) Busch, *Cavity-ringdown spectroscopy. An ultra-trace-absorption measurement technique*, American Chemical Society, Symposium Series 720,. Oxford University Press, Oxford, 1999.
- [222] Joseph T. Hodges, J. Patrick Looney, and Roger D. van Zee, « Laser bandwidth effects in quantitative cavity ring-down spectroscopy », *in: Appl. Opt.* 35.21 (1996), pp. 4112–4116, DOI: 10.1364/AO.35.004112, URL: <http://ao.osa.org/abstract.cfm?URI=ao-35-21-4112>.
- [223] D. Romanini et al., « CW cavity ring down spectroscopy », *in: Chemical Physics Letters* 264.3 (1997), pp. 316–322, ISSN: 0009-2614, DOI: [https://doi.org/10.1016/S0009-2614\(96\)01351-6](https://doi.org/10.1016/S0009-2614(96)01351-6), URL: <http://www.sciencedirect.com/science/article/pii/S0009261496013516>.

-
- [224] I. V. Nikolaev et al., « Measurement of small gas impurity with application of multichannel diode laser spectroscopy », *in: Lasers for Measurements and Information Transfer 2007*, ed. by Vadim E. Privalov, vol. 7006, International Society for Optics and Photonics, SPIE, 2008, pp. 130–137, DOI: 10.1117/12.802275, URL: <https://doi.org/10.1117/12.802275>.
- [225] HT Dai et al., « Airy beams generated by a binary phase element made of polymer-dispersed liquid crystals », *in: Optics express* 17.22 (2009), pp. 19365–19370.
- [226] Pasquale Maddaloni, Marco Bellini, and Paolo De Natale, *Laser-based measurements for time and frequency domain applications: a handbook*, CRC Press, 2019.

STARGATE: A new instrument for high-resolution photodissociation spectroscopy of cold ionic species

Cite as: Rev. Sci. Instrum. 92, 033307 (2021); doi: 10.1063/5.0039627

Submitted: 4 December 2020 • Accepted: 12 February 2021 •

Published Online: 11 March 2021








View Online



Export Citation



CrossMark

Raghd Bejjani,  Anthony Roucou, ^{a)}  Xavier Urbain,  Konstantin Moshkunov,  Guilhem Vanlancker, and Clément Lauzin 

AFFILIATIONS

Institute of Condensed Matter and Nanosciences, Université catholique de Louvain, Louvain-la-Neuve B-1348, Belgium

^{a)} Author to whom correspondence should be addressed: anthony.roucou@uclouvain.be

ABSTRACT

Spectroscopy of transient anions and radicals by gated and accelerated time-of-flight experiment is a new spectrometer developed in UCLouvain. This instrument measures high-resolution photodissociation spectra of mass-selected ions by the combination of a time-of-flight spectrometer including a specific gating, bunching, and re-referencing unit with a nanosecond pulsed dye laser, a pulsed deflection, and an energy selector. The ionic species are generated in a supersonic jet expansion by means of an electric discharge or by the impact of electrons coming from an electron gun. The versatility of the molecular systems that can be addressed by this instrument is illustrated by the presentation of mass spectra of cations, anions, and ionic clusters formed from different gas mixtures and backing pressures. The high-resolution spectrum of the $\tilde{A}^2\Sigma^+(002) \leftarrow \tilde{X}^2\Pi_{3/2}(000)$ and $\tilde{A}^2\Sigma^+(002) \leftarrow \tilde{X}^2\Pi_{1/2}(000)$ rovibronic bands of N_2O^+ has been measured and analyzed to provide refined molecular parameters in the $\tilde{A}^2\Sigma^+(002)$ upper state. The $\tilde{A}^2\Sigma^+(002) \leftarrow \tilde{X}^2\Pi_{3/2}(000)$ band has been used to evaluate the quality of the experimental setup in terms of rotational temperature, time of measurement for certain signal to noise ratio, and the accuracy of the determination of the wavenumber scale.

Published under license by AIP Publishing. <https://doi.org/10.1063/5.0039627>

I. INTRODUCTION

Action spectroscopy has witnessed a tremendous development in several scientific directions since the first studies in atomic and molecular physics.^{1,2} This interest comes from the attractive combination of the sensitivity of mass spectrometry and the tunability of laser radiation. After these pioneering works, ionic cluster spectroscopy has started with the works of Schwarz³ and the important contribution of Lee.^{4–6} This track has been followed and expanded by many others with improvements for every part of a typical action spectrometer, i.e., the ion source, the mass spectrometer, and the light source. A variety of mass spectrometers have been used, such as time of flight-mass spectrometers (TOF-MS)⁷ and Fourier-transform ion cyclotron resonance mass spectrometers (FT-ICR-MS).⁸ Supersonic expansion has been associated with different ionization means including electronic impact,³ electric discharge,⁹ and laser vaporization.^{10,11} The electrospray was then used for mass spectrometry of large biomolecules¹² and infrared photodissociation spectroscopy.¹³ Several continuous and pulsed light

sources were used with these techniques using lasers,⁴ free-electron lasers,⁸ and synchrotron radiation.⁷ Variations on the measured quantity were reported including the counting of electrons,¹⁴ fragmentation products,¹⁵ products of light induced bimolecular reactions,¹⁶ or recently the determination of the magnitude of the inhibition of complex formation.¹⁷ This last example has led to the measurement of the high-resolution spectra of numerous molecular cations including C_{60}^+ ¹⁸ and CH_5^+ ¹⁹ in the infrared.

A review of photodissociation studies with these techniques in the infrared, visible, and ultraviolet spectral ranges was presented by Bieske and Dopfer¹⁵ covering the years from 1986 to 2000. In parallel, the measurement of photoelectronic spectra of neutral molecules²⁰ and anions¹⁴ has been the subject of important developments to retrieve information on the ionization threshold,²¹ the cation structure,²² and transition states in chemical reaction.²³ Finally, such techniques were also applied to study biological molecules such as peptides or glucans.^{24–26}

In this study, we report on the building of the STARGATE photo-fragmentation spectrometer, which aims at measuring

spectral properties of positively or negatively charged molecules and/or of ionic complexes. We detail the different parts of the STARGATE instrument including the ion source and the TOF-MS in Sec. II and the photodissociation setup in Sec. III. The application to high resolution photodissociation spectroscopy is discussed in Sec. IV. This section focuses first on the global analysis of the rotationally resolved $\tilde{A}^2\Sigma^+(002) \leftarrow \tilde{X}^2\Pi_{3/2}(000)$ and $\tilde{A}^2\Sigma^+(002) \leftarrow \tilde{X}^2\Pi_{1/2}(000)$ rovibronic bands of N_2O^+ , where the vibrational quantum numbers v_1, v_2, v_3 are indicated in parentheses, i.e., $(v_1v_2v_3)$. This analysis provides improved molecular constants for the $\tilde{A}^2\Sigma^+(002)$ upper state. These improved parameters are then used to evaluate the rotational temperature of the cations under different experimental conditions. Repeated measurements of the $\tilde{A}^2\Sigma^+(002) \leftarrow \tilde{X}^2\Pi_{3/2}(000)$ allow us to evaluate the required measurement time and achievable signal-to-noise ratio (S/N) and the effect of a bias cell used in high-resolution molecular photodissociation spectroscopy for the first time. Finally, ongoing developments and ideas to improve the quality of our setup are discussed.

II. THE TOF-MS AND THE ION SOURCE

The STARGATE instrument is presented in Fig. 1. It is essentially composed of a pulsed supersonic expansion coupled to an ionization mean (electric discharge or electron gun). The jet goes through a skimmer, item (2) in Fig. 1, which allows for differential pumping and spatial selection of part of the expansion. Ions are then accelerated and enter the TOF-MS. The heart of the TOF-MS includes a single unit, denoted as item (3), able to perform acceleration, bunching, and gating of the ionic beam while re-referencing

it to the ground potential. The ions are focused using an electrostatic lens (4) and may be deflected using a pulsed deflection unit (5). A second differential pumping (6) is performed before the interaction with a pulsed dye laser and right before entering an energy analyzer (8). The ions are then detected using a microchannel plate stack (MCP, Photonis APD-TOF) and the mass spectra are recorded using a digital oscilloscope (Agilent Technologies DSO-X 3104A, 1 GHz). The timing of the various elements is controlled using a multi-channel digital delay generator (model 577—BNC) and pulses are generated from Behlke push-pull high voltage (HV) switches. A chronograph of the STARGATE instrument is presented in Fig. 2. This figure details the duration and the relative timing of the pulsed jet gas injection (see Sec. II A), the two steps of the gating bunching of the ion beam (see Sec. II D), and the mass selection with the pulsed parallel plate deflector (see Sec. III A).

A. The pulsed supersonic expansion source

The pulsed jet has been chosen as a source of molecules. The motivations for this choice are (i) to promote partial condensation and (ii) to simplify the recorded spectra by increasing the density of molecules on few quantum states and hence increasing the S/N . In order to operate at relatively low pressure (10^{-5} mbar), the pulsed nature of the supersonic expansion was chosen to reduce the pumping requirement for a given gas outflow. A dense and intense short pulse of gas is produced using a homemade valve based on a flexing disk of piezomaterial attached to a metallic membrane, as originally developed by Proch and Trickl.²⁷ Unless specified, a nozzle of diameter of $500\ \mu\text{m}$ has been used with a repetition rate of 30 Hz matching that of the dye laser. A minimum pulse duration of $200\ \mu\text{s}$ has been

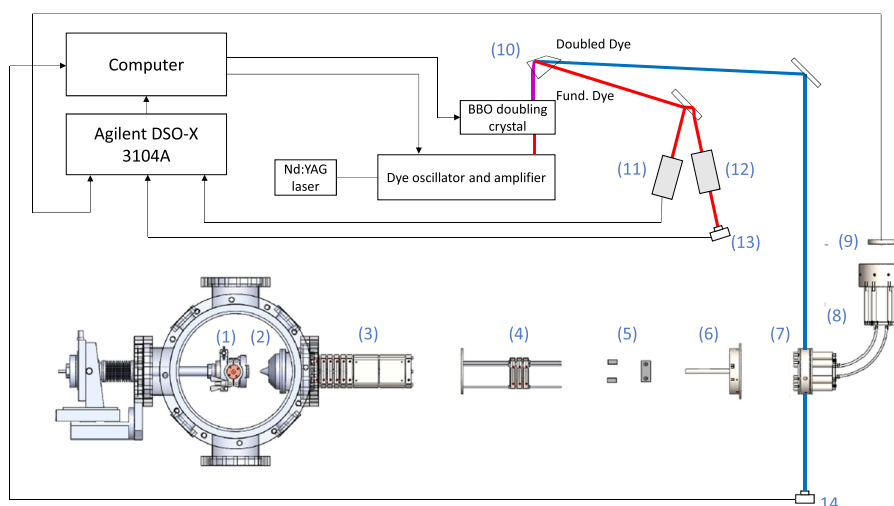


FIG. 1. Design of STARGATE. TOF-MS (bottom) with (1) the source of ionic compounds, (2) skimmer, (3) electrostatic extraction and lens coupled to an ion gating, bunching, and re-referencing unit, (4) electrostatic lens, (5) pulsed 2D deflector, (6) differential pumping tube, (7) laser and ion beam interaction region, (8) 90° cylindrical energy analyzer, and (9) MCP detector. Optical bench (upper part) with the pulsed dye oscillator pumped by a Nd:YAG laser associated with frequency doubler BBO crystal, (10) prism separating the frequency doubled laser (307 nm–327 nm) used for photodissociation spectroscopy from the fundamental dye beam (614 nm–654 nm) used for the frequency calibration of the spectra, (11) hollow cathode, (12) thermalized vacuum solid state etalon, (13) photodiode, and (14) pyroelectric detector (model PE10BB, OPHIR). The calibration Ne optogalvanic spectra (hollow cathode), ionic photofragments (MCP detector), and Fabry Perot interferometer (solid state etalon) are simultaneously measured with an oscilloscope (Agilent DSO-X 3104A) connected to a computer through a USB connector. A LabVIEW™ interface controls the scan of the pulsed dye laser, the transfer of the averaged data from the oscilloscope to the computer, the integration of the time gated signal, and the BBO doubling crystal angle for the UV energy pulse optimization. Items (1), (3), and (5) are all connected to a digital delay generator, and the associated chronograph is displayed in Fig. 2.

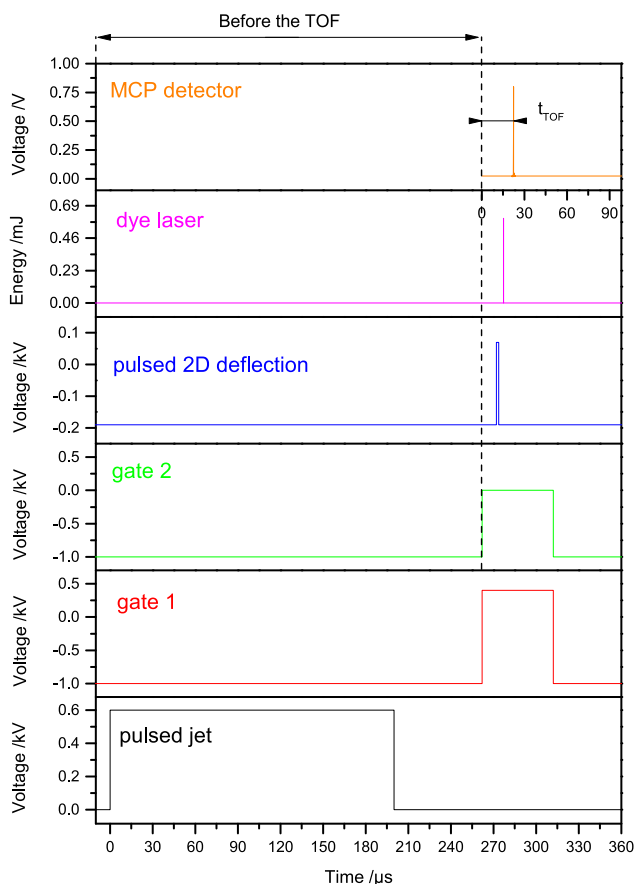


FIG. 2. Chronograph of STARGATE and applied voltages for positive ions. The time scale origin is defined as the rising slope the pulsed molecular jet valve trigger (black). The two steps of the gating bunching of the ions (red and green) and the mass selection of the pulsed 2D deflector (blue) are represented. The time scale origin used for the mass spectrum of N_2O^+ measured with the MCP detector at $t_{\text{TOF}} = 22.4 \mu\text{s}$ (orange) is defined from the beginning of the TOF corresponding to the gating ($L = 1.5 \text{ m}$ with a kinetic energy of 1 keV). In addition, a dye laser pulse of 5 ns interacts with the ions after 1 m in the drift tube for photodissociation spectroscopy ($\approx 15 \mu\text{s}$ for N_2O^+).

measured by scanning the gating delay (cf. Sec. II D) of the TOF spectrometer with respect to the valve trigger, and a maximum 1 kHz repetition rate has been obtained. The piezodisk (model P-286.27, Physik Instrumente) is driven by negative 0.3 kV–1.0 kV pulses generated by a home-made push–pull switch whose rise time has been damped by inserting a 511Ω resistor in series. The fined-threaded aluminum plunger is screwed to the piezodisk, and the adjustment of the tightening is made before to place the valve under vacuum. The pulsed duration is controlled by the multi-channel digital delay generator.

B. The ionization methods

The front plate of the nozzle is grounded, and the jet starts its expansion at the entrance of an electric discharge. This discharge is produced between a stainless steel circular electrode and the front

plate of the nozzle. As illustrated in Fig. 3(a), the electrode is surrounded by two circular Teflon insulators and maintained at a negative DC voltage of 0.8 kV–1.4 kV. The electric discharge is efficient for ion production but is unstable and runs between the electrode and the plunger of the nozzle instead of the front plate of the valve if the voltage is too high.

Another method to produce ionic species has been implemented with the use of an electron gun to allow for more control on the ionization process. The design of this electron gun is based on the work of Hosseinzadeh *et al.*²⁸ and is illustrated in Fig. 3(b). The electrons are produced by thermionic emission from a thoriated tungsten filament, accelerated by the filament bias voltage, focused toward the supersonic gas jet using side electrodes (–60/–70 V) in Pierce geometry, and collected on an electrode placed at a potential of 100 V–500 V.

Most of the results presented in this study were obtained using the electric discharge due to a larger ionic signal. The ionized gas pulse expands toward a conical skimmer of 2 mm diameter. The skimmer allows us to spatially select a part of the jet. The vacuum quality is ensured by using three turbo pumps (Pfeiffer ATH 2300M, Balzers 4306, and Pfeiffer HiPace 700 Plus) and two stages of differential pumping using the skimmer and a pumping tube indexed as items (2) and (6) in Fig. 1, respectively, to finally reach 10^{-7} mbar in the area of the interaction of the ion beam with the laser, the energy analyser, and the MCP detector. This allows also for minimizing the recombination loss or any warming up by colliding with the residual gas.

C. The extraction

A TOF-MS allows us to separate and detect ionized species according to their mass-to-charge ratio m/z .²⁹ The ions with the same m/z form packets with a specific time of flight t spread by a temporal distribution Δt .²⁹ In practice for positive ions, a kinetic energy E_k is given by applying an accelerating voltage of –1 kV

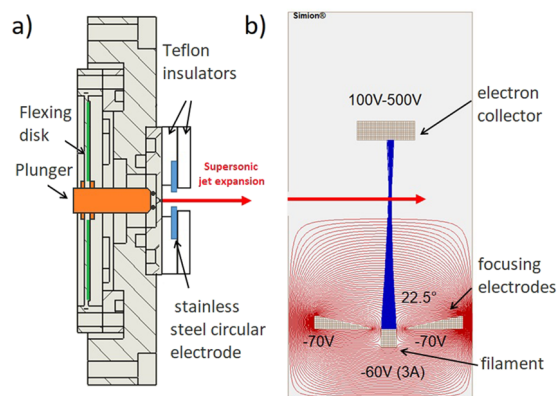


FIG. 3. (a) The supersonic jet expansion can be ionized by an electric discharge (800 V–1400 V) produced from a circular electrode (in blue) enclosed in teflon insulators fixed on the valve. The plunger (in orange) is fixed to the flexing disk of piezomaterial (in green). (b) The electron gun scheme is presented with a SIMION® simulation with the electric equipotential lines. The electrons are extracted from a filament (oriented out-of-plane) and accelerated from applied voltage (60 V) and a charged electron collector (100 V–500 V). Two lateral electrodes (–70 V) allow for focusing the electron beam represented in blue.

before the drift tube of the TOF where the ions travel a distance of $d = 1.5$ m before to be detected. Based on simulations made with the SIMION[®] software, two extraction schemes presented in Figs. 4(a) and 4(b) have been tested. The first one was inspired from the work of Dedman *et al.*³⁰ and consists of a series of six aluminum ring electrodes assembled in a tube and connected via a voltage divider to produce a smooth gradient of accelerating potential on the ions.

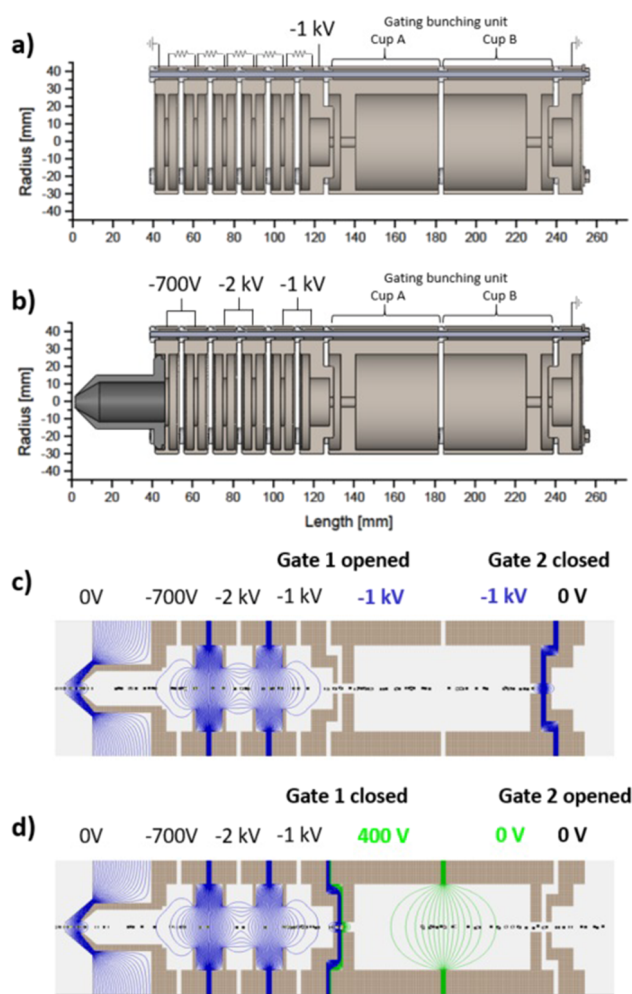


FIG. 4. (a) The first acceleration scheme inspired by Dedman *et al.*³⁰ consisting of a series of six aluminum ring electrodes connected via 100 k Ω resistors to produce a smooth gradient of the acceleration potential. (b) The second acceleration scheme consisting of the association of a first extraction conical electrode (a hole diameter of 6 mm) placed at 1 cm after the grounded skimmer to accelerate and focus the ion beam immediately with a succession of electrodes forming an electrostatic lens. (c) The gating process is simulated from SIMION on the second acceleration scheme using 150 particles of $m = 44$ uma with a charge $+e$ in an initial circular distribution (radius of 1.5 mm and $v = 550$ m/s). The two cup-like electrodes are initially at the acceleration voltage (-1 kV), and a last grounded electrode stops the ion beam reflected in the unit. (d) The first part of the unit is switched to $+400$ V to close the first gate and bunch the ions at the end of the TOF. The second part of the unit is switched to 0 V to let the ions enter the drifting tube. The increments in the electric equipotential lines are 25 V (green) and 30 V (blue) for positive and negative values, respectively.

The electrodes present successive potentials of 0 V, -200 V, -400 V, -600 V, -800 V, and -1000 V and the cations gain kinetic energy from one electrode to the next for a total kinetic energy of 1 keV. The second design is composed of a conical electrode (-700 V) placed 1 cm after the aperture of the grounded skimmer in order to accelerate the ions immediately after the expansion. A succession of two pairs of electrodes at ~ -2 kV and -1 kV allows accelerating the ions on a shorter distance and forming an electrostatic lens to focus the ion beam. This second design allowed us to improve the ion signal by at least a factor 30 while keeping a low rotational temperature. The second design has thus been set up permanently, and all the results presented in this report were obtained with this extraction scheme.

D. The gating, bunching, and re-referencing unit

From what precedes, the accelerated ions are still referenced to the final voltage applied to the extraction column (-1 kV in the case of cations). In order to avoid placing the rest of the setup to high voltage, some re-referencing to the ground needs to be set up. Moreover, the mass resolving power (MRP), $R = m/\Delta m$,³¹ for a time of flight measurement can be related to the ratio of the time of flight t and the time dispersion Δt of the ions. The uncertainties on t and the magnitude of Δt for species having the same m/z can be decreased by an efficient gating and bunching of the ions, respectively. These three actions, re-referencing, gating, and bunching, are done by a single unit directly inspired from the work of Dedman *et al.* The original design leads to a certain mechanical complexity and some specificity for the electronic of the switches.³² This has been simplified in terms of both mechanics and electronics, during this work, by using only two cup-like electrodes facing one another (instead of six plates linked by resistors) denoted as A and B in Figs. 4(a) and 4(b). These form a chamber of 83 mm in length and are polarized using conventional push-pull switches. The two steps of the gating bunching process are presented in Figs. 4(c) and 4(d) with polarities associated with the study of positive ions. Polarities can, of course, be reversed for studying negative ions. The gating allows us to select a time slice of the ion beam and to define the starting time $t = 0$ for the TOF. The bunching is a longitudinal compression of the ion bunch performed by accelerating the ions lagging behind with a positive potential gradient. Initially, the potential of the two cup electrodes is set to the acceleration voltage (-1 kV) of the extraction to open the first gate [gate 1 in Fig. 4(c)] of the unit. The last electrode before the drifting tube is always grounded, and gate 2 is therefore initially closed. When the ion bunch is inside the unit [Fig. 4(d)], the electrode A is switched to a positive value (~ 400 V), while electrode B is switched to ground after a short and adjustable delay, closing gate 1 and opening gate 2, while excluding the rest of the ion beam and creating a gradient of potential inside the two cup electrodes A and B. This adjustable gradient is used to bunch the ions either at the MCP location or at the crossing with the laser. A tunable delay (40 ns) is introduced between electrodes A and B to further improve the bunching performance of the gating unit by improving the simultaneity of the switches in the two cups. The ions are thus re-referenced at ground potential to propagate in the drift tube and start their flight with a kinetic energy of 1 keV on the right part of the cup electrode B.

The time delay of the gating is controlled by the multi-channel digital delay generator and parts A and B of the unit are switched

from -1 kV to 400 V and 0 V, respectively, using two fast HV push-pull switches (rise times of 20 ns). These voltages have been experimentally adjusted and optimized for the bunch of N_2O^+ .

Finally, a three-aperture electrostatic lens composed of a biased electrode (650 V) surrounded by two grounded electrodes is placed after this unit to maintain a low spatial divergence of the ion beam in the TOF drift space (item 4 of Fig. 1).

E. The mass resolving power

A comparison between the bunched and unbunched signals is presented in Fig. 5 for N_2O^+ . Ions were produced from a pure expansion of N_2O (stagnation pressure $P = 5$ bar) and an electric discharge ($V_d = 850$ V). The gating selects a time slice of the ion beam ($\Delta t = 1.25$ μs , i.e., the TOF of N_2O^+ through the gating unit) having a kinetic energy of 1 keV ($v_{\text{N}_2\text{O}^+} = 66$ km/s), which is compressed to $\Delta t = 80$ ns (FWHM), allowing us to observe the $^{14}\text{N}^{15}\text{N}^{16}\text{O}^+$ isotopologues present in natural abundance in the gaseous sample (0.8%). A resulting MRP of $R = 140$ was calculated in the time domain from $R = t_{\text{N}_2\text{O}^+}/2\Delta t$. The bunching thus improves the MRP and the signal-to-noise by a factor 15 and 8, respectively. Our simple TOF design comes with a loss of MRP of factor 2 compared to the one reported by Dedman *et al.*³⁰

F. Production of clusters, cations, and anions

STARGATE is designed to produce different ionic species by controlling the initial conditions of the source, such as nozzle geometry, ionization conditions, seeding gas, and backing pressure. The first mass spectra of cationic and anionic clusters we have recorded are presented in Fig. 6. Large clusters of $[\text{H}(\text{H}_2\text{O})_n]^+$ up to $n = 38$ are depicted in panel (a). These complexes were produced by the expansion from argon bubbling in a water reservoir. This series stops at $n = 38$, but since the detection efficiency decreases with the mass (lower velocities), larger clusters could be present. Note that the MCP front was negatively biased to 2.1 kV, adding up to 3.1 keV kinetic energy at impact. In panel (b), we show the

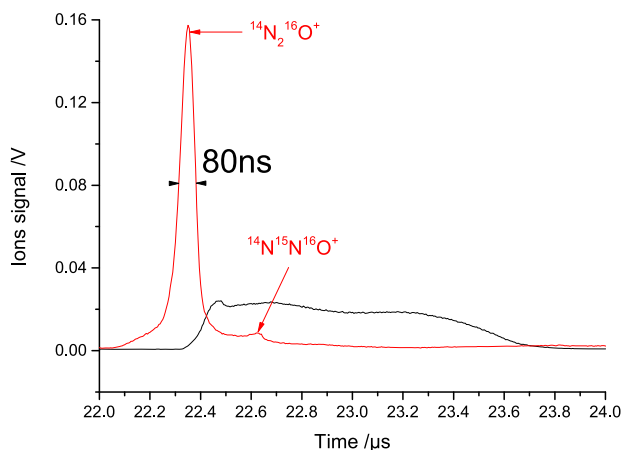


FIG. 5. Comparison between the $\text{N}_2\text{O}^+ m/z$ bunched (red) and not bunched (black) spectra; the x-axis is the time of flight after the gating. The bunching and the associated improvement of the MRP allow the $^{14}\text{N}^{15}\text{N}^{16}\text{O}^+$ isotopologues to be observed.

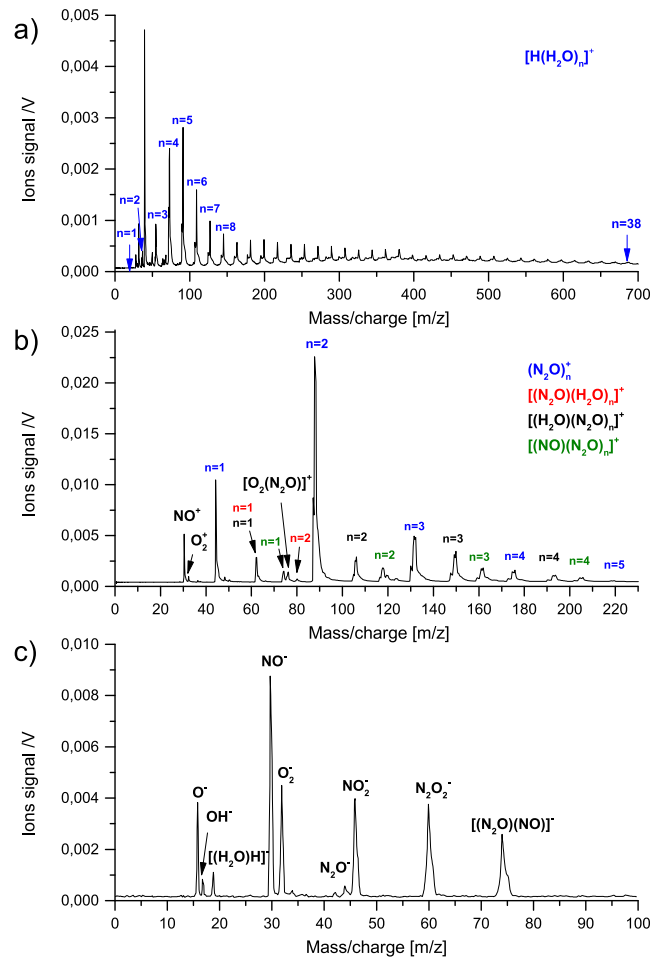


FIG. 6. (a) Production of $[\text{H}(\text{H}_2\text{O})_n]^+$ ionic clusters up to $n = 38$ from argon bubbling in water with a backing pressure of 2 bars using a nozzle of diameter of 1.5 mm with an average pressure of 10^{-5} mbar in the jet chamber and the valve operating at 30 Hz. (b) Production of $(\text{N}_2\text{O})_n^+$ ($n = 1 - 5$), $[(\text{N}_2\text{O})(\text{H}_2\text{O})_n]^+$ ($n = 1 - 2$), $[(\text{H}_2\text{O})(\text{N}_2\text{O})_n]^+$ ($n = 1 - 4$), and $[(\text{NO})(\text{N}_2\text{O})_n]^+$ ($n = 1 - 4$) ionic clusters from N_2O and residual water in the gas line. (c) Production of anions using the electron gun ionization with N_2O with a backing pressure of 2 bars.

formation of pure $(\text{N}_2\text{O})_n^+$ and mixed $[(\text{H}_2\text{O})_m(\text{N}_2\text{O})_n]^+$ hydrate clusters formed from N_2O and water contamination in the gas injection pipes. The first steps of nucleation are clearly visible, as well as the competition between the different routes of nucleation. Anions have also been measured by switching the polarity of the ion optics using the electron gun for ionization of N_2O^+ and replacing the MCP stack with a channel electron multiplier (Sjuts KBL 25 RS) and are presented in panel (c) of Fig. 6. These three panels illustrate the versatility of STARGATE in terms of molecular targets that could be studied. It also provides evidence of an efficient cooling, which will be further demonstrated in Sec. IV D.

III. PHOTODISSOCIATION SPECTROSCOPY

Photodissociation spectroscopy consists of integrating the ionic fragment signal generated by light absorption of a mass selected ion

as a function of the wavelength of a light source; in our case, a pulsed dye laser (30 Hz, 0.6 mJ/pulse, and 5 ns duration from Continuum ND 6000) pumped by a Nd:YAG laser (Continuum Powerlite Precision II). For this kind of measurement to be background free, a selection on the ions has to be performed before and after interaction with the laser. In our case, we perform a mass selection, an energy shift at the location of the ion–laser interaction, and an energy analysis. Hereafter, we detail the pulsed deflection unit we implemented for the first mass selection in Sec. III A, the selective energy shifts of the ions produced by the photodissociation and the associated cylindrical energy analyzer in Sec. III B, and we check the spatial and temporal overlap of the laser with the ions in Sec. III C.

A. The first mass selection of ions

The first mass selection is performed using a pulsed 2D deflection to achieve mass-selected absorption measurements. It consists of a pulsed deflector formed by a pair of steering plates to which pulsed voltage is applied to horizontally steer the ion beam toward the laser interaction region and select the species of interest. The mass selection is performed by time-gated deflection using short voltage pulses (typically $\approx 1\ \mu\text{s}$ with 70 V) using a fast HV push–pull switch (a rise time of 20 ns) and the multi-channel digital delay generator. A second pair of plates ensures proper vertical alignment. The non-selected ions thus collide with the chamber wall. A comparison of the full m/z spectrum obtained from pure N_2O gas injection with that measured with mass selection applied to select only N_2O^+ is presented in Fig. 7.

B. The kinetic energy selection

While the first mass selection selects a species for the laser interaction, other species can result from the collisions of the selected ions with the residual gas in the drift tube. A second selection is performed by a 90° electrostatic deflector after the laser interaction to select the fragments of the photodissociation and to exclude the remaining parent ions and non-photoinduced fragments. A double-focusing 90° electrostatic deflector adopting the design of Kreckel

*et al.*³³ has been implemented for the selection of the fragments depending on their kinetic energy. An electric potential is additionally applied to the laser interaction region by a large cylindrical electrode surrounded by grounded electrodes. This bias cell represented in the left corner of Fig. 8(a) aims at increasing the kinetic energy difference between fragments of the photodissociation process and other fragments or parent molecules.

For example, if N_2O^+ has an energy of 1 keV before the bias cell, the fragments NO^+ produced by collisions in the TOF have the same velocity than N_2O^+ but a different mass, and their kinetic energy can be calculated to be 680 eV. By polarizing the central electrode ($-250\ \text{V}$) of the electrostatic lens surrounding the laser interaction area [Fig. 8(b)], the photodissociation fragments NO^+ are produced from accelerated N_2O^+ having an energy of 1250 eV. With an initial kinetic energy of 852 eV, these fragments are decelerated by leaving the electrostatic lens area to reach a kinetic energy of 602 eV in the 90° electrostatic deflector. This resulting energy is therefore lower than the fragments NO^+ (680 eV) generated outside the interaction region. These fragments can thus be differentiated by tuning the voltages applied on the 90° deflector accordingly. In Fig. 8(b),

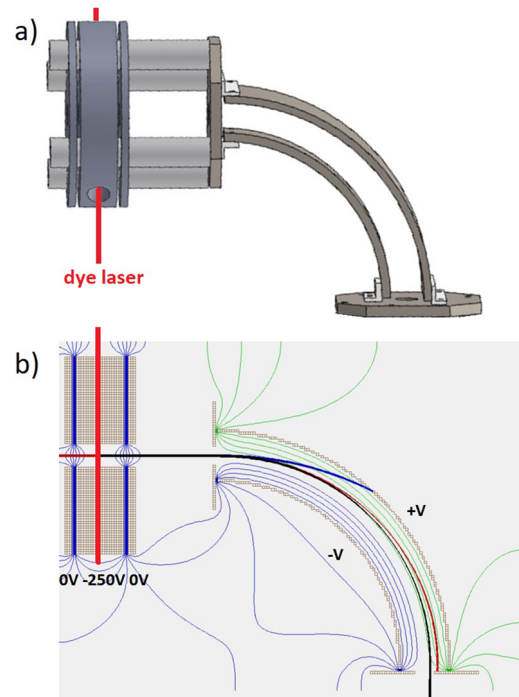


FIG. 8. (a) The 90° electrostatic deflector is represented with the bias cell surrounding the laser interaction region. (b) SIMION simulation performed for the selection of the NO^+ photofragments ($m = 30\ \text{uma}$ and $E_{\text{NO}^+} = 602\ \text{eV}$) represented in black by excluding the non-dissociated N_2O^+ parent ions having a larger kinetic energy represented in blue ($m = 44\ \text{uma}$ and $E_{\text{N}_2\text{O}^+} = 1\ \text{keV}$) and NO^+ fragments resulting from collisions with the neutral residual gas in the drift tube represented in red ($m = 30\ \text{uma}$ and $E_{\text{NO}^+} = 680\ \text{eV}$). The positive and negative electric equipotential lines are represented in green and blue, respectively, with an increment of 30 V. The voltages applied in the simulation are $-250\ \text{V}$ for the middle electrode and $\pm V = \pm 135\ \text{V}$ for each plate of the deflector. The initial energy of the photofragments is $E_{\text{NO}^+} = E_{\text{N}_2\text{O}^+} \times m_{\text{NO}^+} / m_{\text{N}_2\text{O}^+} = 852\ \text{eV}$ with $E_{\text{N}_2\text{O}^+} = 1250\ \text{eV}$ in the middle of the electrostatic field generated by the electrostatic lens.

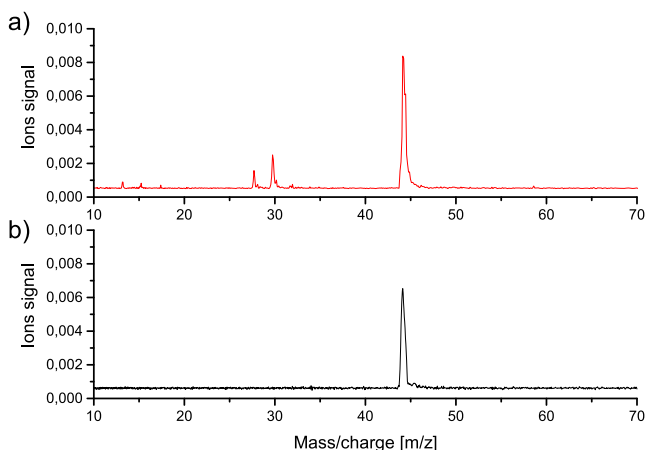


FIG. 7. (a) The m/z spectrum measured with continuous deflection from N_2O gas injection and electric discharge (in red) is compared with (b) the spectrum measured with a pulsed deflection of $1\ \mu\text{s}$ to select only N_2O^+ (in black).

trajectories of N_2O^+ and NO^+ produced by collisions outside the bias cell and NO^+ photofragments are represented in blue, red, and black, respectively. One can notice in this simulation made using the SIMION software that all species do not reach the detector except the NO^+ photofragments. We noticed that a similar effect can be observed by switching the voltage to +250 V and tuning the voltage applied on the deflector accordingly.

C. Overlap of the N_2O^+ ion beam with the pulsed dye laser

The S/N of a photodissociation spectrum depends, for the S part, on the amplitude of the NO^+ signal, which is integrated and averaged at each frequency step of the laser. The photodissociation signal thus requires maximizing the overlap of the mass-selected ions with the laser beam pulse in the time and spatial domain. The time delay of the pulsed gas injection is thus synchronized with the laser pulse by monitoring the photodissociation fragments on the MCP detector. The overlap of the pulsed laser with the bunched N_2O^+ beam has been evaluated in order to check if the MRP of the TOF-MS ($R = 140$) is large enough, i.e., Δt small enough compared to the laser pulse duration (5 ns). The time delay between the laser and the bunched ion beam has been scanned using the multi-channel digital delay generator. Figure 9 presents the NO^+ fragments generated from N_2O^+ as a function of this delay, with the laser tuned at the Q branch frequency of the $\tilde{A}^2\Sigma^+(002) \leftarrow \tilde{X}^2\Pi_{3/2}(000)$ rovibronic band. This scan displays a Gaussian profile of 105 ns FWHM for a typical laser pulse duration of 5 ns. Nevertheless, most of the ions interact with the laser. Indeed, considering a speed of 66 km/s for an ion of 44 amu ($t_{\text{TOF}} \approx 22 \mu\text{s}$, $E = 1 \text{ keV}$), a 105 ns dispersion corresponds to an ion bunch length of 6.9 mm, which is very close to the diameter of the pulsed laser beam estimated to be ≈ 6 mm at the interaction region.

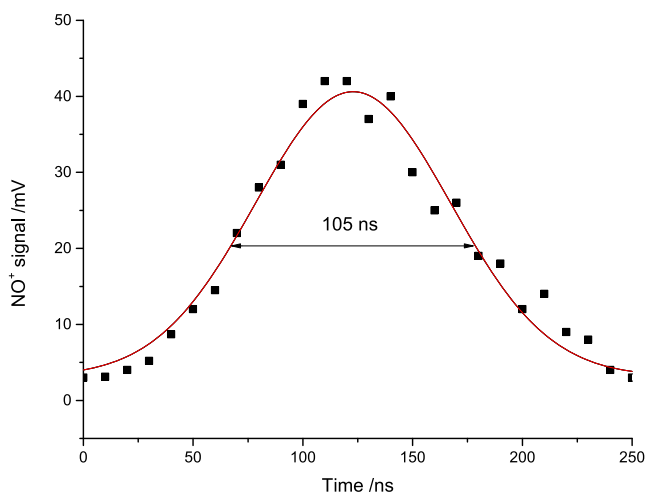


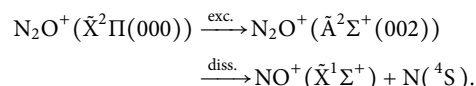
FIG. 9. Laser interaction time profile measured from the NO^+ photofragments by tuning the time delay between the N_2O^+ ion bunch and the laser pulse. The measurements are depicted in black squares and are fitted by a Gaussian profile presented in red. The laser frequency is fixed to the top of the Q branch frequency of the $\tilde{A}^2\Sigma^+(002) \leftarrow \tilde{X}^2\Pi_{3/2}(000)$ rovibronic band (30908.5 cm^{-1}). The origin of the x-axis is arbitrary.

IV. APPLICATION TO HIGH RESOLUTION SPECTROSCOPY OF N_2O^+

To evaluate the performances of our spectrometer in terms of frequency accuracy, measuring time, S/N ratio, and rotational temperature, the rotationally resolved photodissociation spectrum of N_2O^+ corresponding to the $\tilde{A}^2\Sigma^+(002) \leftarrow \tilde{X}^2\Pi_{3/2}(000)$ rovibronic band has been measured several times under different experimental conditions in the UV range by monitoring the apparition of ionic fragments (NO^+) as a function of the laser wavelength. This band has indeed been used to evaluate the performances of several spectrometers based on different action type of measurements.^{34,35} To use refined molecular parameters of the $\tilde{A}^2\Sigma^+(002)$ state in the evaluation of our spectrometer, we started by measuring and analyzing the $\tilde{A}^2\Sigma^+(002) \leftarrow \tilde{X}^2\Pi_{3/2}(000)$ and $\tilde{A}^2\Sigma^+(002) \leftarrow \tilde{X}^2\Pi_{1/2}(000)$ rovibronic bands of N_2O^+ .

A. The $\tilde{A}^2\Sigma^+(002) \leftarrow \tilde{X}^2\Pi(000)$ vibronic band in N_2O^+

The N_2O^+ cation has been extensively investigated in the literature through lifetime measurements,³⁶ optical emission,^{37–42} photoelectron,^{43,44} and photodissociation studies.^{45–54} The photodissociation of $\text{N}_2\text{O}^+(\tilde{A}^2\Sigma^+(002))$ in the 30885 cm^{-1} – 30940 cm^{-1} range has been experimentally characterized in previous studies^{37,51,55} with the following predissociation process:



The $\tilde{A}^2\Sigma^+(002) \leftarrow \tilde{X}^2\Pi_{3/2}(000)$ rovibronic band has already been recorded at high resolution^{37,46} and is one of the most intense in the 30500 cm^{-1} – 32500 cm^{-1} (307 nm–327 nm) spectral range covered by our frequency doubled pulsed dye laser operating with DCM.

We have used here the convention by Herzberg,^{42,43} with ν_1 corresponding to the higher frequency N–N σ^+ stretch, ν_2 to the π bend, and ν_3 to the lower frequency N–O σ^+ stretch and not that in the work of Callomon *et al.*³⁷ The spectroscopic parameters of the $\tilde{X}^2\Pi_{3/2}(000)$ ground state have been taken from the work of Fellows *et al.*³⁹ [$B'' = 0.411601(16) \text{ cm}^{-1}$, $D'' = 0.2072(61) \times 10^{-6} \text{ cm}^{-1}$, $A'' = -132.3551(11) \text{ cm}^{-1}$, $\gamma'' = -0.01424(22) \text{ cm}^{-1}$, $p = 0.1385(74) \times 10^{-2} \text{ cm}^{-1}$, and $q = -0.485(54) \times 10^{-4} \text{ cm}^{-1}$]. Those of the $\tilde{A}^2\Sigma^+(002)$ upper state have been first taken from Frey *et al.*⁴⁶ and improved from the analysis of the two intense bands presented in Fig. 10. A total of 290 line assignments corresponding to 161 blended lines have been fitted with a standard deviation of 0.037 cm^{-1} by least squares methods with PGOPHER.⁵⁶ The resulting line lists are presented in Tables S1 and S2 of the supplementary material, and the fitted molecular constants are compared with previous studies in Table I. Compared with the works of Callomon *et al.*,³⁷ Frey *et al.*,⁴⁶ and Herburger *et al.*,⁴³ our study allowed for determining the vibronic energy transition $\tilde{A}^2\Sigma^+(002) \leftarrow \tilde{X}^2\Pi_{3/2}(000)$ instead of the band head position. A similar analysis also presented in Table I was published very recently by Igosawa *et al.*⁵⁷ Although their measurements present an accuracy similar to ours, our molecular parameter determination is improved by using the merged blended line option of PGOPHER. This option takes into account the relative intensities

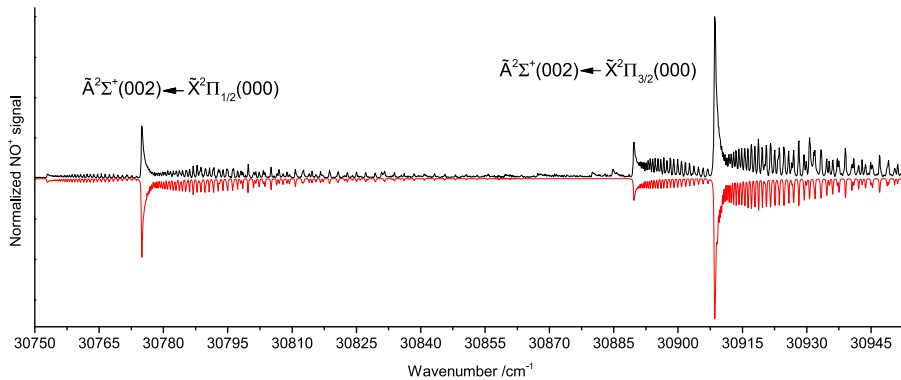


FIG. 10. The photodissociation spectrum (black) has been measured from the interaction of the N_2O^+ beam with a doubled dye laser (0.6 mJ/pulse) for an average of 30 counts per laser step. The simulation (red) is performed with the PGOPHER software⁵⁶ using the parameters of Fellows *et al.*³⁹ for the $\tilde{X}^2\Pi_{1/2,3/2}(000)$ ground state and those of Table I for the $\tilde{A}^2\Sigma^+(002)$ state. A temperature of 300 K and a Voigt line profile have been considered for the simulation, with Gaussian and Lorentzian contributions of 0.2 cm^{-1} and 0.1 cm^{-1} (FWHM), respectively.

TABLE I. Rovibronic parameters (in cm^{-1}) for the $\tilde{A}^2\Sigma^+(002)$ excited state. The rotational constants of the $\tilde{X}^2\Pi$ ground electronic state have been fixed to the values of Fellows *et al.*³⁹ Numbers in parentheses represent 1σ standard deviation in units of the last significant digits.

Parameters	Reference 37	Reference 46	Reference 43	Reference 57	This work
ν_0				30844.3(1)	30844.27(10) ^a
B'	0.4290(5)	0.42893(10)	0.4279(8)	0.42891(2)	0.428883(24)
$D' \times 10^7$	1.69(38)	1.6	0.0	1.9	1.89(17)

^aValue subtracted by 0.1 cm^{-1} (Doppler shift) and standard deviation was calculated from the wavenumber calibration (Sec. IV C for details).

of the transitions in the frequency determination of the merged lines. This improved treatment allowed us to determine the quartic order centrifugal distortion term D' . As detailed hereafter, the $\tilde{A}^2\Sigma^+(002) \leftarrow \tilde{X}^2\Pi_{3/2}(000)$ band is used to test the absolute calibration of our measurements to determine the rotational temperature of the ion beam and to infer the required measurement time to reach a specific signal-to-noise ratio. In the rest of the section, the spectra are compared with the rovibronic simulation calculated with PGOPHER software⁵⁶ using the parameters of Fellows *et al.*³⁹ for the ground state and of Table I for the $\tilde{A}^2\Sigma^+(002)$ state.

B. Effect of the bias cell

The effect of the bias cell on the photodissociation spectrum of N_2O^+ has been studied. The improvement of the S/N by setting 0 V (DC off) or -250 V (DC on) on the central electrode of the bias cell is presented in Fig. 11(a) for the $\tilde{A}^2\Sigma^+(002) \leftarrow \tilde{X}^2\Pi_{3/2}(000)$ band. The time-of-flight spectra recorded for the same laser frequency are also presented in Fig. 11, with the bias cell at 0 V in panel (c) and -250 V in panel (b). On these panels, the black traces correspond to the absence of light and the green and blue traces are recorded with

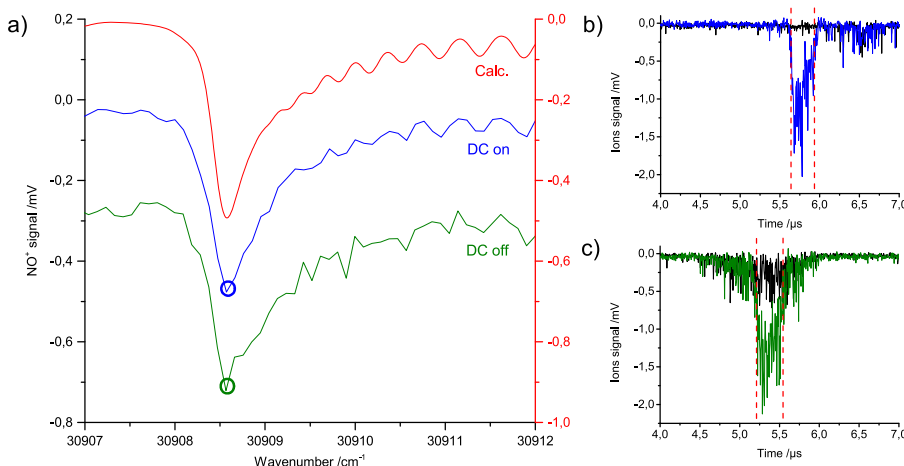


FIG. 11. (a) Q branch region of the $\tilde{A}^2\Sigma^+(002) \leftarrow \tilde{X}^2\Pi_{3/2}(000)$ photodissociation spectrum of N_2O^+ from bottom to top measured with the bias cell at 0 V (DC off) and at -250 V (DC on) and simulated using the PGOPHER software. The right y-axis used for the calculated spectrum (in red) is scaled on experiment. The experimental ion yields have been shifted vertically for clarity. Blue and green mass spectra of the panels (b) and (c) are the NO^+ fragments measured at the maximal intensity of the Q branch for the bias cell on and off, respectively. The mass spectra measured without UV laser are presented in black in panels (b) and (c).

the laser on. One can clearly notice in panel (b) the separation of the photodissociation fragments from the other fragments produced from collisions in the drift tube. This results in a S/N improved by a factor 4 in the photodissociation spectrum and a removal of the collisional background. The presence of ions generated outside of the laser interaction, observable at $6.5 \mu\text{s}$ in panel (b), is due to a still too large aperture at the exit of the 90° deflector (hole diameter of 12 mm). These residual ions can be rejected by the selection of a judicious integration time window. The combination of the bias cell and the choice of integration time window ensure thus a background free measurement.

C. Calibration of the frequency scale

The absolute frequency of the photodissociation spectra was calibrated using Ne lines⁵⁸ measured from a hollow cathode. This optical spectrum and the photodissociation spectrum were simultaneously measured. While the photodissociation spectra have been measured with a frequency doubling BBO crystal in the 307 nm–327 nm spectral range, the atomic Ne lines of the hollow cathode have been measured using the fundamental laser beam (614 nm–654 nm). The absolute calibration of the frequency scale has been performed using three neon lines (640.40177 nm, 650.83255 nm, and 653.46872 nm) with a standard deviation of 0.06 cm^{-1} .

In addition to the absolute calibration, a complementary Fabry Perot interferometer allowed us to check the linearity of the laser

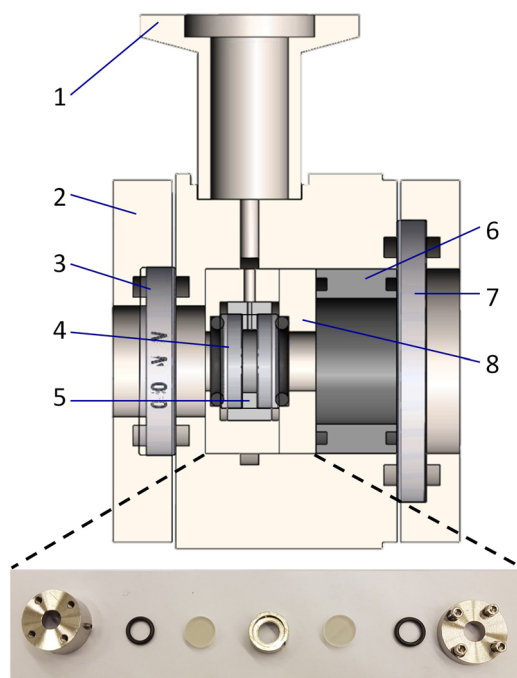


FIG. 12. Fabry Perot etalon composed of (1) KF fitting for etalon evacuation, (2) external chamber of a diameter of 2 in., (3) 1 in. wedged window, (4) 50:50 beam splitters AR coated for 400 nm–700 nm, (5) invar ring of 1.99 mm long, (6) PVC spacer to maintain the position of the stainless steel enclosure in the vacuum chamber, (7) 1.5 in. wedge windows, and (8) stainless steel enclosure. The exploded view of the etalon and its content is presented below.

frequency scanning using a solid state etalon presented in Fig. 12 (complete drawings are given in Figs. S1–S3 of the supplementary material). This interferometer has been designed using an invar ring of 1.99 mm separating two 50:50 beam splitters enclosed in a thermostatically controlled vacuum chamber ($313.0 \pm 0.1 \text{ K}$). The resulting Fabry Perot cavity has also been characterized with the fundamental laser beam (614 nm–654 nm) with a free spectral range of 2.507 cm^{-1} and a finesse of 4.4. The residuals of a linear fit performed on the interferences maxima allowed us to check the linearity of the laser frequency scanning with a standard deviation to linearity of 0.014 cm^{-1} and a maximum local deviation value of 0.04 cm^{-1} .

In addition, a Doppler effect arising from a slight deviation from the perpendicular arrangement between the laser and the ion beam has been estimated using a rooftop mirror for a double pass of the laser beam through the ion beam. The double pass spectrum has been reproduced with a linear combination of the single pass spectrum with itself minus 0.2 cm^{-1} . A frequency shift of $\pm 0.1 \text{ cm}^{-1}$ has been thus estimated for each path, and this corresponds to a tilt of 0.9° from a perpendicular configuration. Besides this effect, which can be corrected by subtracting 0.1 cm^{-1} to the frequency scale, the cumulative errors from relative ($\leq 0.04 \text{ cm}^{-1}$) and absolute (0.06 cm^{-1}) calibrations result in an estimated accuracy of 0.1 cm^{-1} on the calibrated frequency scale.

D. Rotational temperature

The background free measurement allowed us to measure the selected rovibronic band of N_2O^+ produced from the electric discharge in pure N_2O ($P = 5 \text{ bars}$) with a $S/N = 200$ and an acquisition average of 30 laser shots per frequency step (this represents one second per frequency step and a time of acquisition of $\approx 10 \text{ min}$ for each spectrum presented in Fig. 13). The rotational temperature can be obtained from a fitting procedure using the PGOPHER software,

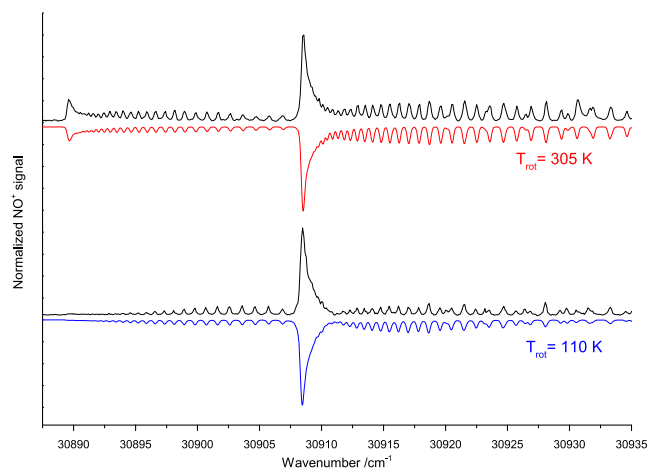


FIG. 13. The photodissociation spectra (black) have been measured from the interaction of the N_2O^+ beam with a doubled dye laser (0.6 mJ/pulse) by probing different part of the ionic beam using different ion extraction timings and distances between the nozzle and the skimmer. An average of 30 counts per laser step allowed us to reach a $S/N = 200$ for each spectrum. The simulations have been done for each measured spectrum using the PGOPHER software⁵⁶ for $T_{\text{rot}} = 305 \text{ K}$ (red) and $T_{\text{rot}} = 110 \text{ K}$ (blue).

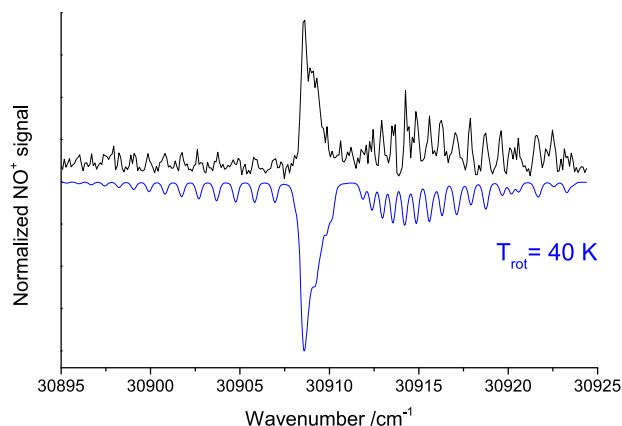


FIG. 14. Photodissociation spectrum (black) measured from a gas mixture of 1% N_2O with 99% Ar ($P = 5$ bars). The simulation (blue) has been done using the PGOPHER software⁵⁶ for $T_{\text{rot}} = 40$ K.

as well as the Gaussian linewidth and the baseline offset. Experimentally, the rotational temperature can be tuned in a certain range by probing different parts of the ion beam using different ion extraction timings and distances between the nozzle and the skimmer. The lowest mean rotational temperature for a pure N_2O expansion ($P = 3$ bars) is 110 ± 4 K and has been obtained using a distance of 1 cm between the skimmer and the nozzle. A maximum mean 305 ± 10 K has been obtained by adding a delay of $12 \mu\text{s}$ between the gas injection and the gating and by extending the distance between the nozzle and the skimmer to 2 cm. The higher temperature can be obtained from more collisions in the selected part of the jet. These two spectra are presented in Fig. 13. It was possible to lower the rotational temperature down to 40 ± 3 K by using a gas mixture of 1% N_2O with 99% Ar and a backing pressure of $P = 5$ bars while probing the early part of the expansion. This spectrum presented in Fig. 14 has been measured with a $S/N = 20$ for 30 shots per frequency step. This temperature is smaller by nearly one order of magnitude than the one reported recently by Hirota *et al.* for N_2O^+ using a cryogenic storage ring³⁵ even for long trapping times.

V. CONCLUSIONS

The versatile STARGATE instrument has been described in this article. The gas injection valve inspired from the work of Proch and Trickl²⁷ has been associated with a skimmer and an electric discharge or an electron gun to produce isolated or aggregated molecular anions and cations. The extraction, acceleration, bunching/gating, and re-referencing of the ionic beam associated with a TOF of $L = 1.5$ m allowed us to reach $R = 140$. Two mass selections performed by using a parallel plate deflector and a 90° toroidal field deflector associated with an energy tagging of the photodissociation fragments allow us to achieve background free rovibronic spectral measurements ($S/N = 200$). The molecular constants in the $\tilde{A}^2\Sigma^+(002)$ upper state have been improved from the analysis at 300 K of the $\tilde{A}^2\Sigma^+(002) \leftarrow \tilde{X}^2\Pi_{3/2}(000)$ and $\tilde{A}^2\Sigma^+(002) \leftarrow \tilde{X}^2\Pi_{1/2}(000)$ rovibronic bands. We have demonstrated that the rotational temperatures can be tuned from 40 K to 305 K. The lowest temperature has been obtained using a gas mixture of N_2O (1%)

carried by argon (99%) and by gating the beginning of the ion beam. The higher temperature has been obtained with a pure N_2O gas injection and by delaying gating with respect to the beginning of the gas pulse. This result opens up many perspectives. The lowest temperatures simplify dense rovibronic spectra and increase the S/N by populating fewer quantum states and may be used to promote partial condensation. The ability to produce higher temperature ions allows us to observe transitions associated with larger total angular momentum J values and hot vibrational bands for small molecular ions (3 to 4 atoms). Thus, additional information on the dynamics of the molecule can be extracted and additional lines can be assigned to help detecting molecular ions in relatively hot environments.

Concerning the possible improvements of our setup, the pulsed supersonic expansion could be improved by reducing the residual pressure in the extraction unit and in the drift tube, thereby limiting the number of detrimental collisions of the ions with the residual gas. Moreover, we have noticed a lack of stability in the design of Proch and Trickl²⁷ after a few hours of operation with an electric discharge. We thus plan to build a faster valve based on the design of Catanese *et al.*⁵⁹ in a near future, preferably used in combination with the electron gun. Shorter pulses are promising in terms of density and temperature and also since only $1.25 \mu\text{s}$ of the ion beam duration (for 1 keV N_2O^+) is selected by the gating bunching unit compared to $200 \mu\text{s}$ of pulsed gas injection. Furthermore, following the results of preliminary SIMION simulations, the MRP of our simplified TOF setup could be improved by using shorter cups. Finally, the sensitivity of the spectrometer could be ameliorated further by using a post acceleration of the ions⁶⁰ between the 90° energy analyzer and the MCP detector to increase the MCP detection efficiency.⁶¹

AUTHORS' CONTRIBUTIONS

R.B. and A.R. contributed equally to this work and should be both considered as first author.

SUPPLEMENTARY MATERIAL

See the [supplementary material](#) for the resulting line lists of N_2O^+ and the drawings of the solid state etalon.

ACKNOWLEDGMENTS

We are grateful to Professor Michel Herman (Université Libre de Bruxelles, ULB) and Professor Arnaud Delcorte (Université Catholique de Louvain, UCLouvain) for their useful comments all along this project. This work was funded by the Action de Recherches Concertées (Grant No. ARC iBEAM-18/23-090) and the Fonds de la Recherche Scientifique (FNRS) under Grant Nos. J.0179.18 and J.0129.20 and IISN Grant No. 4.4504.10. X.U. is a Senior Research Associate of the Fonds de la Recherche Scientifique (FNRS). We also thank the Wallonie-Bruxelles International excellence fellowship (session 2019) for partly funding the post-doctoral research stay of A.R.

DATA AVAILABILITY

The data that support the findings of this study are available from the corresponding author upon reasonable request.

REFERENCES

- ¹H. Andrä, *Progress in Atomic Spectroscopy* (Springer, 1979), pp. 829–953.
- ²M. Carré, M. Druetta, M. L. Gaillard, H. H. Bukow, M. Horani, A. L. Roche, and M. Velghe, *Mol. Phys.* **40**, 1453–1480 (1980).
- ³H. A. Schwarz, *J. Chem. Phys.* **67**, 5525–5534 (1977).
- ⁴M. Okumura, L. Yeh, and Y.-T. Lee, *Laser Spectroscopy VII* (Springer, 1985), pp. 122–125.
- ⁵M. Okumura, L. I. Yeh, J. D. Myers, and Y. T. Lee, *J. Chem. Phys.* **85**, 2328–2329 (1986).
- ⁶J. M. Lisy, *J. Chem. Phys.* **125**, 132302 (2006).
- ⁷M. G. White, R. A. Rosenberg, G. Gabor, E. D. Poliakoff, G. Thornton, S. H. Southworth, and D. A. Shirley, *Rev. Sci. Instrum.* **50**, 1268–1273 (1979).
- ⁸J. Lemaire, P. Boissel, M. Heninger, G. Mauclair, G. Bellec, H. Mestdagh, A. Simon, S. Le Caer, J. Ortega, F. Glotin *et al.*, *Phys. Rev. Lett.* **89**, 273002 (2002).
- ⁹L. I. Yeh, M. Okumura, J. D. Myers, J. M. Price, and Y. T. Lee, *J. Chem. Phys.* **91**, 7319–7330 (1989).
- ¹⁰T. G. Dietz, M. A. Duncan, D. E. Powers, and R. E. Smalley, *J. Chem. Phys.* **74**, 6511–6512 (1981).
- ¹¹K. LaiHing, R. G. Wheeler, W. L. Wilson, and M. A. Duncan, *J. Chem. Phys.* **87**, 3401–3409 (1987).
- ¹²J. B. Fenn, M. Mann, C. K. Meng, S. F. Wong, and C. M. Whitehouse, *Science* **246**, 64–71 (1989).
- ¹³M. F. Bush, J. T. O'Brien, J. S. Prell, R. J. Saykally, and E. R. Williams, *J. Am. Chem. Soc.* **129**, 1612–1622 (2007).
- ¹⁴A. Osterwalder, M. J. Nee, J. Zhou, and D. M. Neumark, *J. Chem. Phys.* **121**, 6317–6322 (2004).
- ¹⁵E. J. Bieske and O. Dopfer, *Chem. Rev.* **100**, 3963–3998 (2000).
- ¹⁶O. Asvany, E. Hugo, F. Müller, F. Kühnemann, S. Schiller, J. Tennyson, and S. Schlemmer, *J. Chem. Phys.* **127**, 154317 (2007).
- ¹⁷S. Chakrabarty, M. Holz, E. K. Campbell, A. Banerjee, D. Gerlich, and J. P. Maier, *J. Phys. Chem. Lett.* **4**, 4051–4054 (2013).
- ¹⁸E. K. Campbell, M. Holz, D. Gerlich, and J. P. Maier, *Nature* **523**, 322–323 (2015).
- ¹⁹O. Asvany, K. M. T. Yamada, S. Brünken, A. Potapov, and S. Schlemmer, *Science* **347**, 1346–1349 (2015).
- ²⁰C. E. H. Dessent and K. Müller-Dethlefs, *Chem. Rev.* **100**, 3999–4022 (2000).
- ²¹C. Lauzin, U. Jacovella, and F. Merkt, *Mol. Phys.* **113**, 3918–3924 (2015).
- ²²U. Jacovella, C. J. Stein, M. Grütter, L. Freitag, C. Lauzin, M. Reiher, and F. Merkt, *Phys. Chem. Chem. Phys.* **20**, 1072–1081 (2018).
- ²³D. M. Neumark, *Acc. Chem. Res.* **26**, 33–40 (1993).
- ²⁴H. S. Biswal, Y. Loquais, B. Tardivel, E. Gloaguen, and M. Mons, *J. Am. Chem. Soc.* **133**, 3931–3942 (2011).
- ²⁵I. Dyukova, E. Carrascosa, R. P. Pellegrinelli, and T. R. Rizzo, *Anal. Chem.* **92**, 1658–1662 (2020).
- ²⁶C. J. Gray, B. Schindler, L. G. Mígas, M. Pičmanová, A. R. Allouche, A. P. Green, S. Mandal, M. S. Motawia, R. Sánchez-Pérez, N. Bjarnholt *et al.*, *Anal. Chem.* **89**, 4540–4549 (2017).
- ²⁷D. Proch and T. Trickl, *Rev. Sci. Instrum.* **60**, 713–716 (1989).
- ²⁸M. Hosseinzadeh and A. Sadighzadeh, “Design and numerical simulation of thermionic electron gun,” *arXiv:1509.06363* (2015).
- ²⁹R. J. Cotter, *Time-of-Flight Mass Spectrometry* (ACS Publications, 1994).
- ³⁰C. J. Dedman, E. H. Roberts, S. T. Gibson, and B. R. Lewis, *Rev. Sci. Instrum.* **72**, 2915–2922 (2001).
- ³¹A. D. McNaught and A. Wilkinson, *Compendium of Chemical Terminology*, Computational Chemistry Terms Vol. 1669 (Blackwell Science Oxford, 1997).
- ³²C. J. Dedman, E. H. Roberts, S. T. Gibson, and B. R. Lewis, *Rev. Sci. Instrum.* **72**, 3718–3720 (2001).
- ³³H. Kreckel, H. Bruhns, K. A. Miller, E. Wählin, A. Davis, S. Höckh, and D. W. Savin, *Rev. Sci. Instrum.* **81**, 063304 (2010).
- ³⁴A. Dzhonson, D. Gerlich, E. J. Bieske, and J. P. Maier, *J. Mol. Struct.* **795**, 93–97 (2006).
- ³⁵A. Hirota, R. Igosawa, N. Kimura, S. Kuma, K. Chartkunchand, P. Mishra, M. Lindley, T. Yamaguchi, Y. Nakano, and T. Azuma, *Phys. Rev. A* **102**, 023119 (2020).
- ³⁶D. Klapstein and J. P. Maier, *Chem. Phys. Lett.* **83**, 590–593 (1981).
- ³⁷J. H. Callomon and F. Creutzberg, *Philos. Trans. R. Soc., A* **277**, 157–189 (1974).
- ³⁸C. E. Fellows and M. Vervloet, *Chem. Phys.* **264**, 203–209 (2001).
- ³⁹C. E. Fellows, *J. Chem. Phys.* **138**, 164316 (2013).
- ⁴⁰L. Lessa, A. Martins, C. Fellows *et al.*, *J. Chem. Phys.* **143**, 166101 (2015).
- ⁴¹L. Lessa, S. D. de Cândido, and C. E. Fellows, *J. Chem. Phys.* **140**, 214311 (2014).
- ⁴²M. A. Gharaibeh and D. J. Clouthier, *J. Chem. Phys.* **136**, 044318 (2012).
- ⁴³H. Herburger, U. Hollenstein, J. A. Agner, and F. Merkt, *J. Chem. Phys.* **151**, 144302 (2019).
- ⁴⁴W. Chen, J. Liu, and C. Y. Ng, *J. Phys. Chem. A* **107**, 8086–8091 (2003).
- ⁴⁵R. G. Orth and R. C. Dunbar, *J. Chem. Phys.* **66**, 1616–1620 (1977).
- ⁴⁶R. Frey, R. Kakoschke, and E. W. Schlag, *Chem. Phys. Lett.* **93**, 227–231 (1982).
- ⁴⁷M. Larzillière and C. Jungen, *Mol. Phys.* **67**, 807–837 (1989).
- ⁴⁸T. F. Thomas, F. Dale, and J. F. Paulson, *J. Chem. Phys.* **67**, 793–800 (1977).
- ⁴⁹M. Larzillière, S. Abed, M. Carré, M. L. Gaillard, J. Lermé, and M. Broyer, *Chem. Phys. Lett.* **119**, 55–60 (1985).
- ⁵⁰H. Xu, Y. Guo, Q. Li, S. Liu, X. Ma, J. Liang, and H. Li, *J. Chem. Phys.* **119**, 11609–11614 (2003).
- ⁵¹H. Xu, Y. Guo, Q. Li, Y. Shi, S. Liu, and X. Ma, *J. Chem. Phys.* **121**, 3069–3073 (2004).
- ⁵²S. Abed, M. Broyer, M. Carré, M. L. Gaillard, and M. Larzillière, *Chem. Phys.* **74**, 97–112 (1983).
- ⁵³M. Larzillière, M. Carre, M. L. Gaillard, J. Rostas, M. Horani, and M. Velghe, *J. Chim. Phys.* **77**, 689–693 (1980).
- ⁵⁴Z. Zhou, H. Liang, Z. Hua, S. Feng, D. Zhao, and Y. Chen, *J. Chem. Phys.* **150**, 226101 (2019).
- ⁵⁵H. Wang, X. Zhou, S. Liu, B. Jiang, D. Dai, and X. Yang, *J. Chem. Phys.* **132**, 244309 (2010).
- ⁵⁶C. M. Western, *J. Quantum Spectrosc. Radiat. Transfer* **186**, 221–242 (2017).
- ⁵⁷R. Igosawa, A. Hirota, N. Kimura, S. Kuma, K. C. Chartkunchand, P. M. Mishra, M. Lindley, T. Yamaguchi, Y. Nakano, and T. Azuma, *J. Chem. Phys.* **153**, 184305 (2020).
- ⁵⁸See https://physics.nist.gov/PhysRefData/ASD/lines_form.html for NIST atomic spectra database.
- ⁵⁹A. Catanese, S. Horton, Y. Liu, and T. Weinacht, *Rev. Sci. Instrum.* **89**, 103115 (2018).
- ⁶⁰J. A. Gibbard, A. J. Shin, E. Castracane, and R. E. Continetti, *Rev. Sci. Instrum.* **89**, 123304 (2018).
- ⁶¹R. Liu, Q. Li, and L. M. Smith, *J. Am. Soc. Mass Spectrom.* **25**, 1374–1383 (2014).



Contents lists available at ScienceDirect

Chemical Physics Letters

journal homepage: www.elsevier.com/locate/cplett

Research paper

The rotationally resolved symmetric 2OH excitation in H₂O-CO₂ observed using pulsed supersonic expansion and CW-CRDSA.S. Bogomolov^{a,b}, A. Roucou^c, R. Bejjani^c, M. Herman^d, N. Moazzen-Ahmadi^e, C. Lauzin^{c,*}^a Institute of Chemical Kinetics and Combustion, Institutskaya Str. 3, Novosibirsk, Russia^b Novosibirsk State University, Pirogova Str. 2, Novosibirsk, Russia^c Institute of Condensed Matter and Nanosciences, Université catholique de Louvain, B-1348 Louvain-la-Neuve, Belgium^d Spectroscopy, Quantum Chemistry and Atmospheric Remote Sensing (SQUARES), Faculté des Sciences, Université libre de Bruxelles (ULB), 50 ave. F-D Roosevelt, B-1050 Brussels, Belgium^e Department of Physics and Astronomy, University of Calgary, 2500 University Drive North West, Calgary, Alberta T2N 1N4, Canada

ARTICLE INFO

Keywords:

van der Waals complex
High-resolution spectroscopy
H₂O-CO₂
Solvation of CO₂
Supersonic expansion

ABSTRACT

The rovibrational band corresponding to a double excitation of the OH symmetric stretch of the H₂O unit in the H₂O-CO₂ van der Waals complex has been recorded using CW-CRDS and a pulsed slit expansion seeded in He. The set-up is presented. The rotational analysis of this band is detailed and the results of the global fit of these data with those of the other 2OH excitation band and of the ground vibrational states are reported including data from the literature. The tunneling frequency and the vibrational predissociation lifetime are shown to decrease with vibrational excitation.

1. Introduction

H-bonded and van der Waals molecular complexes have been the subject of constant interest in the literature to fill the gap between gas and condensed phases [1–3], to study intermolecular chemistry [4–6] and to investigate anomalous energy level structures [7]. Today, this interest is further supported by atmospheric and planetary motivations [8–12].

The H₂O-CO₂ van der Waals complex which we investigate in the present work is the first step in the solvation process of carbon dioxide and is an intermediate species on the reaction coordinate leading to the formation of carbonic acid (H₂CO₃) [13,14]. It demonstrates interesting intermolecular dynamics. It is also predicted to be one of the most abundant neutral hydrated complexes in our atmosphere [15].

H₂O-CO₂ has been studied in the microwave range [16,17] and the (001) ← (000) [18] and (010) ← (000) [19] transitions were investigated in the mid-infrared range, with transitions labeled in terms of the (ν₁ ν₂ ν₃) vibrational quantum numbers of the isolated water molecule. This complex was also studied in Ne matrices in the far-infrared [20] and mid-infrared [21] ranges and in N₂ matrices in the far-infrared region [22]. The intermolecular interaction between water and carbon dioxide was studied theoretically using *ab initio* methods by various authors (e.g. [23,24]).

H₂O-CO₂ presents a C_{2v} symmetry in which the two molecules are linked through an intermolecular bond between the O of H₂O and the C of CO₂, defining the *a* principal axis of inertia, with calculated interaction/dissociation energies of $De/D_0 = 1053/787 \text{ cm}^{-1}$ [24]. A more complete symmetry analysis requires considering the G₈ symmetry group, thus including internal rotation resulting from the permutation of the two hydrogens (or equivalently the two oxygens). This movement is indeed considered as *feasible* with a barrier predicted to be around 287 cm⁻¹ [17]. This internal rotation gives rise to a tunneling splitting of each ro-vibrational energy level into two components, with only one of them populated for each K_a parity, where K_a is the projection of the total angular momentum on the *a* principal inertial axis. Each tunneling component is associated to one nuclear spin isomer with statistical weights 1 and 3 for K_a even and odd, respectively as detailed in ([17,25]).

We already, recently reported on the high-resolution absorption spectrum of the H₂O-CO₂ van der Waals complex in the doubly excited OH stretch region (7240 cm⁻¹) [25]. The observation of two bands can be expected in this range, leading to transitions from the ground state to (200) (of *a*-type i.e. with ΔK_a even and ΔK_c odd) and to (101) (of *b*-type i.e. with ΔK_a and ΔK_c odd), with origins close to those in the water monomer, i.e. 7201.5 and 7249.8 cm⁻¹, respectively. The region instrumentally accessible at the time of these previous experiments was,

* Corresponding author.

E-mail address: clement.lauzin@uclouvain.be (C. Lauzin).<https://doi.org/10.1016/j.cplett.2021.138606>

Received 20 February 2021; Received in revised form 26 March 2021; Accepted 29 March 2021

Available online 5 April 2021

0009-2614/© 2021 Published by Elsevier B.V.

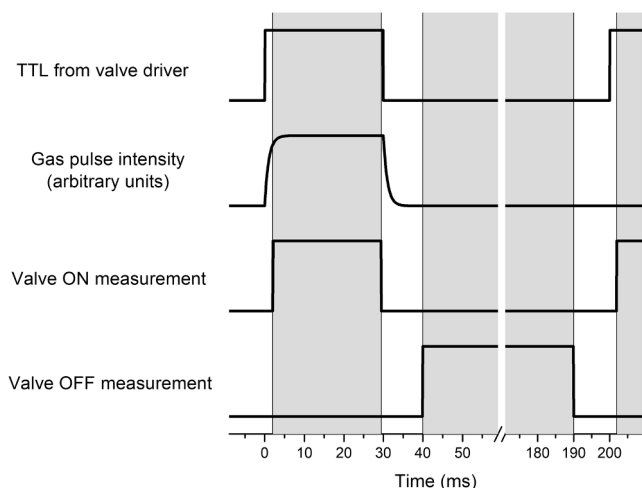


Fig. 1. Illustration of the data recording sequence used to investigate $\text{H}_2\text{O}-\text{CO}_2$ for a pulsed jet working at 5 Hz, the grey areas are measurement periods which allow to discriminate between gas pulse ON and OFF. The vertical axis is associated from the top to the bottom to, the voltage indicating the state of the TTL signal, the gas density in arbitrary units, the voltage of the programmed logic gates allowing to sort the ringdowns as a function of the valve condition, either for the valve ON or OFF.

however, limited to $7230\text{--}7260\text{ cm}^{-1}$ due to restricted available laser coverage, thus forbidding the observation of the lower energy band. Nevertheless, this previous investigation unexpectedly demonstrated the presence of two vibrational bands. As discussed in [25], both bands involve H_2O rather than CO_2 excitation. One of them was assigned to the $(101) \leftarrow (000)$ vibrational excitation. This assignment was based on the proximity in energy with the monomer band origin (red shift of 3 cm^{-1}) and on the observation of the expected b -type rotational structure. The second band, with origin at 7237.6 cm^{-1} could not be assigned to (200) . It is indeed 36 cm^{-1} blue shifted from the expected (200) value and shows b -type rather than the expected a -type structure. It was assigned as a combination band involving (200) and the lowest frequency intermolecular CO_2 libration, ν_{12} as calculated *ab initio* by Wang and Bowman [24] and Andersen et al. [20]. Transition to $(200) + \nu_{12}$ is expected to lead to a b -type band, as observed. The similar intensity observed for the two bands on the spectrum was explained through a Fermi-type resonance mixing the $(200) + \nu_{12}$ and (101) upper states. This assignment was presented as tentative until an a -type band could be reported, with intensity similar to that to (101) and with origin close to 7201.5 cm^{-1} , to be assigned to (200) . The aim of this work is to report on this observation.

The previous spectrum was recorded using the FANTASIO+, CW-cavity ring-down (CW-CRDS) spectrometer built and located at the Université libre de Bruxelles (ULB) [26]. We have again used this set-up, now moved to the Université catholique de Louvain (UCLouvain), using another DFB laser source to extend the wavelength range available and search for the expected $(200) \leftarrow (000)$ band. We also improved the set-up, resulting in a factor 2 increase of the signal-to-noise ratio (S/N), using a pulsed, rather than a continuous slit nozzle and a dedicated sampling procedure. It is described in the next section. The spectral analysis is detailed and discussed in Section 3. It includes a global fit of the data on the (200) state from the present work, on (101) from our previous study [25], and data on the ground vibrational state from the microwave literature [17].

2. Experimental procedure

The high-resolution spectrum of $\text{H}_2\text{O}-\text{CO}_2$ was recorded using (CW-CRDS) spectroscopy and the FANTASIO+ set-up [26]. The cavity mirrors

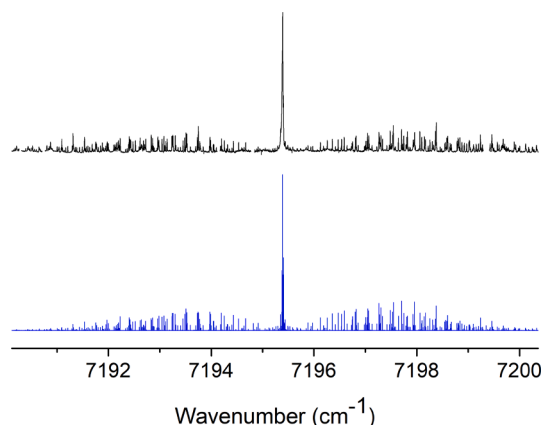


Fig. 2. Experimental spectrum (top) and simulation (bottom) of $(200) \leftarrow (000)$ in $\text{H}_2\text{O}-\text{CO}_2$. The simulation used the spectroscopic parameters from Table 1 and a rotational temperature of 15 K. On this Figure, the vertical axis is proportional to the absorption coefficient.

are mounted on a vacuum chamber pumped by two turbomolecular pumps with total pumping speed of 6400 l/s. The relative wavenumber scale is obtained by linearization of the frequency scale of spectra using the maxima of interference fringes from an evacuated Fabry-Pérot etalon fixed on an invar rod. The wavenumber scale is then absolutely calibrated using water monomer lines positions from the HITRAN database [27]. The measurement precision and accuracy are both estimated to 10^{-3} cm^{-1} . Further information on FANTASIO+ is available in the literature [26]. This set-up has been moved from ULB to UCLouvain and a previously missing DFB laser source was used to record the $(200) \leftarrow (000)$ vibrational transition of the water monomer in the $\text{H}_2\text{O}-\text{CO}_2$ complex.

We took this opportunity to implement a pulsed slit supersonic expansion, allowing the use of He as seeding gas. The gas mixture was composed of CO_2 0.86% and He as carrier gas and was bubbled through H_2O . The slit was assembled from pulsed Parker series 9 valve driven by IOTA ONE power supply, and a home-made multichannel block with 30 mm long and $50\text{ }\mu\text{m}$ spaced jaws similar to those developed in the University of Calgary [28]. The valve operates typically at 5 Hz with 30 ms pulse duration that allowed us increasing backing pressure up to 3

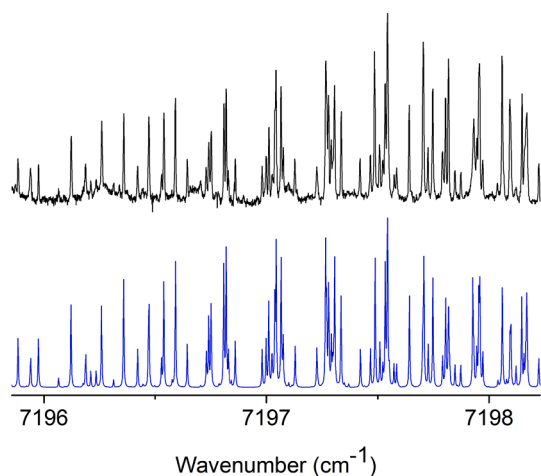


Fig. 3. Zoom in the $(200) \leftarrow (000)$ band of $\text{H}_2\text{O}-\text{CO}_2$ illustrating the agreement between experimental (top) and simulated (bottom) spectra using the constants in Table 1 and a rotational temperature of 15 K. On this Figure, the vertical axis is proportional to the absorption coefficient.

Table 1

Spectroscopic parameters for the ground, (200) and (101) states of H₂O-CO₂ resulting from a global fit procedure (cm⁻¹). Uncertainties in parentheses are 1σ from the least-squares fit. This fit reproduces the observed line positions with a root mean square (RMS) value of 7 · 10⁻⁴ cm⁻¹ (210 MHz) and 2 kHz for the overtone and microwave data, respectively.

	Ground state		(200)		(101)	
	<i>K_a even</i>	<i>K_a odd</i>	<i>K_a even</i>	<i>K_a odd</i>	<i>K_a even</i>	<i>K_a odd</i>
ν_0/cm^{-1}			7195.41414(20)	7195.39732(14)	7246.89497(19)	7247.08961(15)
A/cm^{-1}	0.3840905(12)	0.383647(12)	0.383769(48)	0.383390(18)	0.385458(19)	0.385513(13)
B/cm^{-1}	0.155921933(44)	0.15594370(22)	0.1559404(98)	0.1559425(40)	0.155130(12)	0.155134(13)
C/cm^{-1}	0.110220986(46)	0.11023029(21)	0.1101880(88)	0.1101971(45)	0.109583(13)	0.1097569(92)
$\Delta_K/10^{-5}\text{cm}^{-1}$	-1.054(31)	-1.046(37)	-1.63(39)	-1.191(44)	-0.626(73)	-0.82(10)
$\Delta_{JK}/10^{-5}\text{cm}^{-1}$	1.11650(14)	1.1154(14)	1.169(59)	1.1965(86)	0.683(49)	0.961(84)
$\Delta_J/10^{-7}\text{cm}^{-1}$	9.4785(21)	9.454(23)	10.04(42)	9.42(13)	9.26(83)	11.2(13)
$\delta_K/10^{-6}\text{cm}^{-1}$	7.833(13)	7.72(11)	6.29(62)	8.07(20)	13.6(14)	13.1(21)
$\delta_J/10^{-7}\text{cm}^{-1}$	2.8232(16)	2.81894(82)	3.51(26)	2.902(86)	3.35(61)	2.12(55)

Table 2

Tunneling splittings in excited vibrational states (*S'*) in H₂O-CO₂, as calculated from $\Delta\nu_0 = \nu_0(K_a''\text{even}) - \nu_0(K_a''\text{odd})$ values reported in the literature.

Vibrational state	$\Delta\nu_0 = \nu_0(K_a''\text{even}) - \nu_0(K_a''\text{odd})$	Splitting combinations	<i>S'</i> , considering <i>S''</i> = 0.1356(13) cm ^{-1e}
(010) ^a	0.0070(2)	<i>S''</i> - <i>S'</i>	0.129(2)
(001) ^b	0.268(1)	<i>S''</i> + <i>S'</i>	0.133(2)
(200) ^c	0.0168(3)	<i>S''</i> - <i>S'</i>	0.119(2)
(101) ^d	0.1948(3)	<i>S''</i> + <i>S'</i>	0.059(2)
(200) + ν_{12} ^d	0.1246(5)	<i>S''</i> + <i>S'</i>	-0.011(2)

^a From [19].

^b From [18].

^c This work.

^d From [25].

^e From [17,18].

bar and using He as seeding gas, instead of, previously [25], less than 1 bar and Ar, respectively.

Unexpectedly, the temperature estimated to be 15 K from the rotational structure of the recorded band, was not significantly decreased using this new pulsed He rather than the CW Ar seeded expansion [25].

Ringdowns are sorted following that the molecular beam is ON or OFF using TTL signal from the valve driver as illustrated in Fig. 1.

The ringdowns ON/OFF were measured in between 2/40 and 29.5/

190 ms after the TTL rise. These tunable time windows were implemented using an Arduino Uno and programmed digital logic gates. All other ring-down events were rejected due to unstable molecular beam conditions leading to the appearance of excessive noise on the baseline when one is making the difference between the inverse of ringdowns times for beam ON and OFF. The resulting improvement in S/N is estimated to be a factor 2 for the same measurement time. As with previous experiments reported using FANTASIO+, the rotational analysis demonstrated no sign of nuclear spin relaxation in the expansion [29].

3. Results

The newly observed band with origin at 7195.4 cm⁻¹ is presented in Figs. 2 and 3. It is thus close to the (200)←(000) vibrational excitation in the monomer (6.1 cm⁻¹ red-shift), with the required *a*-type structure and has similar intensity as that of (101). It can thus be reliably assigned to the symmetric 2OH excitation in H₂O-CO₂, i.e. (200)←(000).

As pointed out in the introduction, a single nuclear spin isomer needs to be considered for each *K_a* parity. The rotational analysis was thus performed separately for each isomer, using an asymmetric-top Watsonian [30] in the A reduction as implemented in the PGOPHER software [31]. The resulting assignments are listed in the supplementary materials.

The list of assigned lines shows that the present analysis involves values of the rotational quantum numbers with *J''* ≤ 19 and *K_a''* ≤ 6. This

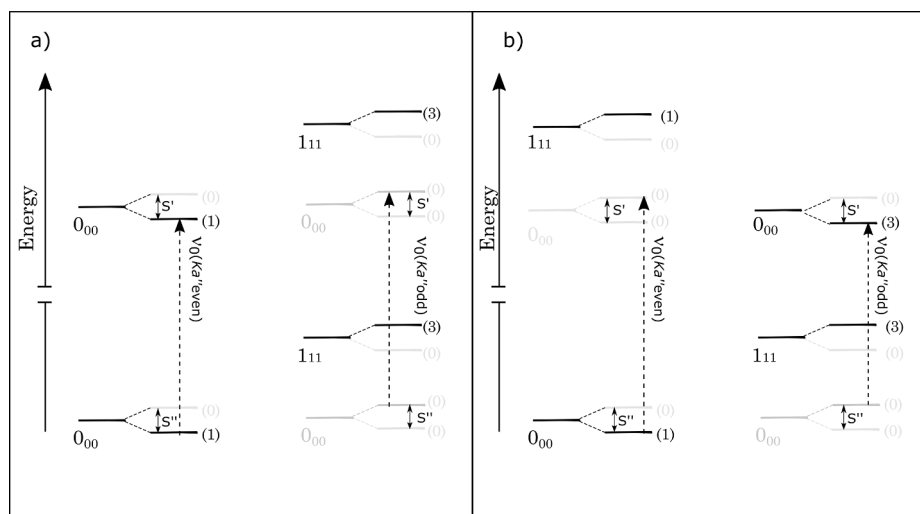


Fig. 4. Procedure for retrieval of tunneling splittings in excited (*S'*) vibrational states in H₂O-CO₂. The physical meaning of the band origins, determined from the fit procedure, depicted as dashed arrow in the figure, is presented for *a*-type transitions in panel a) and for *b*-type in panel b). In both cases non-existing levels are displayed transparently and the statistical weight is given in parenthesis.

is significantly higher than the microwave data in the ground state [17], in which $J'' \leq 6$ and $K_a'' \leq 4$. A global least-squares fit procedure combining the assignments was performed for (200), (101) and the ground state, using data from the present work, refs [25] and [17]. A weight proportional to the precision of the line measurement was given to each set of data. The 455 transition frequencies were used to fit 58 parameters, with a root mean square (RMS) value of $7 \cdot 10^{-4} \text{ cm}^{-1}$ (210 MHz) and 2 kHz for the overtone and microwave data, respectively. The resulting rotational constants for the ground, (200) and (101) states are listed in Table 1, together with their estimated uncertainty. Thanks to the global fit, those for (101) state are slightly modified compared to Table 2 in [25]. The excellent agreement between observed and simulated spectra for the (200) \leftarrow (000) band is illustrated in Fig. 3.

Concerning the microwave data, Columberg et al. [17] considered each K_a parity separately and developed a specific Hamiltonian taking into account the relaxation of the intermolecular distance during the internal rotation process. This Hamiltonian provided physical insights on the tunnelling process but was not mandatory to reproduce the measured line positions within experimental accuracy. The present, near infrared, data include significantly higher J , K_a values in the ground state and we found it adequate to use the same Watsonian to fit the rotational constants for all three states involved to improve the determination of the spectroscopic parameters. The band assigned to (200) + $\nu_{12} \leftarrow$ (000) in [25] was not included in this global fit because of the presence of various unraveled perturbations in this combination band.

The results do not show any evidence for local perturbations. The procedure to estimate the upper state vibrational predissociation lifetime from the experimental linewidths, as described in [32], was applied to the present data. It leads to values of the order of 1.0 ns from all lines in (200). This value does not differ to that in (101) nor in (200) + ν_{12} [25]. This result was to be expected since none of the vibrational excitation directly involves the intermolecular bond and therefore significantly favours shorter predissociation. The predissociation lifetime is thus, as expected, shorter than that for (001), estimated by Block et al. [18] to lie between 100 ns and 200 μs .

The difference between the (200) and (200) + ν_{12} band origins in $\text{H}_2\text{O}-\text{CO}_2$ allows refining the value of ν_{12} to 42.2 cm^{-1} , neglecting the contribution of anharmonicity ($x_{1,j}$). $x_{1,12}$ can actually be expected to be very small, typically 1% of the lowest frequency mode [33], thus less than 1 cm^{-1} .

Trends in the evolution of the tunneling dynamics with vibrational excitation in $\text{H}_2\text{O}-\text{CO}_2$ can be obtained by subtracting band origins ($J'' = J' = 0$) for K_a'' even and K_a'' odd, $\Delta\nu_0 = \nu_0(K_a \text{ even}) - \nu_0(K_a \text{ odd})$. K_a'' even and K_a'' odd values are associated to two different nuclear spin isomers, i.e. to two different molecules in a one to three proportion. It can be shown, see Fig. 4, that $\Delta\nu_0$ corresponds to the sum (for b -type) or difference (for a -type) of the energy splittings due to tunneling in the ground (S'') and excited (S') states. The splittings for all studied vibrational states are reported in Table 2. The value of S' can be calculated assuming $S'' = 0.1356 \text{ cm}^{-1}$ [17,18]. This value was derived from microwave [17] and infrared [18] studies and found to be in good agreement with the *ab initio* prediction [24] of the height of the potential barrier for internal rotation.

The S' values of (001) and (010) are equivalent within error bars and are lower than the value for the ground state. S' further decreases for (200) and even more dramatically for (101) and (200) + ν_{12} . The value of S' associated with this combination state should, however, be taken cautiously since the presence of severe perturbations in the band makes the related rotational parameters less reliable [25]. In any case, S' shows a decrease with vibrational excitation. Intramolecular excitation seems thus to hinder the tunneling dynamics, as observed for other dimers (i.e. $(\text{C}_2\text{D}_2)_2$ [34] and $(\text{HF})_2$ [35]).

In conclusion, the (200) \leftarrow (000) vibrational band in $\text{H}_2\text{O}-\text{CO}_2$ has been observed around the related excitation in the H_2O monomer, thus supporting the vibrational assignment of two additional bands previously reported in the same excitation range, (101) \leftarrow (000) and (200) +

$\nu_{12} \leftarrow$ (000). The frequency of the ν_{12} mode has been refined to 42.2 cm^{-1} . A set of rotational constants has been fitted simultaneously for (101), (200) and the ground vibrational states, providing RMS values of $7 \cdot 10^{-4} \text{ cm}^{-1}$ (210 MHz) and 2 kHz for the overtone and microwave data, respectively. The hindering of the tunnelling dynamics with the vibrational excitation has been highlighted. A shortening of the vibrational predissociation lifetime with the number of quanta of vibrational excitation has been confirmed, with no dependence on the nature of the OH stretch involved. Finally, we highlighted the changes in the FANTASIO + set-up, now using a pulsed slit and He gas in the expansion. These changes with further modifications will hopefully allow to observe larger clusters and more fragile complexes.

Declaration of Competing Interest

The authors declare that they have no known competing financial interests or personal relationships that could have appeared to influence the work reported in this paper.

Acknowledgments

A.B. thanks the financial support of Wallonie-Bruxelles international (WBI) and Uclouvain. A.R. thanks the support of WBI (session 2019). C.L. thanks the FNRS (under Grants n: J.0179.18, J.0129.20 and IISN convention n°4.4504.10) and the Communauté Française de Belgique (ARC IBEAM 18/23-090) for financial support. R.B. thanks UCLouvain for FSR PhD fundings. C.L. warmly thanks the Service SQUARES of ULB for the loan of the FANTASIO + set-up. N.M. thanks the financial support of the Natural Sciences and Engineering Research Council of Canada.

Appendix A. Supplementary material

Supplementary data to this article can be found online at <https://doi.org/10.1016/j.cplett.2021.138606>.

References

- [1] F.N. Keutsch, R.J. Saykally, Proc. Natl. Acad. Sci. USA 98 (2001) 10533.
- [2] J.N. Olliae, M. Dehghany, N. Moazzen-Ahmadi, A.R.W. McKellar, PCCP 13 (2011) 1297.
- [3] A.R.W. McKellar, Y. Xu, W. Jager, Phys. Rev. Lett. 97 (2006) 183401/1.
- [4] F. Madeja, M. Havenith, J. Chem. Phys. 117 (2002) 7162.
- [5] D.J. Nesbitt, Chem. Rev. 112 (2012) 5062.
- [6] C.T. Wolke, J.A. Fournier, L.C. Dzigan, M.R. Fagiani, T.T. Odbadrakh, H. Knorke, K.D. Jordan, A.B. McCoy, K.R. Asmis, M.A. Johnson, Science 354 (2016) 1131.
- [7] A. Barclay, A. van der Avoird, A. McKellar, N. Moazzen-Ahmadi, PCCP 21 (2019) 14911.
- [8] M.Y. Tretyakov, E. Serov, M. Koshelev, V. Parshin, A. Krupnov, Phys. Rev. Lett. 110 (2013), 093001.
- [9] T. Odintsova, M.Y. Tretyakov, A. Ziborova, O. Pirali, P. Roy, A. Campargue, J. Quant. Spectrosc. Radiat. Transfer 227 (2019) 190.
- [10] K. Pfeilsticker, H. Bösch, C. Camy-Peyret, R. Fitzenberger, H. Harder, H. Osterkamp, Geophys. Res. Lett. 28 (2001) 4595.
- [11] N.S. Shuman, D.E. Hunton, A.A. Viggiano, Chem. Rev. 115 (2015) 4542.
- [12] R. Wordsworth, Y. Kalugina, S. Lokshantov, A. Viginin, B. Ehlmann, J. Head, C. Sanders, H. Wang, Geophys. Res. Lett. 44 (2017) 665.
- [13] T. Mori, K. Suma, Y. Sumiyoshi, Y. Endo, J. Chem. Phys. 130 (2009), 204308.
- [14] T. Mori, K. Suma, Y. Sumiyoshi, Y. Endo, J. Chem. Phys. 134 (2011), 044319.
- [15] H.G. Kjaergaard, T.W. Robinson, D.L. Howard, J.S. Daniel, J.E. Headrick, V. Vaida, J. Phys. Chem. A 107 (2003) 10680.
- [16] K. Peterson, W. Klemperer, J. Chem. Phys. 80 (1984) 2439.
- [17] G. Columberg, A. Bauder, N. Heineking, W. Stahl, J. Makarewicz, Mol. Phys. 93 (1998) 215.
- [18] P.A. Block, M.D. Marshall, L.G. Pedersen, R.E. Miller, J. Chem. Phys. 96 (1992) 7321.
- [19] Y. Zhu, S. Li, P. Sun, C. Duan, J. Mol. Spectrosc. 283 (2013) 7.
- [20] J. Andersen, J. Heimdal, D. Mahler, B. Nelander, R.W. Larsen, J. Chem. Phys. 140 (2014), 091103.
- [21] P. Souillard, B. Tremblay, J. Chem. Phys. 143 (2015), 224311.
- [22] X. Zhang, S.P. Sander, J. Phys. Chem. A 115 (2011) 9854.
- [23] J. Makarewicz, J. Chem. Phys. 132 (2010), 234305.
- [24] Q. Wang, J.M. Bowman, J. Chem. Phys. 147 (2017), 161714.
- [25] C. Lauzin, A. Imbreckx, T. Foldes, T. Vanfleteren, N. Moazzen-Ahmadi, M. Herman, Mol. Phys. 118 (2019) 1.

- [26] K. Didriche, C. Lauzin, T. Földes, X. de Ghellinck D'Elseghem Vaernewijck, M. Herman, *Mol. Phys.* 108 (2010) 2155.
- [27] Q. Kou, G. Guelachvili, M. Abbouti Tamsamani, M. Herman, *Can. J. Phys.* 72 (1994) 1241.
- [28] J. Norooz Oliaee, PhD, University of Calgary, 2013.
- [29] M. Herman, T. Földes, K. Didriche, C. Lauzin, T. Vanfleteren, *Int. Rev. Phys. Chem.* 35 (2016) 243.
- [30] J.K.G. Watson, *Vibrational Spectra and Structure. A Series of Advances*, Elsevier, Amsterdam, 1977.
- [31] C.M. Western, B.E. Billinghurst, *PCCP* 19 (2017) 10222.
- [32] C. Lauzin, K. Didriche, P. Macko, J. Demaison, J. Liévin, M. Herman, *J. Phys. Chem. A* 113 (2009) 2359.
- [33] N. Moazzen-Ahmadi, A. McKellar, *Int. Rev. Phys. Chem.* 32 (2013) 611.
- [34] J.N. Oliaee, N. Moazzen-Ahmadi, A. McKellar, *Mol. Phys.* 110 (2012) 2797.
- [35] Z. Yu, E. Hammam, W. Klemperer, *J. Chem. Phys.* 122 (2005), 194318.

Titre : Conception, construction et validation d'instruments scientifiques pour étudier le spectre d'espèces ioniques froides.

Mot clés : Spectroscopie d'action, Spectroscopie d'absorption, Cavité optique, Laser, Photodissociation, Spectrométrie de masse, Ionisation, Transformée de Fourier, Jet supersonique, Tuyère de Laval, Optique d'ion.

Résumé : Ce travail de doctorat réalisé à l'UCLouvain et l'Université de Rennes 1, a exploré deux méthodes expérimentales pour étudier des ions moléculaires. Ces méthodes sont : la spectroscopie de photodissociation sur fond noir à l'UCLouvain, et la spectroscopie d'absorption amplifiée par une cavité à l'Université de Rennes 1. Dans les deux cas nous avons développé l'instrument de bout en bout.

Dans les deux cas afin de produire les espèces ioniques, un jet supersonique a été construit. À l'UCLouvain un jet libre pulsé a été développé pour augmenter la capacité du pompage. Un bon fonctionnement de la vanne pulsée pour une fréquence de répétition qui peut atteindre 1 kHz avec une durée d'impulsion minimale de 250 microsecondes a été démontré. La vanne pulsée est basée sur un dispositif piézo-électrique. Afin d'ioniser le gaz, deux méthodes d'ionisation ont également été testées. La première est une décharge électrique, réalisée en polarisant deux électrodes créant ainsi un champ électrique parallèle à l'expansion. La deuxième méthode consiste à utiliser un canon à électrons. Les électrons sont émis en chauffant un filament de tungstène, focalisés à l'aide de deux électrodes et accélérés à l'aide d'une électrode collectrice. Ainsi un croisement perpendiculaire du faisceau d'électrons et du jet conduit à la formation d'espèces ioniques et froides. Un écorceur a été introduit pour sélectionner la partie centrale et la plus froide de l'expansion, collimater le faisceau et assurer un pompage différentiel entre la chambre de la source et

celle du reste de l'instrument. Nous avons également mis en œuvre un spectromètre de masse à temps de vol (TOF) capable d'augmenter la résolution et constitué d'une unité capable d'accélérer, de regrouper et de ré-référencer le faisceau d'ions à la masse. Le design a été inspiré de celui de Dedman et al [C. Dedman, E. Roberts, S. Gibson, B. Lewis, Review of Scientific Instruments 72 (2001) 2915-2922]. Il est composé d'un ensemble d'électrodes polarisées capables de séparer les cations ou les anions en fonction de leur rapport masse/charge, et de définir un temps de départ pour la mesure du temps-de-vol. La conception a d'abord été simulée à l'aide du logiciel SIMION, puis elle a été testée expérimentalement. Une résolution temporelle élevée est en effet essentielle pour optimiser le recouvrement temporel et spatial des ions sélectionnés en masse avec l'impulsion du faisceau laser, qui dure quelques nanosecondes. Les spectres de masse enregistrés ont pu démontrer l'efficacité de la production d'agrégats d'eau protonés, de différents agrégats mixtes et d'anions. Nous avons également ajouté une lentille électrostatique afin de contrôler la divergence du faisceau. De plus, un déflecteur pulsé a été mis en œuvre afin d'aligner le faisceau d'ions, et d'avoir une première sélection en masse. Nous avons ajouté un tube de pompage différentiel pour obtenir un vide plus élevé dans la zone d'interaction du faisceau d'ions avec le laser. Nous avons également développé un déflecteur électrostatique à double focalisation à 90 degrés capable de sélectionner les fragments en fonction de leur

énergie, permettant une détection sur fond noir des fragments. Le spectre est obtenu en intégrant le signal de photo-fragments en fonction de la longueur d'onde du laser, sur une fenêtre temporelle ajustée. Les premiers tests ont été réalisés sur N_2O^+ . La photodissociation a été réalisée à l'aide d'un laser à colorant doublé en fréquence dans la gamme UV autour de 323 nm. La fragmentation laser de l'ion parent a conduit à la formation d'une espèce ionique (NO^+) et neutre (N). L'analyse du spectre mesuré permet d'estimer la température rotationnelle des ions à 40 K. Ce résultat est encourageant, et laisse percevoir la possibilité d'étudier d'autres ions moléculaire dans un futur proche.

La deuxième partie de ce travail consiste à développer un instrument pour étudier des espèces moléculaires pertinent en astrophysique par spectroscopie d'absorption à haute résolution dans la gamme du visible et proche-infrarouge.

En particulier, l'instrument développé aura pour but d'étudier les grandes chaînes de carbone anionique (C_3^- , C_4^- , C_6^- , C_8^- , C_n^-). En raison des effets de charge d'espace, la densité des espèces ciblées produites en laboratoire est extrêmement faible même dans une expansion supersonique. La source d'ions a été développée. La géométrie choisie était celle d'une tuyère de Laval planaire, adaptée pour atteindre une basse température (40 K). Dans une telle source, la température et la densité sont uniformes sur une longue distance. Le profil planaire est important pour avoir une plus grande distance d'interaction entre les ions produits et le laser. Ces ions sont produits en utilisant une décharge en courant continu couplée à la tuyère. En utilisant un laser supercontinuum comme source incohérente à large bande couplée à une cavité de haute finesse, nous pourrions caractériser ces espèces par spectroscopie. Le spectre d'absorption est obtenu à l'aide d'un

spectromètre à transformée de Fourier. L'optimisation et le développement de l'instrument consistaient à l'optimisation du couplage de la source laser et la cavité optique, et ensuite au spectromètre à transformée de Fourier. Nous avons été confrontés à certains problèmes, car l'émission de la source est faible dans le domaine visible (gamme des miroirs) par rapport à la région du proche infrarouge du coup on a choisi de travailler dans la région entre 650 et 1150 nm. Deux méthodes étaient testées afin d'enregistrer le spectre dans cette région. La première consistait à utiliser plusieurs filtres interférentiels pour couvrir cette région. La deuxième consistait à l'utilisation d'un prisme pour séparer spatialement les longueurs d'onde de cette région. Nous avons réussi à mesurer les spectres d'absorption statique du méthane et de l'acétylène afin de déterminer les paramètres de fonctionnement de l'instrument. La distance effective d'interaction est de 500-600 m, la réflectivité effective des miroirs dans cette région est de 0,9957 et la sensibilité de l'instrument est de $\alpha_{min} = 6.27 \times 10^{-7} \text{ cm}^{-1}$ à la température ambiante. Nous avons ensuite mesuré le spectre froid de l'acétylène. La température du spectre était d'environ 40 K. Ainsi que le spectre d'absorption du méthane à la température ambiante et et à basse température autour de 11250 cm^{-1} . La résolution était de 0.02 cm^{-1} pour ces mesures. En termes de perspectives, différentes améliorations sont envisagées dont un meilleur couplage entre le supercontinuum et le Fourier, cet instrument permettra, dans un futur proche, de réaliser la spectroscopie de chaînes carbonées anioniques. La décharge en utilisant un courant continu sur les électrodes au col de la tuyère est déjà installée et prête à être testée. De plus, les tests auront lieu dans des conditions appropriées de la tuyère de Laval en utilisant le système de guidage d'ion afin d'améliorer la densité des ions produits.